

**A DEXTEROUS SURGICAL ROBOTIC SYSTEM FOR
AUTONOMOUS MINIMALLY INVASIVE
ORTHOPAEDIC INTERVENTIONS**

by

Shahriar Sefati

A dissertation submitted to Johns Hopkins University in conformity with the
requirements for the degree of Doctor of Philosophy.

Baltimore, Maryland

March, 2020

© 2020 Shahriar Sefati

All rights reserved

Abstract

Continuum manipulators have become prevalent in many minimally invasive surgeries due to the advantages they offer, such as enhanced dexterity and better access to confined surgical sites. However, because of their compliant, flexible, and delicate structures, adaptation of these manipulators to orthopaedic interventions—where large contact forces are present—has not yet been apparent. A major challenge in these interventions is the constrained nature of the workspace where the CM may come into contact with the surrounding bone and tissue. As such, this work investigates control and sensing paradigms that enable the use of CMs for orthopaedic applications. In particular, a variety of highly flexible embedded fiber optic sensors, together with model- and data-driven frameworks for real-time shape sensing and contact detection, as well as motion control of the CM are presented and explored.

Motivated by less-invasive treatment of pelvic osteolysis (bone degradation) behind the acetabular cup during total hip revision surgery, a dexterous robotic system for autonomous debridement of osteolytic bone lesions in confined spaces is developed. The proposed redundant system comprises a conventional rigid-link robot with

ABSTRACT

a CM attached to its end. Concurrent control of the hybrid system is achieved via an optimization-based constrained controller that generates control commands on-the-fly during the surgery. The proposed system, allows the surgeons to impose a variety of safety, mechanical, and task-specific constraints to the execution of a desired debridement task. In an envisioned surgical scenario, the surgeon determines the surgical plan and continuously interacts with the system via a graphical user interface, while the robotic system performs the desired task autonomously (i.e. task-level autonomy). Through extensive simulation, as well as phantom and human cadaver experiments, it is shown that performance and dexterity of the developed flexible system are far superior than those of rigid instruments used in conventional treatment approaches.

ABSTRACT

Primary Reader and Advisor:

Mehran Armand, PhD

Research Professor

Department of Mechanical Engineering

Johns Hopkins University

Secondary Readers:

Russell H. Taylor, PhD

Johns C. Malone Professor

Department of Computer Science

Johns Hopkins University

Iulian Iordachita, PhD

Research Professor

Department of Mechanical Engineering

Johns Hopkins University

Acknowledgments

I would like to express my gratitude to all those individuals, without whom this work would have not come about. First and foremost, sincerest thanks to my advisor and mentor, Dr. Mehran Armand, for his tremendous support and guidance throughout my PhD life. It was for him that I had the opportunity to join one of the best places in the world to conduct research in medical robotics and learn from some of the most talented people around.

Secondly, I wish to specially thank Dr. Russell Taylor of Computer Science and Dr. Iulian Iordachita of Mechanical Engineering at Johns Hopkins University who not only accepted my offer to graciously take the time to read this dissertation and be on my defense committee, but more importantly provided me with invaluable academic, career and research feedback throughout the past couple of years as this work evolved.

Many thanks go to Rachel Hegeman, Dr. Farshid Alambeigi, Dr. Ryan Murphy, Paul Wilkening, Michael Pozin, Cong Gao, Qiaozhi Wang, Weiqi Wang, and Frederic Monet who closely collaborated with me and contributed to the development of this work. I have learned a lot from each and every one of them and for that, I am

ACKNOWLEDGMENTS

always grateful. I would like to thank current and former members of the Biomechanical and Image-Guided Surgical Systems (BIGSS) Laboratory, Joshua Liu, Mahsan Bakhtiarinejad, Alireza Chamani, Amirhossein Farvardin, Justin Ma, Robert Grupp, Wei-Lun Huang, and Wenhao Gao, for their support and help.

A huge thank you also goes to Anton Duguet of Laboratory for Computational Sensing and Robotics (LCSR) for working with me through software questions whenever I had them, and Demetries Boston of Johns Hopkins Bayview Medical Center for helping me during running the cadaver experiments. Special thanks to Mike Bernard and Kevin Adams of the Department of Mechanical Engineering, and to Lorrie Dodd, Alison Morrow, Ashley Moriarty, and Jordan Card of LCSR for taking care of the substantial load of administrative work.

My sincerest thanks go to my close friends, Javad, Gilda, Sahar, Lida, Hani, and Nikta, with whom we created and shared so many unforgettable moments in the past six years. It was for them that I was able to quickly settle down in Baltimore and endure the hardships of PhD life. Special thanks to Javad for all the random and academic discussions we had during our coffee breaks. I do hope we can continue to do so in the future. My deepest gratitude to my best friends from college and high school, Sina, Bardiya, Iman, and Amirhossein for showing me that geographical distances cannot get in the way of true friendship.

I am forever thankful to my beloved mother and father who have always supported me with their selfless devotion and endless love. They taught me how to respect the

ACKNOWLEDGMENTS

values of education and encouraged me in this journey since I was a child. The same goes for my brother and mentor, Shahin (also a graduate of LCSR), who has influenced me personally and academically in so many ways and helped me in becoming the person I am today. Thanks to Sadaf, my sister-in-law, whom I have learned a lot of things from and enjoyed so many moments with. Last but not least, my sincerest thanks to my lovely wife and partner in life, Parastoo, for always lifting me up when I am down, guiding me when I am lost, and encouraging me when I am doubtful.

Shahriar Sefati,

March 2020

Dedication

To my treasures in life: mom and dad.

Contents

Abstract	ii
Acknowledgments	v
List of Tables	xviii
List of Figures	xix
List of Acronyms	xxv
1 Introduction	1
1.1 Motivation	1
1.2 Objectives and Scope	4
1.3 Thesis Overview	5
1.4 Contributions	7
2 Background	9
2.1 Summary and Motivation	9

CONTENTS

2.2	Medical Background	10
2.2.1	Total hip arthroplasty	10
2.2.2	Revision total hip arthroplasty	12
2.3	Technical Background	15
2.3.1	Medical Robotics in Orthopaedic Interventions	15
2.3.2	Autonomy in Surgical Robotics	18
2.4	Conclusion	20
2.5	Acknowledgment	21
3	Surgical Workstation Overview	22
3.1	Motivation	22
3.2	Contribution	23
3.3	Envisioned Surgical Workstation	23
3.3.1	Envisioned System	23
3.3.2	Envisioned Surgical Scenario	27
3.3.2.1	Preoperative and Planning Module	28
3.3.2.2	Intraoperative Module	29
3.4	Developed System	30
3.4.1	Rigid-link Positioning Robot	30
3.4.1.1	Contribution	30
3.4.1.2	Choices of Manipulators	31
3.4.2	Continuum Manipulator	33

CONTENTS

3.4.2.1	Contribution	33
3.4.2.2	Design and Fabrication Iterations	33
3.4.2.3	Load Bearing	37
3.4.3	Flexible Debridement Instruments	39
3.4.3.1	Contribution	39
3.4.3.2	Design and Fabrication	40
3.4.4	Actuation Unit	42
3.4.4.1	Motivation and Contribution	42
3.4.4.2	Design and Fabrication Iterations	43
3.4.5	Sensing and Control	48
3.5	Conclusion	49
3.6	Acknowledgments	50
4	Sensor Designs	51
4.1	Motivation	51
4.2	Contribution	54
4.3	Background	55
4.4	Fiber Bragg Grating	58
4.4.1	Polycarbonate Tube Substrate	61
4.4.1.1	Sensor Modeling	63
4.4.1.2	Tube Material Selection	65
4.4.1.3	Tube Geometry and Fabrication	65

CONTENTS

4.4.1.4	Calibration Experiments	66
4.4.1.5	Results and Discussion	69
4.4.2	Notched Nitinol Substrate	70
4.4.2.1	Design Requirements	71
4.4.2.2	Substrate Design and Geometry	72
4.4.2.3	Sensor Characterization	73
4.4.2.4	Sensor Calibration	76
4.4.2.5	Results and Discussion	77
4.5	Distributed Sensing	80
4.5.1	Random Optical Gratings by Ultraviolet Laser Exposure . . .	81
4.5.1.1	ROGUE Writing	82
4.5.1.2	ROGUE fiber triplet	83
4.5.1.3	Results and Discussion	84
4.5.2	Interrogator Devices	86
4.6	Conclusion	87
4.7	Acknowledgments	89
5	Sensing Algorithms	91
5.1	Motivation and Background	91
5.2	Contribution	93
5.3	Model-Based Sensing	94
5.3.1	Motivation and Background	94

CONTENTS

5.3.2	Shape Reconstruction	97
5.3.3	Experiment Design and Setup	101
5.3.4	Ground Truth Data	102
5.3.5	Data Collection	104
5.3.6	Results and Discussion	105
5.3.6.1	Free Environment CM Bending	105
5.3.6.2	Constrained Environment With Obstacles	107
5.3.6.3	S-Bending	108
5.4	Data-Driven Sensing	112
5.4.1	Motivation and Background	112
5.4.2	Distal-end Position Estimation (DPE)	113
5.4.2.1	Linear Regression	117
5.4.2.2	Deep Neural Networks (DNNs)	118
5.4.2.3	Temporal Neural Networks (TNNs)	119
5.4.3	Shape Reconstruction	120
5.4.3.1	Experiment Design and Evaluation Criteria	121
5.4.3.2	Experimental Setup	123
5.4.3.3	Network Training Hyperparameters	124
5.4.3.4	Results and Discussion	124
5.4.4	Collision Detection	134
5.4.4.1	Background and Motivation	134

CONTENTS

5.4.4.2	Data-Driven Collision Detection	136
5.4.4.3	Dataset Creation	138
5.4.4.4	Gradient Tree Boosting	139
5.4.4.5	Real-time Sonification	140
5.4.4.6	Experiment Design	140
5.4.4.7	Experimental Setup and Software	142
5.4.4.8	Results	143
5.4.4.9	Discussion	146
5.5	Conclusion	147
5.6	Acknowledgments	150
6	Control	152
6.1	Motivation and Background	152
6.2	Contribution	155
6.3	Control Framework	156
6.3.1	Model-independent Control	156
6.3.1.1	Constraints	158
6.3.2	Model-dependent Control	160
6.3.2.1	Ground Truth Tip Position	161
6.4	Experiments	164
6.4.1	Model-independent Control Performance	164
6.4.1.1	Results and Discussion	165

CONTENTS

6.4.2	Comparison of Approaches	170
6.4.2.1	Results and Discussion	171
6.5	Conclusion	174
6.6	Acknowledgment	175
7	System Integration and Evaluation	176
7.1	Motivation	176
7.2	Contribution	177
7.3	Constrained Control Framework	178
7.3.1	Constraints	180
7.3.1.1	Programmable Remote Center of Motion	180
7.3.1.2	Hyperplane Virtual Fixture	181
7.3.1.3	Axis Range Virtual Fixture	182
7.3.1.4	Velocity Constraints:	183
7.3.1.5	Joint Limit Constraints:	184
7.3.2	Regularization	184
7.3.2.1	Redundancy Resolution	185
7.3.2.2	Stay Near Axis	185
7.3.2.3	Stay Near Pose	186
7.3.3	Infeasible Problem Recovery Strategy	186
7.3.4	Feedback	187
7.3.4.1	CM Feedback	187

CONTENTS

7.3.4.2	Robot Feedback	187
7.3.5	System Jacobian	189
7.3.6	CM Position Homing	190
7.4	Software	191
7.4.1	Architecture	191
7.4.2	GUI Design	192
7.4.3	Visualization	192
7.4.4	Simulation	194
7.5	Preoperative Clinical Steps	195
7.5.1	Hand-eye Calibration	197
7.5.2	Registration	198
7.6	Experiment Design and Evaluation Criteria	200
7.6.1	Constrained Workspace	203
7.6.2	Dexterity and Manipulability	203
7.6.3	Constrained Controller	204
7.6.4	Sensing	205
7.6.5	Planning and Debridement Performance	206
7.7	Results	207
7.7.1	Constrained Workspace	207
7.7.2	Dexterity and Manipulability	209
7.7.3	Constrained Controller	211

CONTENTS

7.7.4 Sensing	213
7.7.5 Planning and Debridement Performance	215
7.8 Discussion	223
7.9 Conclusion	226
7.10 Acknowledgment	227
8 Conclusion	228
8.1 Summary	228
8.2 Limitations and Future Work	231
Bibliography	234
Vita	272

List of Tables

4.1	Parameters used in the design and fabrication of the polycarbonate tube sensor.	66
4.2	Sensor bias computations for different combinations of fiber and NiTi wires used.	70
5.1	Review of FBG-based continuum manipulator DPE by different research groups (NR = not reported).	96
5.2	CM DPE (tip position) error in free and constrained environments using FBG and OFDR sensors.	110
5.3	CM shape deviation error in free and constrained environments using FBG and OFDR sensors.	111
5.4	Comparison of results for model-dependent and data-driven dpe and shape sensing in free and constrained environments. All units are millimeter.	126
5.5	Fault tolerance capability in CM DPE. Units are millimeters.	134
5.6	K-fold ($k = 4$) cross validation results for hyper-parameter tuning. . .	144
7.1	Comparison of the workspace coverage behind the implant for robotic system and rigid tool subject to axis range virtual fixture	209
7.2	Constrained Manipulability Index Comparison	211
7.3	Comparison of Joint Limits in Simulation and Hardware	213

List of Figures

2.1	Components of a THA implant.	11
2.2	Osteolysis occurring behind the acetabular implant after THA. (a) simulation, (b) X-ray image.	13
2.3	Example curette tool used in treatment of osteolysis during revision THA.	14
2.4	Acetabular component loosening X-ray.	15
3.1	Envisioned surgical workstation.	26
3.2	Cartoon illustration of the less-invasive treatment of osteolysis with a CM.	27
3.3	Developed surgical workstation deployed in a mock operating room.	31
3.4	Examples of positioning robots.	32
3.5	Continuum manipulator for orthopaedic interventions.	35
3.6	(a) Force test experimental setup, (b) close-up view demonstrating the force sensor and CM, (c) end-effector force test result during exertion of out-of-plane distal end force.	39
3.7	Flexible debridement tools.	41
3.8	First generation actuation unit. (a) simulation rendering, (b) developed system.	44
3.9	Second generation actuation unit. (a) simulation rendering, (b) developed system, (c) the collet mechanism restricting the axial and rotational motion of the CM.	46
3.10	Second generation actuation unit integrated with the UR-5 positioning robot.	48
4.1	Fiber Bragg Grating working principle.	60
4.2	Tube fiber optic sensor substrate. (a) Polycarbonate tube cross section under microscope, (b) assembled and fabricated sensor.	62
4.3	The integrated CM-sensor assembly inserted into the screw hole of an acetabular implant used in total hip arthroplasty.	63
4.4	(a) sensor calibration jig, (b) sensor-CM assembly calibration jig	67

LIST OF FIGURES

4.5	Calibration jig placed inside an enclosure to reduce temperature variation.	68
4.6	Top: Sensor calibration results. Bottom: Integrated sensor-CM calibration results	69
4.7	Fiber optic sensor with notched NiTi substrate.	72
4.8	Sensor symmetry validation experimental setup.	75
4.9	Notched NiTi Sensor characterization experiments results.	75
4.10	Notched NiTi Sensor calibration experiments results.	76
4.11	FBG sensors: (a) first generation using two NiTi wires, (b) second generation using polycarbonate tube substrate, (c) third generation using notched NiTi substrate, (d) polycarbonate tube cross section, (e) notched NiTi cross section.	79
4.12	Cartoon illustrating the different OFDR steps for a single sensor along the fiber's length. Steps are: (a) signal in the spectral domain, (b) signal in the spatial domain, (c) gauge length window in the spectral domain, (d) cross-correlation with the reference, (e) cross-correlation result and (f) spectral shift along the fiber's length. Steps (c) to (f) are repeated for every sensing point along the sensing region.	82
4.13	ROGUE writing setup.	83
4.14	Tomography calibration setup. The fiber triplet is held by two fiber clamps (PhotoNova Inc.) that are rotated by a stepper motor across 180°. Every 0.9°, a camera captures the transmitted image, magnified by a microscope objective. A 3-D printed triplet holder maintains the triplet in position, but allows it to rotate freely. The triplet is bathed in a refractive index matching liquid that diminishes the refractive index variation between the polymer and the ambient air.	85
4.15	Reconstruction of the fibers' position inside the triplet by tomography. The center and diameter of the fibers are shown by red dots and circles, respectively. Left: First iteration of the fiber triplet. The oval shape of the overall triplet can be observed. Right: Second iteration of the fiber triplet. As can be observed, the fibers' configuration is much closer to the optimal equilateral triangle.	86
4.16	Interrogator devices used for experiments.	87
5.1	(a) the FBG fiber triplet with three active areas, (b) the ROGUE fiber triplet with distributed sensing, (c) CM during articulation, (d) CM tip view showing the actuation cables, the FBG, and the ROGUE triplet integrated into the CM, (e) NiTi notch pattern in the CM design . . .	98
5.2	CM bending in a) free environment, and b) S-shape. The red markers are used in conjunction with a pair of stereo cameras as ground truth to compare the shape reconstruction.	103
5.3	Stereo camera pair setup.	104

LIST OF FIGURES

5.4	Custom-designed 3-D printed validation jig for the stereo pair setup. .	105
5.5	Stereo camera pair calibration procedure results.	106
5.6	Free-bending CM reconstruction using (a) the FBG-based sensor and (b) the ROGUE-based sensor. In both cases, the asterisk markers show the ground truth, obtained by the pair of stereo cameras, while the solid line show the reconstructed shape, in 2D.	107
5.7	CM shape reconstruction when interacting with obstacles using (a) the FBG-based sensor and (b) the ROGUE-based sensor. In both cases, the asterisk markers show the ground truth, obtained by the pair of stereo cameras. The solid lines show the reconstructed shape when the obstacle is placed at the tip of the CM, while the dashed line correspond to the shape when the obstacle is placed in the middle of the CM. The latter is translated by 6 mm in the graphs to avoid superposition of the plots.	109
5.8	CM S-bend reconstruction using (a) the FBG-based sensor and (b) the ROGUE-based sensor. In both cases, the asterisk markers show the ground truth, obtained by the pair of stereo cameras, while the solid line is the reconstructed shape. Individual plots are translated by 1 mm on the graphs to avoid superposition.	110
5.9	Top: DNN architecture. λ_n is the raw FBG vector at the n^{th} observation. \hat{p}_n is the network output CM tip position. Hyperparameters of the fully connected layers are listed under each block. Bottom: TNN architecture. The concatenation process is illustrated with the time-series data.	119
5.10	Experiments: (a-h) CM bending in constrained space in presence of internal disturbance (flexible tool) and external disturbance (obstacles at various locations), (i) CM bending in free environment, (j) demonstrating the the location of obstacles relative to the CM in cases a through h.	123
5.11	Loss function during training and validation.	125
5.12	Shape reconstruction results using the DNN, TNN, linear, and model methods for (a) experiment with obstacle, (b) free environment experiment with tool, (c) free environment experiment without tool. FBG measurements and the corresponding samples (stars) associated with the reconstruction results are shown in (d), (e), and (f).	128
5.13	Comparison of the absolute shape error using the DNN, TNN, linear, and model methods for (a) all the experiments with obstacles, (b) free environment experiments with tool, (c) free environment experiments without tool.	130

LIST OF FIGURES

5.14	Experimental setup and the proposed framework: preoperative phase involving model training using sensory data and camera images, and intraoperative phase for collision detection and sonification using only sensory data.	137
5.15	Image collision labeling based on number of connected components. Top and bottom rows demonstrate no collision and collision labels, respectively.	139
5.16	Regularization via shrinkage and subsampling to avoid overfitting and enhance generalization. X and Y axis correspond to boosting iterations and loss on test data, respectively.	143
5.17	Real-time collision detection on unseen data (unknown obstacle stiffness and location). CM collides with (a) hand (b) soft gelatin phantom, and (c) soft sponge foam.	146
6.1	Experimental setup for obtaining ground truth CM tip position using optical trackers. Coordinate frames are shown: optical tracker (o), reference body (r), CM straight pose body (s), and the base of the CM (b).	162
6.2	FBG sensor with Polycarbonate substrate integrated with the CM.	164
6.3	Interaction of the CM with soft obstacle.	166
6.4	The CM in interaction with hard obstacle: (a) straight configuration (b) bending configuration (c) x-ray image of the CM inserted into the screw holes of the acetabular component	166
6.5	(a) The CM tip traversed path for three target points in free bending environment, (b) the CM instantaneous configuration when the tip has reached the target points.	167
6.6	Model-independent controller repeatability experiment in free environment (a) changes in string length over time, (b) the estimated Jacobian over time.	168
6.7	(a) The CM tip transversed path for target point $p_3 = [-25, 16.2]$ mm in free bending, soft obstacle, and hard obstacle experiments, (b) the estimated Jacobian comparison in soft and hard obstacle experiments.	169
6.8	The CM Jacobian (J_C) components using the model-based and model-less estimation approaches in (a) free environment, and (b) interaction with obstacle. Path following using the model-based Jacobian in (c) free environment, and (d) interaction with obstacle.	173
7.1	RCM and plane virtual fixtures.	181
7.2	Axis range virtual fixture.	183
7.3	Chain of transformations in the combined system and the custom-designed optical tracker reflective geometries.	188

LIST OF FIGURES

7.4	The developed GUI. (a) Surgical inputs, (b) controller and feedback status window, (c) control window for starting/pausing the instrument as well as adjusting the motion speed and the surgical target points, (d) constraints and parameters window, (e) manual position and velocity control of the CM window, (f) manual UR control in joint space, (g) manual UR control in task space	193
7.5	The visualization window for intraoperative navigation.	195
7.6	The developed simulation environment. (a) accurate models of the positioning robot, the actuation unit, the acetabular implant, and the CM, (b) robotic system satisfying the RCM constraint, (c) the linearized RCM constraint using a prism with 8 faces and the closest point to the RCM on the end-effector shaft, (d) the axis range and plane VF.	196
7.7	Example of a digitization tool with reflective markers used for registration.	199
7.8	Osteolysis phantom 3-D printed from segmented CT.	201
7.9	Workspace comparison of the developed dexterous robotic system and rigid tools such as a curette in (a) and (b) during cadaver experiments, and in (c) and (d) during simulation experiments.	208
7.10	The constrained manipulability ellipsoid volume and semi-axes lengths for (a) combination of UR and CM, and (b) UR only. Figures on the right show snapshots of the evolution of the manipulability ellipsoid for the combination of UR and CM.	210
7.11	Performance of the controller in maintaining the constraints: (a) RCM VF, (b) axis range VF angle, (c) plane constraints bounding the CM's tip position.	212
7.12	Controller performance in executing various motions and surgical plans. (a) a spiral motion, (b) circle, (c) cube, (d) tracing the surface of the outlined osteolysis lesion on the preoperative CT, (e) executing the surgical plan during debridement of hard sawbone phantom	214
7.13	Experiments: (a) CM bending in free space, (e) and (j) colliding with soft obstacle, and colliding with hard obstacles (remaining cases). . .	215
7.14	The registration procedure. (a) digitization of the acetabular cup implant, (b) the overlayed digitized point cloud on the preoperative CT after registration.	216
7.15	Concurrent control of the robotic system during debridement tasks in phantom studies. (a) the experimental setup and the robotic system, (b), (c), (d), and (e) various successful surface debridement tasks on sawbone phantoms mounted on difficult-to-reach locations behind the acetabular cup	217

LIST OF FIGURES

7.16	Snapshots of the CDM insertion into the acetabular cup component and cutting of the PCF 10 saw-bone phantom based on the planned trajectory.	217
7.17	The cutting performance for saw-bone phantom PCF 10 (top row) and PCF 15 (bottom row). (a) and (e) the desired cutting trajectory and the tracked CDM tip position; (b) and (f) the generated task-space velocity; (c) and (g) CDM tip distance from the target points during cutting; d and h) the resulting cutting trajectory on the surface for the two phantoms.	219
7.18	Concurrent control of the robotic system during debridement tasks in osteolysis cadaver study. (a) the robotic system deployed in the operating room, (b) drilling task inside hard bone, (c) surface milling task of hard bone, (d) reaching extremely difficult points right behind the implant while milling hard sawbone phantoms.	220
7.19	Concurrent control of the robotic system during debridement tasks in cadaver study for core decompression of femoral head.	221
7.20	X-ray snapshots of two cadaver experiments demonstrating extreme reach and dexterity of the developed system for top row: core decompression of the femoral head osteonecrosis using the curved-drilling technique, and bottom row: less-invasive treatment of pelvic osteolysis behind the acetabular implant.	222

List of Acronyms

MIS	Minimally Invasive Surgery
CM	Continuum Manipulator
THA	Total Hip Arthroplasty
VF	Virtual Fixture
FOS	Fiber Optic Sensors
DPE	Distal-end Position Estimation
TKA	Total Knee Arthroplasty
CT	Computed Tomography
DOF	Degree of Freedom
RCM	Remote Center of Motion
NiTi	Nitinol
EDM	Electrical Discharge Machining
ID	Inside Diameter
OD	Outside Diameter

LIST OF ACRONYMS

PCB	Printed Circuit Board
EM	Electromagnetic
FBG	Fiber Bragg Grating
OFDR	Optical Frequency Domain Reflectometry
UV	Ultraviolet
SNR	Signal to Noise Ratio
ROGUE	Random Optical Gratings by Ultraviolet Emission
DNN	Deep Neural Network
TNN	Temporal Neural Network
TCN	Temporal Convolutional Network
MSE	Mean Squared Error
GUI	Graphical User Interface
ICP	Iterative Closest Point
PCF	Pounds per Cubic Foot

Chapter 1

Introduction

1.1 Motivation

Advances in robot-assisted surgery have focused on minimizing the invasiveness of a given procedure while also maintaining an optimal outcome [1, 2]. Over the past decades, minimally invasive surgery (MIS) has become an appealing trend in robotic surgery due to the many advantages it offers, such as reducing patient discomfort. Even though robotics has generally improved performance in MIS, adaptation to confined and difficult-to-access surgical sites has been limited [3]. To this end, continuum manipulators (CMs) have played a significant role in enhancing dexterity, workspace reach, and maneuverability in confined spaces during surgeries [3]. Examples of the use of CMs for these purposes can be found across surgical domains such as cardiac [4], abdominal [5], head and neck [6], and transnasal [7]; most of which are concerned with

CHAPTER 1. INTRODUCTION

soft tissues. In comparison to these surgical domains, orthopedic surgeries involve interactions of instruments with hard tissues and bone, resulting in significantly higher contact forces. Under these conditions, CMs must have much higher structural stiffness while also producing comparable curvatures as to maintain the advantages they have produced in other surgical fields. As such, despite all the benefits that CMs offer compared to conventional rigid-link robotic manipulators, their use in orthopaedic interventions has not yet been apparent [3].

Autonomous surgery involves the performance of tasks where part or all of the task is completed by an intelligent robotic system. There are several important advantages of automation in surgery, which include increasing task precision, improvements to surgical efficiency and execution, physiologic tremor filtering and motion scaling, and computer-aided guidance under various medical imaging and sensing modalities [2, 8–10]. Orthopaedics was one of the earliest medical applications for deployment of autonomous surgical robotics in the operating room [11]. A common feature among most of the robotic systems developed so far for orthopaedics, however, is the incorporation of rigid-link robots and instruments as the core system components. While these systems have potentially improved surgical outcome by introducing precision, increasing accuracy, and providing guidance and assistance to surgeons, several challenges and limitations associated with these systems remain unexplored [11]. A restricting factor in use of such systems in orthopaedic interventions is the limited dexterity and access to confined spaces in human anatomy. To

CHAPTER 1. INTRODUCTION

address such limitations, the goal of this research is to develop a surgical workstation that contains a dexterous redundant robotic system for autonomous removal of bone lesions in confined spaces by combining a conventional rigid-link robot for general positioning and a CM developed specifically for orthopaedic applications equipped with advanced embedded sensors.

An immediate orthopaedic surgery candidate that could benefit from the enhanced dexterity offered by the developed system is the treatment of osteolysis in total hip arthroplasty (THA) revision surgery [12]. After THA, the wear of the polyethylene liner leads to the formation of polyethylene particles that cause macrophage activation and consequently degradation of the bone surrounding the acetabular implant. Conventional treatment of osteolysis involves insertion of rigid instruments through the screw holes of the acetabular cup prosthetic. This allows debriding of the osteolysis when the acetabular cup is well-fixed and its detachment from the bone is not preferred due to the invasiveness of the procedure (e.g. damage to the healthy bone). However, a review of the literature indicates that on average, less than 50% of the lesion is successfully removed in this approach [13]. Additionally, there is no guarantee that only the undesired regions of bone and tissue (i.e. the lesions) are removed. The developed system in this research, on the other hand, leverages the high flexibility of the CMs to enable access to regions behind the acetabular cup that are difficult to reach with rigid instruments and also grants the surgeons great control over removing only the target points that they have identified as part of the lesion.

CHAPTER 1. INTRODUCTION

Other orthopaedic surgeries that could potentially benefit from flexibility and dexterity of the robotic system developed in this work include avascular necrosis of the hip [14, 15] (e.g., core decompression of the femoral head), benign lesion removal [16], treatment of metastatic bone disease [17], shoulder and knee arthroscopic surgeries [18, 19], or any other intervention that requires high dexterity and sufficient rigidity during interactions with hard lesions. Examples of such applications could extend to spine [20] and otorhinolaryngology interventions [21] (e.g. lateral skull base surgery).

1.2 Objectives and Scope

The goal of this research is to develop and evaluate a surgical workstation containing a dexterous redundant robotic system for autonomous removing of bone lesions in confined spaces by integrating a rigid-link robot for general positioning and a CM previously developed for orthopaedic applications [22–24]. The CM design allows for a great degree of flexibility and dexterity for enhanced maneuvers in confined spaces, yet sufficient rigidity during interactions with bone or hard tissues. A range of design and manufacturing techniques, as well as mechanics-based and data-driven algorithms are explored to integrate the CM with advanced miniature fiber optic sensing technology enabling real-time shape sensing and distal end position estimation with great accuracy. Flexible instruments with different functionalities and applications are fabricated to perform various debridement tasks while following the CM’s non-constant

CHAPTER 1. INTRODUCTION

curvature shape during articulation. The surgical workstation additionally includes a C-arm for optional intraoperative intermittent X-rays for navigation and monitoring purposes. An optimization-based multi-objective controller framework is designed and implemented to facilitate incorporation of various safety and surgical constraints in the form of virtual fixtures (VFs) applicable to the surgery. The controller generates joint-level velocity commands on the fly to drive the system autonomously toward desired surgical target points specified by the surgeon while satisfying the safety constraints. While the developed system and proposed strategies may be generally used in a variety of applications, this research focuses on less-invasive autonomous treatment of osteolytic lesions.

1.3 Thesis Overview

Chapter 2 orients the reader with medical and technical background associated with THA and history of medical robotics for orthopaedic interventions. Chapter 3 describes the envisioned surgical scenario and the mechanical components of the envisioned and developed surgical system. In particular, a brief history of the design iterations for each of the main components of the system is presented to familiarize the reader with the background and evolution of the system.

Chapter 4 introduces a variety of concepts for design of embedded fiber optic sensors (FOS) for CM sensing during large deflection bending. In particular, two sen-

CHAPTER 1. INTRODUCTION

sors using multi-point fiber optic technology and one sensor using distributed sensing technology are fabricated and calibration and characterization experiments are performed. Subsequently, Chapter 5 discusses various model- and data-driven algorithms for shape sensing, distal-end position estimation (DPE), and contact detection of the CM with the environment. Chapter 6 develops and compares model-dependent and model-independent closed-loop control of the CM in free and constrained environments using the FOS feedback.

Chapter 7 brings all the pieces from previous chapters together for developing and testing of a complete integrated system. The constrained concurrent control framework of the combined system (positioning robot and CM) with various constraints and strategies for autonomous performance of debridement tasks in confined spaces are introduced and discussed. The FOS feedback components developed in Chapters 4 and 5 are combined with the kinematics model and optical tracker feedback from the positioning robot and necessary calibration steps are described. Further, preoperative considerations for calibration, registration and preparation of the system as well as intraoperative steps toward execution of desired tasks are explained. The chapter is concluded with results from various simulation, phantom and human cadaver studies that evaluate the performance of the developed system.

Chapter 8 concludes the work, summarizing important development and inherent limitations. The chapter also identifies future directions for further advancement toward next generations of the workstation.

1.4 Contributions

The author's contributions include:

- Design, fabrication and characterization of different novel fiber optic embedded sensors that address the design criteria and fitting limitations of the non-constant large curvature CM under study, while simplifying the fabrication and CM assembly procedures.
- Development, implementation, evaluation and comparison of mechanics-based, model-dependent methods as well as data-driven supervised machine learning algorithms for shape sensing and contact detection of large curvature CMs both in free and constrained environments using FOS.
- Development and implementation of a simulation framework with real-time visualization for constrained concurrent control of the combined system (positioning robot and CM) using constrained optimization. In addition, implementation and evaluation of different strategies for regularization and recovery of the constrained control optimization problem from infeasible search space in the context of orthopaedic surgeries, particularly the less-invasive treatment of pelvic osteolysis.
- Development and integration of a complete dexterous robotic workstation for autonomous minimally invasive orthopaedic interventions using CMs, with a focus on the robotic-assisted treatment of pelvic osteolysis.

CHAPTER 1. INTRODUCTION

- Conducting extensive experiments in simulation environment, on simulated saw-bone phantoms, and on human cadaveric specimens to identify the performance of the system's components. In addition, experimental evaluation of the surgical workflow and clinical steps including the required calibration and registration procedures during phantom and human cadaver studies.

Chapter 2

Background

2.1 Summary and Motivation

The intention behind this chapter is to provide the reader with relevant medical and technical background associated with the contents of this thesis. The chapter begins by the medical background related to total hip arthroplasty (THA) and treatment of pelvic osteolysis. Conventional treatment methods are described and consequently the motivation behind the need for robotic systems leveraging the flexibility and dexterity of continuum manipulators (CMs) is made apparent. The second part of the chapter describes pertinent technical background about the history of medical robotics in orthopaedic interventions and the levels of autonomy in the state-of-the-art systems.

2.2 Medical Background

2.2.1 Total hip arthroplasty

THA is one of the most common orthopaedic surgeries with over 500,000 conducted annually in the USA and the UK [25]. The rate of primary THA is steadily increasing; there has been a 50% increase in the rate of primary THA from 1990 to 2002 in the USA to 69 per 100000 population [26]. Similar trends can be seen in other countries such as the UK, Finland, Norway, and South Korea [25, 27]. By 2030, a 174% increase of THA is expected when compared to 2005, resulting in 572,000 annual procedures [26]. Of note, there will also be an increase in procedures on younger populations with less than 65 years of age. These patients will make up 50% of THA by 2030 [28], leading to an increased timespan that patients live with implants.

The orthopaedic surgeon John Charnley is considered the father of the modern THA by introducing a low-friction prosthesis that consisted of a small-diameter femoral head and a polyethylene acetabular component [29]. The implant was set in bone using what is commonly referred to as bone cement (polymethylmethacrylate) [29, 30]. Even though different material choices were explored in future design iterations, the low-friction prostheses used today for THA contain identical basic components to the original implant proposed by Charnley (Fig. 2.1).

Severe osteoarthritis is the main condition for patients undergoing THA. Other less common causes include osteonecrosis (bone death), fracture, dysplasia (a shallow

CHAPTER 2. BACKGROUND

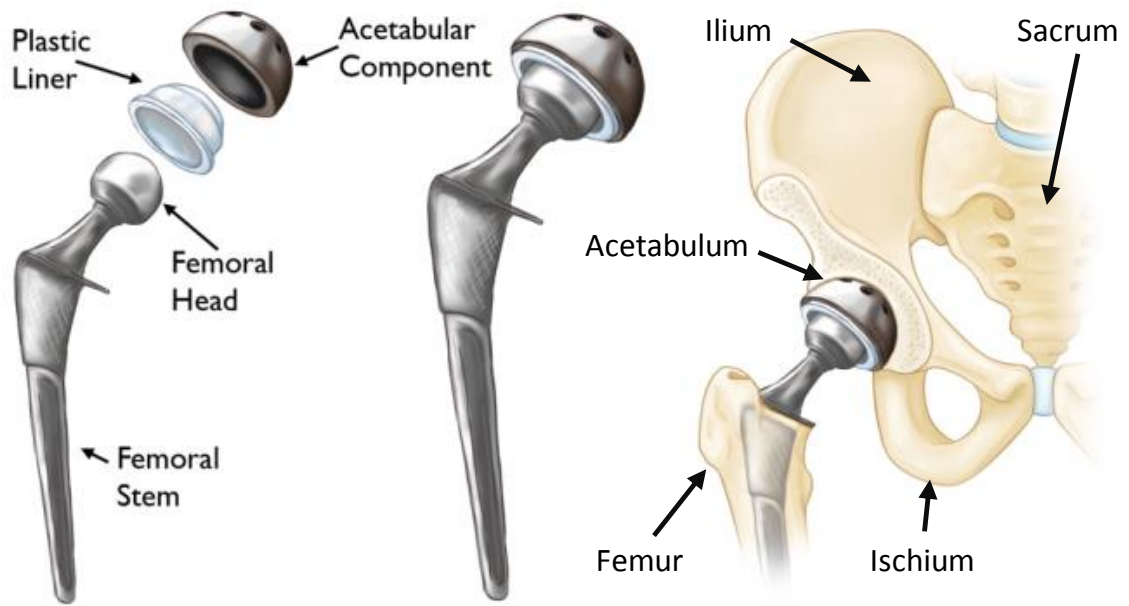


Figure 2.1: Components of an implant used in THA. Image courtesy of <http://orthoingo.aaos.org>.

hip socket) and bone tumors that break down the hip joint [28,31]. THA is typically considered when conservative treatments such as physical therapy, oral pain medication, and weight loss have been ruled out. In these situations, before undergoing surgery the patient continues to exhibit severe pain, stiffness, or limited ability to perform daily activities such as walking [31,32].

Generally, THA comes in two styles: cemented or uncemented [33]. In the cemented approach, bone cement (typically polymethylmethacrylate) is used to fix both the femoral and acetabular implants to the bone. The uncemented approach was developed to reduce complications such as infection and osteolysis (defined in Section 2.2.2) observed in initial uses of cemented implants. For an uncemented THA, surgeons press-fit implants with some surface coating to exploit bone growth into and

CHAPTER 2. BACKGROUND

around the implant. Uncemented implants, however, generally demonstrate poorer results compared with cemented implants [34].

2.2.2 Revision total hip arthroplasty

As with any other mechanical device, a THA can be subject to various forms of mechanical or biological failure. Such a failure may require a reoperation of the hip replacement, called revision THA, to address the cause of failure and its consequences. Although both THA and revision THA procedures have the same goals—to relieve pain and improve function and quality of life—revision surgery is different than primary THA. Revision hip replacement is a longer, more complex procedure. It requires extensive planning, as well as the use of specialized implants and tools. Much like primary THA, rates for revision THA have been increasing [26,28]. By 2030, revisions in the USA are expected to increase 137% to 96,700 operations annually [26].

The possible risks and complications of revision THA include: dislocation, infection, instability, mechanical loosening, implant failure, osteolysis, and fracture [28,31,35]. Many of these indications (instability, loosening, failure, and fracture) generally require replacement of the implant components. Osteolysis is the degradation of bone occurring at the bone-implant interface (Fig. 2.2). This degradation typically occurs due to wear of the polyethylene liner, cement, or metal, causing macrophage activation and osteoclast-mediated resorption [28,31,36,37]. This can occur in both cemented and uncemented implants [34,38].

CHAPTER 2. BACKGROUND

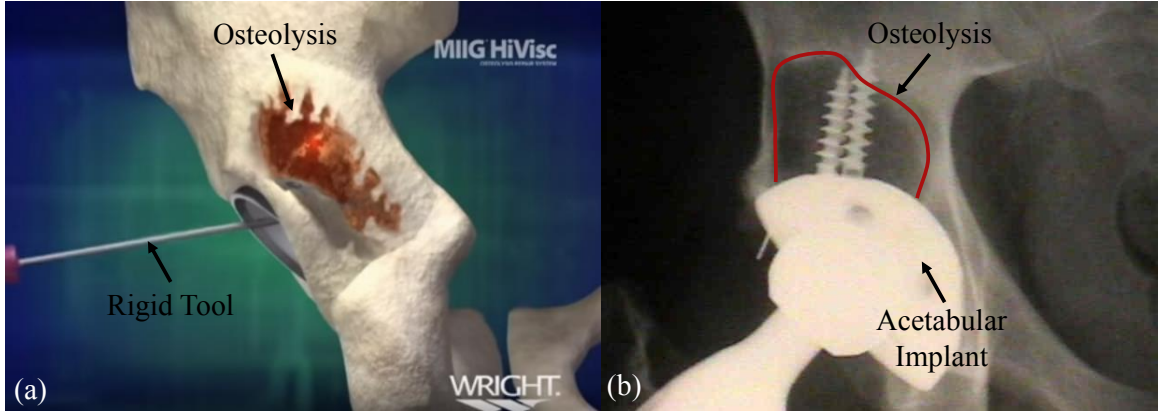


Figure 2.2: Osteolysis occurring behind the acetabular implant after THA. (a) simulation, (b) X-ray image. Images obtained and modified from <https://www.youtube.com/watch?v=Knv61EYQF-U&t=77s> and http://www.wheellessonline.com/ortho/thr_osteolysis

Early reports on the treatment of osteolysis advocated the removal of a well-fixed socket during revision surgery for osteolysis [39]. The removal of the implant allowed exposure of all the osteolytic areas to achieve complete debridement and grafting. However, potential damage and loss of the surrounding bone in this treatment approach may compromise placing of another acetabular component [40]. The more recently proposed less-invasive treatment, however, maintains the well-fixed acetabular component while replacing the liner and the ball of the femoral component [40,41]. In this approach, first an incision is made to obtain wide exposure of the periacetabular bone. This exposure is crucial to allow adequate observation for exchanging the liner, testing the acetabular for stability, and for debridement and bone grafting of osteolytic lesions [40]. The liner and screws are then removed from the acetabular implant to provide a pathway for surgeons to access and treat the osteolytic lesions. By inserting rigid tools such as curettes (Fig. 2.3) through the screw holes of the

CHAPTER 2. BACKGROUND



Figure 2.3: Example curette tool used in treatment of osteolysis during revision THA.

implant, surgeons debride the lesion and graft the bone. However, a review of the literature indicates that on average, less than 50% of the lesion is successfully removed in this approach [13]. This lack of success is likely due to the combination of complex lesion geometries and rigid tools used conventionally. Untreated osteolysis may lead to implant loosening (Fig. 2.4), which may require the more invasive complete component replacement. As such, enhancing the surgeon's access to lesion increases the chances of a better treatment and could potentially improve the outcome of the revision THA. It can further prevent potential future complications and reduce the need for traumatic revision surgery replacing these components.



Figure 2.4: Acetabular component loosening (arrow). Image courtesy of <https://orthoinfo.aaos.org/>.

2.3 Technical Background

2.3.1 Medical Robotics in Orthopaedic Interventions

Robotic technology is one of the fastest growing sectors within the healthcare industry [42]. Over the past decade, robots have augmented nearly two million surgical operations worldwide [11]. There are several important advantages of robot-assisted surgery, which include increasing precision due to sub-millimeter robot control, enhancing surgeons' ability to perform important and subtle tasks (e.g. by filtering hand tremor), promoting surgical safety and consistency, improving surgical efficiency and execution, and computer-aided guidance and navigation under various medical imaging and sensing modalities [8, 9, 43].

The global surgical robotics market is expected to increase substantially, growing

CHAPTER 2. BACKGROUND

from \$4.9 billion in 2016 to \$12.8 billion in 2021 and \$16.74 billion by 2023, with a cumulative annual growth rate of over 20% [44]. In particular, the knee and hip arthroplasty robotics market has grown from \$84 million in 2015 to \$375 million in 2017, and the global orthopaedic medical robots market is anticipated to reach between \$2 billion and \$4.6 billion over the next five to six years as a new generation of robotic devices, systems, and instruments is introduced to address a rising number of orthopaedic conditions [11].

Orthopaedics was one of the earliest medical applications for deployment of surgical robotics in the operating room [11]. ROBODOC (originally Integrated Surgical Systems Inc. Sacramento, CA, USA, currently TSolution One by Curexo Technology Corporation, Fremont, CA, USA) was the first commercially-available active medical robot in any discipline; which allowed precision planning and milling of the femoral component in THA and later Total Knee Arthroplasty (TKA) [45, 46]. CASPAR (Ortho-Maquet/URS Ortho Rastatt, Germany) was another early surgical system for image-guided THA and TKA similar to ROBODOC. Even though CASPAR for THA has been shown to increase the accuracy of femoral preparation, the increased surgery time, blood loss and higher complication rate ceased further clinical use of this system for THA [47, 48]. The Acrobot system (Acrobot Co Ltd., London, UK) was introduced in 1999 which used software based on computed tomography (CT) to accurately plan TKAs pre-operatively and guided the surgeon's hand motion with active constraints intra-operatively [48]. The Robtic Arm Interactive Orthopaedic System

CHAPTER 2. BACKGROUND

(RIO; MAKO Stryker, Fort Lauderdale, Florida), a haptic system, was developed in 2004 for THA and TKA [11, 49, 50]. It acts as a hand-held robotic device enforcing cutting boundary guides on the surgeon's hands via virtual fixtures (VFs) [48]. The iBlock robotic cutting guide (OMNIlife Science, East Taunton, MA, USA) is another example of orthopaedic surgical robotic systems that got FDA approval in 2010 for imageless, bone mounted femoral resections in TKA [48, 51]. The Navio PFS system (Smith and Nephew, London, UK), developed in 2012, is an example of a handheld open platform sculpting device for optimizing accuracy in implant positioning and safety in TKA [49]. ROSA robot (ROSA Knee Robot, Zimmer Biomet, Warsaw, IN, USA) is among the most recent systems developed for TKA that received 510 K approval from the FDA in early 2019 [52].

A common feature among all the above-mentioned robotic systems in orthopaedics is the incorporation of rigid-link robots and instruments as the core system components. While these systems have potentially improved surgical outcome by introducing precision, increasing accuracy, and providing guidance and assistance to surgeons, several challenges and limitations associated with these systems remain unexplored [11]. A restricting factor in use of such systems in orthopaedic interventions is the limited dexterity and access to confined spaces in human anatomy. To address these limitations, flexible robotics has shown great potential in minimally invasive surgery (MIS), laparo-endoscopic single site interventions and natural orifice trans-luminal endoscopic surgery [53–56]. However, despite all the benefits that flexible

CHAPTER 2. BACKGROUND

robotics offer compared to conventional rigid-link robotic manipulators, their use in orthopaedic interventions has not yet been apparent [3, 53].

2.3.2 Autonomy in Surgical Robotics

Robot autonomy refers to the performance of tasks where part or all of the task is completed by an intelligent robotic system [9]. Even though autonomy has been a familiar concept in surgical robotics since the early days, more attempts have been made recently to provide clearer definitions of different levels of autonomy in medical robots, as well as the associated regulatory and ethical considerations [9, 42, 57, 58], similar to other fast-emerging fields such as autonomous self-driving cars [59].

Surgical robotic systems can be divided to different classes depending on their level of dependence on human surgeon during the execution of surgical tasks. A broad classification of the surgical robots with respect to the system type includes autonomous, semi-autonomous, and passive robotic systems [60]. Another naming convention for a similar categorization proposes active systems, semi-active systems, and passive systems (from a surgical operation point of view rather than a mechanical definition) [45, 61]. In these definitions, an active (autonomous) system automatically performs an intervention, a semi-active (semi-autonomous) system performs the intervention under the direct control of the surgeon (e.g. a 'hands on' or 'cooperative control' mode with potential safeguards against motions beyond the surgical plan), while a passive system does not actively perform any part of the intervention (e.g.

CHAPTER 2. BACKGROUND

positions a tool guide). In this classification, the ROBODOC and CASPAR are examples of active (autonomous) system, while Acrobot and RIO are examples of semi-active (semi-autonomous) systems.

The level of autonomy with which a surgical robotic system can perform surgical tasks can be further categorized beyond only autonomous and semi-autonomous systems. Such a classification has been proposed in [9], dividing the levels of autonomy in surgical robotics systems to direct control, shared control, supervised autonomy, and full autonomy. Other such categorization in the context of regulatory, ethical and legal considerations has been proposed in [42, 62] which proposes six levels of autonomy for medical robots. The spectrum spans from level 0 (no autonomy or tele-operation) to level 5 (full autonomy with no human in the loop), with robot assistance, task autonomy, conditional autonomy, and high autonomy as the filling autonomy levels in between the two.

A great example of the level 0 (direct control or tele-operation) system is the da Vinci surgical system (Intuitive Surgical, Inc., Sunnyvale, CA) for minimally invasive laparoscopic surgeries. The Acrobat and RIO are examples of level 1 (robot assistance or shared control) systems where VFs and active constraints provide some mechanical guidance or assistance to the surgeon, and the ROBODOC is an example of a level 2 system with task autonomy (bone milling). Of note, the recent advent of deep learning methods with unprecedented access to data, as well as inexpensive and powerful computing hardware has the potential promise to bring higher level

CHAPTER 2. BACKGROUND

autonomous systems closer to reality. A level 5 surgical robotic system where the robot performs the surgery without the need of a human is, however, currently in the realm of science fiction [42].

With this background in mind, the goal of this research is to develop a surgical robotic system for orthopaedic applications with a focus on the less-invasive treatment of osteolysis that:

- Mitigates the problems associated with rigid-link robots and instruments by incorporating the enhanced dexterity and maneuverability offered by CMs.
- Assists the surgeon by executing their desired surgical plan autonomously (autonomy level 2), while they can supervise the surgery and intervene, if necessary.

2.4 Conclusion

This chapter provided the reader with a brief review of the medical background associated with primary and revision THA, as well as the technical background associated with medical robotic systems for orthopaedic interventions and definitions for different levels of autonomy. In particular, problems and limitations related to conventional rigid-link robotic manipulators and instruments were discussed. In consideration of such limitations, the important role of flexible robotics with high dexterity in the next generation of orthopaedic surgical systems is more apparent. The advantages associated with robot-assisted surgery as well as the different levels of

CHAPTER 2. BACKGROUND

autonomy in such surgical systems were discussed. With the provided background in mind, the goal of this research was outlined as developing an autonomous surgical robotic system for MIS orthopaedic interventions that leverages the flexibility and dexterity of CMs.

2.5 Acknowledgment

I would like to thank Drs. Paul Khanuja, Simon Mears, and Jyri Lepisto for their help in identifying the medical problems associated with osteolysis and Dr. Mehran Armand for proposing the ideas for the robotic-assisted treatment of osteolysis.

Chapter 3

Surgical Workstation Overview

3.1 Motivation

This chapter describes an overview of the envisioned and developed surgical workstation for autonomous minimally invasive orthopaedic interventions in confined spaces. The main design considerations of the system are originated from the requirements for the less-invasive treatment of pelvic osteolysis, even though different orthopaedic interventions (e.g. avascular osteonecrosis) could potentially benefit from the system. The envisioned preoperative and intraoperative steps necessary for the robot-assisted treatment of osteolysis are described. Several components of the system are introduced and the design and fabrication iterations (different generations of the components) are described. The components described herein include: the continuum manipulator (CM), flexible instruments, and the actuation unit. A brief overview of

the sensing and control strategies is also discussed, although thorough exploration of these components is postponed to chapters 4 through 6.

3.2 Contribution

A multitude of individuals were involved with the design and development of different components of the surgical workstation. A detailed list of the contributors is provided in each subsection of the chapter. The author integrated the overall surgical system and contributed to the development of many of the system's components, in particular, the design and characterization of the second generation of the CM and the actuation unit, design and manufacturing of the sensors, development and implementation of the control architecture and software development. Partial components of the work presented in this chapter were submitted to IEEE Transactions On Mechatronics which is currently under review [63].

3.3 Envisioned Surgical Workstation

3.3.1 Envisioned System

The envisioned surgical workstation consists of a redundant robotic system that could explore the anatomy of interest in presence of physical and safety constraints. To mitigate the challenges associated with the rigid-link robotic manipulators and

CHAPTER 3. SURGICAL WORKSTATION OVERVIEW

rigid surgical instruments, a CM exhibiting high dexterity and flexibility is incorporated as the main component of the system for navigation to difficult-to-access locations in the anatomy. To achieve redundancy to perform various surgical tasks, the CM is combined with a six- or seven-degree-of-freedom (DOF) positioning robot. The combined redundant system must then be controlled concurrently to leverage the redundancy of the system while satisfying several safety and physical constraints or virtual fixtures (VFs) to assist the surgeon. These constraints could broadly include:

- Position and velocity limits for the robotic system to avoid potential damages to the system.
- An adjustable programmable Remote Center of Motion (RCM) as the system entry point to patient's body or anatomy of interest.
- Potential task-space or joint-space VFs to limit the motion of the system (entirely or partially) to a desired allowable region.

To achieve precision and fast response in the design of such a controller, a reliable and robust feedback system is essential. A couple of important criteria must be taken into consideration for the feedback component of the system. In particular, the chosen sensing modality must:

- Comply with the flexibility and small size of the manipulator.
- Provide feedback with high streaming rate for incorporation into a real-time controller design.

CHAPTER 3. SURGICAL WORKSTATION OVERVIEW

- Not require a direct line of sight for sensing, since during surgery the manipulator and consequently the sensor are not visible from outside the patient body.
- Not interfere with (or be interfered by) medical sensing modalities present in the operating room such as Magnetic Resonance Imaging (MRI) or X-rays.

Another crucial aspect of the system being developed for orthopaedic interventions is the debridement instruments (tools). There are also certain criteria for designing these instruments for the envisioned system, namely they must:

- Comply with the flexibility and small size of the manipulator.
- Be compatible with different material hardness during debridement tasks (soft and hard tissue and bone).
- Provide sufficient torque for the debridement tasks while adopting to various shapes of the manipulator.

Appropriate actuation mechanisms must also be designed for the CM and accompanying flexible instruments. In particular, the system must include an actuation module for controlling of the CM and an actuation module for driving the instruments. Such an actuation unit device may be mounted on the end-effector of the rigid-link positioning robot and serves as the connecting component and integrator between the CM and the positioning robot.

The envisioned surgical workstation also includes an optional C-arm device for obtaining intermittent X-rays for navigation, registration, confirmation or alteration of

CHAPTER 3. SURGICAL WORKSTATION OVERVIEW

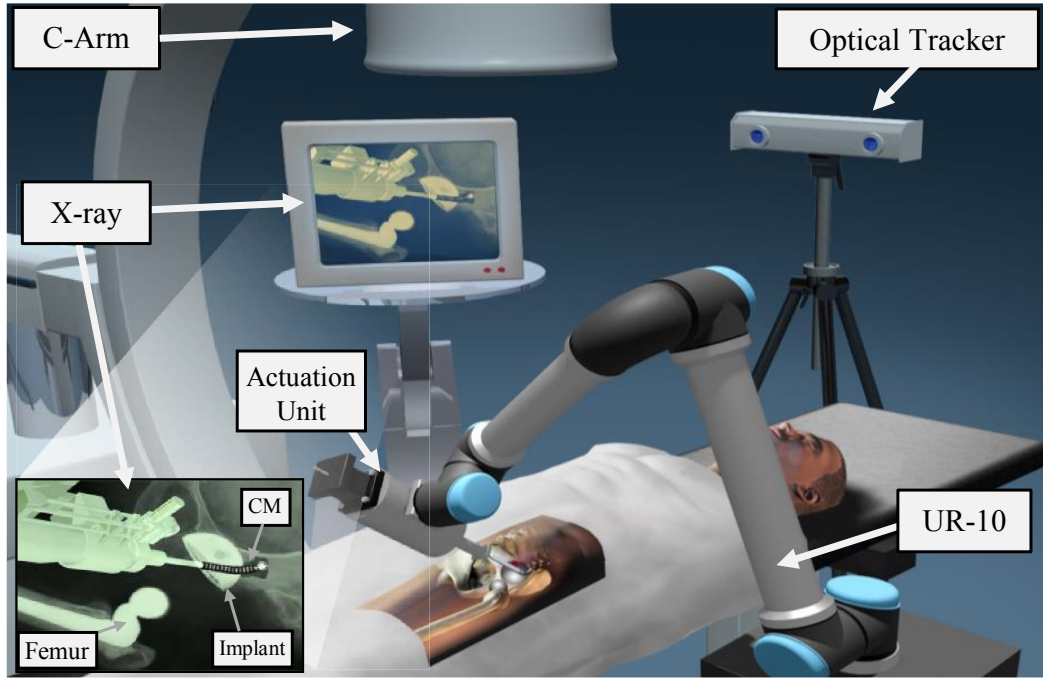


Figure 3.1: Envisioned surgical workstation.

the surgical plan, localization of the CM and instruments with respect to the anatomy and region of interest, and/or for updating the models associated with sensing and control. An optical tracking system is also present in the envisioned workstation for sensing, calibration, and registration purposes. Fig. 3.1 demonstrates the envisioned system and the above-mentioned components for the robot-assisted less-invasive treatment of pelvic osteolysis. In this illustration, a UR-10 robot (Universal Robots, Inc.; Odense, Denmark) has been used as the positioning robot. Fig. 3.2 also demonstrates a cartoon illustration of pelvic osteolysis, and how the CM is exploring the region behind the acetabular implant.

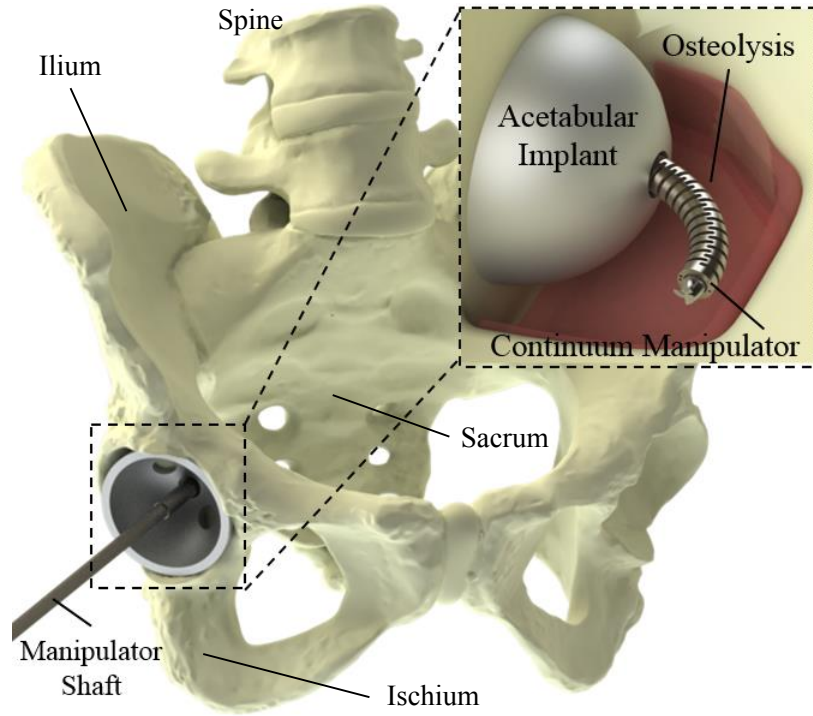


Figure 3.2: Cartoon illustration of the less-invasive treatment of osteolysis with a CM.

3.3.2 Envisioned Surgical Scenario

Our envisioned scenario for the robot-assisted less-invasive treatment of osteolysis would require obtaining a model of the lesions to be removed from behind the acetabular cup implant from computed tomography (CT), or multiple X-ray images. Given proper calibration between the CM and the positioning robot, the combined robotic system will be concurrently controlled to bring the CM's distal end (tip) to the target points, as digitized by the surgeon in the preoperative model, while the flexible instruments passed through the CM debride the lesions. The control loop is closed with the CM tip position feedback from the embedded sensor supplemented

CHAPTER 3. SURGICAL WORKSTATION OVERVIEW

by an optical tracker, intermittent X-ray imaging, and/or endoscopic view, if desired. In addition, appropriate VFs are incorporated into the control algorithm so that the CM can approach and insert the cup screw hole without any collision to the cup, while ensuring safety features to avoid any damage to the patient, rigid-link robot, or the CM. It is worth noting that the key challenge of this procedure is the use of a CM integrated with flexible cutting instruments to interact and accurately mill/drill the sclerotic wall (hardened tissue) surrounding the lesion. The sclerotic wall, a hard material, may cause buckling and undesired behavior of the CM and its flexible instrument during the procedure. Of note, successful osteolytic lesion treatment using this surgical robotic system is dependent on the well-defined performance of all the involved components.

3.3.2.1 Preoperative and Planning Module

A clinical use-case of the system begins with the preoperative and planning module during which the following steps are performed:

- Obtaining a preoperative CT from the anatomy of interest.
- Planning and annotating the desired region (points) of debridement on the preoperative CT by the surgeon.
- Determination of the desired safety and physical constraints as well as VFs such as forbidden regions to be enforced by the surgical system during the surgery.

- Calibration and preparation of the embedded sensors and flexible tools.
- Determination of the transformation between the positioning robot and the CM by performing a hand-eye calibration procedure [64].

3.3.2.2 Intraoperative Module

For execution of the preoperative plan, the robotic system must be registered to the patient (anatomy). The registration step can be performed using either an image-based or image-free approach. In the image-based approach, a 2-D/3-D registration algorithm (e.g. [65,66]) can use the CM as a fiducial to determine the transformation between the preoperative CT, the X-ray projection, and the patient's anatomy. In the image-free approach, an optical tracker together with a digitization tool could be used to touch the surface of the anatomy or implant and collect a 3-D point cloud. A point cloud to surface registration algorithm [67] can then be used to determine the transformation between the coordinate frame of the preoperative CT and coordinate frame of the optical tracker. A hand-eye calibration [64] could further be incorporated to establish the transformation between the robotic system (hand) and the optical tracker (eye).

Once the patient's anatomy is registered to the preoperative CT and proper calibration between the CM and the positioning robot is obtained, the robotic system traces and removes the surgical target points outlined by the surgeon autonomously while ensuring the safety features to avoid any damage to the patient or the system.

CHAPTER 3. SURGICAL WORKSTATION OVERVIEW

The surgeon can intervene at any given point to pause and resume the debridement task, adjust the overall speed of the task execution, modify or skip the pre-planned target points, or even alter the surgical plan completely. Once the surgical plan is executed, the robotic system is retracted from the anatomy and the treated region behind the acetabular implant is grafted.

3.4 Developed System

The following describes the efforts in bringing the envisioned surgical workstation and its components from Section 3.3 to reality. In particular, a range of hardware components of the system such as the CM, rigid-link positioning robot, flexible tools, and actuation unit along with different design iterations are discussed. Further, the sensing modalities, control and software architecture are briefly described (thorough description of these components is postponed to later chapters). Fig. 3.3 shows the developed surgical workstation deployed in a mock operating room.

3.4.1 Rigid-link Positioning Robot

3.4.1.1 Contribution

The author was responsible for integration and bringing about the envisioned system using the UR-5 robot for initial phantom experiments and the UR-10 robot for

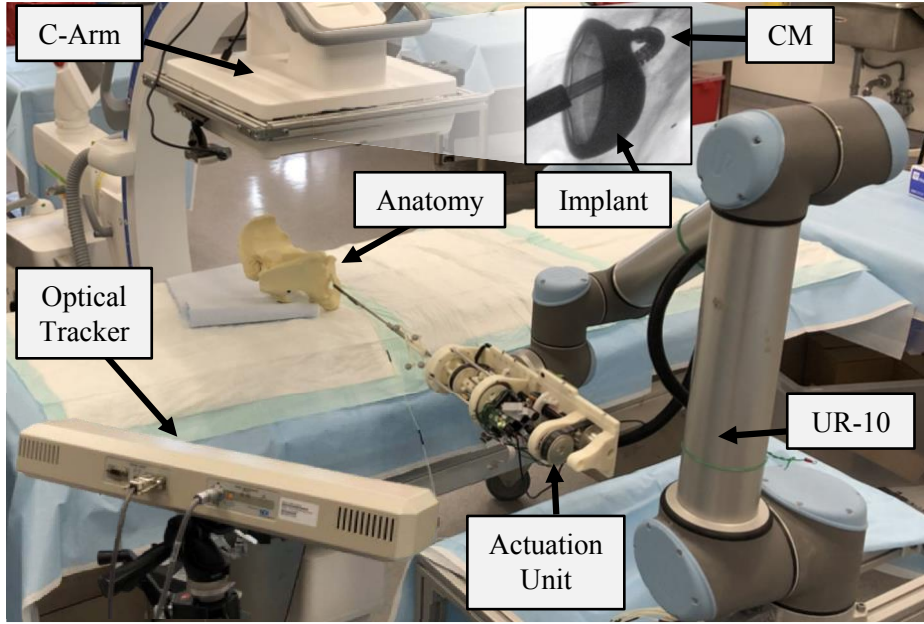


Figure 3.3: Developed surgical workstation deployed in a mock operating room.

further phantom experiments, as well as human cadaver experiments. Additionally, the author tuned and optimized the controllers using each of these robots for the less invasive treatment of osteolysis. Dr. Ryan Murphy and Mr. Paul Wilkening implemented the software for kinematics of the robots and Ms. Rachel Hegeman helped with modifying the software for the robot communication.

3.4.1.2 Choices of Manipulators

The envisioned surgical robotic workstation includes a rigid-link robot for positioning the CM to desired surgical sites. Integration of such robot with the CM brings about additional degrees of freedom for the combined system resulting in a redundant robotic system. Presence of such redundancy is extremely beneficial particularly

CHAPTER 3. SURGICAL WORKSTATION OVERVIEW

when the system is subject to constraints such as a programmable RCM in minimally invasive interventions. As such, a number of different robotic manipulators such as the UR-5 or UR-10 (Universal Robots, Inc.; Odense, Denmark), the lightweight LBR Med robot (KUKA; Ausberg, Germany), the Panda robotic arm (Franka Emika; Munich, Germany) or any other robotic manipulator with six or seven degrees of freedom could be used for positioning the CM in the desired surgical workspace. Fig. 3.4 shows a few of such potential choices. While the algorithms and methods proposed and described in this dissertation are independent of the choice of the rigid-link positioning robot, the UR-5 and the UR-10 manipulators were chosen as the positioning robots to develop the surgical workstation and perform phantom and cadaver evaluation experiments, respectively.

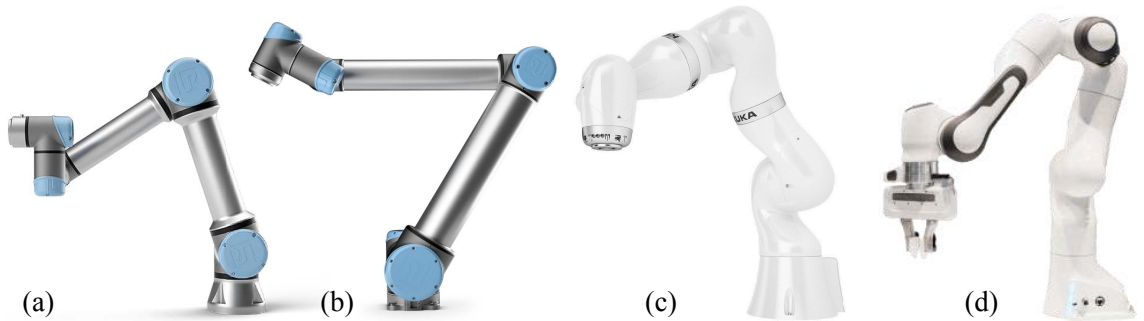


Figure 3.4: Examples of positioning robots. a) UR-5, b) UR-10 (courtesy of Universal Robots, Inc.), c) LBR Med Robot (courtesy of KUKA), d) Panda robotic arm (courtesy of Franka Emika)

3.4.2 Continuum Manipulator

3.4.2.1 Contribution

The original design and manufacturing procedure of the CM used throughout this dissertation was proposed by Kutzer et al. [23]. The second (and current) design iteration of the CM was introduced to address several difficulties associated with the previous manufacturing approach and mitigate the challenges during integration and deployment of the embedded sensors into the manipulator. The author was responsible for the design aspects of the manipulator from the sensor integration standpoint, while Dr. Farshid Alambeigi came up with the design and Dr. Yu Wang and his team at Beihang University in China manufactured the CM from the design concept. The author also performed the evaluation experiments for load bearing capabilities of the CM.

3.4.2.2 Design and Fabrication Iterations

The design concept for the cable-driven CM used in this dissertation was first developed by Kutzer et al. [23] for orthopaedic applications where relatively large interaction forces are present. The main motivating application behind the design of the CM was the less-invasive treatment of pelvic osteolysis described in Chapter 2. The CM was constructed of two superelastic nitinol (NiTi) tubings with several equidistant notches to achieve flexibility in the plane of articulation, while remaining

CHAPTER 3. SURGICAL WORKSTATION OVERVIEW

stiff and force-bearing in all other planes (Fig. 3.5). NiTi, a nickel-titanium alloy, was chosen as the manufacturing material for the CM due to bio-compatibility (suitable for medical applications), and super-elasticity (suitable for large curvature bending and enhanced dexterity of the manipulator).

As demonstrated in Fig. 3.5(c), the CM contained a central open lumen with 4.0 mm diameter as instrument channel and four channels with 0.5 mm diameter running internally through the length of the manipulator (two on each side) for embedding the actuation cables and potential sensing units. One major advantage of such design was that the sensors, instruments and actuation cables were encapsulated within the walls of the manipulator, which safeguarded against potential damages during interaction with tissues and bones.

In the fabrication procedure proposed by Kutzer et al. [23], the first-generation CM was built from two nested NiTi tubes. The reason behind choosing two NiTi tubes was to enable the manufacturing process for wire electrical discharge machining (EDM) of the four internal channels. Considering the application requirement of passing the CM through the screw holes of an acetabular implant, the inside diameter (ID) and outside diameter (OD) of the outer tube were chosen 5.0 mm and 6.0 mm, respectively, while those of the inner tube were chosen 4.0 mm and 5.0 mm. As mentioned before, the inner tube 4.0 mm open lumen was designed for passing different flexible tools through the manipulator for debridement tasks. The outer diameter of 6.0 mm was also chosen such that the CM could fit into the screw hole of an

CHAPTER 3. SURGICAL WORKSTATION OVERVIEW

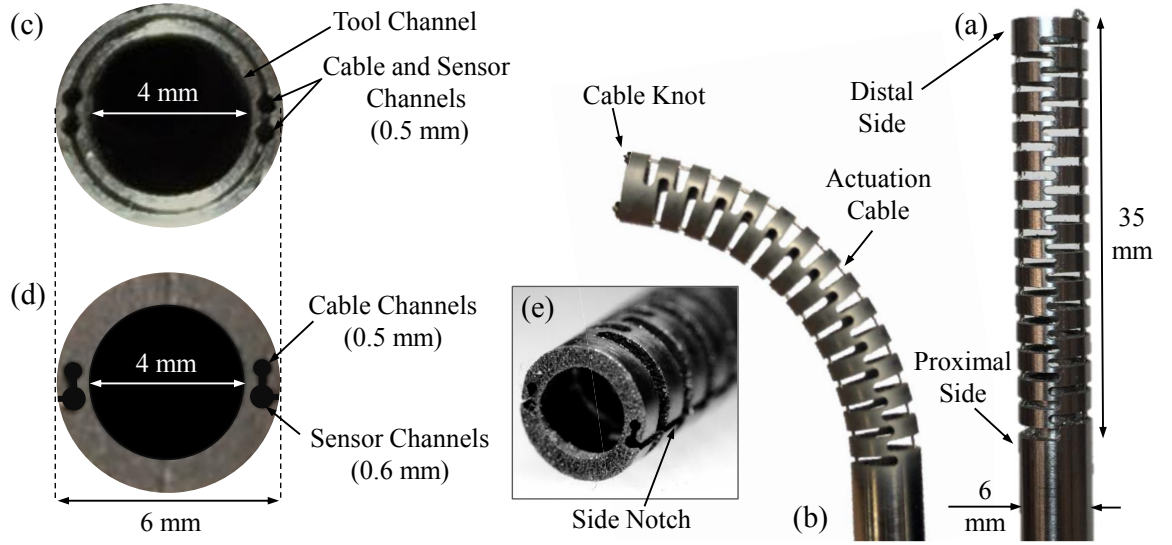


Figure 3.5: Continuum manipulator developed for minimally invasive orthopaedic interventions. (a) straight configuration (unbent), (b) bent configuration, (c) distal end cross section view of the first generation CM (nesting of two NiTi tubes), (d) distal end cross section view of the second generation CM (single NiTi rod with enlarged sensor channels), (e) side notch as a result of introducing the wire EDM from the side of the manipulator.

acetabular implant with screw holes greater than 6.0 mm. For instance, the Zimmer Trilogy acetabular component (Cat. No. 6200-48-22) has three 6.6 mm diameter screw holes. The overall length of the CM was also optimized at 35.0 mm such that the CM could exhibit substantial lesion converge when fully inserted into a lesion [22, 23, 68].

The manufacturing process for the first CM generation was as follows: after cutting the inner and outer tubes to length on a lathe, the drive cable channels on the outside of the inner tube were cut. After mounting the outer tube over the inner tube, an EDM wire threaded through the existing inner tube channels cut the cable channels on the inside of the outer tube. A machine vice pressed the tubes together and an EDM process cut the notches into the manipulator. This manufacturing process,

CHAPTER 3. SURGICAL WORKSTATION OVERVIEW

however, required a lot of effort especially during the tight nesting of the two NiTi tubes and the wire EDM step to cut the cable channels on the outer tube such that they were aligned with the inner tube half-channels. To mitigate these challenges, for the second generation CM, a few alterations were considered in the manufacturing process and channel dimensions, so that the machining process could be done in a cheaper and simpler fashion and the embedded sensor assembly could be performed easier and more reliably.

For the second generation of the CM, a few key aspects from the earlier iteration remain unaltered. For instance, the overall ID and OD of the CM were kept at 4.0 mm and 6.0 mm, respectively, so that the CM could fit through the screw holes of the acetabular implant, and also flexible debridement tools could be inserted through the inner lumen. The overall length of the manipulator also remained at 35.0 mm. To reduce the manufacturing procedure challenges, however, rather than two NiTi tubing, a single NiTi rod was used in the second design to avoid the complications associated with fitting of the two tubes. To cut the sensor channel, however, the wire EDM was introduced from the side of the manipulator on each side and was moved inside the NiTi material such that the actuation cable and sensor channels on one side were created in a continuous motion. This procedure was repeated on the other side of the manipulator to create two additional channels.

An obvious advantage of such approach was the great access to the surface of the manipulator for performing the wire EDM procedure in a single step. Additionally,

CHAPTER 3. SURGICAL WORKSTATION OVERVIEW

the small notch on the side of the manipulator as a results of the wire EDM (see Fig. 3.5(e)) enabled further access to the embedded sensors during assembly into the CM channels and application of adhesive for securing them on the CM. To allow further simplification in the sensor assembly process and to ensure less constrained relative motion of the sensor in the CM channel, the diameter of the sensor channels were changed from 0.5 mm to 0.6 mm, compared to the first CM generation design.

3.4.2.3 Load Bearing

As mentioned in the previous section, the CM was particularly designed for orthopaedic interventions where the contact forces are relatively high. As such, the CM capabilities in bearing large loads must be evaluated. Kutzer et al. [23] performed various end-effector force testing experiments within the CM's bend plane. The goal of the experiments was to determine the manipulator's end-effector reaction force while the CM cables were actuated to push the manipulator against a load cell placed at the distal end of the manipulator. A series of seven CM configurations were considered in those experiments with the total bend angle ranging from -135° to 135° with a 45° step. For the considered experiments in the plane of bend, end-effector reaction forces as large as nearly 2.00 N were reported. The out of plane load-bearing experiments were, however, inconclusive since the maximum bearing load sustainable by the CM before rupture was not reported in that study.

To this end, experiments were performed to determine the maximum distal-end

CHAPTER 3. SURGICAL WORKSTATION OVERVIEW

force that the CM can sustain before breaking. For the purpose of this experiment, the CM was rigidly fixated on an actuation unit with the plane of bend parallel to the table. The actuation cables were counter-tensioned to 4.00 N to hold the CM firmly at the straight configuration (zero bend angle). The reason for performing the experiment at this configuration was that the maximum end-effector moment arm about the base of the CM (proximal end) occurs at the straight configuration. As a result, for a fixed end-effector force, the CM is more susceptible to being damaged in zero bend angle due to larger moments about the base of the CM.

As shown in Fig. 3.6, a three-axis force sensor (OMD-10-SE-10N, OptoForce; Budapest, Hungary) was mounted on a linear stage equipped with a feed lever for adjusting the vertical (z-direction) position. The initial position of the linear stage was set such that the force sensor was in visible contact with the distal end of the manipulator while maintaining a 0.00 N reading. The feed lever was rotated slowly to move the linear stage downward, exerting larger end-effector forces on the distal end of the CM and consequently larger moments on the proximal end of the CM. The motion was continued until the CM was ruptured from the proximal end. Fig. 3.6 demonstrates the evolution of the end-effector force applied perpendicular to the plane of bend during this experiment. A maximum force of 11.54 N was observed before occurrence of rupture which is sufficient for contact forces observed during interaction with and debridement of hard simulated bone and soft tissue [69,70]. Sustaining such a large out-of-plane distal end force is one of the unique features of this particular

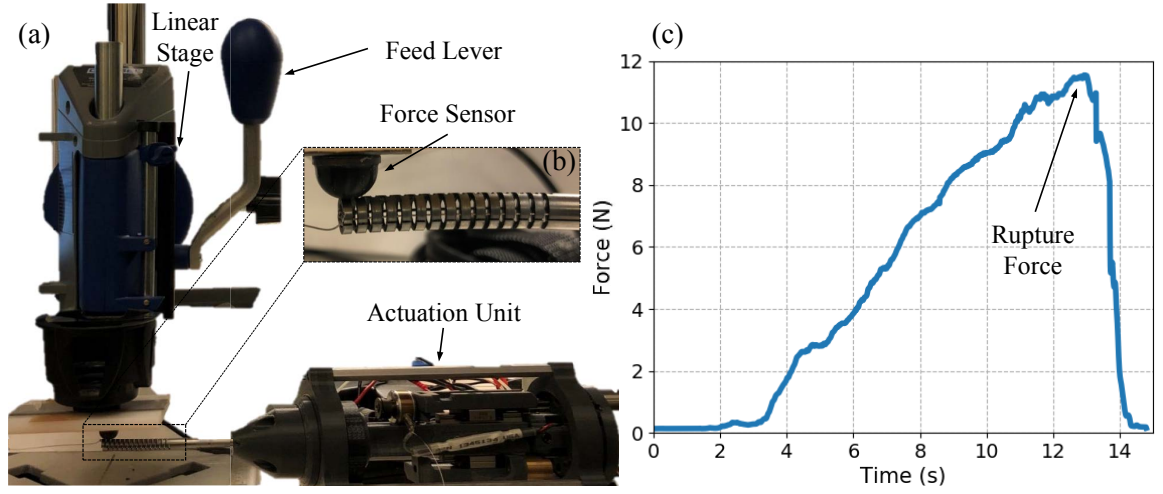


Figure 3.6: (a) Force test experimental setup, (b) close-up view demonstrating the force sensor and CM, (c) end-effector force test result during exertion of out-of-plane distal end force.

CM, making it a great candidate for orthopaedic interventions.

3.4.3 Flexible Debridement Instruments

3.4.3.1 Contribution

The original idea and initial testings for the design and manufacturing of the flexible instruments were introduced and performed by Dr. Mehran Armand. Dr. Farshid Alambeigi and Dr. Yu Wang designed and manufactured the flexible instruments for treatment of hard tissues and Dr. Hao Liu designed and manufactured the micro debrider for soft tissue debridement. The author manufactured several flexible instruments with various tool-tip head dimensions for quick and simple integration into the developed surgical robotic system.

3.4.3.2 Design and Fabrication

As described in Section 3.4.2, the CM used in the developed surgical system contains an instrument channel of 4.0 mm and outer diameter of 6.0 mm, designed to fit through the screw holes of an acetabular implant. The CM is flexible in a single plane (plane of bend) and stiff and force-bearing in all other planes. Flexible tools passing through the instrument channel for debridement tasks must therefore comply with the dimensions of the instrument channel and also be flexible enough to adopt to the shapes attained by the CM. Furthermore, despite lacking a thoroughly rigid shaft, the flexible tools should be able to transmit the torque necessary for debridement tasks.

To this end, various flexible instruments were custom-designed for different lesion debridement tasks including side milling and drilling of soft [70] and hard tissue and bone [69]. All the instruments consisted of a rigid stainless steel tube (2.5 mm outer diameter) and a 35.0 mm length flexible torque coil (Asahi Intec USA, Inc.) with 3.5 mm outside diameter. The torque coil provided sufficient torque to the tip of the tool for debridement tasks, while it adapted to various shapes of the CM.

For soft tissue debridement, a micro debrider with engaging teeth and suction capabilities was designed and studied in removing simulated soft tissue (soft gelatin phantoms) [70] (Fig. 3.7(a)). The interested reader can consult [70] for thorough explanation on the design concepts and evaluation experiments of the micro debrider on soft gelatin phantoms. For the removal of the sclerotic tissue (hard tissue), a

CHAPTER 3. SURGICAL WORKSTATION OVERVIEW

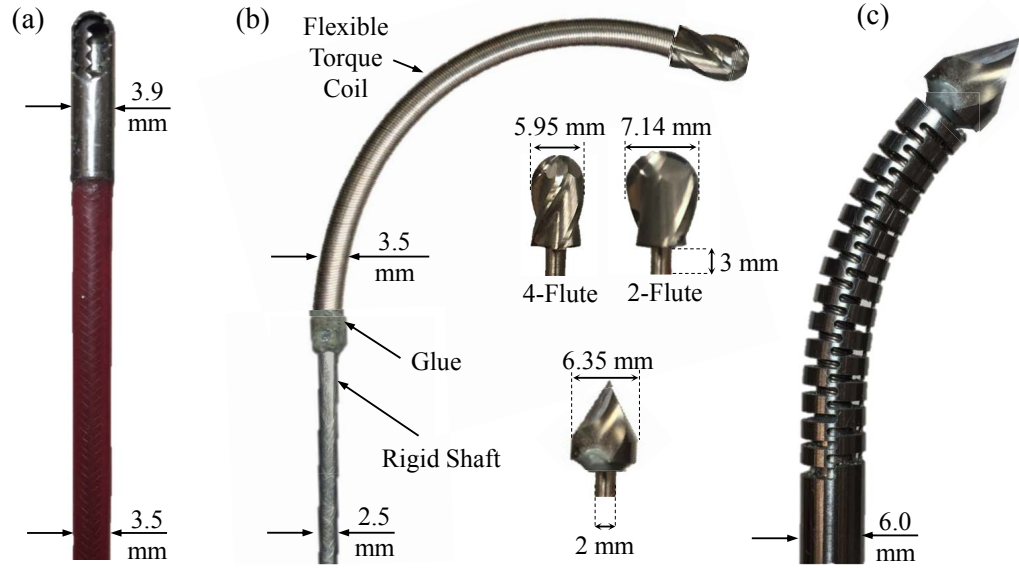


Figure 3.7: Flexible debridement tools [63, 69, 70]. (a) micro debrider for soft tissue debridement, (b) tool for hard tissue and bone debridement tasks consisting of a rigid shaft, a flexible torque coil for following the CM shape and different tool heads, (c) CM and flexible tool integration.

variety of end-mill instrument heads were fabricated from carbide with two and four spiral flutes (Fig. 3.7(b)) and with outside diameters of $9/64''$ (3.57 mm), $13/64''$ (5.16 mm), $15/64''$ (5.95 mm), $1/4''$ (6.35 mm), and $9/32''$ (7.14 mm). In particular, the end-mill shafts were first machined down to 2 mm outer diameter and 3 mm in length. The trimmed end-mills were then inserted into the torque coils and secured in place by reinforced epoxy (J-B Weld 8265S).

From the surgical workflow perspective, the flexible instruments must contain the capability to be quickly interchanged according to the surgical plan and different phases of the surgery. The decision on choosing a particular tool-head size depends on the realization of the trade-off between larger lesion removal and easier integration

CHAPTER 3. SURGICAL WORKSTATION OVERVIEW

with the CM. For a fixed motion and contact with the specimen, a larger tool head can remove a greater chunk of the lesion, while a smaller tool head (less than 4.0 mm) can be easily interchanged and integrated during the surgery from the proximal side of the manipulator. Of note, for other surgical applications such as the less-invasive treatment of osteonecrosis by core decompression of the femoral head, different flexible tool heads might be required. Fig. 3.7(c) demonstrates a drilling bit instrument integrated with the CM for such application [69].

3.4.4 Actuation Unit

3.4.4.1 Motivation and Contribution

As outlined for the envisioned system in Section 3.3, an actuation unit serving as the connector between the CM and positioning robot must be designed and developed. The mechanism must contain separate and appropriate modules for actuation of the CM and the flexible instruments. Several dimension considerations must be taken into account to ensure the actuation unit is compatible with the design requirements.

The first generation of the actuation unit with robot-mounting capabilities was designed and developed by Dr. Farshid Alambeigi and Dr. Yu Wang. After preliminary phantom and cadaver experiments (both pelvic osteolysis and the core decompression of the femoral head) conducted by the author, the second generation of the actuation unit with several improvements and modifications over the first generation unit was

CHAPTER 3. SURGICAL WORKSTATION OVERVIEW

designed and fabricated by Mr. Gavin Sun, Ms. Rachel Hegeman and Dr. Farshid Alambeigi with the help of the author with integration of the sensor housing and modification of the parts during the course of the phantom and cadaver experiments.

The first generation custom-designed C++ code for position and velocity control of the actuation cables were implemented by Dr. Ryan Murphy. The author further improved the controller by developing and implementing an automatic position homing (desired cable pre-tension) procedure for the CM, as well as implementing a cable tension force control algorithm via velocity commands that could be used for the debridement tasks.

3.4.4.2 Design and Fabrication Iterations

Preliminary evaluations on a human cadaver with an acetabular implant suggested that the combination of an axial roll motion about the CMs shaft and the bending motion of the CM (in-plane articulation) provided sufficient dexterity and workspace for the robot-assisted less-invasive treatment of osteolysis. Since the CM's primary use-case was determined to be orthopaedic interventions in confined spaces, a remote mechanism to actuate the CM and the flexible instruments from the proximal side of the manipulator seemed as a suitable option. Additionally, certain design and dimension considerations were taken into account to ensure the actuation unit was located far enough from the point of entry to the patient's body for the minimally invasive interventions.

CHAPTER 3. SURGICAL WORKSTATION OVERVIEW

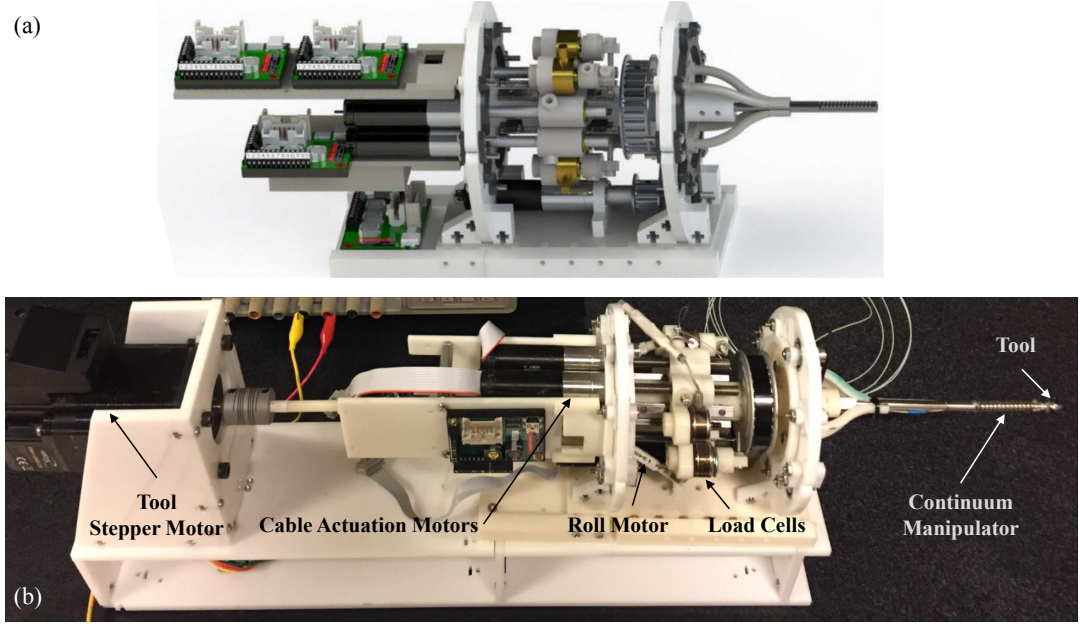


Figure 3.8: First generation actuation unit [71, 72]. (a) simulation rendering, (b) developed system.

The appropriate actuation unit must meet certain design and application requirements such as:

- At least two actuators for generating cable displacements for controlling the planar CM to c-shape articulations. The number of actuators could be changed depending on the particular CM being used for the surgery. In particular, three or four actuators may be required for creating s-bend articulations (curved shape with an inflection point) and six actuators may be required for actuating CMs with three dimensional motion capabilities.
- Force sensing capability may be required for direct measurement of the cable actuation forces. This is beneficial for integration of force into the control algo-

CHAPTER 3. SURGICAL WORKSTATION OVERVIEW

rhythms and also to avoid potential cable damage during control (e.g. excessive force applied beyond the allowable range).

- Appropriate tool actuation unit is required to provide sufficient torque for rotating the flexible instruments during various debridement tasks. In addition, the actuation unit must contain the capability for easy integration of the instruments from the proximal side of the unit (the side that the actuation unit mounts onto the positioning robot).
- Depending on the choice of positioning robot, the weight and size of the actuation unit must comply with the robot's maximum allowable payload (e.g. 5 kg for the UR-5).

Following the design requirements mentioned above, the first generation of the actuation unit was designed and developed [69] (Fig. 3.8). This actuation unit contained two DC motors (RE16, MaxonMotor Inc.) with spindle drives (GP16, Maxon Motor, Inc.) to actuate the CM cables. In addition, the actuation unit was rotated about its central axis by another DC motor (RE16, GP16C, Maxon Motor Inc.) adding another DOF (roll motion) to the integrated robotic system. The actuation unit additionally included four load cells (Model 31 Mid, Honeywell Inc.) for measuring the CM cable tensions. The actuation unit provided a central channel for passing the flexible instruments through its central structure. The instruments were rotated by the tool actuation unit mechanism comprising of a DC motor (EC 22, GP22C,

CHAPTER 3. SURGICAL WORKSTATION OVERVIEW

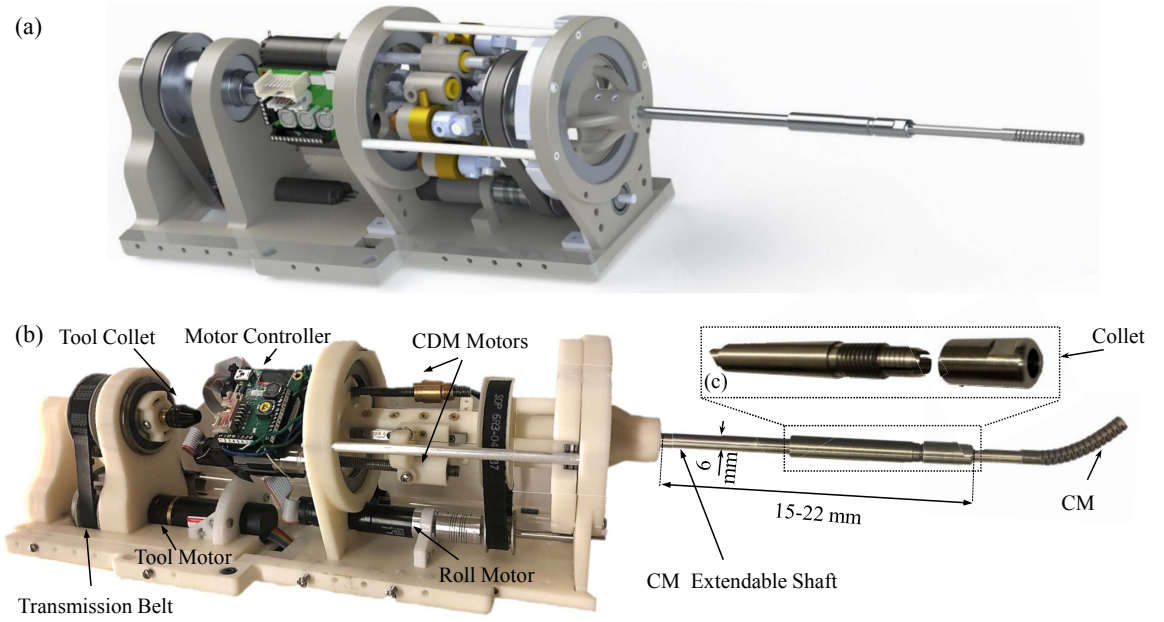


Figure 3.9: Second generation actuation unit [63]. (a) simulation rendering, (b) developed system, (c) the collet mechanism restricting the axial and rotational motion of the CM.

Maxon Motor Inc.), a transmission and a quick connection mechanism. In this actuation unit, a custom-designed printed circuit board (PCB) was used to power and connect the individual Maxon controllers (EPOS 2, Maxon Motor Inc.) on a CAN bus. A load cell mounted in series with each motor measured the tension in the cable and was routed through an instrumentation amplifier on the PCB. A custom C++ interface performed independent velocity or position control of each motor using provided libraries by Maxon which communicated with the PC over a single mini-USB cable.

Even though beneficial for the preliminary experiments, the first generation actuation unit exhibited room for improvement in design and assembly. In particular, with

CHAPTER 3. SURGICAL WORKSTATION OVERVIEW

the goal of simplifying the assembly procedure, reducing the existing backlash, and enhancing adaptability to various minimally invasive interventions, a second generation of the actuation units was designed and developed. To increase structural stiffness, several of the laser-cut acrylic sheet components of the first generation design were replaced by sturdier 3-D printed elements. To reduce friction while maintaining compactness of the design, thrust bearings were incorporated into the roll DOF of the actuation unit (first generation design did not contain bearings). The CM mounting mechanism on the first generation actuation unit also lacked proper axial and radial restriction of the CM shaft. In the second generation design, a threaded collet mechanism (Fig. 3.9(c)) was incorporated to restrict the CM from radial motion, while a step limit together with a pair of set screws were added to the system to limit the CM shaft's axial motion.

Further, preliminary cadaver experiments (both pelvic osteolysis and core decompression of the femoral head) revealed that the actuation unit shaft's length must be elongated to avoid potential collision of the unit with the patient's body or surgical table. To remedy this problem, an extendable shaft mechanism with adjustable length (15.0 cm to 22.0 cm) was designed from Aluminum as the central shaft of the second generation actuation unit. Fig. 3.9 shows the simulation rendering and the developed second generation actuation unit, and Fig. 3.10 demonstrates the integrated UR-5 positioning robot and the actuation unit.

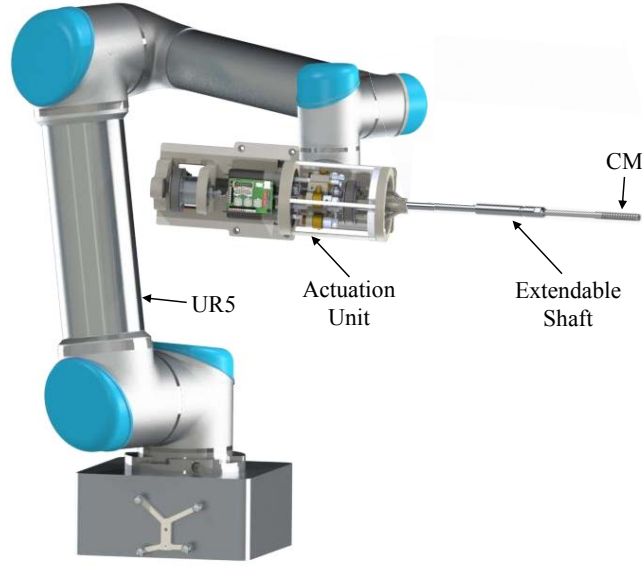


Figure 3.10: Second generation actuation unit integrated with the UR-5 positioning robot [73].

3.4.5 Sensing and Control

Successful deployment of the developed surgical workstation for autonomous minimally invasive interventions can be achieved only with suitable accompanying sensing and control modules. For these modules, several challenges are introduced at the mechanical, algorithmic, and software design level. The size and dimension limitations associated with the CM, flexibility of the CM, workspace constraints and stiff environment properties associated with orthopaedic interventions impose restrictions on the choice of the sensing modalities and incorporated control strategies. Potential collision and contacts of the CM with the unknown rigid and soft obstacles require development of advanced algorithms to enhance the sensing accuracy and robustness for reliable control of the system. Furthermore, a complex system such as the

CHAPTER 3. SURGICAL WORKSTATION OVERVIEW

developed workstation with several components and elements requires a software architecture that provides reliable connection and fast communication among all the components and autonomously generates control commands in real-time given the surgeon's input.

The detailed description and evaluation of various sensing and control strategies as well as software considerations for the developed system are postponed to the next chapters. In particular, different sensor designs and algorithms for the CM will be discussed in Chapters 4 and 5, CM control strategies are described in Chapter 6, and closed-loop concurrent control of the combined system with feedback is explained and evaluated in Chapter 7.

3.5 Conclusion

An overview of the envisioned and developed surgical workstation and its components were presented in this chapter. Design and manufacturing requirements and considerations for each system component were discussed and the evolution of design and fabrication iterations were described. The envisioned surgical workflow and the preoperative planning and intraoperative execution were briefly explained. The following chapters will focus on the sensing and control strategies and provide an in-depth overview of the preoperative and intraoperative steps in realistic phantom and cadaver studies.

3.6 Acknowledgments

I sincerely thank Dr. Mehran Armand, Dr. Russell H. Taylor, and Dr. Iulian Iordachita for the insightful discussions and their helpful collaborations over the course of developing the system. Special thanks to Ms. Rachel Hegeman, Dr. Ryan J. Murphy, Dr. Farshid Alambeigi, Dr. Yu Wang, and Mr. Paul Wilkening for their invaluable contributions to the design and fabrication of different system components.

Chapter 4

Sensor Designs

4.1 Motivation

Shape sensing is essential to accurate closed-loop control of continuum manipulators (CMs). Previous efforts [22, 74–77] involved developing models for estimating shape from CM actuation cable length or tension force measurements. A great body of research exists for modelling the internal device friction (e.g. tendon/channel interaction) [78–82] that could potentially enhance the accuracy of the model-based shape sensing algorithms. However, due to system uncertainties such as backlash, inaccurate modeling assumptions, and unknown tissue/lesion interactions, these model-based approaches may not be sufficiently accurate for CM shape estimation.

As such, in presence of such uncertainties, direct sensing of shape may yield more accurate and reliable results. The small size and also flexibility of the CMs, how-

CHAPTER 4. SENSOR DESIGNS

ever, restricts the choice of suitable sensors. Furthermore, minimally invasive surgery imposes additional requirements and limitations on the selection of the sensor. The application specifics for the less-invasive treatment of osteolysis, for instance, demand the manipulator to be capable of reaching and maneuvering in the environment behind the implant, hence limiting CM visibility to optical tracking systems or external cameras. As such, a shape sensing technique not requiring direct line of sight must be incorporated. The CM is also designed for large curvature bending applications, therefore requiring a shape sensing method that could withstand and detect local large curvatures on the CM up to at least 66 m^{-1} (corresponding to 15 mm radius of curvature).

Several approaches exist for shape and tip sensing of CMs. Examples of such sensing approaches include electromagnetic (EM) tracking [83–85], infrared imaging [86], external cameras [87–90], and medical imaging methods such as fluoroscopy [91], X-ray [66, 92] and ultrasound [93, 94]. While in principal, the integration of existing external sensors such as camera systems or EM tracking coils are feasible, in practice the small size of CMs and the clinical setting usually impede straightforward implementation of these sensors. EM tracking requires an environment without any magnetic objects that could interfere with the magnetic field and decrease accuracy [84]. External cameras require line of sight with the robot, which is not possible in minimally invasive interventions [3].

Even though in a medical application, the use of medical imaging modalities such

CHAPTER 4. SENSOR DESIGNS

as fluoroscopy and X-ray seems relevant, there is limitation in extensive intraoperative use of these methods for real-time shape sensing due to radiation exposure. Ultrasound is also a cost-effective choice for real-time imaging in applications where the robot is surrounded by liquid or soft tissue (e.g., cardiac, vascular, or abdominal surgery) [3] and is not suitable for orthopaedic applications, which is the focus of this dissertation. Optical fiber shape sensing [95, 96], however, provides real-time feedback without requiring a direct line of sight. Their small size, flexibility, and minimal effects on stiffness are advantages that make these sensors a great candidate for integration in CMs [84, 97, 98].

As such, this chapter is pursued with the intention of proposing several fiber optic sensors (FOS) for robust and reliable shape sensing of large deflection CMs. In particular, two sensors using optical fibers with Fiber Bragg Grating (FBG) [96] and one sensor with higher spacial resolution using the Optical Frequency Domain Reflectometry (OFDR) technique [99] are proposed. The OFDR technique is specifically beneficial in capturing local deflections and inflexion points when the CM takes on complex shapes. The main goal of the chapter is to introduce sensor design variations to maximize sensor manufacturing reliability and repeatability, as well as ease of integration with the CM, while minimizing the fabrication complexity and effort. Characterization procedures for verification of successful sensor fabrication are also discussed. Current chapter focuses on the design, characterization, and calibration of different optical fiber sensors for large curvature CM sensing, while Chapter 5 is

dedicated to various sensing algorithms for shape, distal-end position estimation, and contact sensing using the sensors introduced in this chapter.

4.2 Contribution

The author's contributions in this chapter are as follows:

- Proposing two FBG-based optical fiber sensor designs to reduce strenuous CM sensor manufacturing steps compared to previous work in the literature.
- Integration of an OFDR-based sensor into the CM and evaluation of the sensor-CM assembly.
- Introducing metrics for realization and optimization of the trade-off between sensor sensitivity and ease of assembly by computation of the sensor assembly neutral axis location.
- Proposing and conducting characterization and calibration procedures for verification of successful sensor fabrication.

Mr. Michael Pozin helped the author during the characterization and calibration experiments for the notched nitinol (NiTi) FBG sensor. Mr. Frederic Monet and his team at the Polytechnique Montreal affiliated with University of Montreal graciously developed and fabricated the OFDR-based sensor, while the author equally

CHAPTER 4. SENSOR DESIGNS

contributed during integration of the sensor with the CM as well as the design, performing, and analyzing the evaluation experiments.

The work presented in this chapter was published in two IEEE Sensors conferences (2016 and 2017) [100, 101] and in International Symposium on Medical Robotics (ISMR) 2018 [72].

4.3 Background

FOS have been widely employed for strain, curvature, force, torque, temperature measurements and pressure monitoring in various applications [102, 103]. Several advantages are associated with FOS such as small size, light weight, flexibility, biocompatibility, immunity to radio frequency interference and EM interference, high accuracy, facilitation of distributed sensing, capability of remote sensing, and high data streaming rate [96, 102]. These characteristics make fiber-optic-based sensing very suitable for shape estimation of small CMs and other flexible medical devices such as biopsy needles [104–109] and catheters [110–114].

FOS can be broadly divided into two categories [102]: 1) multi-point sensing for which the active portion of the fiber is usually less than 1 cm, and 2) distributed sensing where the entire fiber is the sensor (higher spacial resolution). A particular type of multi-point FOS are Bragg-grating-based sensors, termed FBGs, that are written onto an optical fiber at several points along the length of the fiber [96, 115]. The

CHAPTER 4. SENSOR DESIGNS

important feature of a written grating is that depending on the local strain, it reflects particular wavelengths of the light that is sent through the fiber and transmits all others [96]. The reflected wavelength information can be detected by an interrogation device and be used to estimate strain and subsequently curvature at each active segment.

Distributed sensing FOS also follow a similar concept but they can use a regular fiber instead of written FBG sensors. As such, the spatial resolution is no longer dependant on the number and physical position of the FBGs, but rather on the fiber interrogator parameters. A trade-off between multi-point and distributed FOS, however, exists in spatial resolution, cost of fabrication and associated challenges, and complexity of interrogation techniques. As a result of these trade-offs, in recent years, adaptation to the FBG-based sensors has been more apparent in sensing applications for CMs and other flexible medical devices, compared with distributed FOS [3, 84].

A multitude of FBG sensor designs and techniques for embedding the sensor in CM can be found in the literature [84]. The type of FBG fibers used in these studies can be divided to single- [116] and multi-core fibers [117]. Multi-core fibers are more expensive than single core fibers, whereas the smaller cross sectional area of the multi-core fibers could be beneficial when space limitation is a concern [117]. The relative placement of fibers and sensor substrate can be broadly categorized into triangular [118], rectangular [117], and helical [97, 119]. While each design is advantageous from certain perspectives, the most commonly incorporated approach with simpler design

CHAPTER 4. SENSOR DESIGNS

considerations seems to be the triangular configuration [84]. A variety of sensor substrates such as NiTi wires [116, 118] and polymer tube [120] have been used for different CMs. Embedding of the FBG sensor into the CM can be divided to either direct attachment or placement on the central back-bone of the CM or insertion into allocated sensing channels within the body of the manipulator [84, 98, 116, 118].

In terms of the incorporated number of fibers and FBGs in the FOS, various researchers implemented and evaluated different combinations depending on the application and used CM. Roestious et al. [116] attached three fibers each with four FBGs to a 1.0 mm outside diameter (OD) NiTi substrate and placed it in the hollow shaft of a cable-driven CM. Ryu et al. [120] suggested a 1.05 mm OD polymer tube as sensor substrate instead of NiTi and developed a prototype sensor with only one single fiber. Xu et al. [97] proposed a helically wrapped sensor with three FBG fibers attached to a 2.0 mm OD NiTi tube for simultaneous curvature/torsion/force measurements of concentric tube robots. Wei et al. [121] also suggested a helically wrapped sensor using only one fiber with multiple FBG nodes that was wrapped around a helically notched 0.3 mm NiTi substrate.

The above-mentioned studies have reported maximum curvature sensing of $22.7\ m^{-1}$ using FBGs [98]. In an effort to increase the curvature detection range of the FBG-based sensors Liu et al. [118] and Farvardin et al. [122] proposed a novel method of detecting large deflections by attaching a fiber array with three FBG active areas to two $125\ \mu\text{m}$ OD NiTi wires as substrates. The components were glued together to con-

CHAPTER 4. SENSOR DESIGNS

struct a sensor with triangular cross section. The sensor assembly was subsequently integrated into the sensor channels of the CM. While results indicated effectiveness of these sensors in detecting large deflections, it was subjected to a complicated, cumbersome and strenuous fabrication process requiring several trial and error runs to ensure accurate attachment of the components. Maintaining the geometry of the assembly (relative position of the fiber array and NiTi wires) and consistent repeatable fabrication procedure were also not guaranteed in their proposed method. In an effort to minimize the challenges associated with design and fabrication of FOS for large curvature CM shape sensing, in this chapter, the author developed two FBG-based sensor designs using two different substrates that enhance sensor manufacturing repeatability and reduce sensor assembly complexities. Moreover, to the best of our knowledge, for the first time this thesis introduces a distributed FOS for high resolution sensing with capability to detect complex CM shapes.

4.4 Fiber Bragg Grating

An FBG sensor is normally written onto a short segment of an optical fiber, and it is able to reflect particular wavelengths of the input light with the full spectrum while transmitting all the other ranges [96,102,123]. This is achieved by creating a periodic variation in the refractive index of the fiber core, which generates a wavelength-specific dielectric mirror [115]. Fig. 4.1 demonstrates an FBG sensor and the working

CHAPTER 4. SENSOR DESIGNS

principle. The optical fiber itself is made of silica glass or plastic as thin as a human hair. It consists of two parts: the inner core and the outer cladding [96]. Cladding is a glass layer made up of lower refractive index glass to maintain guidance of light within the core. Both parts are encapsulated by a single or multiple layers of primary polymer coatings for protection and easiness of handling.

An interrogator device emits light through the fiber and detects the wavelength of the reflected light associated with each FBG segment on the fiber. The fundamental principle behind the operation of an FBG is Fresnel reflection [124], where light traveling between media of different refractive indices may both reflect and refract at the interface. The refractive index will typically alternate over a defined length. The reflected wavelength λ_B , called the Bragg wavelength, is defined by the relationship:

$$\lambda_B = 2 n_e \Lambda \quad (4.1)$$

where n_e is the effective refractive index of the grating in the fiber core and Λ is the grating period (Fig. 4.1). The effective refractive index and the grating period are affected by changes in mechanical strain and temperature. Changes in the effective refractive index, subsequently, results in a change in the Bragg wavelength according to 4.1. An FBG sensor can therefore be used as a sensor for either measuring mechanical strain or temperature. The shift in the Bragg wavelength ($\Delta\lambda_B$) due to

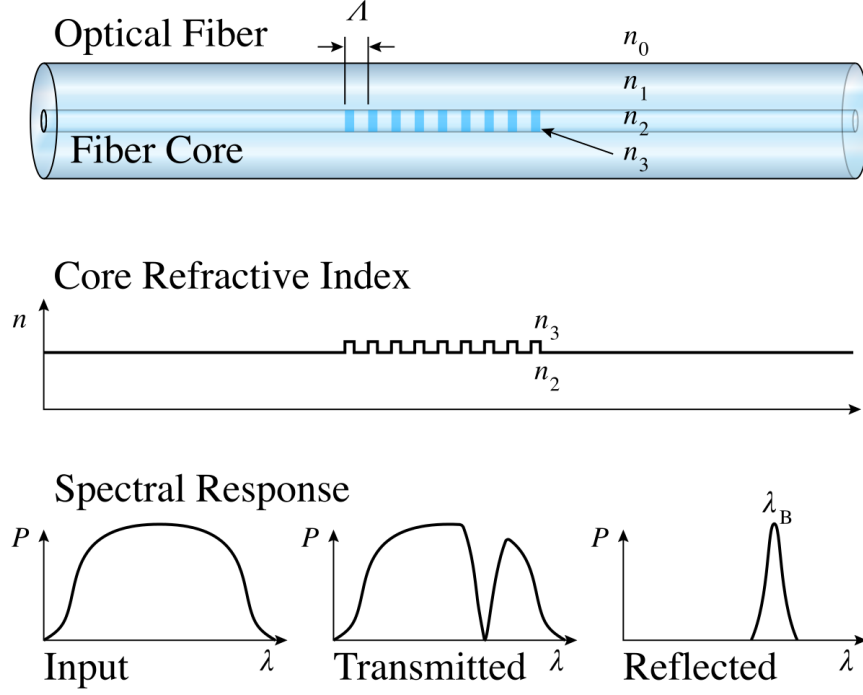


Figure 4.1: Fiber Bragg Grating working principle. Image obtained from https://en.wikipedia.org/wiki/Fiber_Bragg_grating.

applied strain (ϵ) and change in temperature (ΔT) is given by [123]:

$$\Delta\lambda_B = \lambda_B \left[\underbrace{(1 - p_e)\epsilon}_{\text{strain}} + \underbrace{(\alpha_\Lambda + \alpha_n)\Delta T}_{\text{temperature}} \right] \quad (4.2)$$

where p_e is a constant containing photoelastic contributions, and α_Λ and α_n are the thermal expansion coefficient and the thermo-optic coefficient of the fiber, respectively.

The principle behind detection of mechanical strain in FBG-based FOS follows that of a cantilever beam as proposed in mechanics of materials textbooks [125, 126]. A fiber alone does not detect any mechanical strain in bending because the FBG nodes

are placed at the neutral plane of the fiber. As such, a mechanical substrate must be incorporated to offset the FBG nodes from the neutral plane of the fiber-substrate assembly. This offset in FOS is sometimes referred to as sensor bias [98,118]. Inline with beam theory principles, the points located at a larger offset from the neutral plane of the beam experience larger mechanical strain during bending [125,126]. With this principle in mind, two different sensor substrates for large curvature shape sensing of CMs are proposed, while minimizing the fabrication and assembly complexities.

4.4.1 Polycarbonate Tube Substrate

According to beam theory principles, the key aspect of large deflection shape sensing is the bias distance between the FBG array location relative to the neutral plane of the sensor. To address the limitations in maximum curvature detectable by FOS proposed by researchers (Section 4.3), Liu et al. [98,118] proposed an FBG-based shape sensor incorporating two 125 μm OD NiTi wires as sensor substrate. They used acrylate ultraviolet (UV) adhesive to attach these wires to a single FBG optical fiber along the longitudinal axis in a triangular configuration with trial and error. A major challenge associated with this assembly was the lack of control over the relative location of the wires and fiber. Further, there was no guarantee that the triangular configuration was maintained throughout the length of the sensor.

To mitigate the above-mentioned challenges, the author proposes the use of a tube substrate made of e.g. polymer (material selection discussed in Section. 4.4.1.2) with

CHAPTER 4. SENSOR DESIGNS

longitudinal lumens in a triangular configuration (the most commonly used configuration) for integration of fibers and potential NiTi wires to strengthen the overall structure. The predefined geometry of the tube and lumens will dictate a known precise relative distance between the components. Moreover, the fixed locations of the lumens provide more control during assembly of the components since after insertion of any component, the lumen channel geometry will guide the component all the way to the other end of the sensor. Fig. 4.2(a) shows the tube design and associated lumens.

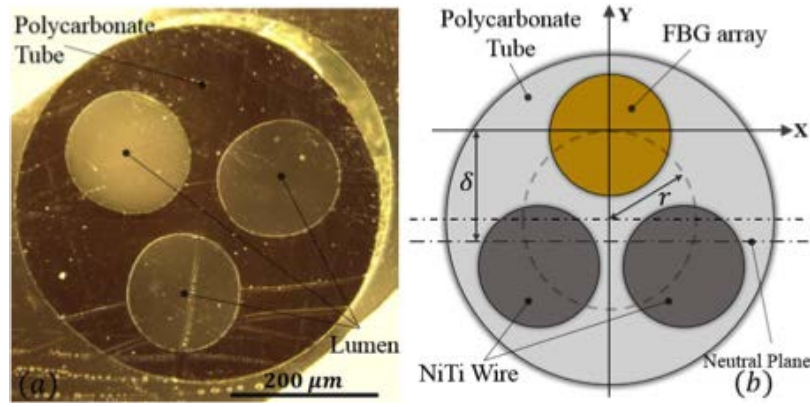


Figure 4.2: Tube fiber optic sensor substrate [100]. (a) Polycarbonate tube cross section under microscope, (b) assembled and fabricated sensor.

For assembly, a component (e.g. fiber or NiTi wire) is inserted at the proximal side of the tube and passed through the length of the tube until it protrudes from the distal end of the tube by the length of the tube. A small amount of adhesive is applied to the segment of the component that is exposed at the distal end. The component is then retracted slowly from the proximal side until the distal ends of the component and tube line up. To ensure secure fixation, a small amount of adhesive

CHAPTER 4. SENSOR DESIGNS

is then applied both to the proximal and distal end of tube.

To capture the local curvatures along the length of the CM, two sensors are fabricated using the procedure outlined above and the sensors are embedded into the two sensor channels of the CM. To fixate the sensors to the CM, small amount of adhesive is applied at the distal end of the manipulator (Fig. 4.3) such that the distal end of the sensors are restricted, but the remainder of the sensors can still move freely with respect to the CM sensor channels.

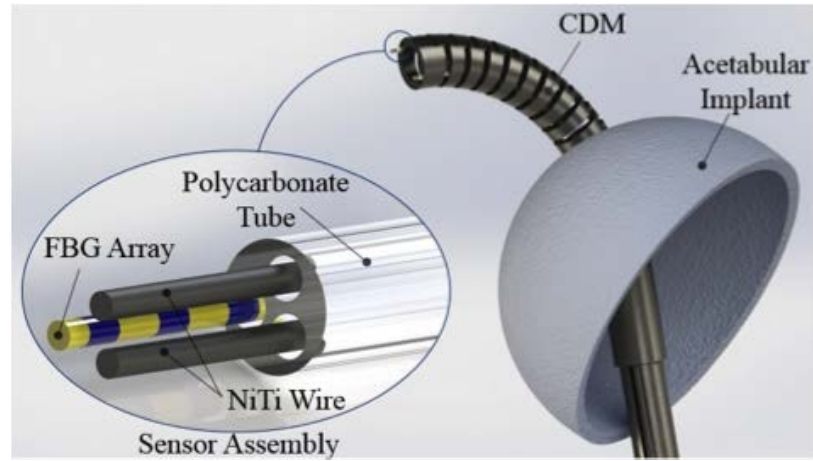


Figure 4.3: The integrated CM-sensor assembly inserted into the screw hole of an acetabular implant used in total hip arthroplasty [100].

4.4.1.1 Sensor Modeling

To better understand the model of the proposed sensor assembly, its neutral plane is calculated. It is assumed that the sensor assembly is a composite beam comprised of components with different moduli of elasticity in the cross section. The neutral plane can be calculated from the equilibrium of forces acting on a cross section of the

CHAPTER 4. SENSOR DESIGNS

assembly:

$$\sum_{i=1}^4 \int_{A_i} \sigma_i dA_i = 0$$

$$\sigma_i = \frac{E_i(y + \delta)}{\rho}$$
(4.3)

where σ_i , A_i , and E_i correspond to the stress, cross sectional area and modulus of elasticity of the i^{th} component of the sensor assembly, namely the tube, FBG array and NiTi wires. ρ and δ correspond to radius of curvature and sensor bias (offset between the FBG array and neutral plane), respectively, while y corresponds to the vertical distance between the center of each component (i.e. fiber or NiTi) and the coordinate frame attached to the center of the fiber (Fig. 4.2(b)). The bias for the sensor assembly can be computed as:

$$\delta = \frac{(3E_n D_n^2 + E_t(D_t^2 - 3D_l^2)) r}{E_f D_f^2 + 2E_n D_n^2 + E_t(D_t^2 - 3D_l^2)}$$
(4.4)

Where the subscripts n , f , t and l correspond to nitinol wire, FBG array, tube and lumen, respectively. E is the modulus of elasticity, D is the diameter, and r is the radius of the circle on which the centers of three circular lumens are located (Fig. 4.2(b)). The sensor bias relates the curvature and mechanical strain at a particular cross section of the sensor using the following:

$$\epsilon = \delta \kappa$$
(4.5)

where κ and ϵ refer to the curvature and strain. The computed strain from (4.5) can

CHAPTER 4. SENSOR DESIGNS

be substituted into (4.2) to show that if temperature variations are negligible (i.e. $\Delta T \approx 0$), wavelength shift and curvature follow a linear relationship:

$$\Delta\lambda_B = \underbrace{\lambda_B(1 - p_e)}_{\text{constant}} \delta \kappa \quad (4.6)$$

4.4.1.2 Tube Material Selection

Of note, the sensor assembly must tolerate large deflections with great elasticity. In addition, according to (4.4), the tube modulus of elasticity (E_t) plays an important role in sensor bias calculation; larger E_t raises the sensor bias δ . The manufactured tube with the selected material must also have smooth surface to avoid introducing significant friction with the CM sensor channel and hysteresis in the sensor assembly. Due to their flexibility, polycarbonate and low density polyethylene (LDPE) were chosen as two possible tube material candidates for the proposed sensor design. Considering the aforementioned criteria, polycarbonate (Shore hardness of 80) was chosen due to higher modulus of elasticity.

4.4.1.3 Tube Geometry and Fabrication

The OD of the designed sensor assembly must be slightly smaller than the CM sensor channels ($600\ \mu\text{m}$) to ensure easy sliding of the sensor assemblies within the channels. Further, examination of (4.4) demonstrates the effect of tube geometry on the sensor bias. The coefficients D and r in (4.4) represent the role of tube OD

CHAPTER 4. SENSOR DESIGNS

Table 4.1: Parameters used in the design and fabrication of the polycarbonate tube sensor.

Young's Modulus	Value (GPa)	Dimension	Value (μm)
E_f	70.0	D_f	125.0
E_n	75.0	D_n	125.0
E_t	2.6	D_t	500.0
		D_l	150.0
		r	100.0

and location of the symmetric lumens on the sensor bias. Considering the limitation associated with the CM assembly and increasing the sensor bias, a tube with outer diameter of $500 \pm 15 \mu m$ and three symmetric $150 \pm 5 \mu m$ lumens (Paradigm Optics, Inc.) was designed. The rest of the parameters (diameters and modulus of elasticity) used in the design of the tube are listed in Table. 4.1. It should be noted that a circular cross section was chosen due to easier manufacturing process. The manufacturing was done by a straight draw method on polycarbonate (Incom Inc., Charlton, MA, USA). Fig. 4.2(a) shows the geometry of the cross section of the manufactured tube under microscope (LEICA DMi8 A).

4.4.1.4 Calibration Experiments

Two sets of experiments were conducted to evaluate the fabricated sensor:

1. Sensor separate calibration
2. Integrated sensor-CM assembly calibration

CHAPTER 4. SENSOR DESIGNS

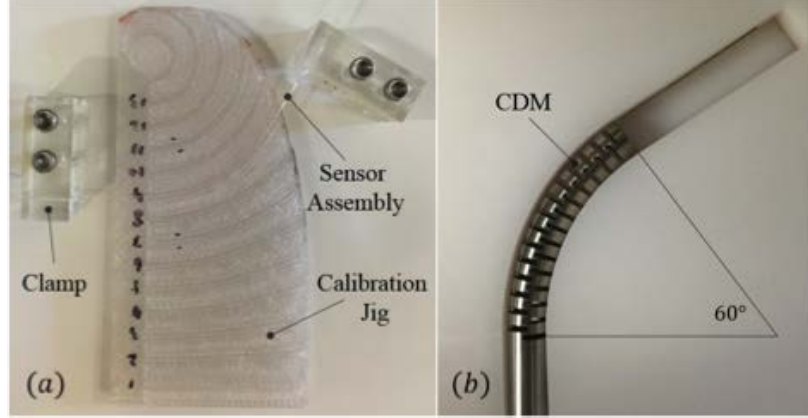


Figure 4.4: (a) sensor calibration jig, (b) sensor-CM assembly calibration jig

Previous studies have reported maximum curvature sensing of 22.7 m^{-1} using FBGs [98]. In experiment (1), the curvature-wavelength linearity was validated using a 3D-printed calibration jig with constant curvatures ranging from 0 to 66.66 m^{-1} ; nearly three times as large compared to previous studies (Fig. 4.4). The orientation of the sensor assembly was maintained throughout the calibration process by using two clamps, one on each end of the curved slots on the jig. During each experiment, the sensor was placed in each curvature slot and a three-minute waiting time was imposed to ensure no motion was present (static behavior). Then 200 FBG readings were recorded by the interrogator (Micron Optics sm130) with a frequency of 100 Hz. To ensure robustness and elimination of outliers, each experiment was carried out a total of five times. To reduce temperature variations, the calibration jig was placed within an enclosure (Fig. 4.5).

In experiment (2), the behavior of the sensor in detecting the CM large deflec-

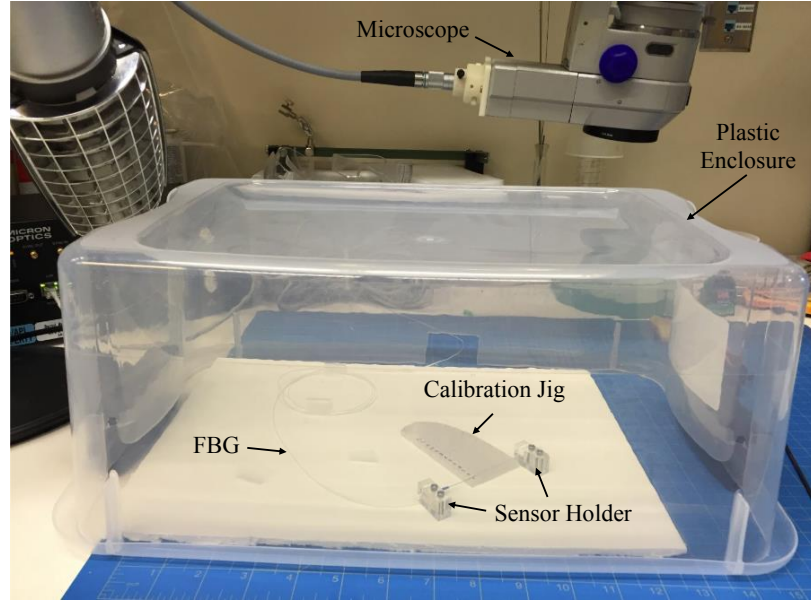


Figure 4.5: Calibration jig placed inside an enclosure to reduce temperature variation.

tion was evaluated. For this purpose, the sensor was embedded into the CM sensor channel and small amount of adhesive was applied to the distal end (tip) of the manipulator to secure the sensor. The sensor-CM assembly was then calibrated in five different CM bending angles (30° , 45° , 60° , 75° , 90°). Fig. 4.4 demonstrates the 60° calibration board as example. Similar to the sensor-only calibration, the experiments were repeated five times and experimental setup was confined within an enclosure to reduce temperature variations. Sampling rate and waiting time before recording data were similar to those used during the sensor-only calibration experiments. To validate the linearity between curvature and wavelength readings, the wavelength-curvature linear fit equation was generated using four of the calibration angles. The wavelength data from the fifth bending angle was then used in the fit equation to predict the curvature and measure prediction error (leave-one-out experiment).

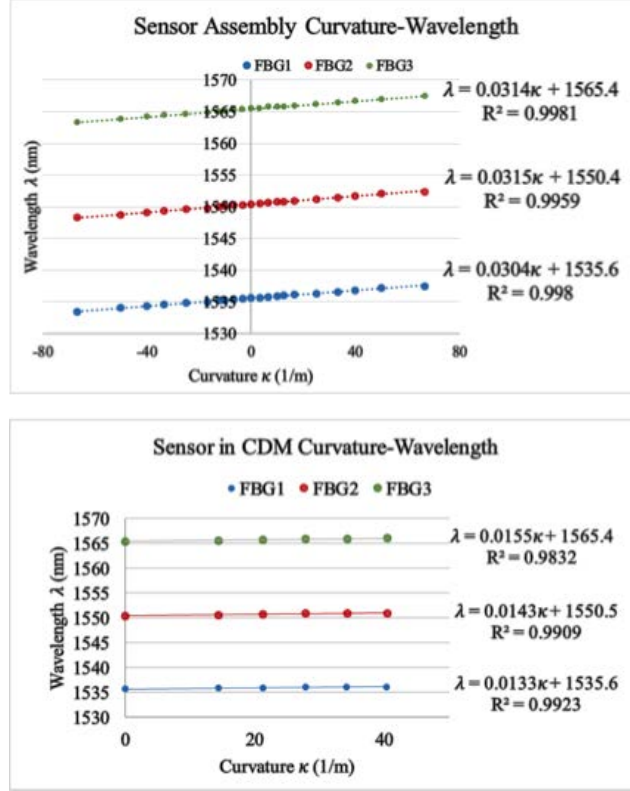


Figure 4.6: Top: Sensor calibration results. Bottom: Integrated sensor-CM calibration results

4.4.1.5 Results and Discussion

The average of the five wavelength data corresponding to a specific curvature in each set of experiment is plotted in Fig. 4.6. With the r-squared correlation coefficient $R^2 \approx 0.99$, results validate the linear wavelength-curvature relationship for all three FBGs in both sets of experiments. Additionally, all three lines in each graph have exhibited nearly similar slopes. The leave-one-out experiment reported 3.3% error in detecting the curvature. Consistent calibration results indicate the capability and reliability of the new simplified sensor assembly method in detecting large deflections.

CHAPTER 4. SENSOR DESIGNS

Table 4.2: Sensor bias computations for different combinations of fiber and NiTi wires used.

Number of fibers	Number of NiTi wires	$\delta(\mu m)$
1	2	125
2	1	73
3	0	55

This improves manufacturing efficiency and assembly accuracy of large deflection shape sensors.

Of note, the three lumens considered in the design of the polycarbonate tube can be used for embedding different combinations of fiber and NiTi wires. There would then be a trade-off between the number of sensory information (potentially more accurate sensing), cost (if more fibers with FBGs are used) and the sensor bias (if more NiTi wires are used). Since the modulus of elasticity of a NiTi wire is larger than that of fiber, incorporation of two NiTi wires increases the sensor bias and consequently sensitivity of the sensor. Table 4.2 reports the computed sensor bias for different combinations of fiber and NiTi wire components used in the sensor assembly.

4.4.2 Notched Nitinol Substrate

The geometry of the polycarbonate tube described in Section 4.4.1 guaranteed a unique pattern for the fiber and NiTi wires integration, motivating manufacturing repeatability, while meeting other criteria such as flexibility and high bend capability.

CHAPTER 4. SENSOR DESIGNS

Despite the manufacturing improvements over the previously designed shape sensors (e.g. [98, 118, 122]), the polycarbonate tube assembly introduced new issues such as non-uniform adhesive distribution along the length of the fiber due to the enclosed geometry and lack of complete exposure and access to the lumens. In addition, as can be observed from the calibration results in Fig. 4.6, the small line slopes indicates low sensitivity of the fabricated sensor to small curvature changes, leading to a small signal to noise ratio (SNR). In such situations, shape reconstruction becomes more susceptible to noise introduced by the FBGs and temperature variations. These limitations encouraged the development of a new sensing technology which could address the above-mentioned issues. As such, another sensing unit for large deflection shape sensing in CMs is developed and methods for characterization, evaluation, and calibration of the proposed sensor assembly are described.

4.4.2.1 Design Requirements

Considering the mentioned challenges for shape sensing of a CM with large deflection, the following criteria are defined for the shape sensing unit. In particular the attempt is to design and a sensor which:

1. is easy to fabricate, assemble, and evaluate
2. is inexpensive when compared to other fabrication methods including multicore FBGs

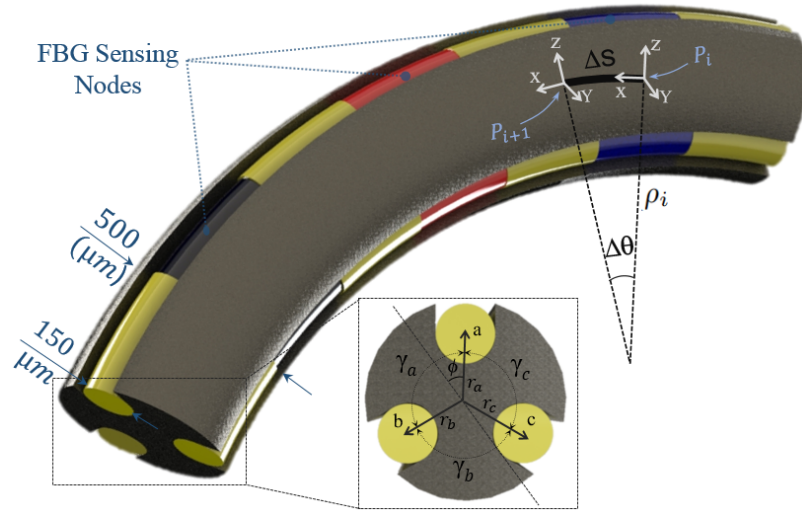


Figure 4.7: Fiber optic sensor with notched NiTi substrate.

3. can be used for 2-D and 3-D shape sensing of CMs
4. can be used for large deflection shape sensing
5. exhibits large SNR
6. demonstrates high sensitivity to small local deformations

4.4.2.2 Substrate Design and Geometry

To address the design requirements, the aim is to develop a sensing unit that provides better access to the sensor components during integration and assembly. As such, considering the equations governing the behavior of the FBG sensors (i.e. (4.2) and (4.6)), a sensor is designed that consists of a 60 mm long NiTi wire as substrate with 500 μm OD and three 150 μm diameter grooves along the longitudinal axis of

CHAPTER 4. SENSOR DESIGNS

the NiTi. The length of the substrate was chosen longer than that of the CM for facilitation of the sensor integration with the CM. The grooves on the NiTi substrate were engraved 120° radially from one another by laser (Potomac Laser, Baltimore, MD), (Fig. 4.7) to ensure easy placement of the sensor components (requirements 1 and 3). NiTi was chosen as a substrate for the sensing unit due to its superelasticity, providing flexibility and large deflection capability, yet greater structural strength as compared to the polycarbonate substrate introduced in Section 4.4.1 (requirement 4). In addition, larger radial distances of the grooves from the center of the NiTi provide for larger sensor bias, leading to higher sensitivity, when compared to the previously developed polycarbonate-substrate sensor (requirement 5 and 6). Three $125\mu\text{m}$ diameter cladding polyimide optical fibers (Technica Optical Components, China), each with three active FBGs were placed and glued (JB Weld Quick Setting Epoxy Syringe) onto the easily accessible grooves along the length of the NiTi (requirements 2 and 3).

4.4.2.3 Sensor Characterization

With the presence of the manufacturing concerns, validation of the assembly procedure (fiber attachment, active area placement along the length of sensor, etc.) and wavelength-to-curvature calibration is necessary to identify potential manufacturing mistakes and to avoid error propagation in shape reconstruction. After fabricating the sensor, the structural symmetry and integrity of the sensor was validated. The

CHAPTER 4. SENSOR DESIGNS

data acquired by this experimentation enabled the characterization of the sensor to ensure its successful manufacturing.

To perform the experiments, the sensor was cantilevered using a pin vise and mounted on a manual axial rotational stage attached to a manual z-directional linear stage mounted to an optical table (Fig. 4.8). The sensing unit was clamped in the pin vise and oriented such that a single fiber component was aligned facing vertically upwards (yellow fiber shown in Fig. 4.9(b)). The opposing side of the cantilever was point-supported and placed on a scale to measure applied force to the free end of the cantilevered sensor. The entire experimental setup was enclosed from the surrounding environment such that external vibrations, temperature fluxes, and surrounding air currents effects on the sensor were minimized.

Three configurations at 120° intervals were tested such that each fiber component was facing the positive z-direction once. In each configuration, the linear stage was adjusted at 0.5 mm increments in the negative z-direction from the height of point support contact resulting in a total of 6.0 mm deflection. It was then returned to its original height at the same incremental rate to evaluate hysteresis effect. Each set of experiments for each of the three sensor configurations was repeated five times. Overall, a total of 390 experiments were carried out. Fig. 4.9 depicts the average of five trials wavelength shift versus the average measured force values for three different configurations (a, b, and c).

CHAPTER 4. SENSOR DESIGNS

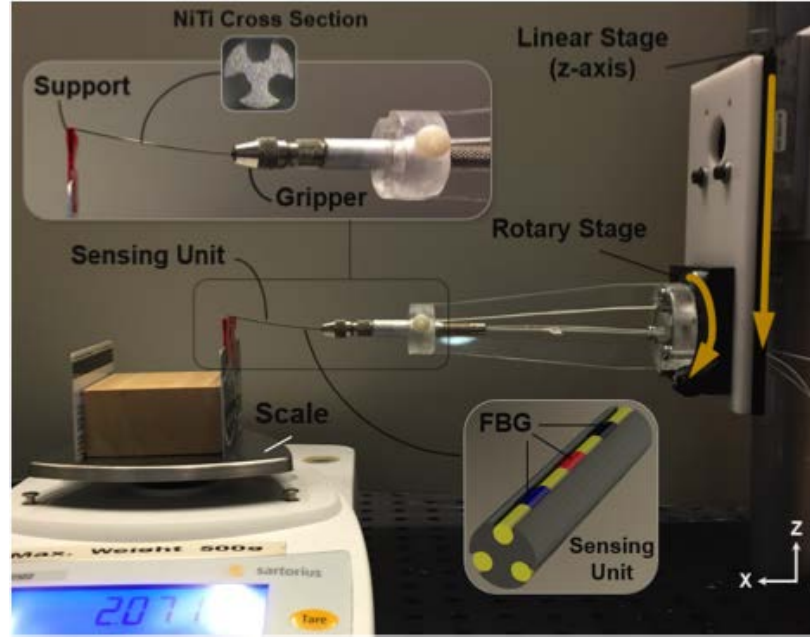


Figure 4.8: Sensor symmetry validation experimental setup [101].

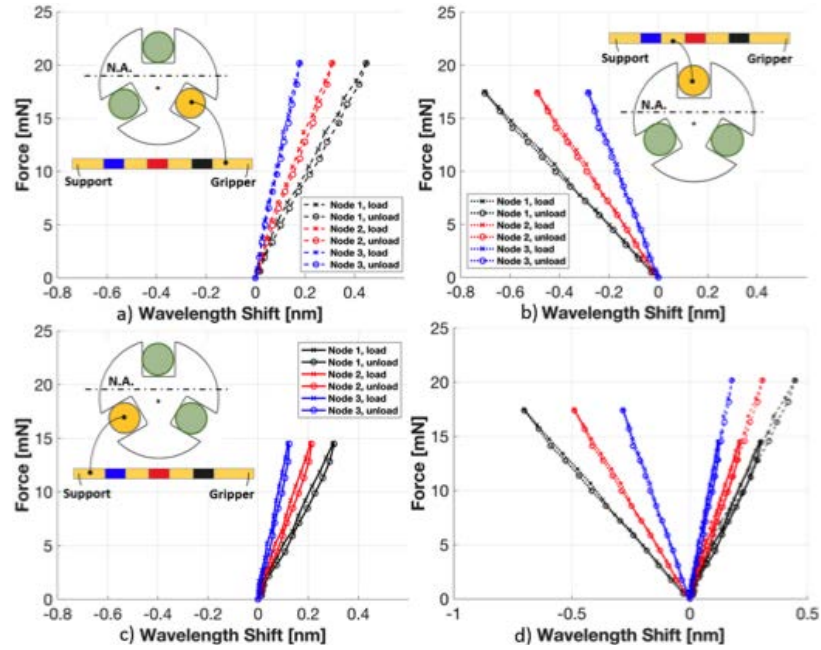


Figure 4.9: Notched NiTi Sensor characterization experiments results. (a), (b), (c) force-wavelength shift relationship in different configurations of an individual fiber with three FBGs (black, red, blue), (d) overlay plot of all experiments

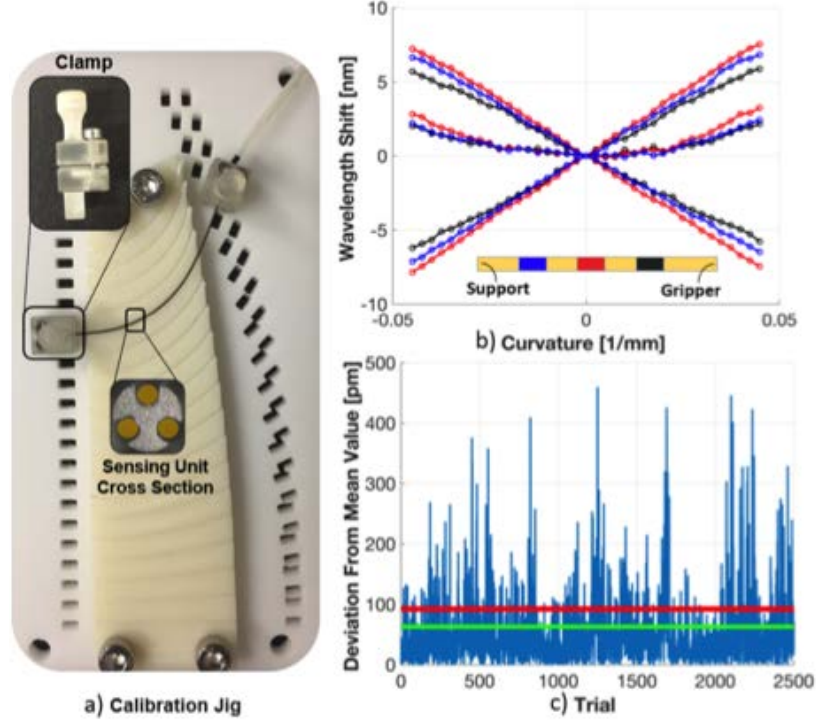


Figure 4.10: Calibration experiment results. a) calibration setup, b) curvature-wavelength shift relationship for an individual fiber in different configurations, c) wavelength deviation from mean values over five trials

4.4.2.4 Sensor Calibration

For shape reconstruction, the relationship between the curvature and the wavelength shift of the nine integrated FBG sensor nodes (three on each fiber) is required. A calibration jig with discrete constant curvature slots ranging from 0° to 90° of deflection with 5° intervals and constant arc length was developed (Fig. 4.10). The sensing unit was fixed between two clamps, which rigidly interacted with the calibration jig such that the sensor was always concentrically aligned with the edge of slot. The length of the sensor was accommodated to fit within the calibration slots, while the two clamps maintained the orientation of the sensor relative to the clamp.

CHAPTER 4. SENSOR DESIGNS

Once the clamp-sensor assembly was placed into the selected slots, the sensor was completely fixed in the x-y plane with all nodes undergoing a constant curvature. Complimentary jigs were developed such that the positive and negative effect of curvature could be investigated. The sensors were examined at all radii of curvature (ranging from 0 to 20 mm) provided by both jigs (positive and negative) and were each sampled a total of five times. Three configurations at 120° intervals of rotation of the sensor relative to the clamps were tested such that each fiber was facing the positive z-direction once. Five trials were conducted at each orientation. Data were collected at a rate of 100 Hz for two seconds. Data from all five trials were averaged and plotted in Fig. 4.10(b).

4.4.2.5 Results and Discussion

Fig. 4.9 demonstrates the behavior of all three active areas (marked in black, red, blue, respectively) on an individual fiber (shown in yellow), when the fiber is in different configurations. The active area marked in black and blue are closest to the gripper side (see Fig. 4.8) and the support, respectively (experiment A, Fig. 4.9).

The following are the observations deduced from Fig. 4.9:

- Wavelength shift for all active areas are positive (tension) when the fiber is in configuration a and c (since it is below the neutral axis), as opposed to configuration b, which has all negative (compression) wavelength shift values (since the fiber is above the neutral axis)

CHAPTER 4. SENSOR DESIGNS

- Maximum wavelength shift for each individual active area is greater in configuration b, compared to configurations a and c, due to an increased distance of the fiber relative to the neutral axis in configuration b
- In all three configurations, the active area closest to the gripper undergoes a greater wavelength shift, due to larger deflections near the gripper (Fig. 4.8)
- The force-wavelength relationship is linear (r-squared measure of 0.99), with little hysteresis in loading and unloading experiments (average force and wavelength shift hysteresis 0.47 mN and 17 pm, respectively)
- Force to wavelength ratio (line slope) is similar for all the active areas in configuration a and c (Fig. 4.9-d, where all configurations data are overlaid), since the fiber distance to the neutral axis is the same for these two configurations.

These results confirmed the proper fabrication and attachment of the fibers to the NiTi substrate. Any deviation from the observed behavior in Fig. 4.9 suggests issues with gluing or inconsistent structural integrity of the sensor assembly.

Fig. 4.10(a) shows the calibration jig used for the calibration experiments. Fig. 4.6 (b) demonstrates the wavelength shift relation with curvature for an individual fiber, when placed in different configurations. Experimental results demonstrate higher sensitivity (up to 8 nm wavelength shift) of the sensor to changes in curvature, compared to the polycarbonate sensor described in Section 4.4.1 (up to ≈ 4 nm) and Liu et al [98, 118] (up to ≈ 5 nm). Such large wavelength shifts diminish the effect of

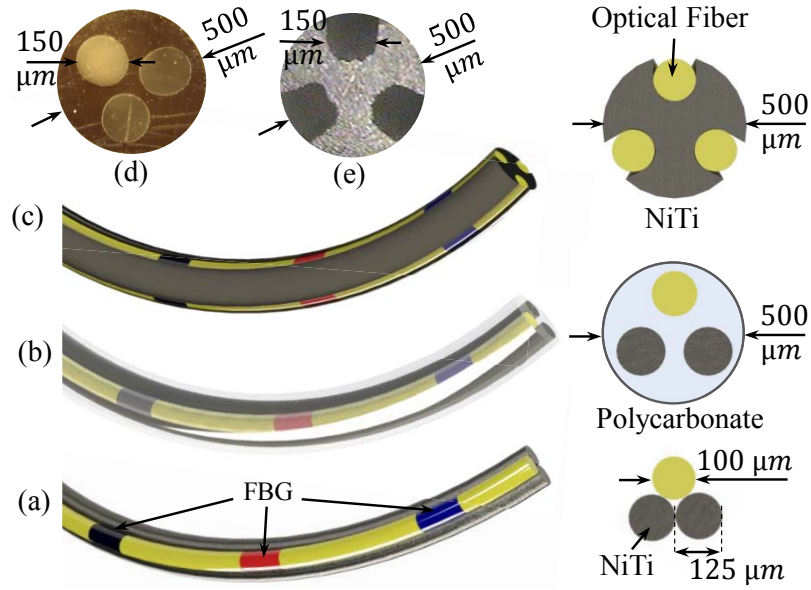


Figure 4.11: FBG sensors: (a) first generation using two NiTi wires, (b) second generation using polycarbonate tube substrate, (c) third generation using notched NiTi substrate, (d) polycarbonate tube cross section, (e) notched NiTi cross section.

noise, such as temperature variation, and enable detection of small curvature changes.

Wavelength shift deviations from the average value in each set of five experiments is plotted in Fig. 4.10(c), which indicates a root mean square error of 92 pm (red line) and a mean error of 63 pm, both of which are small relative to the sensitivity of the sensor, meeting the sensor assembly requirements.

Of note, Fig. 4.11 shows the three different generations of FBG sensors developed for the system (note the differences in the geometry, choice of substrate, and number of fibers used in each design). The first generation was developed by Liu et al. [98, 118], while the second (polycarbonate substrate) and third generation (notched NiTi substrate) were described in this chapter.

4.5 Distributed Sensing

Even though FBG-based FOS have shown great potential in shape sensing of CMs and other flexible medical devices, due to the limited number of sensing locations, these sensors become unreliable in the presence of many inflection points in complex shapes. Distributed sensing with higher spatial resolution using the OFDR technique can address such problems. OFDR is an interferometric technique that was first developed as a way to measure optical fibers' reflectivity, and therefore detect losses or breaks in the fibers. The OFDR method for distributed sensing was first described by Froggatt et al. in 1998 [99]. They showed that it could also be used for sensing strain and temperature variations along a fiber's length in the same way as a regular FBG, but in a completely distributed approach. As such, regular fiber can be used instead of expensive FBG sensors, and spatial resolution is no longer dependant on the physical position of those FBGs in the fiber, but rather on the fiber interrogator parameters. OFDR-based sensing has since been demonstrated to be very accurate for temperature and strain sensing [127], but also for distributed shape sensing [128–130].

OFDR interrogators are currently available with very fast acquisition speed (250 Hz) and spatial resolutions of less than 1 mm. However, SNR is typically very low due to the small backscattering of regular optical fibers. This limits the sensing accuracy that can be obtained with such high acquisition speeds and spatial resolutions.

In order to perform the strain measurements, a tunable laser source scans the fiber under test across a certain scanning bandwidth $\Delta\lambda$ (see Fig. 4.12(a)). A Fourier

CHAPTER 4. SENSOR DESIGNS

transform is then performed to transfer this signal in the spatial domain, thus obtaining the fiber reflectivity as a function of position. For every sensing point x_m in the fiber, a certain gauge length Δx is then defined (dashed rectangle in Fig. 4.12(b)). This gauge length defines the spatial resolution of the system. A longer gauge length means more data points can be used, and thus better sensing resolution can be obtained, but the spatial resolution decreases. An inverse Fourier transform is then performed across this gauge length to return in the spectral domain. The sample measurement is then compared to a reference measurement, and the cross-correlation between sample and reference measurement results in a peak, shown in Fig. 4.12(e). The position of that peak gives the spectral shift for this specific point across the fiber length. This spectral shift is proportional to both temperature and strain variations between reference and sample measurements, as was described in (4.2).

4.5.1 Random Optical Gratings by Ultraviolet Laser

Exposure¹

In order to enhance the sensing accuracy, random optical gratings by ultraviolet emission (ROGUEs) can be written in the fiber core to increase backscatter by up to 50 dB. This enhancement in backscatter results in more than an order of magnitude improvement in sensing accuracy [132]. As such, those sensors can provide very

¹The development and characterization of ROGUE fiber triplet was performed by Frederic Monet and his team at Polytechnique Montreal.

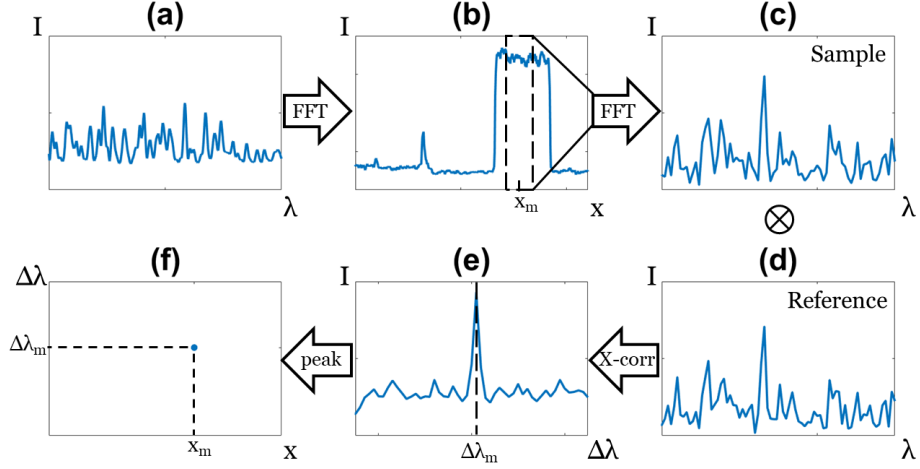


Figure 4.12: Cartoon illustrating the different OFDR steps for a single sensor along the fiber's length [131, 132]. Steps are: (a) signal in the spectral domain, (b) signal in the spatial domain, (c) gauge length window in the spectral domain, (d) cross-correlation with the reference, (e) cross-correlation result and (f) spectral shift along the fiber's length. Steps (c) to (f) are repeated for every sensing point along the sensing region.

accurate measurements at a high acquisition rate and spatial resolution.

4.5.1.1 ROGUE Writing

The ROGUE fabrication process is covered in [132]. Briefly, the random grating is written using a 213 nm Q-switched laser in a Talbot interferometer scheme, presented in Fig. 4.13. The phase mask separates the ultraviolet light in two beams, which are then recombined on a moving optical fiber, resulting in an interference pattern written on the photosensitive fiber as it is being moved. The random electric signal applied on the piezoelectric element results in an overall random pattern written in the fiber, generating the ROGUE. The fiber used was an SMF-28 from Corning,

CHAPTER 4. SENSOR DESIGNS

a standard telecommunications fiber, that was loaded with deuterium to enhance photosensitivity. However, because the standard fiber coating has very high UV absorption, it had to be removed prior to the ROGUE writing.

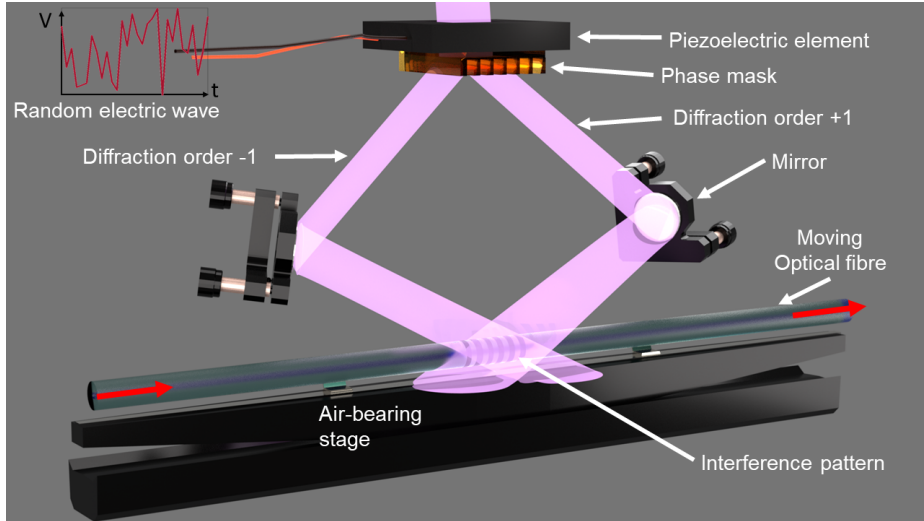


Figure 4.13: ROGUE writing setup [132].

4.5.1.2 ROGUE fiber triplet

The ROGUE fiber triplet used for the OFDR was fabricated using a different manufacturing technique, described in [133]. Using a polymer extrusion, this technique protects the uncoated optical fibers where the ROGUEs were inscribed by encapsulating them in a polymer coating, as well as fixing their geometrical configuration. Furthermore, as all three fibers are being pulled continuously, this allows the fabrication of triplets of arbitrarily large lengths, thus enabling possible industrial implementation.

CHAPTER 4. SENSOR DESIGNS

Because this fabrication method does not offer a control on the fiber position which is as accurate for the method used for the FBGs, additional steps were taken to characterize the fibers' arrangement inside the triplet. To do so, a tomography workbench was developed to non-destructively image and reconstruct the fibers' positions along the triplet's length. Fig. 4.14 shows this characterization setup. The triplet is imaged in transmission, and rotated across 180° . This results in a tomogram of the transmitted light as a function of the rotation angle. This transmitted light is simply the line integral of the light's propagation through the triplet, and the tomogram consists of different projections of this line integral. In order to recover the cross-section image of the fiber triplet, all that is needed is to apply the correct transformation. In this case, the transformation is the inverse Radon transform, as described by A. M. Cormack [134].

4.5.1.3 Results and Discussion

Fig. 4.15 displays the reconstruction of the first and second iteration of the fiber triplet manufacturing. As it can be observed in the left image, if an equilateral triangle configuration had been assumed for the triplet, the results for the first iteration would be very inaccurate. Such an important deviation from the expected triangular shape can be explained by the triplet fabrication process. As the initial triplet was over $600\mu\text{m}$ in diameter, it was too large to fit inside the CM's sensing channels. Therefore, some of the excess polymer had to be melted off to reduce the triplet's

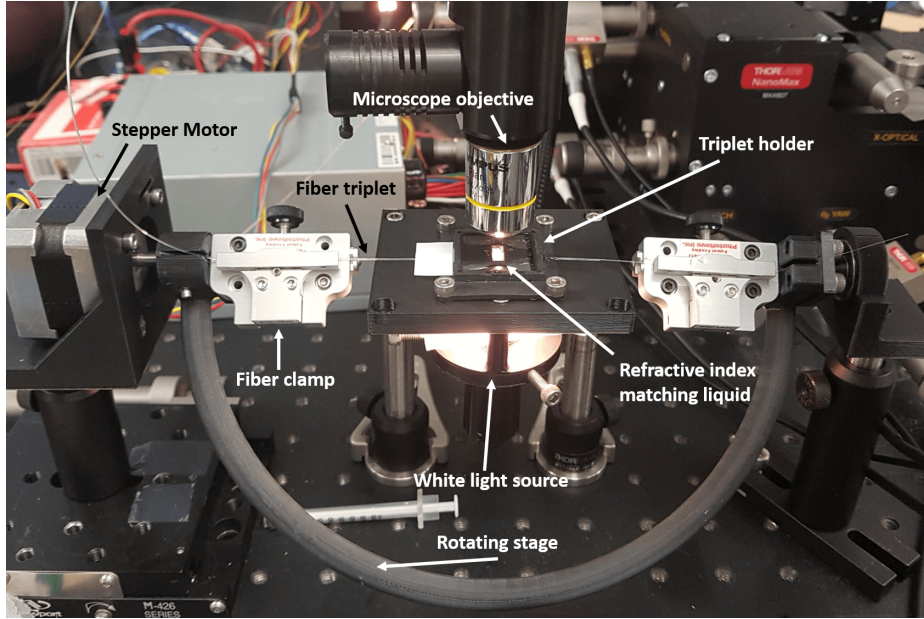


Figure 4.14: Tomography calibration setup [131]. The fiber triplet is held by two fiber clamps (PhotoNova Inc.) that are rotated by a stepper motor across 180° . Every 0.9° , a camera captures the transmitted image, magnified by a microscope objective. A 3-D printed triplet holder maintains the triplet in position, but allows it to rotate freely. The triplet is bathed in a refractive index matching liquid that diminishes the refractive index variation between the polymer and the ambient air.

diameter. However, this caused the fibers inside the triplet to move away from the triangular arrangement, further confirming the importance of this characterization step. The triplet fabrication process could be optimized to achieve triplets of smaller diameter, either by better control of the extrusion parameters (speed, temperature, etc.) or by the choice of a polymer with different properties. This would ensure better control over the geometrical configuration of the fibers. The second iteration of the triplet extrusion demonstrated progress in optimizing the manufacturing process, as demonstrated by the extruded sensors displayed in the right image of Fig. 4.15.

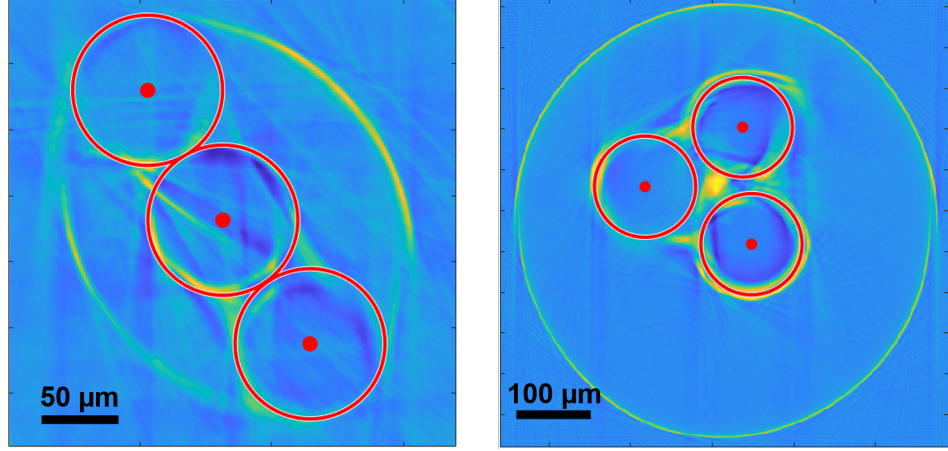


Figure 4.15: Reconstruction of the fibers' position inside the triplet by tomography. The center and diameter of the fibers are shown by red dots and circles, respectively. Left: First iteration of the fiber triplet. The oval shape of the overall triplet can be observed. Right: Second iteration of the fiber triplet. As can be observed, the fibers' configuration is much closer to the optimal equilateral triangle.

4.5.2 Interrogator Devices

The FBG and distributed FOS each require specific interrogation devices to measure the wavelength shift associated with each sensor. Currently available commercialized interrogators for FBGs can generally provide faster data streaming rate compared to those developed for distributed sensors. This is due to the higher spatial resolution (more active sensing points) and excessive computation steps during the signal processing procedure for the distributed sensors, as described in Section. 4.5.

During all the experiments in this thesis, the FBG sensors were interrogated using a commercially available interrogator with max streaming rate of 1 KHz (Micron Optics sm 130, Atlanta, GA, USA), while the distributed triplet was interrogated using a commercially available OFDR interrogator (ODiSI-B, Luna Innovations Inc.,

CHAPTER 4. SENSOR DESIGNS



Figure 4.16: Interrogator devices used for experiments. Left: For FBG-based sensors (image courtesy of Micron Optics). Right: For distributed OFDR-based sensors (image courtesy of Luna Innovations Inc.).

Roanoke, VA, USA) with maximum streaming rate of 250 Hz with a spatial resolution of 2.6 mm. For a higher spatial resolution with the distributed sensor during our experiments, however, the interrogation settings were set to 24 Hz, with a 0.65 mm spatial resolution. Those settings were the ones that offered the best spatial resolution, but are however limited in the acquisition speed. As such, the trade-off between the sensor's spatial resolution and rate of data acquisition must be considered depending on the application and requirements. Fig. 4.16 shows the interrogator devices used for the FBG and distributed sensors.

4.6 Conclusion

This chapter explained the importance of use of FOS for real-time shape feedback of flexible medical devices such as CMs. Design and fabrication requirements associated with fiber optic shape sensors for CMs with large deflection bending capa-

CHAPTER 4. SENSOR DESIGNS

bilities were described and the trade-offs between the design, use, and interrogation of multi-point (FBG-based) and distributed (OFDR-based) sensors were discussed. While distributed sensors provide higher spatial resolution compared to FBG-based sensors, it is also possible to fabricate sensors with larger FBG density, thus increasing spatial resolution. However, the manufacturing costs would increase accordingly, and the fabrication of a sensor with FBGs spaced by as little as 0.65 mm would be a major challenge in itself. On the contrary, the interrogation of FBG sensors can be performed with faster rates due to easier and fewer computation steps.

Compared to other proposed approaches [98,116,118,120], the polycarbonate tube substrate improved the control over sensor geometry and increased repeatability of fabrication. Even though the enclosed design of the lumens provided safe placement of fiber and NiTi components in the sensor, it also introduced challenges associated with uniform application of adhesive for secure fixation of the fiber and substrate. However, the the accessibility of the grooves in the proposed notched NiTi substrate design, provided great advantage and control in optical fiber placement and attachment over the previously developed sensing units resulting in a higher SNR and sensitivity to small local curvatures. The small size of the NiTi substrate (0.5 mm) compared to e.g. [106] also increased the flexibility of the sensor for large deflection bending applications such as the one studied in this thesis.

Commercially-available robotic technologies have also reported the use of FOS for

CHAPTER 4. SENSOR DESIGNS

shape and force sensing [95, 135–138]. The Ion² (Intuitive Surgical, Inc., Sunnyvale, CA), a robotic-assisted endoluminal platform for minimally invasive peripheral lung biopsy, is an example of such systems. This system features a 3.5 mm outer-diameter catheter with a 2.0 mm working channel that can move 180° in all directions and pass through small and difficult-to-navigate airways within the lung. In addition, the Fiber Optic RealShape (FORS) technology (registered trademark of Koninklijke Philips N.V.) [139–141] enables the Ion system with active robotic control of the catheter’s position throughout the entire navigation and biopsy process. The FORS technology uses one or more optical fibers structurally configured under the OFDR principle for extracting high density strain measurements of the optical fiber derived from light emitted into and reflected back within the optical fiber(s). The FORS technology enables shape sensing of the Ion’s catheter at 100 Hz. At the time of writing of this dissertation, however, no other information regarding the spatial resolution, method of assembly, and shape reconstruction accuracy of the Ion is available.

4.7 Acknowledgments

I would like to thank Mr. Michael Pozin, Mr. Weiqi Wang, and Ms. Qiaozhi Wang for their help with the notched NiTi substrate sensor characterization experiments. Special thanks to Mr. Frederic Monet and his team at the Polytechnique Montreal for

²<https://www.intuitive.com/en-us/products-and-services/ion>

CHAPTER 4. SENSOR DESIGNS

the design, fabrication and characterization of the fiber triplet with ROGUE writing.

Last but not least, sincerest thanks to Dr. Iulian Iordachita for providing me with his continuous support, experience and expertise during the design and development of the fiber optic sensors within the last couple of years.

Chapter 5

Sensing Algorithms

5.1 Motivation and Background

This chapter introduces several sensing algorithms using fiber optic sensors (FOS) for shape reconstruction, distal-end position estimation (DPE) and contact detection for continuum manipulators (CMs) in constrained environments. Conventionally, these problems are approached by development of mechanics- or -kinematics-based models that rely on many assumptions about the geometry or physical properties of the CM or its environment [3, 84]. Models can provide insightful information about the effect of individual parameters on the performance. Moreover, they can help in improving the design by developing intuition and physical understanding of the behaviour. The performance of such model-dependent algorithms, however, is heavily influenced by the accuracy of the models, their capability to capture the

CHAPTER 5. SENSING ALGORITHMS

underlying physics of the problem, and validity of the assumptions. Furthermore, the uncertainties or unanticipated disturbances present in previously unseen constrained environments (e.g. during a surgical intervention) may result in poor performance of these models.

Another drawback of the traditional model-driven approaches is that they may not accommodate adequate complexity due to model simplifications (such as model linearization) [142]. They also require a deep understanding of the system or the process to account for all the necessary variables that could capture the underlying physics of the system. With recent unprecedented access to data, as well as inexpensive and powerful computing hardware, data-driven approaches have demonstrated the ability to capture richer information from raw input data by learning representations of data with multiple levels of abstraction [143, 144].

The first aim of this chapter is to study the complications and challenges associated with these model-dependent sensing approaches in CMs using FOS for shape reconstruction and contact detection. The second goal is to propose several data-driven model-independent methods to mitigate these challenges in presence of uncertainties such as unknown obstacles during surgical interventions. These methods are evaluated in various cases in free and constrained environments mimicking real surgical scenarios.

5.2 Contribution

The contributions of the author in this chapter include:

- Development, implementation, and evaluation of several data-driven model-independent approaches such as Deep Neural Network (DNN), Temporal Neural Network (TNN) and linear regression for fiber optic shape sensing and DPE of CMs in free and constrained environments.
- Evaluation and comparison of model-dependent approaches for shape sensing and DPE with the proposed data-driven methods.
- Development and implementation of a data-driven contact detection method without any prior knowledge about the CM workspace or constrained kinematics model as well as evaluation of the proposed method in constrained environment with soft and hard obstacles.
- Evaluation and comparison of shape sensing accuracy of CMs using multi-point fiber Bragg grating-based (FBG-based) and distributed random optical gratings by ultraviolet emission (ROGUE-based) FOS for large deflection bending and reconstruction of CM complex shapes in free and constrained environments.

Mr. Cong Gao helped the author in implementing the data-driven methods for DPE and conducting the evaluation experiments. Mr. Frederic Monet equally con-

tributed with the author in performing the shape sensing experiments using the distributed FOS.

The work presented in this chapter was published in International Conference on Robotics and Automation (2020) [131], International Conference on Medical Image Computing and Computer-Assisted Intervention (MICCAI) 2019 [145] and International Symposium on Medical Robotics (ISMR) 2019 [146]. Also the remainder of the presented work is currently under review at IEEE Sensors Journal [147].

5.3 Model-Based Sensing

5.3.1 Motivation and Background

Compared to rigid link robots, CMs can adopt to various shapes and exhibit compliance when interacting with obstacles and contacting organs [3]. Although beneficial for minimally invasive surgery (MIS) applications, the flexibility and conformity of the CMs makes accurate shape sensing and DPE challenging. As outlined in Chapter 4, FOS offer several benefits compared to other sensing modalities and hence they have gained attention as a suitable method for CM shape sensing and DPE.

In recent years, a multitude of FBG-based FOS for CM shape sensing have been studied in the literature. Roesthuis et al, [116] reported CM shape sensing in free environment using a triangular configuration sensor (three optical fibers) with four FBGs on each fiber. They reconstructed the shape using a model-driven approach

CHAPTER 5. SENSING ALGORITHMS

and performed an additional calibration step to correct for inaccuracies in DPE by scaling the reconstructed values from the algorithm. Liu et al. [118] and Farvardin et al. [122] developed two triangular configuration FOS each constructed of one fiber with three FBGs and embedded the sensors in the wall channels of a large deflection CM. They reconstructed the shape by performing a calibration to establish a mapping between the curvature and FBG wavelength information, followed by a model-driven geometrical approach to estimate the shape in free and constrained environments. Ryu et al. [120] developed a prototype FBG sensor using one fiber attached onto the surface of a polymer tube and reported the model-dependent shape reconstruction results only in free space. Xu et al. [97] introduced the concept of helical configuration sensor design with three fibers for simultaneous curvature, torsion and force sensing. However, they did not provide any evaluation study on the accuracy of curvature estimation and shape reconstruction using the proposed method. Wei et al. [121] further explored this concept by incorporating only one fiber wrapped around a nitinol (NiTi) wire back and fourth along the length of the substrate. Similarly, no evaluation studies on the accuracy of estimations were provided. Table 5.3.1 summarizes the sensor design and model-driven shape reconstruction and DPE results reported in the above-mentioned studies.

As can be observed from Table 5.3.1, while previous studies have provided good insight about design considerations of FBG-based sensors for CMs, they lack a comprehensive and unified evaluation of the shape reconstruction and DPE results, spe-

Table 5.1: Review of FBG-based continuum manipulator DPE by different research groups (NR = not reported).

Research Group	FBG Sensor Design					Manipulator		DPE Mean (Std) (mm)	
	# Fibers	# FBGs	Substrate (OD)	# Sensors	Configuration	Length	Sensor Assem.	Free	Constrained
Roesthuis et al. [116]	Three	Four	NiTi wire (1.0 mm)	One	Triangular	160 mm	Integrated in Backbone	No Calib.: x: 2.04 (1.58) y: 2.03 (1.77)	NR
Roesthuis et al. [116]	Three	Four	NiTi wire (1.0 mm)	One	Triangular	160 mm	Integrated in Backbone	With Calib.: x: 0.96 (0.46) y: 0.44 (0.26)	NR
Liu et al. [118]	One	Three	2 NiTi wires (0.125 mm)	Two	Triangular	35 mm	Embedded in Side Lumen	0.41 (0.3)	0.61 (0.15) 0.93 (0.05) 0.23 (0.1)
Xu et al. [97]	Three	One	NiTi tube (2.0 mm)	One	Helical	90 mm	Wrapped on Manipulator	NR	NR
Farvardin et al. [122]	One	Three	2 NiTi wires (0.125 mm)	Two	Triangular	35 mm	Embedded in Side Lumen	1.14 (0.77) 0.81 (0.99) 3.49 (1.13)	2.73 (0.77) 0.96 (0.35)
Ryu et al. [120]	One	NR	Polymer tube (1.05 mm)	One	Triangular	80 mm	Glued along Substrate	0.84 (0.62)	NR
Wei et al. [121]	One	Four	NiTi wire (0.3 mm)	One	Helical	110 mm	Wrapped on Manipulator	NR	NR

CHAPTER 5. SENSING ALGORITHMS

cially when the CM takes more complex shapes during interaction with obstacles and contacts with the environment. Moreover, there are many differences associated with these studies with regard to the design specifications of the CM and FBG sensor (such as length, substrate material and geometry, number of optical fibers and FBGs, etc), as well as the design of the evaluation experiments. As an example, the maximum bending curvature enforced on the CM during the experiments or the complexity of the CM shapes has not been reported in many of the previous evaluation studies. As such, a conclusive comparison between these results may not be readily achieved. With such variations in previous experimental studies, a thorough comparison study on a single sensor and CM assembly in various experimental scenarios (free and constrained environment) could be beneficial. Further, all the previous studies focus only on integration of FBG-based (multi-point) FOS into CMs. We therefore provide a thorough evaluation study and compare the results of model-driven shape reconstruction algorithms using FBG- and ROGUE-based sensors in free and constrained environments using the large deflection CM introduced in Section 3.4.2. Of note, the FBG sensor is fabricated using the notched NiTi substrate outlined in Section 4.4.2. Fig. 5.1 shows these sensors integrated with the CM.

5.3.2 Shape Reconstruction

A common technique for shape sensing and DPE using FBG sensors is to find the curvature at discrete locations, interpolate curvature along the length of the

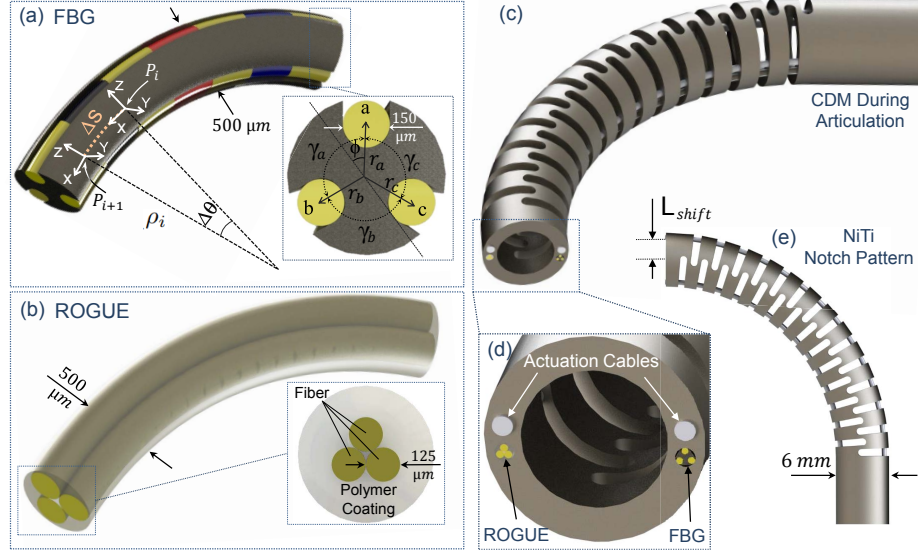


Figure 5.1: (a) the FBG fiber triplet with three active areas, (b) the ROGUE fiber triplet with distributed sensing, (c) CM during articulation, (d) CM tip view showing the actuation cables, the FBG, and the ROGUE triplet integrated into the CM, (e) NiTi notch pattern in the CM design

sensor, compute slopes and reconstruct the shape from proximal to distal end of sensor (base to tip) by integration [84, 98, 105, 106, 116, 118]. Particularly, in this model-driven approach, first the strain at each sensor cross section with FBG nodes is found by (5.1). This equation follows a rearrangement of (4.2) with the assumption that temperature variation among the FBGs located at a particular cross section is negligible [123].

$$\epsilon = \frac{\Delta\lambda_B}{\lambda_B(1 - p_e)} \quad (5.1)$$

where λ_B is the Bragg wavelength, p_e is the strain constant for optical fiber and ϵ is strain. Based on the sensor's geometry, a system of nonlinear equations (5.2) is then solved at each cross section with three FBG nodes in a triangular configuration (Fig.

CHAPTER 5. SENSING ALGORITHMS

5.1) to find local curvature (κ), curvature angle (ϕ), and a strain bias (ϵ_0) entailing the temperature effects or common mechanical strain at the cross section:

$$\begin{cases} \epsilon_a = -\kappa r_a \sin(\phi) + \epsilon_0 \\ \epsilon_b = -\kappa r_b \sin(\phi + \gamma_a) + \epsilon_0 \\ \epsilon_c = -\kappa r_c \sin(\phi + \gamma_a + \gamma_b) + \epsilon_0 \end{cases} \quad (5.2)$$

where subscripts a , b , and c correspond to the three fibers, and r , γ are geometrical parameters which can be obtained from design or estimated in a calibration procedure [106, 116]. Assuming a relationship (typically linear [98, 106, 116, 118]) between curvature and arc length, and dividing the sensor length to n sufficiently small segments, curvature (κ) and its direction (ϕ) can be interpolated between each two consecutive FBG points and extrapolated at the proximal and distal end of the sensor to establish discrete mappings f and g :

$$\begin{cases} \kappa_i = f(s_i) \\ \phi_i = g(s_i) \end{cases} \quad \text{for } i = 1, \dots, n \quad (5.3)$$

Now using the curvature at each segment (κ_i for $i = 1, \dots, n$), the slope of each segment Δs with constant curvature can be found by:

$$\Delta\theta_i = \frac{\Delta s}{\rho_i} = \kappa_i \Delta s \quad (5.4)$$

Establishing an appropriate local coordinate frame to the beginning of each segment (Fig. 5.1), the shape and consequently the distal-end position can be recon-

CHAPTER 5. SENSING ALGORITHMS

structed segment by segment using (5.5):

$$P_{i+1} = R_i^{x,\phi} P_i + \Delta P_i \quad (5.5)$$

$$\Delta P_i = \begin{bmatrix} \rho_i \sin(\Delta\theta_i) & 0 & -\rho_i(\rho_i - \rho_i \cos(\Delta\theta_i)) \end{bmatrix}^T$$

where $\rho_i = 1/\kappa_i$ is the radius of curvature and $R^{x,\phi}$ is the rotation of ϕ about the local x axis. Using (5.5) for $i = 1, \dots, n$, the tip position of the sensor (P_n) can be found. For CMs in which the FBG sensor is not placed on the center axis of the CM, all P_i should be shifted by the distance between sensor's and CM's centers (L_{shift} in Fig. 5.1(e)) to obtain the 3-D position of the center-line of the CM.

It must be noted that in absence of at least three FBGs at each active cross section of the sensor, estimation of local curvature (5.3) can be performed by calibrating the FBG sensor wavelength data (λ) against curvature (κ), typically using a 3D-printed or laser-cut calibration jig with constant curvatures such as the ones demonstrated in Fig. 4.4:

$$\kappa = \Pi(\lambda) \quad (5.6)$$

where Π is the mapping between the raw wavelength data and the local curvature at sensor cross sections with FBG nodes. One downside to the calibration-based approach for local curvature estimation is that the approach is limited to planar motions only, since the angle of curvature is assumed to be constant in this approach. That said, the approach is still useful when fewer than three FBGs are available at

each cross section.

5.3.3 Experiment Design and Setup

Using the model-driven reconstruction approach presented in the previous section, we aim to evaluate the performance of both FBG- and ROGUE-based FOS in free and constrained environments. In particular, inspired by CM workspace in a MIS surgical procedure, three sets of experiments were considered:

1. The CM was bent in free environment, without any obstacles. In this case, the curvature is relatively uniform along the CM's length, resulting in a C-like shape. Fig. 5.2(a) shows the snake bending in free environment.
2. Obstacles were placed in different places along the CM's path. This forced the CM to take on a more complex shape, resulting in a more complex curvature to recover. These experiments were designed to imitate the behaviour of the CM in real work environment, where obstacles such as bone, tissue, organs, etc. are inevitable.
3. An S-shape was forced on the CM, in order to see the limitations of both techniques when attempting to resolve a more complex shape. This S-shape is presented in Fig. 5.2(b).

As described in Section 4.4.2, the FBG sensor consisted of three fibers each with three FBGs 10 mm apart (last FBG located at 5 mm from the distal end of the manip-

CHAPTER 5. SENSING ALGORITHMS

ulator) attached to the longitudinal grooves of the 0.5 mm diameter NiTi substrate. The FBG data streamed by an optical sensing interrogator (Micron Optics sm 130) at 100 Hz. The ROGUE-based sensor was constructed according to specifications described in Section 4.5.1.2 and the interrogation settings (ODiSI-B, Luna Innovations Inc.) were set to a 0.65 mm spatial resolution, resulting in 24 Hz data streaming rate. As such, for the 35 mm length of the CM and sensor, a total of 53 points were being sensed in the optical frequency domain reflectometry-based (OFDR-based) sensor. Both sensors were integrated into the sensor channels of a second generation CM (Section 3.4.2) and secured with small adhesive applied to the distal end of the manipulator. The CM was mounted on a first generation actuation unit equipped with a stereo camera system providing the ground truth shape (described in Section 5.3.4). Of note, the red markers attached to the CM in Fig. 5.2 serve as the ground truth information tracked by the stereo camera system. All experiments were run on a computer with an Intel 2.3 GHz core i7 processor with 8GB RAM, running Ubuntu 16.04.

5.3.4 Ground Truth Data

In order to generate ground truth data for the true shape of the CM at any given instance, a stereo camera setup with 1024×768 resolution cameras (Flea2 1394b, FLIR Integrated Imaging Solutions Inc.) was used to track colorized markers attached to the center-line of the CM. The stereo camera pair was calibrated using the

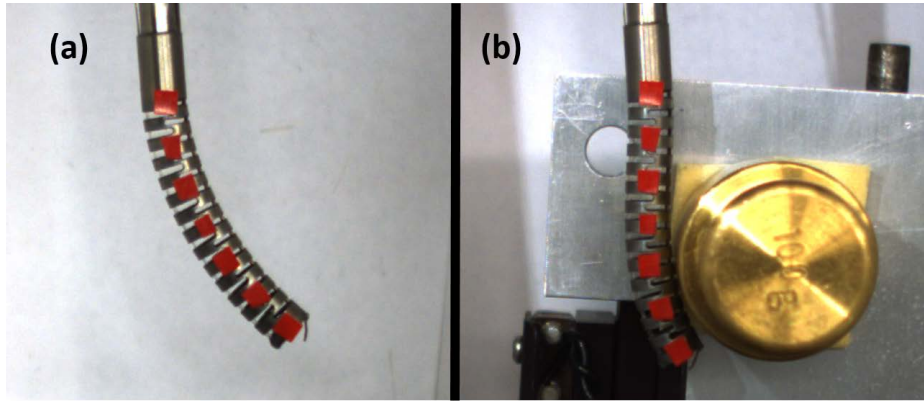


Figure 5.2: CM bending in a) free environment, and b) S-shape. The red markers are used in conjunction with a pair of stereo cameras as ground truth to compare the shape reconstruction.

stereo camera calibration toolbox in MATLAB and using a 8×6 checkerboard with 5 mm squares. Fig. 5.5 demonstrates the results of the stereo pair calibration with an overall mean error of 0.12 pixels. For each stereo image pair, the 2-D pixel locations of the marker centers were found in each image by applying a color segmentation with experimentally-determined thresholds. An interactive graphical user interface was written in Python to facilitate the process of determining the color segmentation thresholds. The intrinsic and extrinsic parameters from the calibration procedure were then used in custom-written Python code to find the corresponding markers within the two color-segmented images and obtain the 3D location of the markers by triangulation [148]. An erosion morphological operation, followed up with a dilation were applied to the segmented images to remove potential noise in the color segmentation algorithm. Of note, a custom-designed jig (Fig. 5.4) containing three markers with known pre-determined spatial locations was used for validation pur-

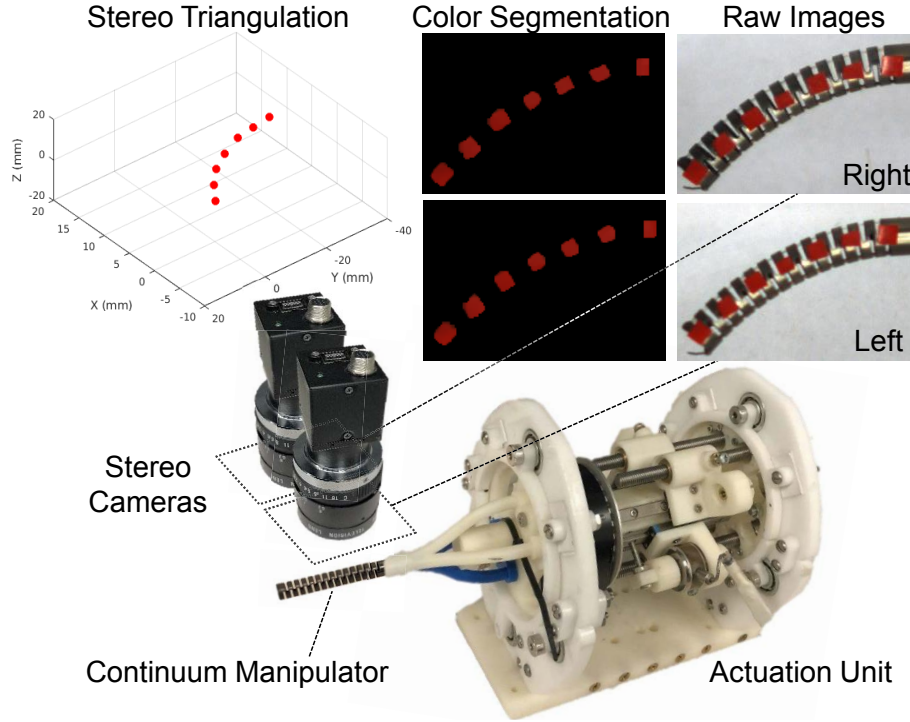


Figure 5.3: The experimental setup including the CM actuation unit integrated with a calibrated stereo camera pair. Raw images obtained from the camera pair are first color-segmented and then 3-D locations of the markers are computed by triangulation.

poses. The jig was translated and rotated in the desired workspace of the stereo pair and a sequence of image pairs were recorded. Using the parameters obtained from the calibration process, a 0.02 mm mean 3-D position accuracy error was observed when triangulating and measuring the distance between the markers.

5.3.5 Data Collection

FBG and OFDR data were streamed at 100 Hz and 24 Hz, while the images from the stereo pair camera system were obtained at 30 Hz frequency. A thread-safe

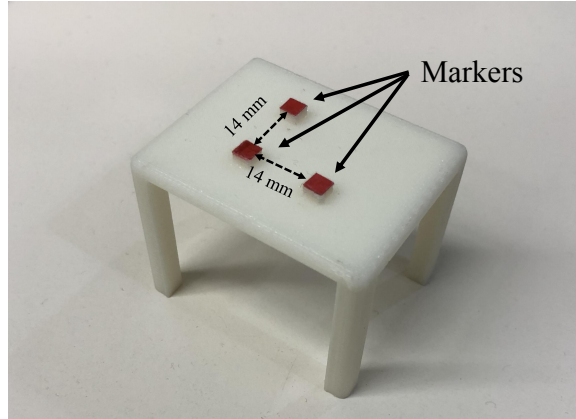


Figure 5.4: Custom-designed 3-D printed validation jig for the stereo pair setup.

mechanism from open source C++ cisst-saw libraries¹ [149,150] was used to record the data for each of these sources in parallel, using a separate CPU thread for each source. All the data was time-stamped and pre-processed during the evaluation experiments to choose the corresponding data from each source with similar time-stamps.

5.3.6 Results and Discussion

5.3.6.1 Free Environment CM Bending

The first measurement was performed when the CM was bent in free environment. Previous studies showed good accuracy for FBG-based sensing, typically for relatively small needle and CM curvatures (below 22.7 m^{-1}) [84,106]. In these experiments, however, we evaluate the capabilities of the shape sensing algorithms in large curvatures associated with a radius of curvature as small as 20.0 mm (50.0 m^{-1} curva-

¹Code repository located at <https://github.com/jhu-cisst/cisst-saw>

CHAPTER 5. SENSING ALGORITHMS

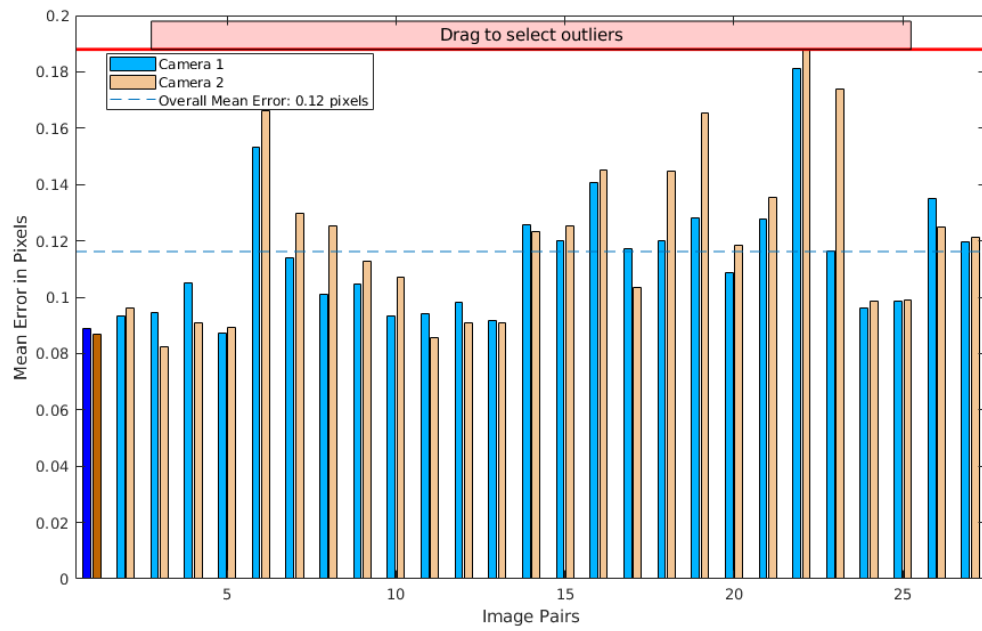
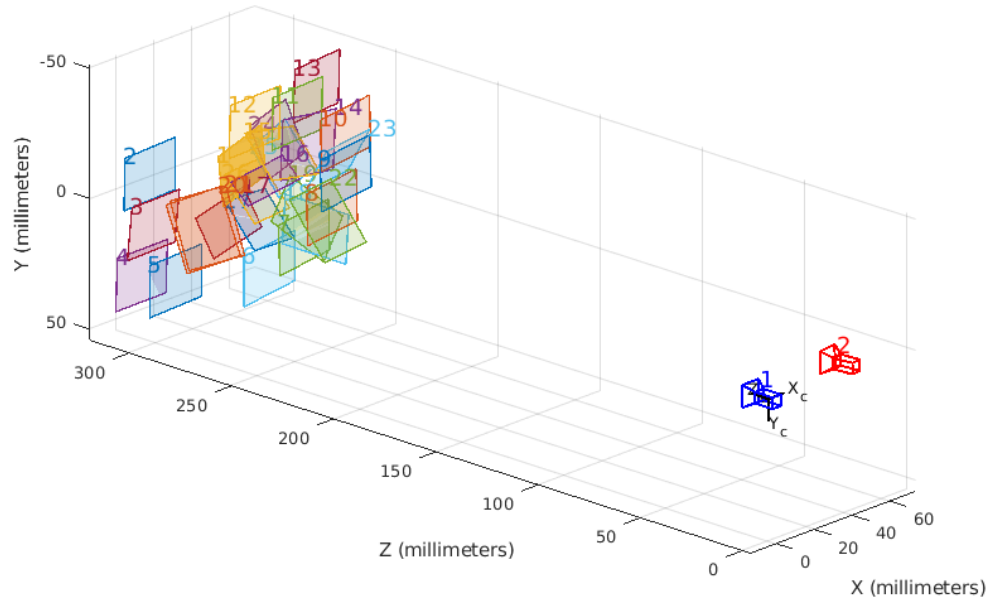


Figure 5.5: Top: Stereo pair calibration images and location of cameras. Bottom: Mean calibration error in pixels for each image-pair.

ture). Fig. 5.6(a) shows the results of the FBG-based sensor, while Fig. 5.6(b) shows the results for the ROGUE-based sensor, recovered by the OFDR technique. As can be observed, both methods show relatively good accuracy in small curvature bends associated with $\approx 5\text{mm}$ of distal-end deflection. As the curvature becomes larger, however, the FBG-based method's accuracy in DPE decreases while the OFDR-based technique still accurately estimates the distal-end position of the manipulator. In this case, the maximum DPE error associated with the FBG- and OFDR-based sensors are 2.34 mm and 0.96 mm, respectively.

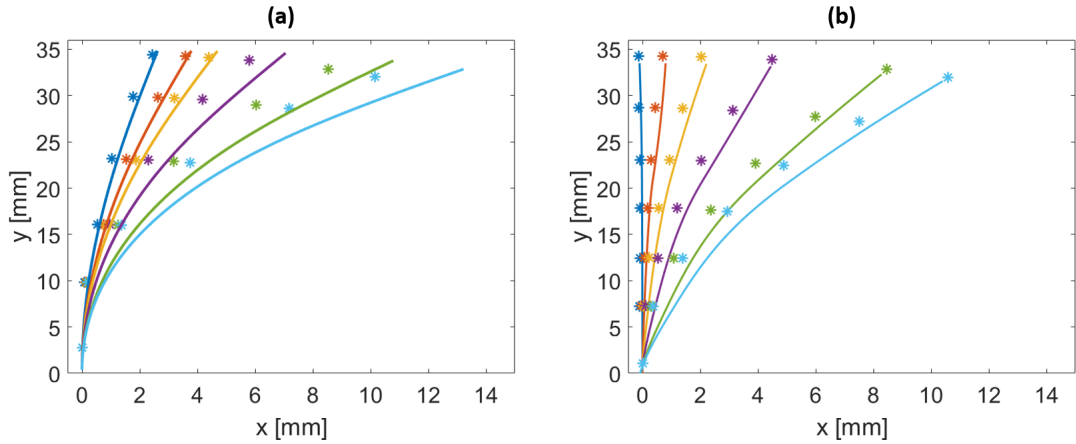


Figure 5.6: Free-bending CM reconstruction using (a) the FBG-based sensor and (b) the ROGUE-based sensor. In both cases, the asterisk markers show the ground truth, obtained by the pair of stereo cameras, while the solid line show the reconstructed shape, in 2D.

5.3.6.2 Constrained Environment With Obstacles

In the second set of experiments, obstacles were located in the workspace of the CM such that the CM would interact with them during bending. Indeed, the inter-

CHAPTER 5. SENSING ALGORITHMS

action with obstacles forces the CM to adopt a more complex shape, with quicker variations in curvature along the CM's length. Since the FBG triplets can only perform sensing where the FBGs are inscribed (in this case, in only three locations), they cannot recover the shape as accurately as the triplets based on the OFDR technique, which can perform sensing all along the sensor's length with much higher spatial resolution. Fig. 5.7 compares the accuracy of both sensors, with obstacles placed at the tip of the CM (solid lines) and in the middle (dashed lines). As can be observed, the OFDR technique clearly outperforms the FBG technique when interacting with obstacles placed both at the tip of the CM and alongside it. The maximum DPE error obtained by the FBG and OFDR methods in these experiments were 3.02 mm and 0.76 mm, respectively.

5.3.6.3 S-Bending

The "S-bends" are the most complex shapes that were investigated, due to their multiple inflection points. These shapes could be the result of the CM's interaction with multiple obstacles, or could be intentionally achieved to go around a solid obstacle for example. They can also evaluate the limits of both sensors. Fig. 5.8 shows the reconstruction of S-bends applied on the CM again both for FBG and ROGUE sensors, for increasingly complex shapes. As can be observed on Fig. 5.8(a), even the most simple S-bend cannot be accurately measured by the FBG sensors with limited number of sensing points, and as the bend curvature increases, the tip error becomes

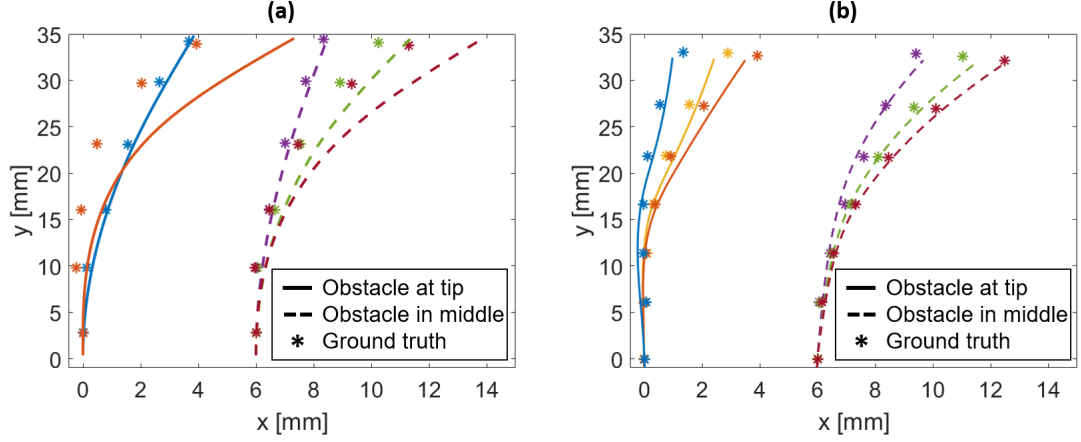


Figure 5.7: CM shape reconstruction when interacting with obstacles using (a) the FBG-based sensor and (b) the ROGUE-based sensor. In both cases, the asterisk markers show the ground truth, obtained by the pair of stereo cameras. The solid lines show the reconstructed shape when the obstacle is placed at the tip of the CM, while the dashed line correspond to the shape when the obstacle is placed in the middle of the CM. The latter is translated by 6 mm in the graphs to avoid superposition of the plots.

increasingly large. On the contrary, on Fig. 5.8(b), a fairly accurate reconstruction can be observed for the investigated S-bends. The maximum DPE error obtained from the FBG and OFDR techniques in these experiments were 3.96 mm and 0.72 mm, respectively.

From those results, the tip position error can be obtained by comparing the ground truth and the shape reconstruction. Tip position errors for all three experiments are compiled and the two investigated techniques are compared in Table 5.2. As can be observed, the OFDR technique outperforms the conventional FBG method by a factor of 2 for both free-bending and obstacles interaction. The tip position error is even more precise in the case of S-bending, where the mean error is 2.27 mm in

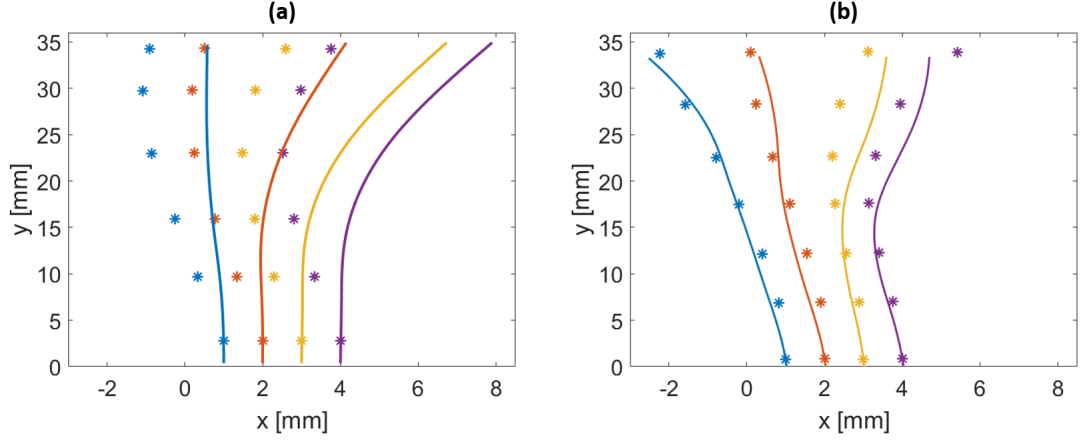


Figure 5.8: CM S-bend reconstruction using (a) the FBG-based sensor and (b) the ROGUE-based sensor. In both cases, the asterisk markers show the ground truth, obtained by the pair of stereo cameras, while the solid line is the reconstructed shape. Individual plots are translated by 1 mm on the graphs to avoid superposition.

Table 5.2: CM DPE (tip position) error in free and constrained environments using FBG and OFDR sensors.

Experiment	Mean (mm)		Std (mm)		Max (mm)	
	FBG	OFDR	FBG	OFDR	FBG	OFDR
Free-Bending	0.83	0.32	0.89	0.29	2.34	0.96
Obstacles	0.80	0.41	0.97	0.21	3.02	0.76
S-bend	2.27	0.45	1.16	0.22	3.96	0.72

the case of the FBG technique, while it remains very low at 0.45 mm for the OFDR technique.

In order to compare not only the tip position accuracy of both methods, but also the overall shape deviation, errors between all ground truth markers and the reconstructed shapes were calculated. Those results are compiled in Table 5.3. As can be observed, while the mean errors for the FBG technique is relatively low for the free-bending and obstacles experiments, the maximum error is still large and definitely

CHAPTER 5. SENSING ALGORITHMS

Table 5.3: CM shape deviation error in free and constrained environments using FBG and OFDR sensors.

Experiment	Mean (mm)		Std (mm)		Max (mm)	
	FBG	OFDR	FBG	OFDR	FBG	OFDR
Free-Bending	0.50	0.28	0.64	0.30	2.34	1.37
Obstacles	0.44	0.17	0.64	0.17	3.02	0.76
S-bend	1.33	0.27	1.06	0.24	3.96	0.96

outperformed by the OFDR technique. Furthermore, it can be observed that while the OFDR technique is also able to reliably reconstruct S-bends with comparable accuracy, the FBG technique exhibits large errors with maximum error of 3.96 mm.

It should be noted that, while the FBG sensor used in this study only had three FBGs written in each fiber, it would be possible to have sensors with a larger FBG density, thus increasing the spatial resolution. However, the manufacturing costs would increase accordingly, and the fabrication of a sensor with FBGs spaced by as little as 0.65 mm would be a major challenge in itself. The ROGUE-based fibers, on the other hand, require special setups developed for the purpose of fabricating the sensors. Even though in the recent years, FBG-based sensors have been the dominant method in FOS for sensing of flexible medical devices, the distributed sensing techniques such as the OFDR-based sensor with ROGUE writing is expected to become more prevalent and be used to fabricate sensors of arbitrary lengths with high spatial resolution at relatively low costs.

5.4 Data-Driven Sensing

5.4.1 Motivation and Background

Model-driven approaches require deep understanding of the system followed by simplifying assumptions to allow modeling of complex systems in a feasible manner. As such, perfect emulation of the system with a model containing sufficient complexity to capture the underlying physics of the system is challenging and a cumbersome task. Another drawback of the traditional model-driven approaches is that key variables are difficult to measure online due to the complexity of the design and environment uncertainties. Data-driven methods, however, provide stable and reliable online estimation of these variables based on historical measurements [151, 152].

In the context of CMs in MIS, accurate shape sensing and reliable contact detection capability have been the focus of heavy research in the past years. Several studies have attempted to tackle these problems by deriving kinematics- or mechanics-based models (with or without using additional sensors) to detect CM contacts with the surrounding environment [153–159] and to reconstruct shape [3, 22, 74, 84, 116]. These approaches, however, are specific to the particular design of CM and used sensors and thus require burdensome model development for the distinct system under study. To minimize the effort in developing system-specific calibration devices (e.g. 3-D printed jigs) and models with simplifying assumptions, we propose and develop data-driven model-independent approaches to tackle shape sensing and contact detection of CMs

by extracting meaningful information from the structure of the embedded FOS data. In the context of surgical applications, another advantage of such approaches is that the data-driven model can be established by fast preoperative data collection and training as discussed in this chapter.

5.4.2 Distal-end Position Estimation (DPE)

As described in Section 5.3.2, the common model-driven technique for shape sensing and DPE using FOS is to find the curvature at discrete locations, interpolate and extrapolate curvature along the length of the sensor, compute slopes and reconstruct the shape from proximal to distal end (base to tip) by integration [84, 106, 118]. For a distributed sensor with high resolution such as the OFDR-based one described in Section 4.5.1.2, the model-driven can recover the shape reliably. For low resolution sensors such as FBG-based sensors (Section 4.4.2) with limited number of sensing points, however, this method becomes susceptible to curvature estimation errors. In particular, the downsides associated with the model-driven shape reconstruction approach include:

1. It relies on many geometrical assumptions about the sensor or CM design.
2. It requires extraneous calibration procedures for system parameter identification.
3. Due to limited number of active sensing locations on the fibers, the method is

CHAPTER 5. SENSING ALGORITHMS

prone to error propagation during integration and shape reconstruction.

4. It uses only a subset of FBG measurements located at a particular active area cross section for estimation of local curvature.
5. Due to the proximal to distal end integration approach for shape reconstruction, the error is accumulated toward the distal end, resulting in poor DPE accuracy for sensors with low spatial resolution.

To address the drawbacks associated with the conventional model-dependent shape reconstruction approach, we introduce a new data-driven paradigm for reconstructing the CM shape and DPE. We define the problem of CM shape reconstruction as a supervised regression problem for estimating the CM distal-end position, followed by an optimization problem that reconstructs the shape of the manipulator. The input to this algorithm is the sensory data obtained from the embedded FBG sensor and the output is the DPE as well as the reconstructed shape. Similar to other supervised learning algorithms, the proposed method consists of an offline dataset creation step, during which the sensory data is labeled with correct distal end position. Three different supervised machine learning algorithms (linear and nonlinear) are incorporated and trained on the collected dataset to learn the mapping from FBG measurements to CM's distal end position. This information is then passed to an optimization problem that reconstructs the shape of the CM.

In surgical applications such as the less-invasive treatment of osteolysis, typi-

CHAPTER 5. SENSING ALGORITHMS

cally the goal is to control the distal end of the CM is to target locations in human anatomy [3]. Accurate DPE is, therefore, critical for precise execution of the surgical task and enhanced patient safety. One of the major drawbacks of the conventional model-dependent sensing approach outlined in Section 5.3.2 is that the DPE is a byproduct of the shape reconstruction algorithm after integration of curvature information from proximal to distal end of the sensor. Consequently, the reconstruction error propagates toward the distal end of the manipulator. This error can be reduced with high spatial resolution sensors such as distributed sensors (OFDR-based sensors) or multi-point sensors that contain several FBG active areas along the length of the sensor. For FBG sensors containing only a limited number of active areas, however, the error propagation is more apparent. To remedy this problem in low spatial resolution FBG sensors, we introduce a novel data-driven paradigm for reconstructing the CM shape and DPE using supervised machine learning methods. The paradigm consists of two steps:

1. DPE step: estimating the CM distal end position using a supervised regression learning model with FBG measurements as input.
2. Shape reconstruction step: reconstructing the shape of the CM via an optimization approach using the DPE from step (1) as input.

For the DPE step, we aim to find a regression model that predicts the CM's distal end tip position in 3-D, given a set of raw FBG wavelength data along the sensor. This

CHAPTER 5. SENSING ALGORITHMS

can be formulated as the following regression problem with the FBG measurements (λ) as the independent variables and the CM distal position (p) as the dependent variables:

$$p = \Psi(\lambda, \beta) \quad (5.7)$$

where $p \in \mathbb{R}^3$ is the 3-D position of the CM tip, $\lambda \in \mathbb{R}^m$ is the vector containing the raw wavelength data of the m FBG nodes on the sensor, β is the vector of unknown parameters, and $\Psi : \mathbb{R}^m \rightarrow \mathbb{R}^3$ is the regression model that predicts the CM 3-D tip position, given the wavelength information of the complete set of FBG nodes on the sensor at any given time. Of note, the effect of temperature change and common axial force in sensor readings for a single cross section can be eliminated by subtracting the common mode from Bragg wavelength shift of each sensor, as proposed in [160, 161]. Additionally, to avoid sensitivity of the data-driven algorithm to scale of the input features, we apply a normalization (standardization) to the sensor measurements to achieve a data distribution with mean of zero and standard deviation of one:

$$\hat{\lambda}_n = \frac{\lambda_n - \mathbb{E}[\lambda_n]}{\sqrt{Var[\lambda_n]}} \quad (5.8)$$

where \mathbb{E} is the expected mean, Var is the variance and $\hat{\lambda}_n$ is the normalized measurement input to the model at time step n . Depending on the degrees of freedom of the CM, complexity of the environment, and the shapes that the CM can obtain, different regression models could be incorporated to capture the unknown parameters

CHAPTER 5. SENSING ALGORITHMS

β . We hereby propose, describe and evaluate three different models for this purpose:

1) linear least square model, 2) DNN, and 3) TNN.

5.4.2.1 Linear Regression

Linear regression is a common regression method that models the dependent variables as a linear combination of the unknown parameters. The DPE can be modeled as a least squares optimization problem:

$$\min_B \sum_{n=1}^N r_n^2 = \min_B \|\Lambda B - P\|_2^2 \quad (5.9)$$

where r_n is the residual error for the n^{th} observation, $\Lambda \in \mathbb{R}^{N \times m}$ is a stack of N observations of the m FBG node data, $P \in \mathbb{R}^{N \times 3}$ is the stack of N ground truth CM distal end position observation data, and $B \in \mathbb{R}^{m \times 3}$ is the matrix of unknown parameters. Using (5.9), the regression model can be trained preoperatively on N observations of the FBG and ground truth data to find the unknown parameters B using the generalized inverse:

$$B = (\Lambda^T \Lambda)^{-1} \Lambda^T P \quad (5.10)$$

The trained model can then be used intraoperatively to predict CM tip position values given the current FBG wavelength data:

$$\hat{p}_n = B^T \hat{\lambda}_n \quad (5.11)$$

where \hat{p}_n is the predicted the CM distal end position, given the normalized FBG wavelength n^{th} data observation ($\hat{\lambda}_n$).

5.4.2.2 Deep Neural Networks (DNNs)

DNNs are becoming popular due to their increased flexibility to fit complex models compared to traditional regression methods. Unknown parameters in the DNN model can be trained end-to-end in a data-driven manner through backpropagation. We define the trainable parameters in the DNN as $W = \{W^{(i)}\}_{i=1}^L$ for $W^{(i)} \in \mathbb{R}^{F_i \times F_{i-1}}$ with a corresponding bias vector $b^{(i)} \in \mathbb{R}^{F_i}$, where i is the layer index and F_i is the layer size hyperparameter. For normalized raw FBG wavelength data vector at the n^{th} observation, $\hat{\lambda}_n \in \mathbb{R}^m$, we compute activations $E = \{E_n^{(i)}\}_{i=1}^L$ for $E^{(i)} \in \mathbb{R}^{F_i}$ with:

$$E_n^{(1)} = f(W^{(1)} \cdot \hat{\lambda}_n + b^{(1)}), \quad (5.12)$$

$$E_n^{(l)} = f(W^{(l)} \cdot E_n^{(l-1)} + b^{(l)}), \quad (5.13)$$

where $f(\cdot)$ is the Rectified Linear Unit (ReLU) non-linear activation function, $l \in \{2, \dots, L\}$ are the second to the last layer of the network and $F_0 = m$. The DNN output is the corresponding n^{th} CM distal end position $\hat{p}_n \in \mathbb{R}^2$. We use Mean Squared Error (MSE) as loss function to optimize $\|\hat{p}_n - p_n\|_2^2$, where $p_n \in \mathbb{R}^2$ is the ground truth tip position observation. Fig. 5.9 illustrates the architecture design of the DNN.

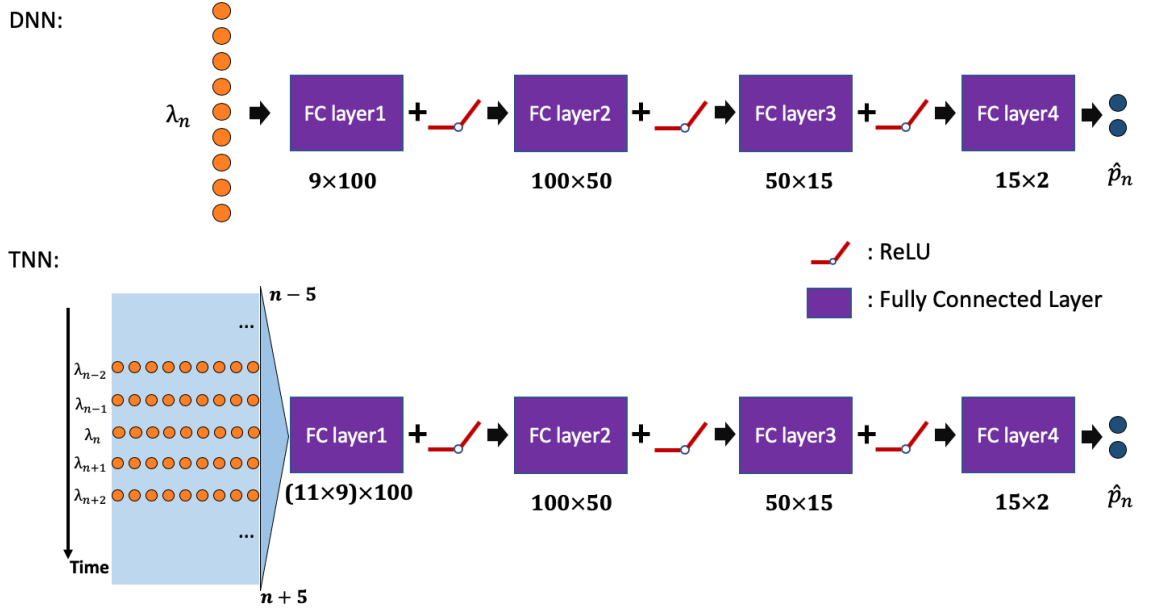


Figure 5.9: Top: DNN architecture. λ_n is the raw FBG vector at the n^{th} observation. \hat{p}_n is the network output CM tip position. Hyperparameters of the fully connected layers are listed under each block. Bottom: TNN architecture. The concatenation process is illustrated with the time-series data.

5.4.2.3 Temporal Neural Networks (TNNs)

All the aforementioned models are trained only with individual sensor observations at a particular time step, without consideration of the time-series information. In prior work, temporal convolutional networks (TCN) have been proposed to improve video-based analysis models and makes use of time-varying features to make predictions [162, 163]. The intuition behind utilizing a time-series model lies with the observation that input data features are often changing continuously. In the present application, the CM manipulation and deformation also occur in a continuous manner. Thus, we take the inspiration from the design of the TCNs to design a TNN for CM DPE.

CHAPTER 5. SENSING ALGORITHMS

Fig. 5.9 presents the hierarchical structure of the TNN. We follow the above notations and denote the input concatenated feature with respect to time as $\hat{\lambda}_{cat,n,k} = [\hat{\lambda}_{n-k}, \dots, \hat{\lambda}_{n-1}, \hat{\lambda}_n, \hat{\lambda}_{n+1}, \dots, \hat{\lambda}_{n+k}] \in \mathbb{R}^{m \times (2k+1)}$, where $(2k+1)$ is the number of samples covered in this concatenated feature. The TNN is trained to predict the DPE corresponding to the middle data sample \hat{p}_n . In spite of introducing a small delay in predictions (in the order of a couple of milliseconds), the intuition behind the proposed embedding of the time-series is to incorporate information about changes in the sensory data as a result of potential contacts with the environment or stopping the CM actuation. For the TNN, we use the same MSE loss used in the DNN approach.

5.4.3 Shape Reconstruction

Once accurate estimate of the distal end position of the CM is obtained from the regression model, the shape of the CM can be reconstructed. To do so, we model the CM as a series of rigid links connected by passive elastic joints using a pseudo-rigid body model [77, 164–166]. In particular, the CM in this study can be modeled as a n -revolute-joint mechanism due to the planar motion of the CM. Depending on the design of the particular CM, spherical joints can also be assumed for the CM in a general case. At any given instance, the DPE (\hat{p}) output from the regression model (Section 5.4.2) is passed as input to the constrained optimization (7.12) to solve for

CHAPTER 5. SENSING ALGORITHMS

the joint angles and consequently the shape is reconstructed:

$$\begin{aligned}
& \underset{\Theta_c}{\text{minimize}} && \|\hat{p} - f(\Theta_c)\| \\
& \text{subject to} && \Theta_c \leq \Theta_{max} \\
& && f_x = d.(\sum_{i=1}^n \sin(\sum_{j=1}^i \Theta_j)) \\
& && f_y = d.(\sum_{i=1}^n \cos(\sum_{j=1}^i \Theta_j))
\end{aligned} \tag{5.14}$$

where $\Theta_c \in \mathbb{R}^n$ is the CM joint angles from the pseudo-rigid body model, $d = L_c/n$ is the distance between two consecutive joints, $f(\Theta_c) : \Theta_c \rightarrow \mathbb{R}^2$ is the CM forward kinematics mapping from joint space to task space, and Θ_{max} is the maximum angle each joint can take, which can be determined experimentally [22]. There is a trade-off between choosing a more complex pseudo-rigid body model (large number for n) and the computational complexity of (7.12).

5.4.3.1 Experiment Design and Evaluation Criteria

Similar to the experiments described in Section 5.3.2, the FBG-based sensor containing three fibers each with three active area placed on the notched NiTi substrate integrated with the CM was used for the evaluating the performance of the proposed approaches when limited number of sensing points are available. Inspired by CM motions in a MIS surgical procedure, two sets of experiments were considered and the shape reconstruction and DPE from both model-dependent and data-driven

CHAPTER 5. SENSING ALGORITHMS

paradigms were evaluated and compared. In the first case, the CM was bent in free environment to large curvatures up to $\kappa = 50 \text{ m}^{-1}$ (corresponding to 20 mm radius of curvature). To simulate the real scenario of the using the CM during surgery, we performed these experiments both in presence and absence of a flexible debridement instrument embedded in the CM open lumen (internal disturbance), as described in Section 3.4.3. In the second case, 3-D printed obstacles (external disturbance) were distributed at 8 different locations along the body of the CM in its workspace (Fig. 7.16). Presence of obstacles enforced the CM to take on more complex shapes compared to free environment bending, resulting in more challenging shape sensing problems. These experiments were designed to imitate the behaviour of the CM in real surgical scenarios, where presence of obstacles such as bone, tissue, organs, etc. is inevitable.

In each experiment, the CM started from its straight pose and the actuating cable was pulled for a maximum of 7 mm to bend the CM. The CM cables were actuated with a velocity of 0.2 mm/s to obtain training data with high resolution. To test generalization capability of the data-driven approach to the unknown location of the obstacles, a K-fold cross validation technique was used to evaluate the performance by splitting the data to training and validation sets. Particularly, each experiment was separately chosen as the validation experiment and the models were trained on the remainder of the experiments to evaluate the generalization of the models in predicting unseen sensory data of the validation experiment.

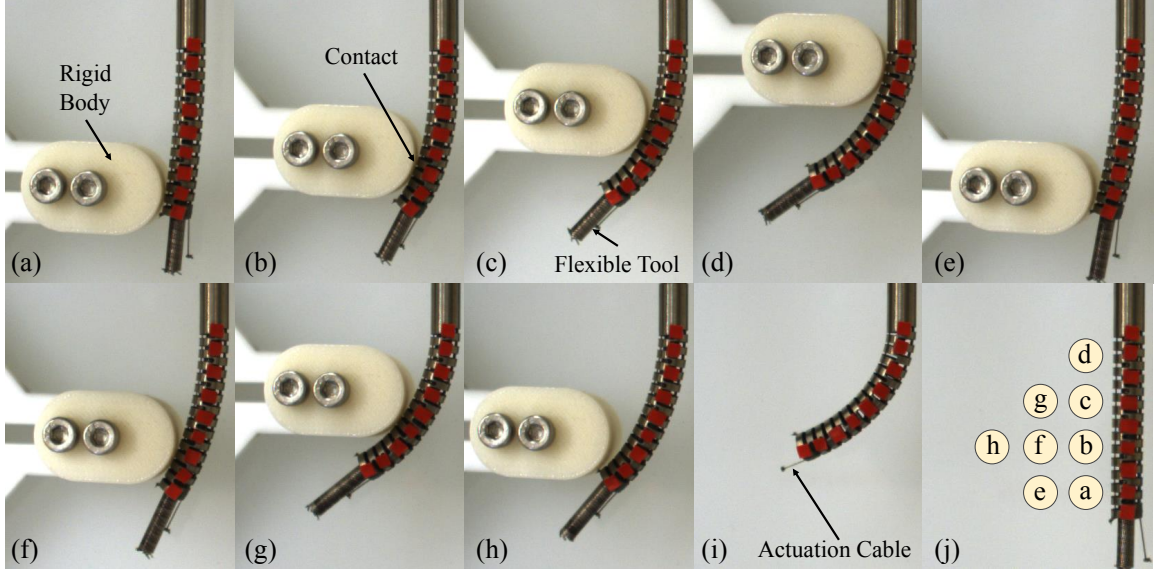


Figure 5.10: Experiments: (a-h) CM bending in constrained space in presence of internal disturbance (flexible tool) and external disturbance (obstacles at various locations), (i) CM bending in free environment, (j) demonstrating the the location of obstacles relative to the CM in cases a through h.

5.4.3.2 Experimental Setup

For conducting the experiments, an experimental setup similar to that of Fig. 5.3 was used. To generate the ground truth shape, red markers were attached to the center-line of the CM that were tracked by the stereo camera pair. FBG data was streamed by the same optical sensing interrogator (Micron Optics sm 130) at a frequency of 100 Hz, while the images from the stereo pair camera system (Flea2 1394b, FLIR Integrated Imaging Solutions Inc.) were obtained at 30 Hz frequency. The thread-safe mechanism from open source C++ `cisst-saw`² [149,150] was used to record the data for each of these sensor sources in parallel, using a separate CPU thread for

²Code repository located at <https://github.com/jhu-cisst/cisst-saw>

CHAPTER 5. SENSING ALGORITHMS

each source. All the data was time-stamped and pre-processed during the training phase to choose the FBG data that corresponds to each image pair sample, since the FBG data was streaming at a higher frequency. All experiments were run on a computer with an Intel 2.3 GHz core i7 processor with 8GB RAM, running Ubuntu 16.04.

5.4.3.3 Network Training Hyperparameters

Both the DNN and the TNN were trained with learning rate of 1.0×10^{-3} and batch size of 128, determined experimentally yielding best performance. We used the Adam optimizer [167] with a weight decay of 1.0×10^{-5} . Fig. 5.11 presents an example of the reduction of the loss function during training and validation of the DNN model as the number of epochs evolve. Of note, the concatenation feature length $2k + 1$ in the TNN model controls how much temporal information is included for prediction. The k value was chosen experimentally as 5. Thus, a concatenation feature covers $2k + 1 = 11$ samples in the TNN model.

5.4.3.4 Results and Discussion

A summary of the performance of the data-driven and sensor-model-dependent approaches in shape sensing and DPE is presented in Table 5.4. In particular, using the DNN, TNN, linear regression, and the sensor-model-dependent model, the mean, standard deviation, and maximum error for shape reconstruction and DPE in both

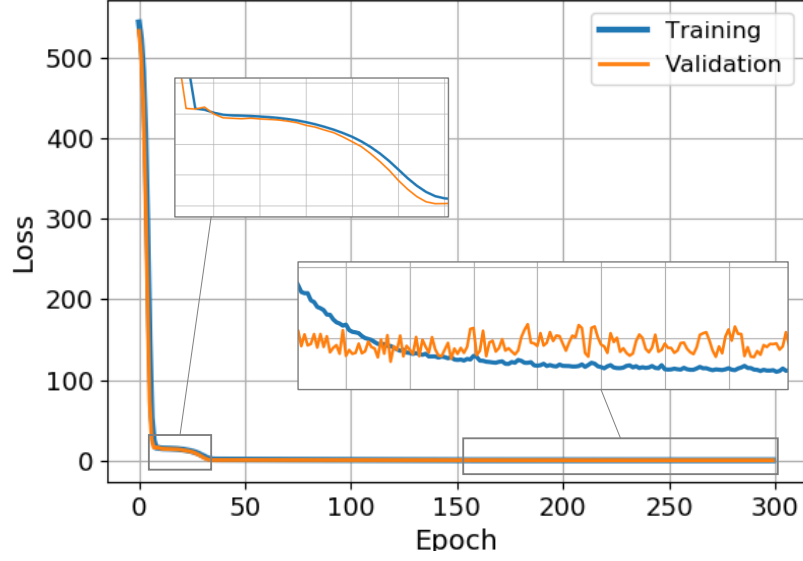


Figure 5.11: Loss function during training and validation.

constrained spaces and free environment are presented. Inspired by orthopaedic applications, the CM was equipped with a flexible instrument during the constrained space experiments with obstacles, while the free environment experiments were performed both in presence and absence of the flexible instrument. From a shape sensing and DPE perspective, the presence of a flexible instrument is regarded as internal disturbance while the presence of obstacles in the surrounding of the CM is regarded as external disturbance. The last three columns of the table demonstrate the average errors observed in the constrained cases (in presence of obstacle) as well as the free environment with and without flexible instruments. A comparison of the DPE results reveals that the DNN model achieves better generalization and outperforms the other models on average with sub-millimeter accuracy performance in constrained and free

Table 5.4: Comparison of results for model-dependent and data-driven dpe and shape sensing in free and constrained environments. All units are millimeter.

Method			Obs a	Obs b	Obs c	Obs d	Obs e	Obs f	Obs g	Obs h	Obstacles	Free (Tool)	Free (No Tool)
Shape	DNN	Mean	0.32	0.89	1.16	0.49	0.39	0.48	0.53	0.90	0.64	0.65	0.67
		Std.	0.21	0.60	0.71	0.32	0.25	0.22	0.29	0.50	0.28	0.35	0.52
		Max	0.65	1.74	1.95	1.22	0.81	0.65	0.98	1.51	1.95	1.16	1.22
	TNN	Mean	0.37	0.82	1.10	0.58	0.40	0.48	0.49	0.62	0.61	0.72	0.65
		Std.	0.24	0.55	0.83	0.42	0.25	0.28	0.27	0.32	0.23	0.48	0.36
		Max	0.70	1.70	2.27	1.25	0.76	0.84	0.93	0.98	2.27	1.31	1.65
	LIN	Mean	0.32	0.73	0.81	0.54	0.40	0.40	0.62	0.77	0.57	0.66	0.62
		Std.	0.22	0.46	0.98	0.78	0.25	0.19	0.36	0.41	0.18	0.36	0.45
		Max	0.66	1.52	2.74	1.74	0.84	0.65	1.19	1.31	2.74	1.24	1.44
	MODEL	Mean	0.23	1.14	0.78	1.08	0.32	0.42	1.07	1.24	0.78	1.67	1.30
		Std.	0.12	1.13	0.84	0.63	0.19	0.28	0.62	0.67	0.38	0.96	0.72
		Max	0.41	3.19	2.40	2.14	0.57	1.03	2.20	2.19	3.19	3.20	2.45
DPE	DNN	Error	0.23	0.48	0.16	1.22	0.36	0.38	0.93	1.11	0.61	0.11	0.78
	TNN	Error	0.23	0.64	1.72	0.50	0.52	0.34	0.93	0.78	0.71	0.28	0.68
	LIN	Error	0.21	0.98	2.74	0.87	0.32	0.13	0.49	1.31	0.88	0.29	0.86
	MODEL	Error	0.41	3.19	2.40	2.14	0.57	1.03	2.21	2.19	1.76	3.20	2.45

CHAPTER 5. SENSING ALGORITHMS

spaces. The linear and TNN model also show relatively good performance, while the sensor-dependent-model approach can lead to DPE with maximum error as high as 3.20 mm and 3.19 mm in large deflection bendings of the CM in presence of internal and external disturbances, respectively. For the experiments with presence of obstacles (external disturbance), the maximum observed DPE error using the DNN, TNN, linear, and sensor-model-dependent approach is 1.22 mm, 1.72 mm, 2.74 mm, and 3.19 mm, respectively.

The slightly superior performance of the DNN compared to the TNN in maximum reported errors (maximum CM bend) can be explained by noting that the network mostly experiences continuous changes in data during motion of the CM, whereas there is only one appearance of a motion stop in each experiment (at maximum CM bend). Given the limited number of data associated with motion stops, the TNN model may not be able to predict the stops and as a result may slightly overshoot the predicted DPE. Such behaviour could be mediated by either adding more stop/motion occurrences in the data set or by incorporating action information (e.g. actuation cable displacement or motor current) in the input to the network.

Fig. 5.12 shows the shape reconstruction results using the four approaches and their comparison with the ground truth data obtained from the markers attached to the CM. Fig. 5.12(a), 5.12(b), and 5.12(c) correspond to the shape reconstruction in presence of obstacle, free environment with embedded flexible tool, and free environment without flexible tool, respectively. Fig. 5.12(d), 5.12(e), 5.12(f), demonstrate

CHAPTER 5. SENSING ALGORITHMS

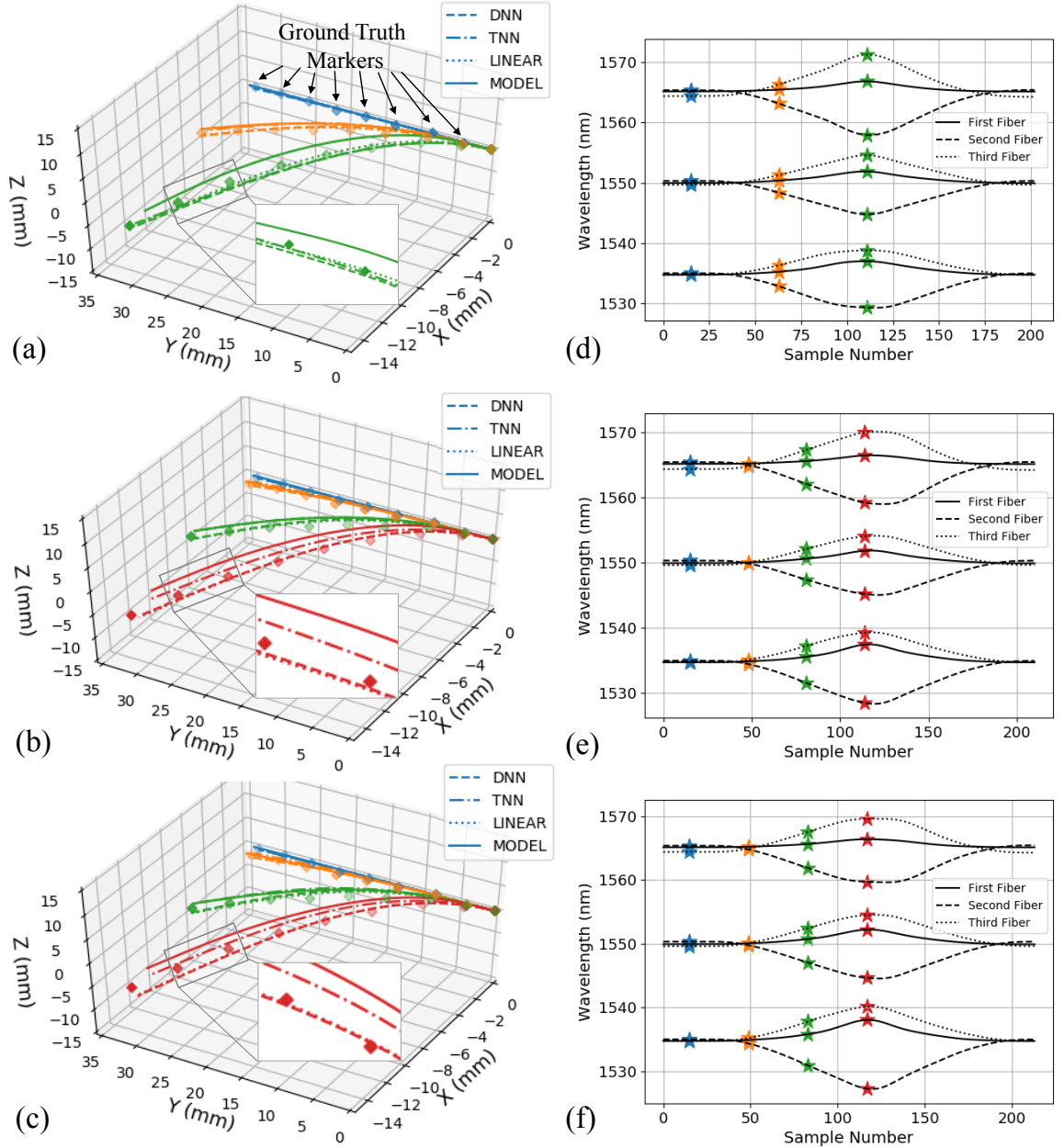


Figure 5.12: Shape reconstruction results using the DNN, TNN, linear, and model methods for (a) experiment with obstacle, (b) free environment experiment with tool, (c) free environment experiment without tool. FBG measurements and the corresponding samples (stars) associated with the reconstruction results are shown in (d), (e), and (f).

CHAPTER 5. SENSING ALGORITHMS

the evolution of the 9 FBG measurements over the course of the experiments as well as the sample number used for shape reconstruction starting from straight pose of the CM all the way to maximum bend in each experiment.

Quantitatively, the shape reconstruction results are shown in Fig. 5.13, where the mean, standard deviation and maximum errors in shape reconstruction using each method are plotted in constrained environment, free environment with flexible tool, and free environment without flexible tool, respectively. It can be observed that the sensor-model-dependent approach yields to maximum shape deviation of 3.20 mm and 2.45 mm from the ground truth markers in free environment with and without flexible tool, respectively. The increased error in presence of flexible tool can be explained by the variations that the flexible tool may impose on the local curvature profile of the CM which may not be captured by the limited number of sensing nodes along the length of the sensor. Moreover, the model-dependent approach results in average maximum error of 1.76 mm in all obstacle cases, with the worst performance in case of obstacle (b) with 3.19 mm maximum error. For the data-driven approaches, the DNN model outperforms the TNN and linear model with smaller maximum shape deviation error in comparison. For the obstacle cases, the DNN, TNN, and linear models yield maximum shape deviation error of 1.95 mm, 2.27 mm, and 2.74 mm, respectively. For the free environment with and without the presence of tool, all three methods result in similar accuracy performance, with the DNN model showing slight superior performance over the TNN and linear model.

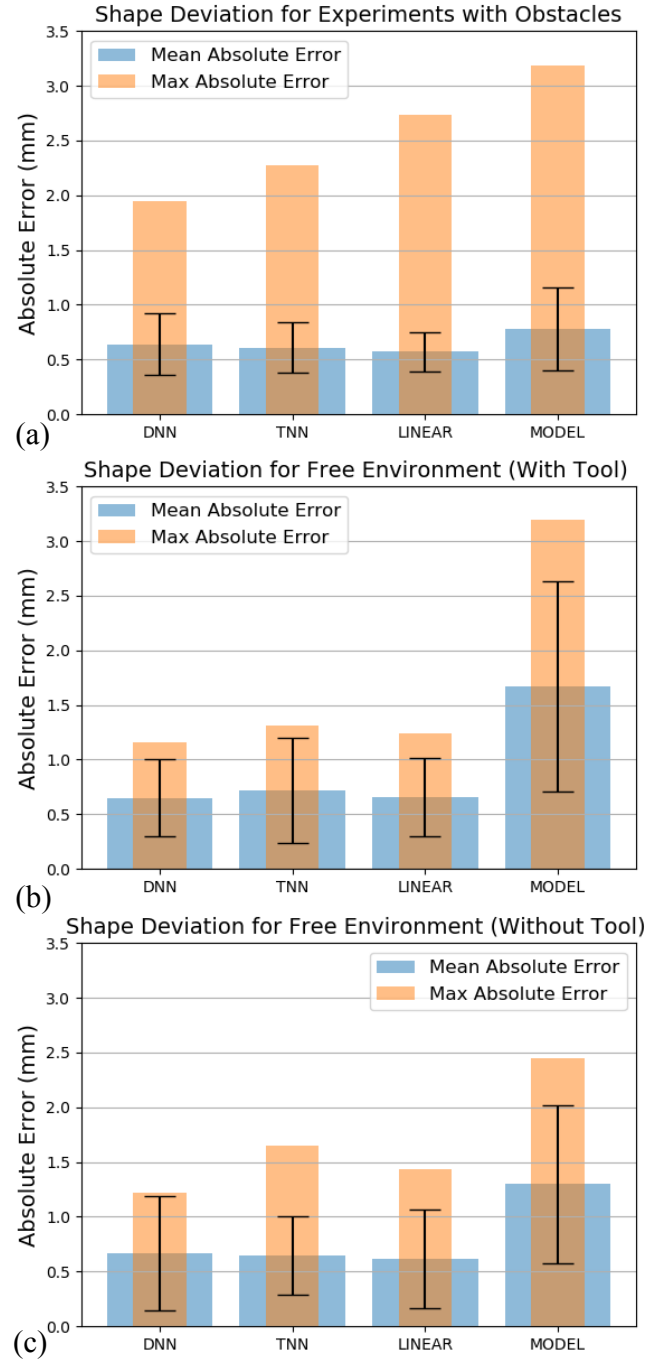


Figure 5.13: Comparison of the absolute shape error using the DNN, TNN, linear, and model methods for (a) all the experiments with obstacles, (b) free environment experiments with tool, (c) free environment experiments without tool.

CHAPTER 5. SENSING ALGORITHMS

The CM used in this study is a non-constant curvature CM, which makes the modeling of the CM and sensor more challenging due to more complex underlying behaviour. An overview of the previous studies (Table 5.3.1) reveals that compared to other studies where the fibers are directly attached to the CM or the backbone, the integration of the FBG sensor into the side lumens of the manipulator used in this study further increases the modeling complexities. As such, a data-driven approach could be beneficial by skipping the step for making several geometrical assumptions. In addition, a segment by segment shape reconstruction in conventional model-dependent methods suffers from error propagation especially in CMs with large deflection (similar to the CM used in this study), since any inaccuracy in curvature estimation at cross sections close to the base of the CM will establish an incorrect direction for the remainder of shape reconstruction, causing inaccurate DPE.

While previous studies have demonstrated valuable insight into the design considerations of the FBG sensor and integration into different CMs, they have not provided thorough evaluation experiments on the shape sensing method accuracy in practical cases. The comprehensive results presented in this study can therefore be used as a baseline for the performance and accuracy of the FBG-based shape sensing with limited number of sensing locations for CMs with large curvature bending in free and constrained environments. Moreover, the proposed data-driven approaches for DPE and shape reconstruction have proven valuable for such manipulators. One reason for this outperformance is that on the contrary to the conventional shape reconstruc-

CHAPTER 5. SENSING ALGORITHMS

tion methods where only wavelength information of a few FBG nodes at a certain cross section are used to predict curvature locally, in the data-driven approach, the wavelength information of all FBG nodes on the sensor are incorporated into the model during each tip position prediction. Of note, the data-driven method can also be applied to CMs with multiple backbones by incorporating separate data-driven models for each segment and subsequently estimating the distal end position of the next segment.

One important aspect of the data-driven approaches lies at the creation of the dataset, as with any supervised machine learning approach. While this can be considered an additional step in preparation and use of the sensor, the benefit of learning the parameters from real data rather than imperfect geometrical and mechanical assumptions and conjectures, outweighs the hardships associated with dataset creation. Additionally, for the conventional mechanics-based model-dependent approaches also a calibration experiment of some sort must be performed. The calibration could be meant for establishing a wavelength-curvature relationship or estimating some of the parameters present in the model (system identification). For the data-driven approaches, the average required time for collecting the data associated with each experiment in this study was less than one minute. As a result, a combination of e.g. 10 experiments could be done in the order of 10 to 15 minutes. Of note, in a practical setting (e.g. surgical scenario), the required data for the data-driven approach can be generated on the fly by articulation of the CM (and consequently the embedded

CHAPTER 5. SENSING ALGORITHMS

FBG sensor) and incorporation of an external source of information such as X-ray or camera images. In another scenario, a baseline data-driven model could be established preoperatively, while the model is updated intraoperatively as additional data (such as ground truth data from intermittent X-ray) is incorporated into the model for updating the network parameters (weights).

Fault tolerance is the property that enables a system to continue operating properly in the event that some of its components fail [168]. A fault-tolerant design enables a system to continue its intended operation, possibly at a reduced level, rather than failing completely, when some part of the system fails [169]. Optical fibers used for CM sensing applications are delicate and susceptible to damage from excessive strain or contact with sharp objects. In the context of medical applications, therefore, it is important for the patient safety that the sensor can still function in case of partial failure (e.g. fiber damage) so that appropriate system recovery procedure can be followed. The model-driven sensing approach described in Section 5.3.2 requires at least three optical fibers (three FBGs at each active cross section) to detect curvature and consequently reconstruct shape. As such, failure of even one fiber in the sensor assembly results in total breakdown. The data-driven method, on the contrary, can still estimate CM's distal-end position in 3-D with fewer than three fibers. This can be beneficial in case one or two fibers malfunction or get damaged during the operation. Such occurrences could be detected by the interrogator device whenever the number of detected peak signals do not match the number of FBG nodes on a single fiber.

Table 5.5: Fault tolerance capability in CM DPE. Units are millimeters.

	Fibers	Mean	Std.	Max
Model-driven	3	1.52	0.67	3.63
Data-driven	3	0.11	0.10	0.62
Data-driven	2	0.30	0.16	1.01
Data-driven	1	1.98	1.13	4.62

Table 5.5 summarizes the results obtained from TPE using the conventional model-dependent approach and the data-driven regression method using different number of FBG fibers. It can be concluded that the data-driven method not only improves performance compared to the conventional model-dependent method, but is still capable of estimating the tip position in absence of one or two FBG fibers as well.

5.4.4 Collision Detection

5.4.4.1 Background and Motivation

Compared to conventional rigid-link robots, CMs exhibit higher dexterity, flexibility, compliance, and conformity to confined spaces, making them suitable for minimally invasive interventions. Examples of the use of CMs in medical applications include, but not limited to neurosurgery [170], otolaryngology [6], cardiac [4], urology [171], and abdominal [5] interventions. In these medical interventions, the CM may be used for steering in curvilinear pathways, manipulating tissue, or merely as a flexible pathway for navigation of flexible instruments to a desired surgical site, all

CHAPTER 5. SENSING ALGORITHMS

of which accentuating the necessity of detecting CM collision or contact with bone, tissue, or organs.

Detecting CM collisions with the environment is of great to enhance safety. This problem has been studied in the literature. In [155], CM collisions were detected by monitoring the distance between expected and the actual instantaneous screw axis of motion, measured from the unconstrained CM kinematics model and electromagnetic (EM) sensory information, respectively. In [172], collisions were detected by obtaining the exact model of a continuum manipulator featuring multiple constant-curvature sections and a modeled object using polygonal mesh. In [153], two model-dependent approaches were presented: 1) using the deviation of joint forces from the nominal CM model, and 2) using a modified CM kinematics model to detect contacts. These studies, in addition to sensory information, required exact modeling of the CM or objects, relying on geometrical assumptions and properties specific to the choice of continuum manipulator.

This study aims at enhancing safety during teleoperation or autonomous control of CMs in proximity of sensitive organs in confined spaces. We propose a data-driven machine learning algorithm that solely relies on data from any already-available sensor, independent of the CM kinematics model, without any prior assumption or knowledge regarding the geometry of the CM or its surrounding environment. The key idea behind our proposed method is to define the problem of collision detection as a classification problem, with sensory information as the input, and occurrence/no-

CHAPTER 5. SENSING ALGORITHMS

occurrence of CM collision with the environment as the output classes. A machine learning model is trained preoperatively on the sensory data from the CM, and is then used intraoperatively to detect collisions with the unknown environment. This information can then be conveyed to the surgeon as audio or haptic feedback to safeguard against potential trauma and damage to sensitive organs. We implement our proposed method on the CM used in this thesis which is equipped with the notched NiTi substrate FBG-based sensor for shape estimation. Using the proposed method, the FBG sensor will serve as a dual-purpose simultaneous shape sensor and collision detector, preserving CM small size from additional sensors.

5.4.4.2 Data-Driven Collision Detection

Most conventional CM collision detection algorithms are physics- and geometric-based models. These approaches may lead to very complex models that do not accurately detect collisions. This might be in part due to the lack of knowledge of reliable physical models of the components, and/or due to lack of knowledge of the topology of interacting components. To this end, we propose a data-driven approach to directly identify a collision detection model for CMs based on empirical data. In particular, we formulate the problem of collision detection as a supervised classification problem with two classes: collision, and no collision. The input to this method is the sensory data obtained from the CM and the output is the corresponding class of collision. Similar to other supervised learning algorithms, the proposed method consists of an

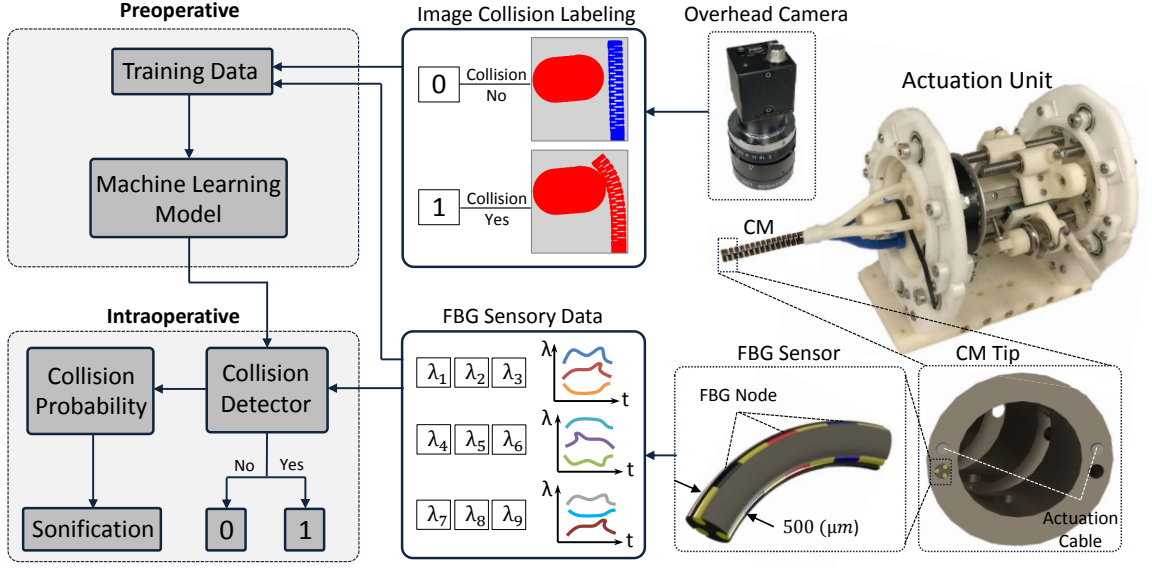


Figure 5.14: Experimental setup and the proposed framework: preoperative phase involving model training using sensory data and camera images, and intraoperative phase for collision detection and sonification using only sensory data.

offline dataset creation step during which, the sensory data is labeled with correct collision class. A supervised machine learning model is trained on the collected dataset to learn the nonlinear mapping from sensory data to the appropriate class of collision. The trained model is optimized by tuning the hyper-parameters via a K-fold cross validation by splitting the data to training and validation sets. Performance of the tuned model is then evaluated on unseen test data from CM collisions with obstacles with different stiffness and properties (hard and soft), placed at random unknown locations relative to the CM. Fig. 5.14 demonstrates the proposed framework.

5.4.4.3 Dataset Creation

To create an appropriate dataset, a vision-based algorithm based on a connected components labeling algorithm [173] is used to segment preoperative images captured via an overhead camera looking at the CM and the surrounding obstacles. The images are first converted to binary format by applying appropriate thresholds. An erosion morphological operation [174], followed up with a dilation, both with small kernel sizes are applied to the binary image to remove potential background noise and ensure robust connected region detection. The connected components labeling algorithm then segments the binary image to distinguish between the background, the CM, and obstacles present in the scene. A particular sensor sample is labeled with the collision class, if the CM and the obstacle form a connected region in the corresponding image frame. Fig. 5.15 indicates the segmented regions in collision and no collision instances during the training phase.

To follow a simple and easy-to-repeat dataset creation procedure, a random-sized oval-shaped obstacle was 3D-printed and placed in five random locations in the CM surrounding volume. The CM was then actuated to collide with the obstacles, while capturing synchronized sensory data and overhead camera images. The captured images were then segmented using the vision-based algorithm to generate the corresponding collision labels.

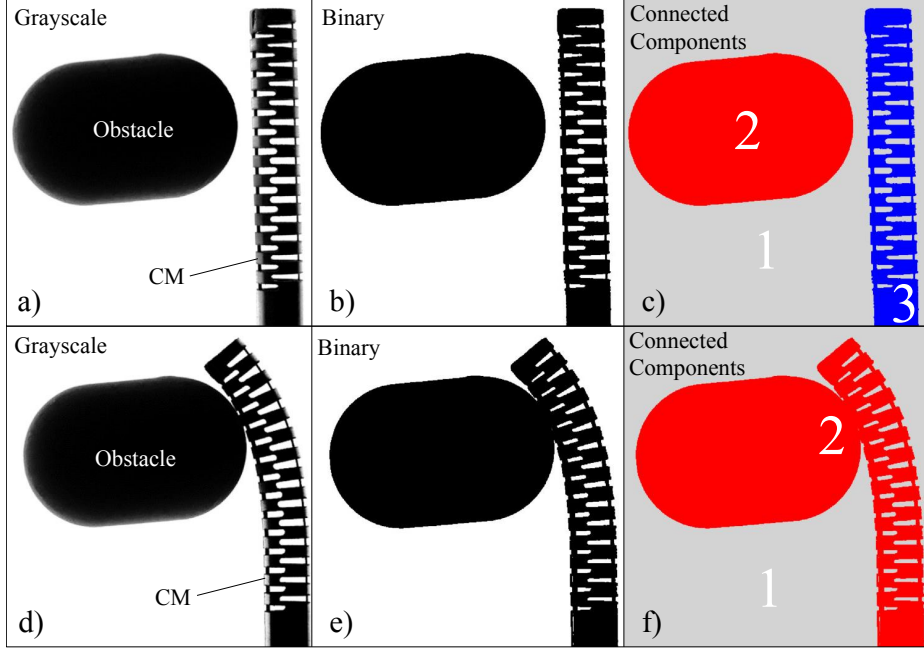


Figure 5.15: Image collision labeling based on number of connected components. Top and bottom rows demonstrate no collision and collision labels, respectively.

5.4.4.4 Gradient Tree Boosting

Gradient boosting is a powerful machine learning technique for classification and regression problems. It builds a model in a sequential way and combines an ensemble of relatively weak simple models (base learners) [175]. Let $\{x_k\}_{k=1}^N$ be a sequence of observations, where $x_k \in \mathbb{R}^n$ (n is the number of FBG sensory data at frame k) represents the observation at frame k . Let y_k be their corresponding labels (1 collision, 0 no collision). Given the training data, we train a gradient boosting classifier with decision trees as base learners (gradient tree boosting) to detect collision. The classifier scores can be used as probability of predicting collision. It should be noted that gradient tree boosting, similar to most other ensemble models, are less likely to

CHAPTER 5. SENSING ALGORITHMS

overfit to training data which are suitable for generalization of the model to different obstacles placed at unseen locations. Algorithm (1) shows the training of the gradient boosting classifier by combining an ensemble of weak learners.

5.4.4.5 Real-time Sonification

Visual feedback is one of the most common means of conveying information to the surgeon during surgery. However, augmentation of this feedback method with many sources of information is prone to the risk of missing crucial information [176]. Particularly, during teleoperation and control of CMs in confined spaces, the visual feedback may be compromised by occlusion or miss-interpretation due to cluttered background; increasing the risk of damaging sensitive organs or tissues. As a workaround to these challenges, we convey the information associated with the collision detection via sonification, i.e. the use of non-speech audio to convey information. More specifically, the probability of collision occurrence (classifier scores) are used to alarm the user (surgeon) if the CM is in contact with the environment. A threshold of 80% certainty is applied to the classifier prediction outputs to only notify the user when the algorithm is confident that the CM is colliding with its surrounding.

5.4.4.6 Experiment Design

To create the dataset explained in Section 5.4.4.3, we 3-D printed an oval-shaped obstacle from plastic ABS material, placed it at five random locations around the

Algorithm 1: Gradient Boosting Classifier Training

Input : Training set $\{(x_k, y_k)\}_{k=1}^N$

Differentiable loss function $L(y, F(x))$

Number of iterations M

Output: Trained model, $F(x)$ for collision classification

```

1 Initialize model with a constant value:  $F_0(x) = \underset{\gamma}{\operatorname{argmin}} \sum_{k=1}^N L(y_k, \gamma)$ 

2 for  $m = 1$  to  $M$  do
3   for  $i = 1$  to  $N$  do
4     Compute pseudo-residuals:  $r_{k,m} = - \left[ \frac{\partial L(y_k, F(x_i))}{\partial F(x_i)} \right]_{F(x)=F_{m-1}(x)}$ 
5   end
6   Fit a base (weak) learner  $h_m(x)$  to pseudo-residuals, i.e. train using the
      training set  $\{(x_k, r_{k,m})\}_{k=1}^N$ 
7   Compute multiplier  $\gamma_m$  by solving:
      
$$\gamma_m = \underset{\gamma}{\operatorname{argmin}} \sum_{k=1}^N L(y_k, F_{m-1}(x_k) + \gamma h_m(x_k))$$

8   Update the model:  $F_m(x) = F_{m-1}(x) + \gamma_m h_m(x)$ 
9 end
```

CHAPTER 5. SENSING ALGORITHMS

CM body, and collected the sensory data and overhead images, which we refer to as *offline* dataset. This dataset was the baseline for training and tuning the collision detector. Additionally, to evaluate the trained collision detector’s performance and robustness on unseen data, we designed experiments that involved CM collisions with objects with different shapes and stiffness, such as soft gelatin, sponge foam, and also plastic ABS, but placed at locations different from the ones in the *offline* dataset, and also hand collisions at various points along the CM body.

5.4.4.7 Experimental Setup and Software

Fig. 5.14 demonstrates the used experimental setup. Similar to the shape sensing experiments (described in Section 5.3.2), a first generation actuation unit was used to mount and actuate the CM. The CM was similarly equipped with the fiber optic sensor consisting of three fibers each with three FBG nodes attached to the 0.5 mm OD NiTi substrate. A single Flea2 1394b (FLIR Integrated Imaging Solutions Inc.) camera was used to capture the overhead images for dataset creation. Model training and testing were programmed in Python using Scikit-learn open source library [177], and UDP communication transferred the trained model’s output data to Max/MSP [178] (Cycling ’74, San Francisco, USA) for sonification. FBG data and camera images are streamed and recorded at 100 Hz and 30 Hz, respectively.

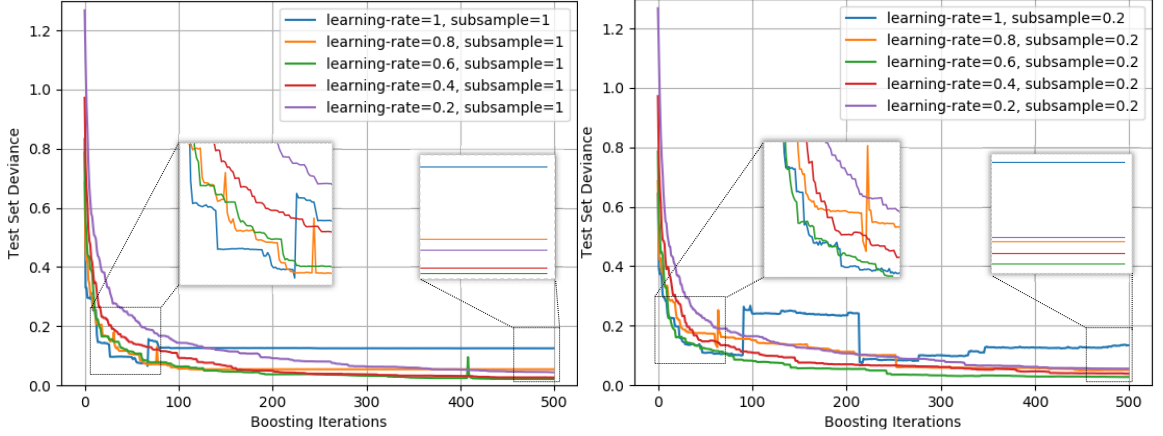


Figure 5.16: Regularization via shrinkage and subsampling to avoid overfitting and enhance generalization. X and Y axis correspond to boosting iterations and loss on test data, respectively.

5.4.4.8 Results

To establish a baseline for optimal collision detection performance, the boosting tree hyper-parameters such as learning rate, number of max features, max depth, and boosting iterations (number of estimators) were tuned by running a randomized k-fold cross-validation on the *offline* dataset. To avoid overfitting to the particular *offline* dataset, and to enhance generalization to future unseen observations, we explored different regularization techniques such as shrinkage (learning rate < 1), stochastic gradient boosting (subsample < 1), and variation on maximum number of features (using all or \log_2 of the features). An initial a k-fold ($k = 4$) validation on different number of estimators ($\{100, 250, 500\}$) and max depths ($\{3, 5, 7\}$) yielded optimal performance with these parameters set to 500 and 3, respectively.

Fig. 5.16 demonstrates the performance results on the *offline* dataset with 57000 samples for five experiments, over 500 boosting iterations, with max depth of 3, and

Table 5.6: K-fold ($k = 4$) cross validation results for hyper-parameter tuning.

Learning Rate	0.2				0.6				1			
Max Features	all		log2		all		log2		all		log2	
Sub-Sample	1.0	0.2	1.0	0.2	1.0	0.2	1.0	0.2	1.0	0.2	1.0	0.2
Mean Accuracy (%)	97.8	97.8	97.7	97.5	97.7	98.2	98.6	98.0	97.0	93.5	82.1	97.9
Std. Deviation (%)	0.05	0.07	0.07	0.03	1.48	0.14	0.04	0.20	2.06	6.95	18.0	0.23
Training Time (s)	108.0	65.3	47.5	40.4	94.7	64.2	46.1	40.0	77.9	64.5	41.9	37.9

CHAPTER 5. SENSING ALGORITHMS

with different combinations of learning rates ($\{1, 0.8, 0.6, 0.4, 0.2\}$) and subsampling values ($\{1, 0.2\}$). It is observed that shrinkage yields improvements in model's generalization ability over gradient boosting without shrinking (left figure). Additionally, subsampling can increase performance when combined with shrinkage (right figure and Table 5.6). Table 5.6 summarizes boosting tree performance results for various combinations of learning rates, subsampling values, number of maximum features, and training times. Comparing the results, the optimal hyper-parameters (shown in bold font in table 5.6) are chosen to maximize the k-fold mean accuracy and minimize the standard deviation of performance among all combinations of training and testing sets in a k-fold split. The performance of this optimized model is then evaluated on unseen data in real-time collisions with hard and soft objects different from the ones in the *offline* dataset, placed at new locations around the CM.

Fig. 5.17 indicates successful CM collision detection with hand, gelatin, and foam. The collision probabilities from the gradient boosting collision detector with 9 FBG sensory data as input are shown and compared to ground truth collisions from the overhead camera. Of note, the time needed for *offline* dataset collection is within a few minutes, depending on the number of locations for obstacle placement during the training phase.

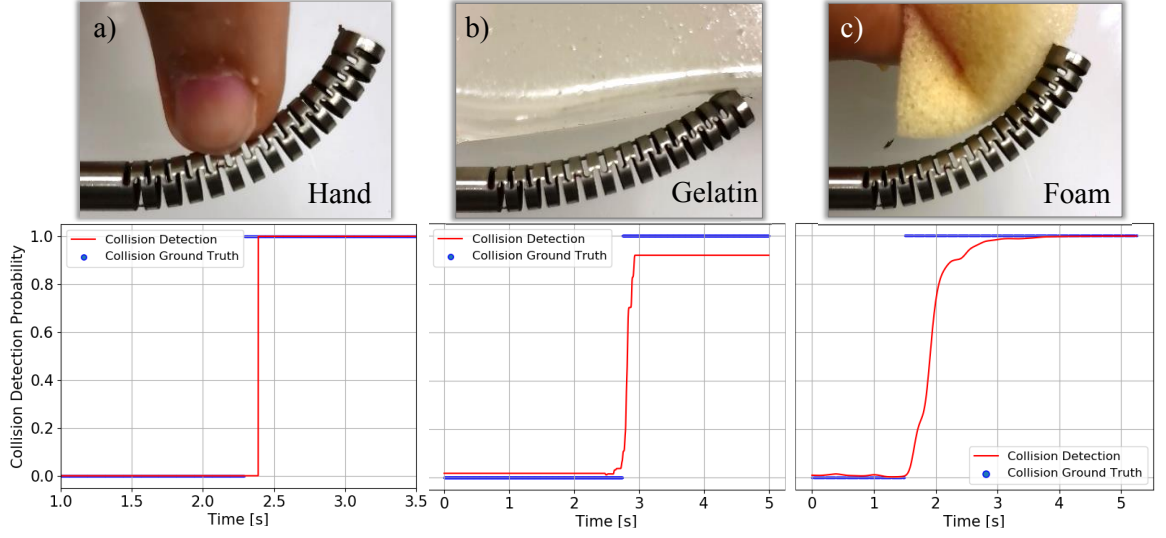


Figure 5.17: Real-time collision detection on unseen data (unknown obstacle stiffness and location). CM collides with (a) hand (b) soft gelatin phantom, and (c) soft sponge foam.

5.4.4.9 Discussion

We proposed a data-driven machine learning approach to collision detection in CMs without prior models, using only the available sensory data such as FBG. The proposed framework consisted of a preoperative offline training and tuning step via k-fold cross validation on a dataset created with a 3-D printed object placed at five locations around the CM, and an intraoperative online collision detection step, as well as sonification, during which only the FBG data was fed to the trained model. Results demonstrated successful detection of collisions on unseen data in constrained environments with soft and hard obstacles of different properties and unknown location.

It should be noted that other types of sensors (e.g. EM tracking) could be substi-

tuted for FBGs, since the algorithm only relies on the raw sensory data. Additionally, even though the CM used in the experiments is restricted to planar bending, the FBG sensor is capable of detecting 3-D motions (since using three fibers), therefore, the method could potentially be extended to 3-D manipulators. Such collision detection algorithm could enhance safety in minimally invasive interventions where the CM is operating in confined cluttered spaces near sensitive organs.

The demonstrated collision detection technology could be incorporated in teleoperation or autonomous control of CMs. In a teleoperation (direct control) setting, the classifier scores could be conveyed to the surgeon via visual or auditory feedback. In an autonomous system, on the other hand, the data could be fed to the controller as feedback for potential switching of the control scheme (e.g. from position control to impedance control).

5.5 Conclusion

In this chapter, we evaluated both FBG- and OFDR-based FOS during model-driven shape reconstruction of the CM in free and constrained environments. While the OFDR-based technique demonstrate superior performance in recovering complex shapes due to higher spatial resolution, the limitations associated with the interrogator device restrict full adaptation of these sensors for real-time application use. The FBG-based sensors and the associated interrogators, on the other hand, are currently

CHAPTER 5. SENSING ALGORITHMS

well established and better suited for practical system development. The data-driven methods proposed in this chapter, can make up for the lower spatial resolution of the FBGs by incorporating empirical data to estimate a more accurate model for sensing.

We proposed several data-driven regression models for DPE, shape sensing, and contact detection of the CM with large deflections without requiring any prior assumptions about the sensor or CM. Results exhibited accuracy improvement especially in large deflections compared to the conventional model-dependent approach. This improvement could be explained as a result of making no assumptions regarding the sensor's geometry, as well as simultaneously using all FBG nodes on the sensor to estimate the CM tip position, rather than only a few at specific cross sections. In addition, using the data-driven approach, even with fewer than three fibers the FBG sensor could still be functional in estimating the CM tip, in case of fiber malfunction or damage during surgery (fault tolerance capability).

It should be noted that the proposed data-driven methods are independent of the sensor modality (e.g. stereo cameras) used for obtaining off-line true CM shape information that is fed to the regression models during the training phase. For instance, medical imaging modalities such as X-ray images could be incorporated in a surgical setting to generate the ground truth data for training. Even though in this chapter, we investigated several data-driven models with complete off-line training steps, an online training procedure could also be used to feed the ground truth data and update the model parameters on the fly as for instance, X-ray images are obtained. In this

CHAPTER 5. SENSING ALGORITHMS

approach, a weak pre-trained model from another sensor could be used as a baseline for training.

The data-driven approaches presented in this chapter demonstrated successful CM shape sensing and contact detection capabilities. However, these approaches alone ignore the fundamental laws of physics and can potentially result in ill-posed problems or non-physical solutions [179]. Modelling approaches, on the other hand, could reveal useful information about the underlying physics of the system. Conventionally, fusion techniques such as variants of Kalman filtering [180,181] were incorporated to combine a dynamics model and sensory measurements containing statistical noise and other inaccuracies, in order to estimate the internal state of a dynamic system. In the context of CM shape sensing, a future direction of research could be the incorporation of a Kalman filter (or similar probabilistic approaches) to fuse the estimations from model- and data-driven approaches presented in this chapter.

With the recent advancements in data-driven methods, recently, several studies have aimed to combine the data- and model-driven approaches to leverage the capabilities associated with each body of work. These studies suggest that the two approaches could naturally complement each other to create robust predictive models that integrate data with the underlying physics to manage ill-posed problems [179,182]. HybridNet [183] is an example of such work that integrates model-based and data-driven learning to predict evolution of dynamical systems. Omran et al. [184] also explored unifying deep learning and model-based techniques for human pose and

CHAPTER 5. SENSING ALGORITHMS

shape estimation by integrating a statistical body model within a CNN. These examples and similar approaches could serve as another future direction of research to further enhance the accuracy in CM shape sensing and contact detection.

In this chapter, a data-driven technique for contact (collision) detection was introduced and evaluated. This research could be explored further for localization of the contact points along the body of the manipulator using temporal sensory information (e.g. a TNN). This can be achieved by introducing additional classes in the supervised classification problem where each class is associated with a particular region along the body of the manipulator. Another beneficial technology is to be able to not only detect contacts, but to predict the contact force as well. It should be noted that a body of research exists for model-based FBG-based force sensing in CMs, biopsy needles and surgical tools [97, 161, 185–187]. An important direction of future research is the incorporation of these model-based approaches with a data-driven method to further enhance the accuracy of estimations.

5.6 Acknowledgments

I would like to sincerely thank Dr. Iulian Iordachita for providing his tremendous support and invaluable expertise during the development and evaluation of the algorithms. Special thanks to Mr. Frederic Monet and their team at the Polytechnique Montreal for fabrication of the distributed OFDR-based sensor. Thanks to Mr. Cong

CHAPTER 5. SENSING ALGORITHMS

Gao for their help in conducting the shape sensing evaluation experiments.

Chapter 6

Control

6.1 Motivation and Background

In recent years, continuum manipulators (CMs) have been used for a variety of applications including locomotion, manipulation, and medical [3, 188, 189]. Several tasks in these applications require the manipulator to maneuver through a constrained environment which takes advantage of the flexibility of these manipulators. In osteolysis, for instance, the CM may interact with soft and hard tissues with unknown geometries and physical properties behind the acetabular implant, making the control problem challenging. With limited prior knowledge of the constrained environment geometry and possible interactions with unknown obstacles, it is vital to choose appropriate shape sensing technique and control algorithm to successfully guide the CM to desired target sites. Chapters 4 and 5 thoroughly covered the shape sensing part.

CHAPTER 6. CONTROL

The motivation behind this chapter is to introduce suitable strategies for closed-loop control of the CM, given position feedback from the fiber Bragg grating (FBG) sensors described in the said chapters.

Previously, several kinematic- and mechanical-based models have been developed for various types of CMs. Many of these strategies assume constant-curvature bending of the manipulator and/or do not account for interactions with the environment and their possible effects on the control and kinematics of the manipulator. For medical applications, control strategies have also been proposed for specific CMs such as tendon-driven robots [190–196] and precurved concentric tube robots [197–201]. Simaan et al. [190] incorporated kinematic redundancy resolution, which is control in the null space of the Jacobian to avoid obstacles or maximize dexterity. Mahvash et al. [191] coupled kinematic and static models, but required knowledge of the wrench applied at the distal-end of the manipulator. Rucker et al. [198, 199] considered mechanics-based models that required sensing of the applied wrench. Mahl et al. [193, 194] considered a variable curvature robot and feed-forward Jacobian control, but did not account for external constraints. Dupont et al. [197] described a Fourier-series approximation of the forward kinematics allowing an inverse kinematic solution which enabled real-time position control but did not consider the external environment.

Although most of the mentioned studies have primarily considered free environment motion of the manipulator, some investigators have begun developing methods to account for external loads in presence of obstacles in the workspace of the ma-

CHAPTER 6. CONTROL

nipulator. For instance, Rucker et al. [154, 199] proposed an approach to estimate contact forces from manipulator deflection and modeled the robot Jacobian using a mechanics-based approach. Wei and Simaan [202] derived a kinetostatic model for force sensing and control of a concentric tube robot under distal-end load. Li and Xiao [203] studied manipulation of a large scale robot in a cluttered environment assuming known *a priori*.

To address some of the challenges and complexities associated with model-based approaches, Yip et al. [204] proposed a model-independent (termed 'model-less') approach for controlling a manipulator during interactions with the environment by continuously updating the robot Jacobian. Their algorithm considered the optimal control to achieve a desired trajectory, followed by an update of the Jacobian. They incorporated visual feedback for sensing the manipulator tip position and considered tension sensors for the actuating cables. Murphy [68] investigated a similar approach but also incorporated the covariance of the tip position into the algorithm and used the cable string lengths (i.e., motor encoders) rather than tension force.

Even though both model-based and model-independent approaches have demonstrated advantages [68, 204, 205], the criteria for selection and preference of one framework over the other for a particular application is not readily apparent. In this chapter, we test and evaluate both methods on the variable curvature CM designed for orthopaedic applications and provide some insight into how the two approaches differ. In consideration of the minimally invasive surgery application and unavailability of

a direct line of sight, we incorporate real-time feedback from the fiber optic sensors (discussed in Chapter 5) compared to visual sensing previously used in the literature for model-less approaches [68, 204].

6.2 Contribution

This chapter implements both the model-dependent and model-independent approaches for controlling the CM in free and constrained environments inspired by the work of Yip [204] and Murphy [68]. The approaches herein extend the previous work by proposing a method for identification of the environment rigidity using the Jacobian estimations and also incorporation of real-time feedback from embedded FBG sensors, eliminating the need for external visual sensing systems requiring direct line of sight. In addition, this chapter provides a performance comparison of the two frameworks (model-dependent and model-independent) during CM manipulation in free and constrained environments. Dr. Ryan Murphy initially implemented the model-independent algorithm, while the author added several modifications to the software for optimal performance and integration with FBG sensor feedback. The author performed all other implementations, experiments and analyses described.

The work presented in this chapter was published in IEEE/RSJ International Conference on Intelligent Robots and Systems (IROS) 2018 [206]. The remainder of the work is currently under review at the IEEE Transactions on Mechatronics [63].

6.3 Control Framework

6.3.1 Model-independent Control

The CM Jacobian (J_c) is a configuration-dependent function that maps the actuation input velocities (\dot{l}) to the end-effector velocities (\dot{x}):

$$\dot{x} = J_c \dot{l} \quad (6.1)$$

Using (6.1), for each time step k , the changes in the end-effector position for an infinitesimal time period can be estimated based on the changes in the actuation input:

$$J_c^k \approx \frac{\Delta x^k}{\Delta l^k}. \quad (6.2)$$

where Δl^k and Δx^k are the changes in the actuation inputs and the end-effector displacements, respectively. Considering (6.2), one reasonable strategy for controlling the CM to a target point is to find the incremental actuation input that moves the CM end-effector to the target point. Further, real world problems have various constraints, e.g. the CM actuation input might be subject to some motion constraints. Constrained control of robotic manipulators have been extensively studied in the literature [207–210]. We incorporate a similar strategy by formulating the control

CHAPTER 6. CONTROL

task as the following constrained optimization problem:

$$\begin{aligned} & \underset{\Delta l^k}{\text{minimize}} && \|\Delta x_{des} - J_c^k \Delta l^k\| \\ & \text{subject to} && A \Delta l^k \leq b \end{aligned} \tag{6.3}$$

where Δx_{des} is the end-effector required tip position displacement to reach the desired goal point, and $A \in \mathbb{R}^{m \times n}$ and $b \in \mathbb{R}^{m \times 1}$ denote m inequality constraints on Δl^k (\mathbb{R}^n), at the time step k . These inequality constraints define the feasible region for the optimization variable Δl^k , which are important considering the possible limitations in the physical application.

In each time step (k), given the actuation control input calculated from (6.3), the CM is moved. Then the correct Jacobian that would have made the movement of Δx^k from an actuation control input of Δl^k is calculated using (6.4). To make a smoother transition from the current Jacobian at the time step k to the next step, we minimize the Frobenius matrix norm of ΔJ_c^k :

$$\begin{aligned} & \text{minimize} && \|\Delta J_c^k\| \\ & \text{subject to} && \Delta x^k = J_c^{k+1} \Delta l^k \\ & && J_c^{k+1} = J_c^k + \Delta J_c^k \end{aligned} \tag{6.4}$$

where Δl^k is the calculated actuation control input from (6.3) and Δx^k is the end-effector tip position displacement read from the FBG sensors between the last Jacobian estimate at time step k and the next time step. A threshold (ϵ) can be specified as the termination factor of the algorithm. The size of this threshold can be defined

CHAPTER 6. CONTROL

experimentally and based on the noise of the sensor feedback. In other words, the control input and the Jacobian will be updated as long as Δx_{des} is greater than this threshold value. It should be noted that a major advantage of estimating the jacobian on the fly using (6.4) is that regardless of the type of environment surrounding the CM (e.g. free space or with obstacle interactions), the CM actuation inputs for next step is computed accordingly by incorporating information about the CM behavior in that environment. Algorithm (2) summarizes the proposed control strategy for tracing a list of target points ($\mathcal{L}_{targets}$).

6.3.1.1 Constraints

Considering (6.3), we need to define A and b based on the constraints imposed by the application. Mechanically, there is a maximum allowable cable actuation that prevents the CM from breaking [22]. In addition, to avoid large actuation inputs in each step of (6.3), we limit the displacement of the cables. Considering the constraints, we can define matrix A and vector b as:

$$A = \begin{bmatrix} 1 & 0 & -1 & 0 & 1 & -1 & 1 & 0 \\ 0 & 1 & 0 & -1 & 1 & -1 & 0 & 1 \end{bmatrix}^T$$

$$b = \begin{bmatrix} 1 & 1 & 1 & 1 & 0.1 & 0.1 & b_1 & b_2 \end{bmatrix}^T$$

$$b_1 = b_2 = l_c - l_{max}$$

Algorithm 2: Optimization-based Control Algorithm

Input : Initialized CM Jacobian , J_c

List of N target tip positions, $\mathcal{L}_{targets}$

Termination threshold, ϵ

Matrix A and vector b

```

1 for  $i = 1$  to  $N$  do
2   Set  $x_{target}$  to  $\mathcal{L}_{targets}^i$ 
3   Query  $x_{current}$  from FBG sensors
4   Compute  $\Delta x_{desired} = x_{target} - x_{current}$ 
5   while  $\Delta x_{desired} \geq \epsilon$  do
6      $\Delta l \leftarrow \text{argmin} \quad \|\Delta x_{des} - J_c \Delta l\|$ 
7     subject to  $A \Delta l \leq b$ 
8      $\Delta J_c \leftarrow \text{argmin} \quad \|\Delta J_c\|$ 
9     subject to  $\Delta x = (J_c + \Delta J_c) \Delta l$ 
10    Set  $J_c = J_c + \Delta J_c$ 
11    Query  $x_{current}$  from FBG sensors
12    Update  $\Delta x_{desired}$ 
11  end
12 end

```

CHAPTER 6. CONTROL

where l_{max} and l_c are the maximum allowable cable length and the cable length at the current iteration (computed from the initial 'zero' position of the cable), respectively. The first four rows in A and b ensure that the change in string length in each iteration is less than 1 mm. Rows five and six will make the sum of changes in both string lengths to be less than 0.1 mm (i.e., ensure both cables have approximately the same amount of movement to avoid excessive counter-tensioning). These constraints account for the pull-pull behavior of the two cables which ensures that the cables are not interfering with each other. The last two rows guarantee that the achieved length of the cables at the next iteration of the algorithm does not exceed the maximum allowable length. l_{max} is chosen 7 mm to avoid potential damage to the manipulator.

6.3.2 Model-dependent Control

Since the primary goal in osteolysis is to bring the CM tip to surgical target points, knowledge of the CM tip Jacobian is sufficient for control purposes. As such, the mapping between the actuation space and CM tip position changes can be found off-line by fitting a model to empirical data obtained from the actuation cable length (l_c) and CM tip position (p). Preliminary investigation of manipulator bending [211] suggested that p may be a polynomial function in l_c . Different choices for the basis of the polynomial exist such as power basis (n^{th} degree polynomial) or Bernstein basis. The Bernstein polynomial, however, offers improved numerical stability and robustness as compared to the power bases [212]. Investigation of the collected data by

CHAPTER 6. CONTROL

Murphy et al. [211] suggested a sinusoidal relationship between the two components of the CM tip position. As such, we also first relate l_c to p_x component of the CM tip using a Bernstein polynomial of degree 7 [68] and subsequently relate the two components of the CM position, p_x and p_y , with a sinusoidal mapping:

$$\begin{cases} p_x = \sum_{i=0}^7 \beta_i \binom{7}{i} \hat{l}_c^i (1 - \hat{l}_c)^{7-i} \\ p_y = \sum_{j=1}^3 a_j \sin(b_j p_x + c_j) \end{cases} \quad (6.5)$$

where β_i , a_j , b_j , and c_j are the mapping parameters found in a least square fashion using the training data (explained in Section 6.3.2.1), and $\hat{l}_c = (l_c + l_{max})/l_{max}$ is the normalized CM cable length with l_{max} as the maximum pull length of the cable. Note that we incorporate the convention that l_c is a negative value when the actuation motor pulls the cable for bending, hence \hat{l}_c becomes 0 and 1 when the CM is at full-bend and initial unbent configurations, respectively. The linear component of CM Jacobian expressed in the CM base frame can be obtained by taking the derivative of $p = [p_x \ p_y]^T$ with respect to the cable parameters \hat{l}_c .

6.3.2.1 Ground Truth Tip Position

We use an optical tracker (Polaris, NDI Inc.) for obtaining the true CM tip position for the purpose of establishing the model-dependent Jacobian. We follow a two step procedure to find the tip position of the CM relative to its base using the optical tracker (frame o). First, we establish a coordinate frame (s) at the CM

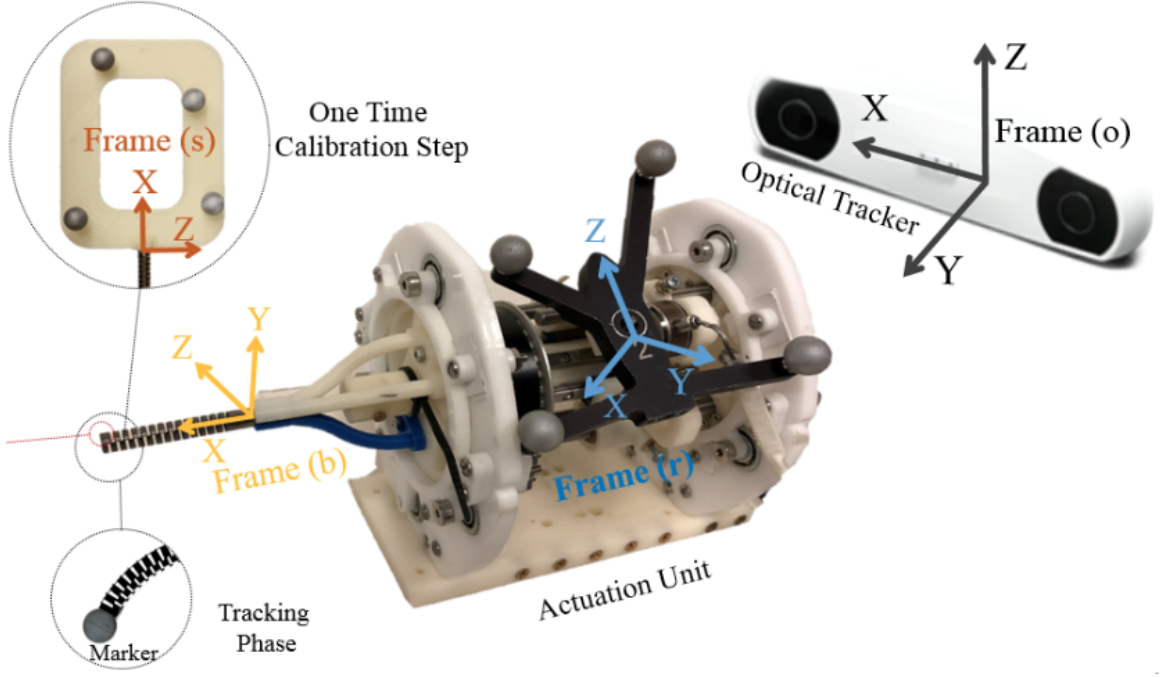


Figure 6.1: Experimental setup for obtaining ground truth CM tip position using optical trackers [146]. Coordinate frames are shown: optical tracker (o), reference body (r), CM straight pose body (s), and the base of the CM (b).

tip when it is straight with respect to a reference body that is attached to the fixed actuation unit (frame r). To ensure the CM is at straight configuration, we use a custom-designed 3-D printed rigid body with four reflective spherical markers and a 35-mm straight shaft that is inserted into the instrument channel of the CM and ensures the CM is straightened (Fig. 6.1):

$$T_{sr}^0 = (T_{os}^0)^{-1} T_{or}^0 \quad (6.6)$$

where T_{ij}^0 denotes frame j with respect to frame i during the one-time coordinate frame establishment (time 0). The advantage of knowing the transformation between

CHAPTER 6. CONTROL

frames s and r is that later all the information will be reported with respect to the reference body, independent of where the optical tracker is located.

For tip tracking during CM bending, a single spherical marker attached to a post is placed into the instrument channel of the CM. The tracked position with respect to the optical tracker coordinate (p^o) frame can be represented with respect to the base of the CM (frame b) by:

$$p^b = T_{bs} T_{sr}^0 (T_{or}^c)^{-1} p^o \quad (6.7)$$

where T_{or}^c is the reference body coordinate frame with respect to the optical tracker coordinate frame at its current location (in case the location of optical tracker changes).

T_{bs} , brings the CM tip position explained in frame s to the CM base frame (p^b):

$$T_{bs} = \left[\begin{array}{c|c} I_{3 \times 3} & p_{bs} \\ \hline 0_{1 \times 3} & 1 \end{array} \right] \quad (6.8)$$

where $p_{bs} = [0, 0, L_{CM}]^T$ and L_{CM} is the length of the CM (35 mm). From (6.7), the CM tip position is known with respect to the coordinate frame at the base of the CM (frame b) and can be used for establishing a data-set used for computing the unknown parameters of (6.5). In particular, p_x and p_y in (6.5) are the two components of p^b found from (6.7).

It should be noted that the optical tracker was only used to obtain the ground truth tip position data for establishing the fixed model-based Jacobian in free envi-

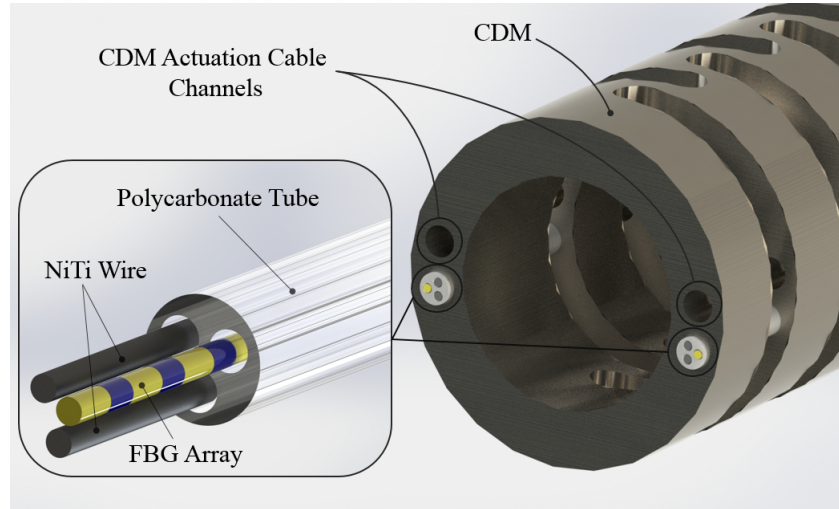


Figure 6.2: Distal-end view of the CM, indicating the actuation cable channels, and two FBG Sensors with Polycarbonate tube substrates embedded in the sensor channels [206].

ronment, while FBG data was used during the manipulation of the CM in free and constrained environments (evaluation experiments). The FBG sensor used for the controller evaluation purposes was the sensor with Polycarbonate substrate described in Section 4.4.1. The integration of the sensor with the CM can be seen in Fig. 6.2.

6.4 Experiments

6.4.1 Model-independent Control Performance

To evaluate the performance of the model-independent controller, we designed three sets of experiments inspired by the osteolysis procedure: 1) free environment bending, 2) CM interactions with soft obstacles mimicking soft tissues, and 3) CM

CHAPTER 6. CONTROL

interactions with hard obstacles mimicking bone or sclerotic tissue.

We first tested the behavior of the algorithm for the CM control in an environment without any obstacles. In this experiment, the controller's ability to move the CM tip to three different target points was evaluated. We chose target points $p_1 = [-10, 32.1]$ mm, $p_2 = [-22.6, 21.4]$ mm, and $p_3 = [-25, 16.2]$ mm, corresponding to different levels of bending. A target point list of $\mathcal{L}_{targets} = \{p_1, p_2, p_3\}$ was passed to the Algorithm (2) as input. In addition, to ensure repeatability, in another experiment, the CM performed the following moving sequence: 1) from straight configuration ($p_0 = [0, 35]$) to the target position p_1 ; 2) from position p_1 to the straight configuration p_0 ; 3) from straight configuration p_0 to target position p_1 ; and 4) from position p_1 to the straight configuration p_0 . In this case, the input target point list was set to $\mathcal{L}_{targets} = \{p_1, p_0, p_1, p_0\}$.

To study the behavior of the controller for the interaction of the CM with soft and hard environments, we arbitrarily placed soft (Fig. 6.3) and hard (Fig. 6.4) objects in the bending path of the CM in separate experiments. and chose p_3 as the target point in these experiments.

6.4.1.1 Results and Discussion

Fig. 6.5 shows the CM configurations and the traversed tip paths as it is moving from the straight configuration (p_0) toward the three aforementioned target points ($p_1, p_2, and p_3$) in the free bending environment. Due to the variable-curvature be-

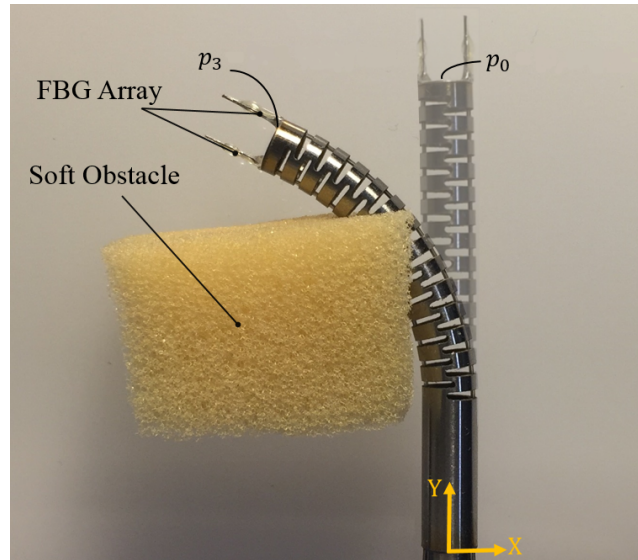


Figure 6.3: Interaction of the CM with soft obstacle.

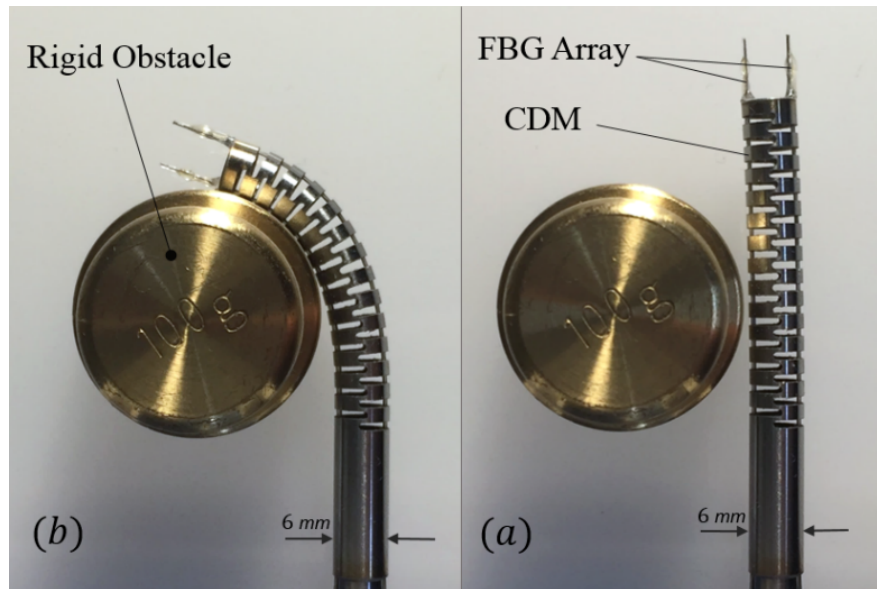


Figure 6.4: The CM in interaction with hard obstacle: (a) straight configuration (b) bending configuration (c) x-ray image of the CM inserted into the screw holes of the acetabular component

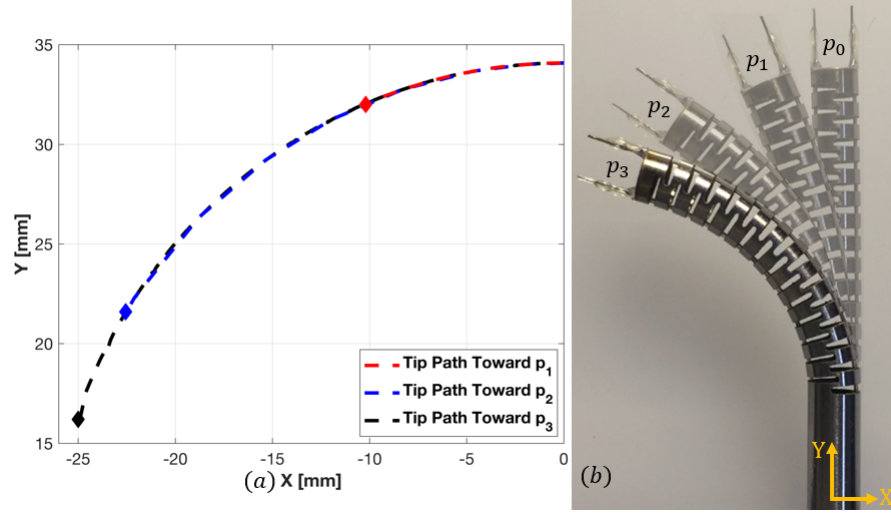


Figure 6.5: (a) The CM tip traversed path for three target points in free bending environment, (b) the CM instantaneous configuration when the tip has reached the target points.

havior of the CM [22], its dynamics alters as the CM is undergoing different levels of bending. As observed in Fig. 6.5, the proposed control algorithm can address this change of dynamics by guiding the CM toward the desired targets. Further, similar traversed paths in different experiments confirm repeatability of the CM bending behavior and show negligible hysteresis.

Fig. 6.6 indicates the repeatability of the proposed method in terms of the control input and norm of the adapted Jacobian matrix. As shown, similar patterns are observed both in control input and norm of the Jacobian for the repeated experiments. In both figures, the rising parts of the plots demonstrate the bending motion of the CM toward the target point p_1 , while the falling parts indicate the movement toward the target point p_0 . Investigation of the control input demonstrates small peaks at the beginning of each rising and falling part (blue circles in Fig. 6.6(a)). This behavior

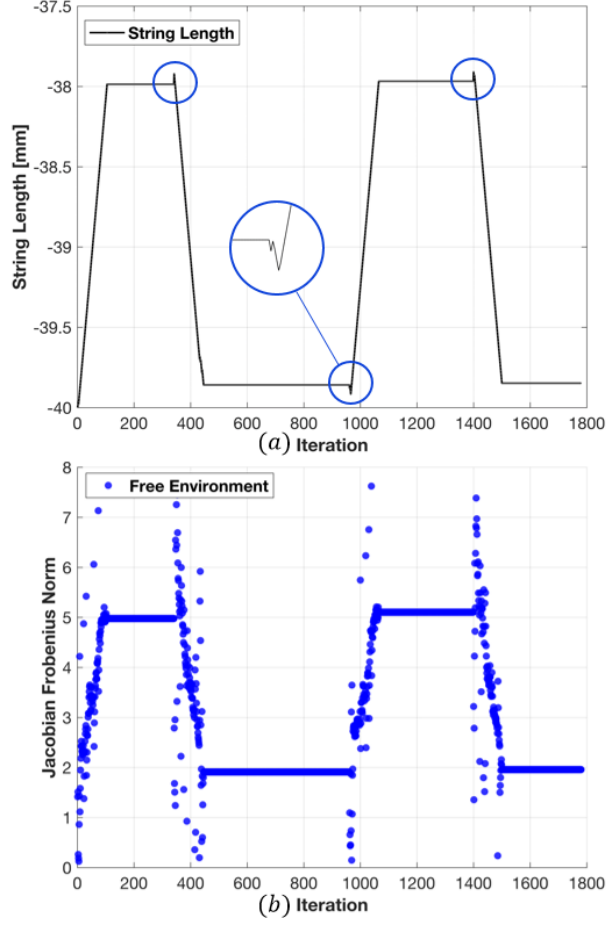


Figure 6.6: Model-independent controller repeatability experiment in free environment (a) changes in string length over time, (b) the estimated Jacobian over time.

illustrates the learning step of the proposed control method, where the controller tends to obtain the correct movement direction toward the target point. Further, similar behavior is observed in the norm of the calculated Jacobian (Fig. 6.6(b)), supporting the learning step behavior. In addition, values of the Jacobian norm increased as the CM moved toward p_1 and decreased when moved toward p_0 . This means that in a highly bent configuration of the CM, a specific control input (i.e. change of the cable lengths) results in a larger displacement of the CM tip as compared to the less bent

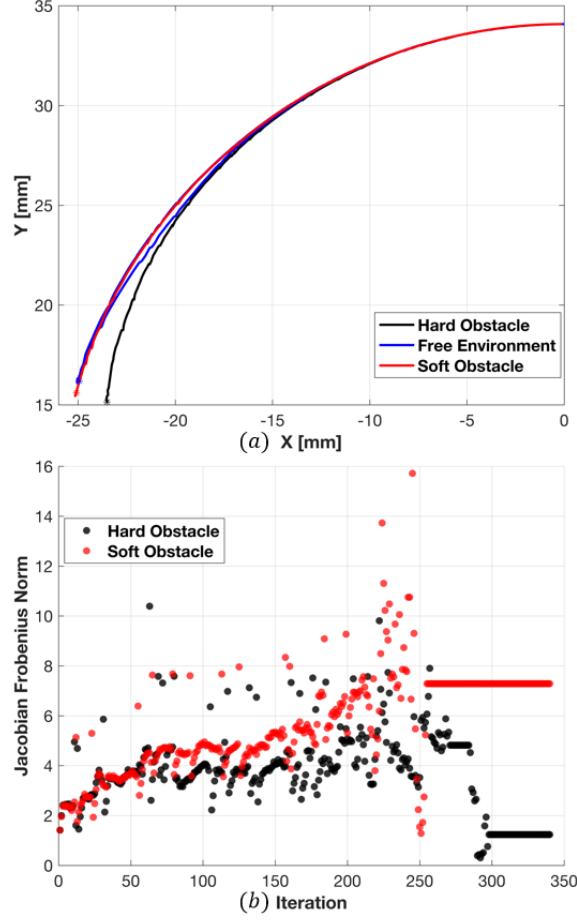


Figure 6.7: (a) The CM tip transversed path for target point $p_3 = [-25, 16.2]$ mm in free bending, soft obstacle, and hard obstacle experiments, (b) the estimated Jacobian comparison in soft and hard obstacle experiments.

configurations.

Fig. 6.7(a) compares the CM traversed tip paths—reported by the FBGs—during movement toward the target point p_3 in the soft obstacle, the hard obstacle and the free bending experiments. As shown, regardless of the external contact forces exerted by the soft obstacle, the CM traversed approximately similar paths to the free bending experiment. This indicates that the proposed method can compute effective control

CHAPTER 6. CONTROL

inputs to overcome the unknown disturbance imposed by the contact force. Further, in the hard obstacle experiment, we observe higher deviation from the free bending traversed path (as expected), since the CM cannot penetrate the hard obstacle, as opposed to the soft obstacle case (Fig. 6.4 and Fig. 6.3). The higher error in the hard obstacle experiment between the desired target point and the final achieved tip position is because the CM cannot physically reach the target point.

Fig. 6.7(b) demonstrates the norm of the adapted Jacobians over time for both of the soft and hard obstacle experiments. These plots show similar behavior before iteration 60, where there is no contact between the CM and obstacles. After collision, the norm of the Jacobian changes; in the soft obstacle case the norm of the Jacobian is larger compared the other case. A higher reduction in the Jacobian norm for the hard obstacle interaction demonstrates a higher contact force compared to the soft obstacle interaction. Furthermore, the last movements in the hard obstacle experiment (i.e. iterations ≥ 280) demonstrate a reduction in the Jacobian norms. Physically, these iterations correspond to the situation when the CM is wrapping around the cylindrical obstacle and cannot proceed toward the desired target (Fig. 6.4). In this case, any specific input command (i.e. string length) results in a small CM tip displacement.

6.4.2 Comparison of Approaches

In this section, we compare the fixed model-dependent Jacobian obtained from derivation of the CM kinematics (Section 6.3.2) with the model-independent (model-

CHAPTER 6. CONTROL

less) Jacobian approach (Section 6.3.1) where the CM Jacobian is updated on-the-fly during the experiment. To fully study the trade-off between the two approaches, we performed two sets of experiments where the CM was commanded to a desired goal tip position in free environment and while it collided with an obstacle. In these experiments, we first obtained the fixed model-based CM Jacobian in free environment bending by recording the tip position and cable tension and fitting a Bernstein polynomial to the collected data, as described in Section 6.3.2. The tip position was collected in a similar fashion as outlined in Section 6.3.2.1 using an optical tracker reflective marker mounted on the CM distal end. In the first part of each experiment, the model-based Jacobian was used and cable displacement commands were generated by (6.3) while the joint position and velocity constraints were applied to avoid over-tension of the cables or damage to the CM. The second part of each experiment was composed of initializing the CM Jacobian with the model-based Jacobian and then iteratively updating it via (6.3) through the rest of the experiments while generating cable displacements using (6.4).

6.4.2.1 Results and Discussion

Results are demonstrated in Figs. 6.8(a) and 6.8(b), where the components of the Jacobian column associated with the CM actuation cable are plotted for the free environment and obstacle interaction experiments, respectively. The path tracking for each of these experiments are plotted in Figs. 6.8(c) and 6.8(d). As observed in

CHAPTER 6. CONTROL

Fig. 6.8(a), both the fixed model-dependent Jacobian obtained experimentally and the computed model-independent Jacobian follow a similar trend in free environment motion, as expected. When the CM interacts with obstacles (Fig. 6.8(b)), the two approaches still exhibit a similar behavior, although the magnitude of the Jacobian columns in the model-dependent approach become slightly inaccurate compared to the estimated Jacobian from the model-independent approach. The target points are, however, reached successfully despite the interaction with the obstacle and the slightly inaccurate CM Jacobian. This can be justified by noting that the most important factor when generating joint commands using (6.3) is the accuracy of the Jacobian direction. In other words, as long as the model-dependent Jacobian is functional enough in the correct direction, the generated commands will lead the CM toward the goal.

The model-less Jacobian approach, on the other hand, generates noisy estimations, as expected from numerical methods. This noise can be problematic in certain cases, for instance when the CM is close to its straight pose. As observed in Figs. 6.8(a) and 6.8(b), before nearly iteration 20 (when the CM is straight), the estimated Jacobian values from the model-less approach sometimes generates values that are not in the correct direction (incorrect sign) caused by numerical errors. This incorrect sign of Jacobian components was also observed in Fig. 6.6 in the previous section, when the CM was starting the motion from straight pose. The numerical instability in the model-independent approach can be mitigated by introducing a smoothing factor in

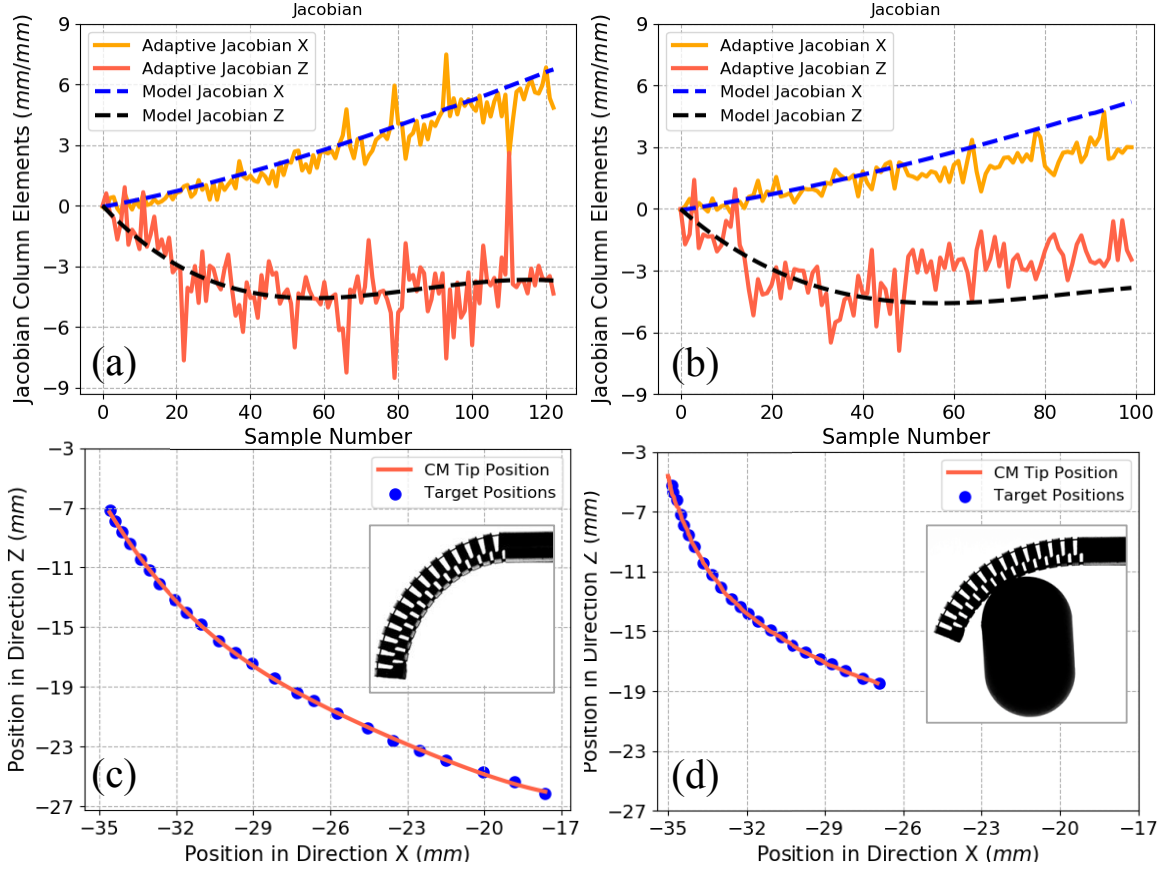


Figure 6.8: The CM Jacobian (J_C) components using the model-based and model-less estimation approaches in (a) free environment, and (b) interaction with obstacle. Path following using the model-based Jacobian in (c) free environment, and (d) interaction with obstacle.

the optimization problem (6.4) [204]. In particular, the Jacobian at time step $k + 1$ can be written as $J_c^{k+1} = J_c^k + \Upsilon \Delta J_c^k$, where Υ is the smoothing factor such that values between 0 and 1 (obtained experimentally) could avoid sudden large changes to the Jacobian values. It should be noted, however, that any value for Υ other than 1 introduces a trade-off between the accuracy of the estimated Jacobian and the improvement of the numerical stability [68]. An alternative approach to remove the noise is to apply a low-pass filter to the Jacobian estimations, which again, may

CHAPTER 6. CONTROL

reduce the accuracy of the estimations.

The model-independent approach presented in this chapter, even though beneficial in estimating accurate Jacobian estimations especially during interactions with the environment, suffers from numerical instability, as mentioned above. The model-dependent approach, on the other hand, is more stable but requires an additional step of collecting tip position data. In addition, as shown in Fig. 6.8, the Jacobian values from the model-dependent approach generally follow the ones from the model-independent approach with slight inaccuracy; yet both methods are successful during path tracking. The reason for this behavior lies in the planar motion of the CM under study and the associated small actuation velocities, as were shown optimal for debridement tasks in [69, 70]. For the planar CM, the two directions of bending (left and right) translate to the sign of the Jacobian components, therefore, as long as the Jacobian components' signs are correct and the values are accurate enough, the optimizer (6.3) will generate small actuation commands toward the desired target points.

6.5 Conclusion

This chapter demonstrated model-dependent and model-independent strategies for closed-loop control of the CM distal-end position with real-time FBG feedback even in presence of unknown obstacles in the environment. A comparison of both

approaches was presented and trade-offs in choosing each framework were discussed. The developed robotic system for treatment of pelvic osteolysis requires the concurrent control of the positioning robot as well as the CM, which will incorporate the control considerations discussed in this chapter for the CM part.

6.6 Acknowledgment

Special thanks to Dr. Ryan Murphy for implementing the initial version of the model-independent control approach. I would also like to thank Mr. Justin Ma and Dr. Farshid Alambeigi for their help in conducting the evaluation experiments.

Chapter 7

System Integration and Evaluation

7.1 Motivation

The goal of this chapter is to orient the reader with all the necessary algorithmic and software components for integration of the robotic system for autonomous less-invasive treatment of osteolysis. The sensing and control components from Chapters 4, 5, and 6 are revisited for adaptation to the concurrent feedback control of the entire system, i.e. positioning robot and continuum manipulator (CM). A variety of safety, geometrical, and task constraints are presented and implemented in the form of virtual fixtures (VFs) and strategies are presented to allow for recovery of the system from situations where the robotic system gets to the proximity of said constraints' boundaries (i.e. solution to the constrained controller becomes infeasible).

The integrated system is deployed in a mock operating room and evaluated in

CHAPTER 7. SYSTEM INTEGRATION AND EVALUATION

simulation, phantom, and human cadaver experiments. The performance of different system's components (such as sensing, control, target placement accuracy, etc) are evaluated. The enhanced dexterity and improved reach of the developed system is further shown in cadaver experiments both for the less-invasive treatment of pelvic osteolysis and treatment of avascular femoral osteonecrosis using the curved-drilling technique. Finally, the necessary preoperative and intraoperative steps for use of the developed system for robot-assisted orthopaedic interventions are performed and fully discussed.

7.2 Contribution

A multitude of individuals were involved with the development of separate components of the system. Dr. Farshid Alambeigi developed and implemented the base of the constrained controller framework in MATLAB simulation, while Mr. Paul Wilkening and Dr. Ryan Murphy implemented an early version of the controller software on a limited version of the system hardware using the first actuation unit version with no fiber Bragg grating (FBG) feedback for the CM.

The author integrated the complete surgical system with real-time FBG feedback and improved the initial control architecture with additional VFs and regularization techniques for safe recovery from infeasible optimization problems. The author also developed several components of the system such as the graphical user interface (GUI)

CHAPTER 7. SYSTEM INTEGRATION AND EVALUATION

and a complete constrained control simulation framework with real-time visualization for easy integration and deployment of new constraints. The author further performed all the simulations, phantom and cadaver experiments (both pelvic osteolysis and core decompression of the femoral head). Ms. Rachel Hegeman contributed equally to the system software development and helped the author in performing the phantom and cadaver experiments. Dr. Rob Grupp and Dr. Ryan Murphy implemented the ICP registration algorithm.

The work presented in this chapter is currently under revision at IEEE Transactions on Mechatronics (T-MECH) [63] and IEEE Transactions on Robotics (T-RO) [73].

7.3 Constrained Control Framework

The aim is to concurrently control all the system components while satisfying several safety and physical constraints associated with the surgical task. As such, a versatile optimization-based multi-objective constrained control framework is developed and built upon previous work [210, 213, 214] to address this problem for our system. The main objective of any lesion debridement task is tracing a desired path (i.e. a set of target points). This can be formulated as an unconstrained optimization problem of finding the necessary infinitesimal configuration space motion (Δq), given

CHAPTER 7. SYSTEM INTEGRATION AND EVALUATION

the objective infinitesimal task space motion (Δx_{obj}):

$$\underset{\Delta q}{\text{minimize}} \quad \|\Delta x_{obj} - J_s \Delta q\| \quad (7.1)$$

where $\|\cdot\|$ is the L2 norm, $J_s \in \mathbb{R}^{6 \times 9}$ is the system Jacobian (discussed in Section 7.3.5), and $q = [\theta_{R1} \ \dots \ \theta_{R6} \ \theta_A \ l_{C1} \ l_{C2}]$ is the stack of system joint variables including the six rigid-link robot revolute joints, the actuation unit roll joint, and the two CM actuation cable displacements.

A surgical scenario, however, typically includes additional objectives beyond only tracing a desired path. For instance, physical or safety constraints in various forms having to do with the operating room, the patient, the surgical staff or the robotic system itself may be present. Moreover, each surgical intervention may require the robotic system to satisfy certain motion constraints specific to the surgery. Consequently, we extend our control framework to a more generalized constrained optimization problem:

$$\begin{aligned} &\underset{\Delta q}{\text{minimize}} \quad \alpha \|\Delta x_{obj} - W J_s \Delta q\| + \beta R(\Delta q) \\ &\text{subject to} \quad H \Delta q \leq h \end{aligned} \quad (7.2)$$

where $R(\Delta q)$ could be a secondary controller task appeared in the form of a regularization or penalty term, $H \in \mathbb{R}^{n \times 9}$ and $h \in \mathbb{R}^{n \times 1}$ define n inequality constraints, and $W \in \mathbb{R}^{6 \times 6}$, a diagonal weight matrix, and scalar β (damping factor) are optional parameters for enforcing priority on specific joints. Any equality constraint can be

added to the optimization problem (7.2) by separation to two inequality constraints.

7.3.1 Constraints

We hereby provide the formulation for several safety and physical constraints immediately applied to the less-invasive treatment of osteolysis and potentially useful for other orthopaedic surgical procedures. The general idea is that given the system joint state at current step k , i.e. q^k , the Δq^k command in (7.2) is found such that the resulting Cartesian motion, $J\Delta q^k$, takes the system to a state at step $k + 1$ that satisfies a particular constraint.

7.3.1.1 Programmable Remote Center of Motion

A programmable remote center of motion (RCM) [2] is a versatile software approach for systems that do not contain a mechanical RCM. A great advantage is that the desired RCM can be readily set in the software and the robotic system maintains the constraint without incorporation of any special mechanical design. The constraint can be derived by restricting the point on the robot that is closest to the programmed RCM to stay in the vicinity of the RCM bounded by ϵ within a prism with m faces (Fig. 7.1). This can be formulated as m inequality constraints in (7.2), where:

$$\left. \begin{aligned} H_i &= v_i^T J_{RCM}^v \\ h_i &= \epsilon + v_i^T (p_{RCM} - p_{closest}^k) \end{aligned} \right\} \text{for } i = 1, \dots, m \quad (7.3)$$

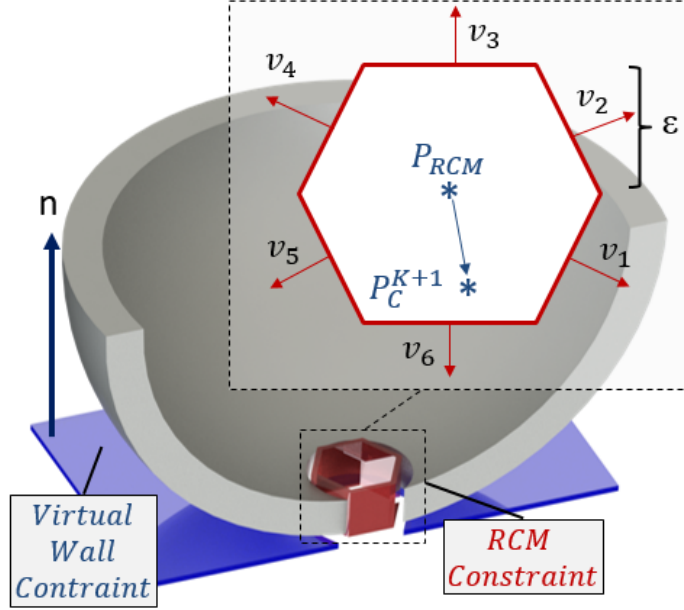


Figure 7.1: RCM and plane virtual fixtures. The RCM allowable region is approximated with a prism with m faces (e.g. $m=6$ in this figure).

where J_{RCM}^v corresponds to the linear component of the Jacobian resolved at a point on the robotic system that is closest to the RCM at time step k and v_i 's are the normals to the faces of the prism.

7.3.1.2 Hyperplane Virtual Fixture

Another useful constraint is to prohibit a particular point on the robotic system to pass a desired plane (virtual wall). An example of such scenario arises when a sensitive region in the anatomy should be avoided by the instrument. Another use-case of this VF is to limit the amount that the end-effector shaft can be inserted into the anatomy. Assuming the desired hyperplane is defined as $ax + by + cz = d$, with the normal $n = [a \ b \ c]^T$, the constraint can be written as a single inequality constraint

(the normal to the virtual wall constraint as shown in Fig. 7.1):

$$\begin{aligned} H &= -n^T J_p^\omega \\ h &= n^T p_p^k - d \end{aligned} \tag{7.4}$$

where the subscript p refers to the desired point on the system (e.g. the instrument tip or the CM base) that must avoid entering a particular region. Of note, a multitude of these hyperplanes could be incorporated as inequality constraints to define a forbidden (or allowable) region.

7.3.1.3 Axis Range Virtual Fixture

To increase patient and system safety, the range of motion for the robotic system end-effector shaft must be restricted. A conical VF can be defined to limit the axis of the robotic system to always stay within a cone with the set RCM as its apex, tapered along a programmable desired axis ($axis_{des}$) with maximum allowable deviation ϕ_a (Fig. 7.2). At time step k , this VF can be formulated as a single inequality constraint:

$$\begin{aligned} H &= -axis_{des}^T J_{sh}^\omega \\ h &= axis_{des}^T axis_{sh}^k - \cos(\phi_a) \end{aligned} \tag{7.5}$$

where $axis_{sh}^k$ refers to the direction of the end-effector shaft at time step k , and J_{sh}^ω is the angular component of the Jacobian resolved at any point on the shaft (e.g. CM base).

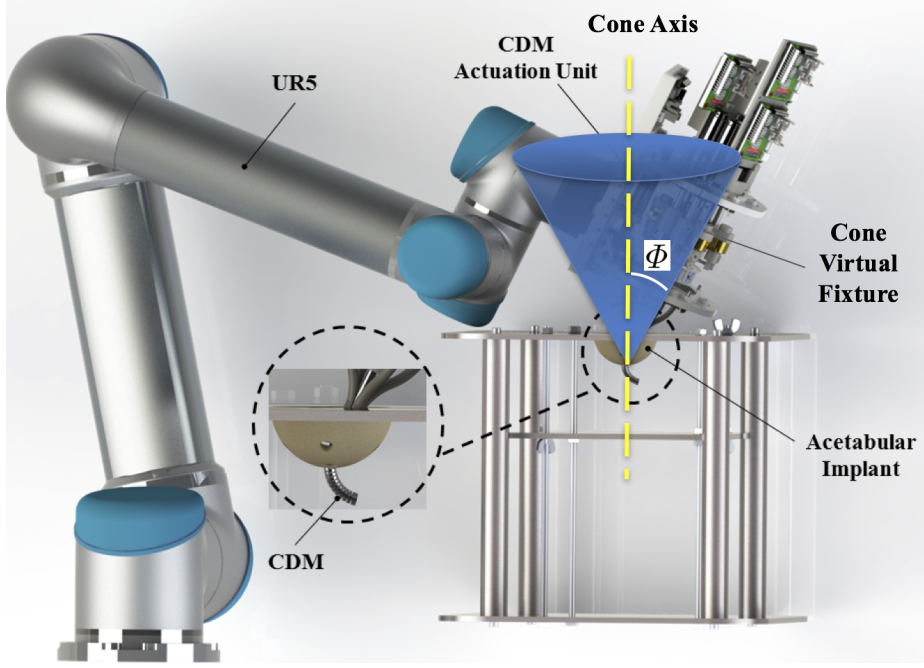


Figure 7.2: Axis range virtual fixture. The allowable region is defined as a cone. Image modified from [215].

7.3.1.4 Velocity Constraints:

To make sure that the system runs at speeds that are both safe and beneficial for cutting but also efficient [69, 70], velocity constraints both in configuration and task-space could be added to the optimization problem:

$$\begin{aligned}
 H &= [-I_{9 \times 9} \quad I_{9 \times 9} \quad -J_s^T \quad J_s^T]^T \\
 h &= [-q_{v,l}^T \quad q_{v,u}^T \quad -\xi_{v,l}^T \quad \xi_{v,u}^T]^T
 \end{aligned} \tag{7.6}$$

where the lower and upper joint and task-space velocity bound vectors, $q_{v,l}$, $q_{v,u}$, $\xi_{v,l}$, and $\xi_{v,u}$ respectively, were experimentally determined by assessing safety constraints as well as smoothness of operation across test runs of the system.

7.3.1.5 Joint Limit Constraints:

To ensure safe manipulation of the system, joints positions are constrained to $q_{p,l}$ and $q_{p,u}$ to avoid potential damage to the system due to collision, actuation cable damage, etc. These constraints can be formulated as:

$$\begin{aligned} H &= [-I_{9 \times 9} \quad I_{9 \times 9}]^T \\ h &= [q - q_{p,l} \quad -q + q_{p,u}] \end{aligned} \tag{7.7}$$

7.3.2 Regularization

Secondary tasks or other constraints can be introduced to the constrained optimization problem (7.2) in the form of regularization or penalty. A constraint appeared in the main objective function as regularization ($R(\Delta q)$) is generally more relaxed compared to when appeared in the inequality constraints. This is since in the latter, the solution search space is shrunken down, whereas in the former, the search space is unchanged and the optimizer merely attempts to minimize the objective function the best possible. Another way to interpret the regularization term is that it enforces the optimizer to prefer particular solutions over others. We provide formulation for redundancy resolution and enforcing stay near axis constraint using the objective function.

7.3.2.1 Redundancy Resolution

The redundancy in the developed system (9 degrees of freedom) can be resolved at the velocity level by introducing a regularization term in the form of $R(\Delta q) = \|\Delta q\|_{\Gamma} = \Delta q^T \Gamma \Delta q$, where $\|\cdot\|_{\Gamma}$ is the generalized norm and Γ is a diagonal matrix with desired weights (penalties) associated with each joint. Presumably any joint is prohibited from moving too fast, resulting in a more controllable motion and increased safety. Additionally, the redundancy available beyond that required for the CM tip motion may be freely used to assist in the realization of some chosen objective. For instance, the weight matrix Γ can be chosen such that for execution of a particular task, specific system joints (e.g. CM joints) are employed more than the rest. This can be achieved by applying a larger penalty (weight) to the joints that should not move as much.

7.3.2.2 Stay Near Axis

The axis range VF mentioned in Section (7.3.1.3) merely restricts the end-effector shaft to remain within a desired conical region. In particular surgical scenarios, however, it may be useful to enforce the end-effector shaft to stay near a desired axis. This can be added to the objective function of (7.2) as a regularization term formulated by:

$$\gamma \|axis_{des}^T (J_{sh}^{\omega} \Delta q + axis_{sh}^k) - 1\| \quad (7.8)$$

CHAPTER 7. SYSTEM INTEGRATION AND EVALUATION

where γ is the damping factor and the goal is to generate configuration space commands at step k that drive the end-effector shaft axis closer to a desired axis. In another scenario, (7.8) can be used as the main objective function to recover from an infeasible optimization problem as will be described in Section 7.3.3.

7.3.2.3 Stay Near Pose

During the performance of a surgical task, it might be desired to bring the system (all or few of the system joints) to the proximity of a desired configuration (q_{des}). Given the configuration of the system at time step k (q^k), this can be formulated in the objective function as:

$$\eta \|\Delta q - (q_{des} - q^k)\| \quad (7.9)$$

7.3.3 Infeasible Problem Recovery Strategy

A common occurring scenario with activated axis range VF is that the optimization problem (7.2) inevitably becomes infeasible when the end-effector shaft axis approaches the boundaries of the cone VF. As such, a recovering strategy must be deployed to drive the system back toward feasible region while still maintaining the constraints such as the RCM. A reasonable strategy is to switch to a secondary control mode where the goal is to escape the infeasible region by bringing the end-effector shaft toward the center of the cone using (7.8) or bringing the system toward the

initial configuration using (7.9). The secondary control mode is achieved by setting either $\gamma = 1$ or $\eta = 1$ in (7.8) and (7.9) and setting $\alpha = 0$ in (7.2) while maintaining the H and h constraints. As soon as the end-effector shaft axis is sufficiently far from the cone boundaries (by measuring the angle from the screw hole axis), the controller can be switched back to the primary mode ($\alpha = 1, \beta = 0, \gamma = 0$) to continue with the main surgical task (i.e. tracing surgical target points).

7.3.4 Feedback

7.3.4.1 CM Feedback

Several strategies were discussed in Chapter 5 for shape sensing and distal-end position estimation (DPE) of the CM used in our developed system. For the purpose of running the evaluation experiments in this chapter, we have incorporated the notched nitinol FBG sensor (described in Section 4.4.2) and used the data-driven linear regression method for DPE and shape reconstruction of the CM (described in Section 5.4.2). In the following sections, we denote the distal-end position estimated from the FBG sensor as p_{fbg} .

7.3.4.2 Robot Feedback

The robot end-effector shaft (actuation unit shaft) pose could potentially be obtained from the forward kinematics, however, the uncertainties due to the backlash

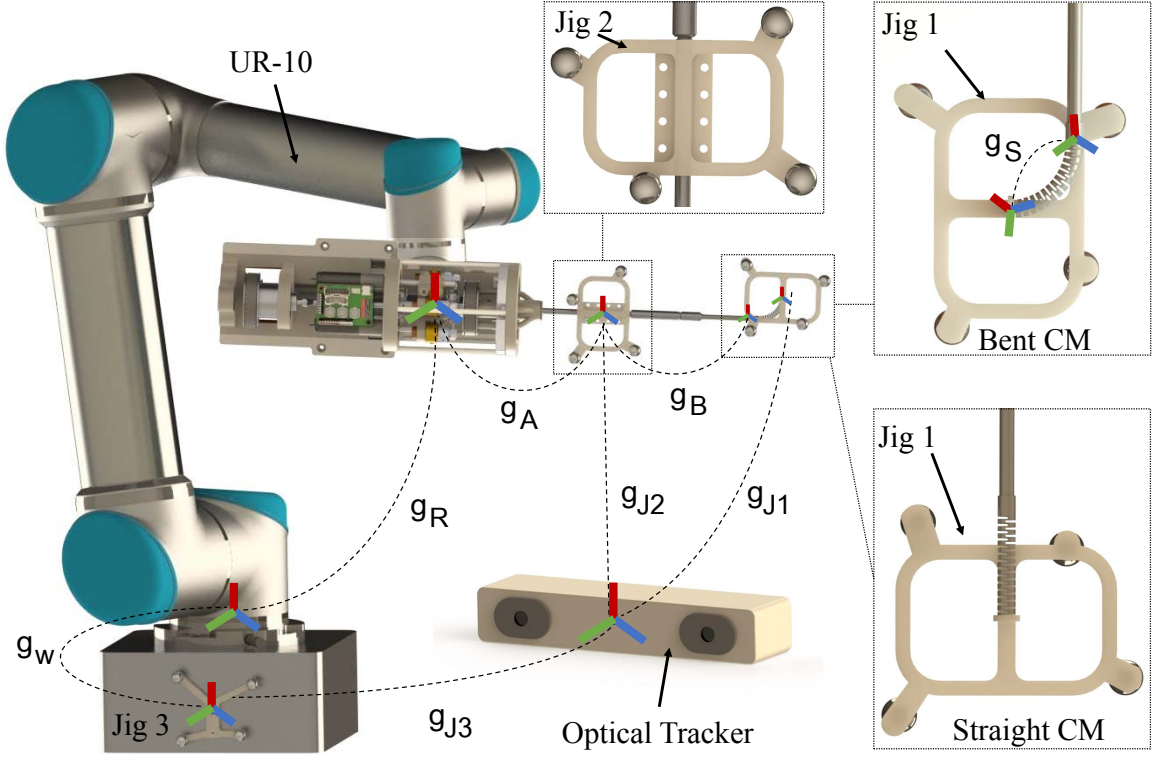


Figure 7.3: Chain of transformations in the system and the custom-designed optical tracker reflective geometries: jig 1 mounted on the distal end of the CM for evaluation purposes, jig 2 mounted on the end-effector shaft, and jig 3 mounted on the base of the robot.

and friction of the actuation unit pulley transmission system can cause inaccuracies in this estimation. Consequently, an optical tracker reflective jig is mounted on the end-effector shaft for direct measurement of the pose (jig 2 in Fig. 7.3). To reduce measurement uncertainties, a Butterworth low-pass filter has been incorporated that rejects the unwanted high frequency components of the received signal. The system tip position expressed in the robot base frame, x_{tip}^k , can be found at time step k by establishing appropriate coordinate frames. Given the immediate goal point at this time step, x_{goal}^k , and incorporating a PD controller to tame the behavior in presence

CHAPTER 7. SYSTEM INTEGRATION AND EVALUATION

of disturbance and overshoot, the Δx_{obj}^k can be found by:

$$\begin{aligned} x_{tip} &= g_{J3}^{-1} \cdot g_{J2} \cdot g_B \cdot p_{fbg} \\ \Delta x_{des}^k &= x_{goal}^k - x_{tip}^k \\ \Delta x_{obj}^k &= k_p \Delta x_{des}^k + k_d (\Delta x_{des}^k - \Delta x_{des}^{k-1}) \end{aligned} \tag{7.10}$$

where k_p and k_d are the proportional and derivative gains, respectively.

7.3.5 System Jacobian

The overall system Jacobian can be written as $J_s = [J_r \ J_a \ J_c]$, where the subscripts r , a , and c correspond to the UR-10 robot, the actuation unit roll joint, and the CM, respectively. We derived the geometrical linear and angular components of the Jacobian (J^v and J^ω) as instructed in [216]. Since all the joints of the UR-10 and the actuation unit are revolute, for the i^{th} joint (and the associated column in the Jacobian) we can write:

$$\begin{cases} J^{v_i} = z_i \times (o_r - o_i) \\ J^{\omega_i} = z_i \end{cases} \tag{7.11}$$

where o_r is the location of a desired point r where the Jacobian is resolved at, and z_i and o_i are the axis and spacial position of the revolute joints expressed in the robot base coordinate frame. To find these parameters, note that for the six UR-10 joints (J_r) the DH parametrization of the forward kinematics (g_R) is used, whereas for the

CHAPTER 7. SYSTEM INTEGRATION AND EVALUATION

roll joint on the actuation unit (J_a) direct measurements from the optical tracker reflective jig (jig 2 in Fig. 7.3) is used to decrease uncertainties and errors due to backlash and friction.

The CM Jacobian was extensively discussed in Chapter 6. For better numerical stability and enhanced performance of the overall system, we derived a kinematics-based (model-dependent) Jacobian for the CM (described in Section 6.3.2) and used that Jacobian as the baseline for the concurrent system control. Of note, the derived kinematics-based Jacobian in Section 6.3.2 was described with respect to the coordinate frame attached to base of the CM. To express this Jacobian in the robot base coordinate frame, the rotation matrix between the base of the robot and the base of the CM (R_C^R) is applied to this matrix to find $J_c^v \in \mathbb{R}^{3 \times 2}$. Clearly, bending of the CM does not alter the orientation of the end-effector shaft and therefore $J_c^\omega = 0_{3 \times 2}$.

7.3.6 CM Position Homing

For automatic setup of the system, a position *homing* based on cable tension force has been incorporated such that the Maxon motors' *zero* positions are set when the CM cable tension has reached a desired pre-tension force, e.g. F_h . Even though the *zero* position for the Maxon motors could be achieved by manual controlling of the cables to the point right before the CM starts bending, such a capability automates the process and simplifies the system setup procedure.

7.4 Software

7.4.1 Architecture

All the software has been developed in C++ for real-time purposes. The CISST open-source multi-tasking library [149] was used for thread-safe parallel communication between different components of the system, i.e. the UR-5, the CM actuation motors, the flexible instrument motor, the FBG sensing interrogator, and the controller. The controller was implemented as a mid-level periodic task sitting in between the surgeon’s high-level control input through the GUI and the low-level controller tasks associated with the UR-10, and the actuation unit’s motors for the CM cables and the flexible instruments. The controller task obtains the system’s joints states and the sensory information (FBG and optical tracker) from the respective device-specific task, then sets up and solves the optimization problem and sends the commands to UR-10 and Maxon motor low-level controllers through their designated tasks. A custom C++ interface performed low-level velocity control of the Maxon motors while the UR-10 low-level control was implemented by writing a client application (URScript) and connecting to URControl using a TCP/IP socket.

7.4.2 GUI Design

For intuitive and easy interaction of the surgeon with the system during the surgical procedure, a main GUI containing all the information about the system state, the controller status, and the surgical plan (a list of target points) was developed. Additionally, a separate panel provided the surgeon with full control over activation of their desired constraints, configuration of the parameters associated with the constraints, and execution of the surgical plan. At any point during the surgery, the surgical plan could be modified or altered altogether, and the execution of the plan could be paused or continued with the surgeon's supervision. Other GUI tabs were also developed for direct control capability of the CM and UR-10, if desired. Fig. 7.4 demonstrates the developed GUI components.

7.4.3 Visualization

To assist the surgeon with better overview of the surgical task execution, a VTK-based [217] visualization window containing the patient's preoperative computed tomography (CT) overlaid with the planned target trajectory, the RCM point and the current system tip position was developed in C++. The visualization is synced with the controller and the system state is demonstrated to the surgeon in real-time. Fig. 7.5 shows this window during the execution of a surgical task.

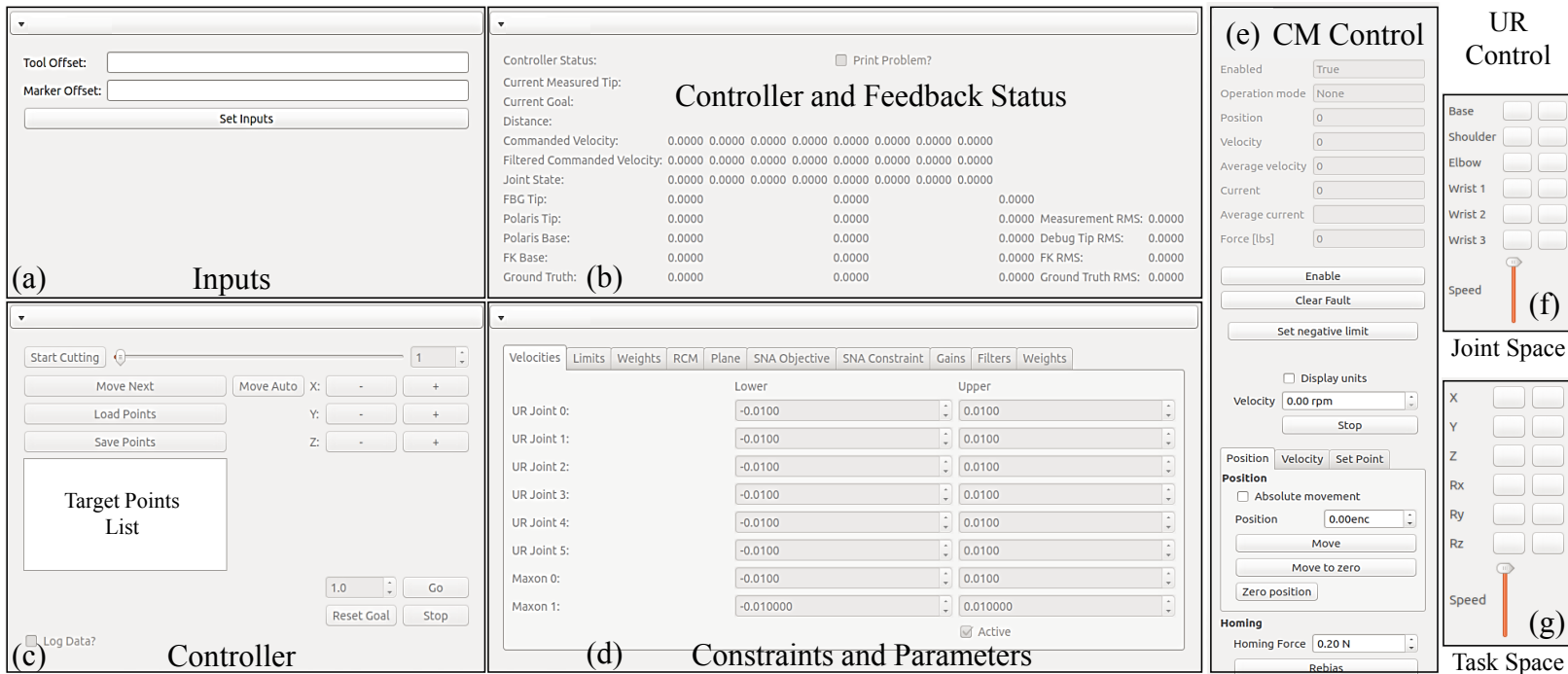


Figure 7.4: The developed GUI. (a) Surgical inputs, (b) controller and feedback status window, (c) control window for starting/pausing the instrument as well as adjusting the motion speed and the surgical target points, (d) constraints and parameters window, (e) manual position and velocity control of the CM window, (f) manual UR control in joint space, (g) manual UR control in task space

7.4.4 Simulation

To evaluate the proposed controller and realize the appropriate combination of constraints imposed during a surgical scenario, a complete simulation framework was developed using the robot simulator CoppeliaSim (formerly V-REP) [218]. The constraint control framework (Section 7.3) was implemented in Python and the solution was communicated with the simulator using the Python remote API to update the simulation. While for the physical system, both the UR-5 and UR-10 were used for the evaluation experiments, For the purpose of the simulation framework, a UR-5 robot was used as the positioning robot and its forward kinematics and Jacobian were implemented using (7.11) [219]. For the simulation visualization, the CM was modeled as a 27-revolute-joint mechanism and given any actuation cable length, first the tip position (p) was computed from (6.5) and then a constrained optimization inverse kinematics was incorporated to solve for the joint angles:

$$\begin{aligned}
 & \underset{\Theta_c}{\text{minimize}} && \|p - f(\Theta_c)\| \\
 & \text{subject to} && \Theta_c \leq \Theta_{max} \\
 & && f_x = d.(\sum_{i=1}^{27} \sin(\sum_{j=1}^i \Theta_j)) \\
 & && f_y = d.(\sum_{i=1}^{27} \cos(\sum_{j=1}^i \Theta_j))
 \end{aligned} \tag{7.12}$$

where $\Theta_c \in \mathbb{R}^{27}$ is the CM joint angles, $d = L_c/27$ is the distance between two consecutive joints, $f(\Theta_c) : \Theta_c \rightarrow \mathbb{R}^2$ is the CM forward kinematics mapping from joint

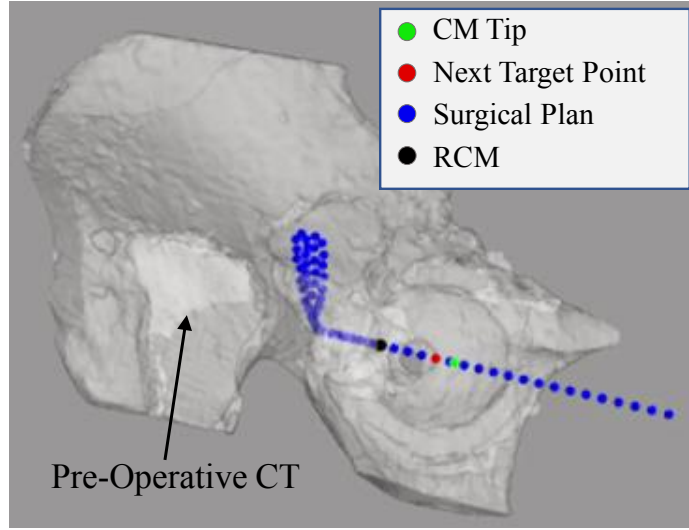


Figure 7.5: The visualization window for intraoperative navigation.

space to task space, and Θ_{max} is the maximum angle each joint can take and is chosen as 7.9 degree [22]. The simulation framework enables easy integration of any number of the constraints described in Section 7.3. This is an extremely helpful approach and a cost-free first step in realizing the necessary constraints and parameters associated with any surgical procedure. Additionally, implementation debugging can take place much faster within the simulation framework compared to the physical system.

7.5 Preoperative Clinical Steps

The preoperative clinical steps include calibration and registration procedures. In this section, we describe each of these procedures in the context of the robot-assisted pelvic osteolysis.

CHAPTER 7. SYSTEM INTEGRATION AND EVALUATION

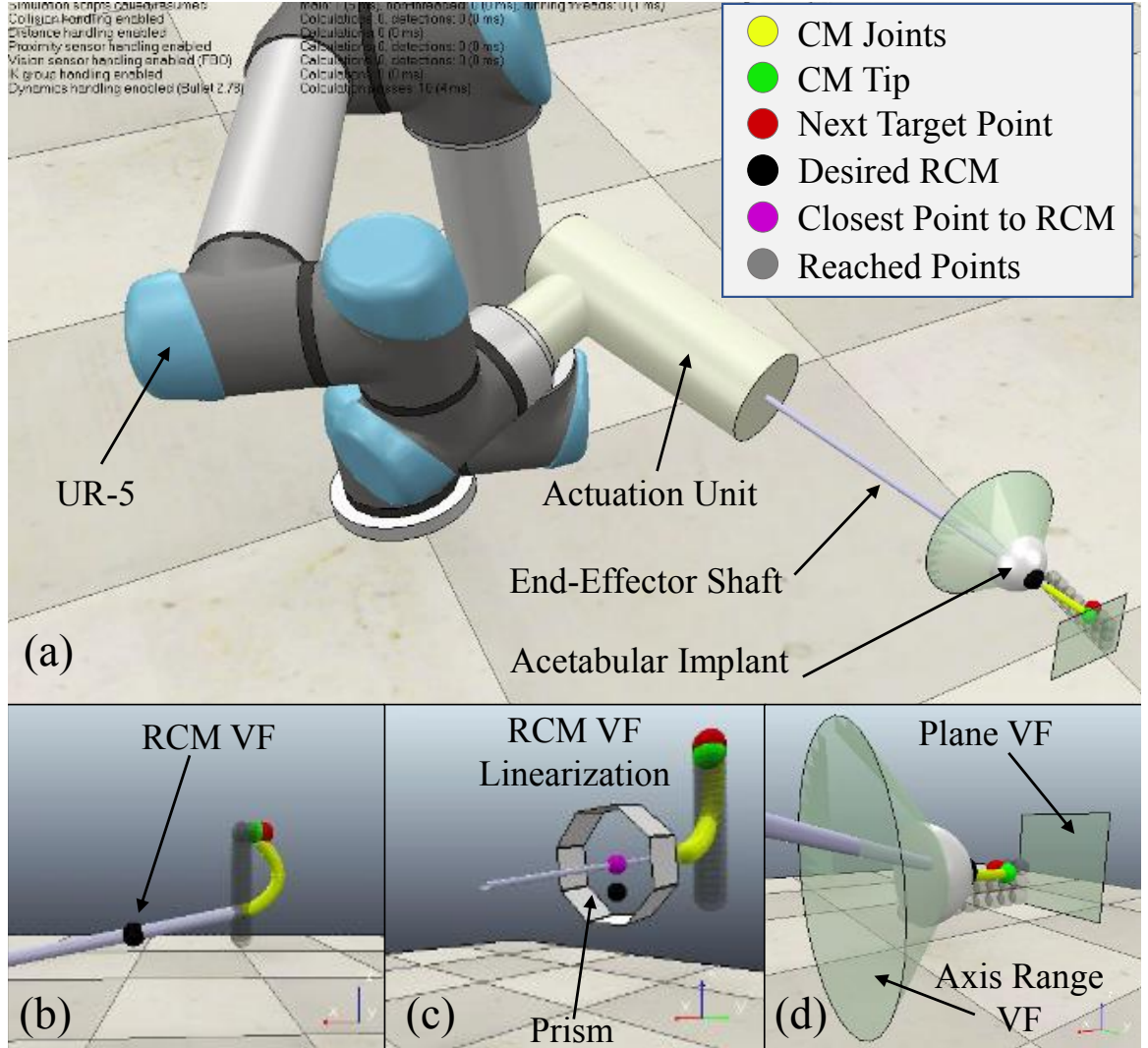


Figure 7.6: The developed simulation environment. (a) accurate models of the positioning robot, the actuation unit, the acetabular implant, and the CM, (b) robotic system satisfying the RCM constraint, (c) the linearized RCM constraint using a prism with 8 faces and the closest point to the RCM on the end-effector shaft, (d) the axis range and plane VF.

7.5.1 Hand-eye Calibration

To complete the forward kinematics of the system, the relationship between the robotic system (hand) and the optical tracker (eye) must be known. For this purpose, first an optical tracker reflective jig (jig 3 in Fig. 7.3) was mounted at the base of the positioning robot which serves as the fixed (*world*) coordinate frame. Next, the transformation associated with the actuation unit, g_A (transformation between the positioning robot's end-effector and jig 2 mounted on the actuation unit's shaft), as well as the transformation between the world reference geometry and the base of the positioning robot (g_W) were obtained by performing a hand-eye calibration. The chain of transformations (see Fig. 7.3) can be written as:

$$g_R \underbrace{g_A}_{Unknown} = \underbrace{g_W}_{Unknown} g_{J3}^{-1} g_{J2} \quad (7.13)$$

To solve this problem, the unknown g_w is written with respect to g_A by taking an observation from the optical tracker and robot's forward kinematics (observation denoted by superscript o):

$$g_W = g_R^o g_A (g_{J2}^o)^{-1} g_{J3}^o \quad (7.14)$$

Substituting (7.14) in (7.13) and rearranging:

$$\underbrace{(g_R^o)^{-1} g_R}_A \underbrace{g_A}_X = \underbrace{g_A}_X \underbrace{(g_{J2}^o)^{-1} g_{J3}^o g_{J3}^{-1} g_{J2}}_B \quad (7.15)$$

which is the conventional $AX = XB$ problem with solutions proposed in [220, 221]. To find the solution, the robot must be moved to various configurations and in each configuration the known transformations g_R , g_{J3} , and g_{J2} are saved and used for solving the problem. Next, the solution for g_A can be substituted in (7.13) to solve for g_W to obtain a complete known chain of transformations.

7.5.2 Registration

In the envisioned surgical scenario, the surgical plan is determined by the surgeon preoperatively on the patient's CT scan. The CT entails additional information such as the RCM location, axis of the screw hole, and the geometry of the lesion, all expressed in the CT coordinate frame. In order to use this information intraoperatively, the preoperative CT and the robotic system must be registered to the patient. To do so, a 3-D point cloud is collected by digitizing the surface of the acetabular implant as well as the surface of any exposed part of the surrounding bone. A digitization tool such as the one shown in Fig. 7.7 can be used to form this point cloud which is expressed in the *world* coordinate frame (jig 3 in Fig. 7.3).

An iterative closest point (ICP) approach is incorporated to compute the transformation that relates the collected point cloud to the associating mesh surface on the CT. The first step is to compute an initial registration (T_0) guess for the algorithm. This is done by selecting a couple of points on the screw holes of the implant (Fig. 7.14) in the CT (P_{ct}) and digitizing the same points on the patient with respect

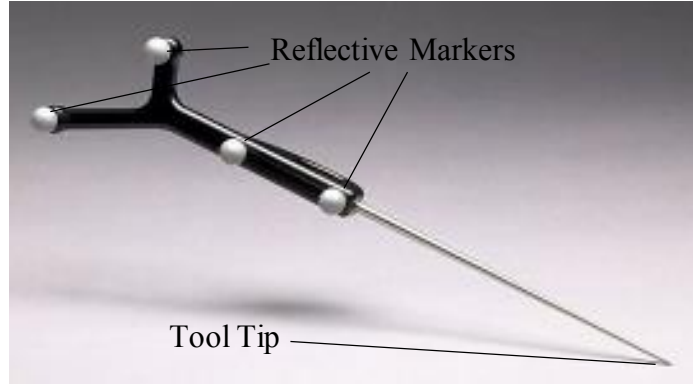


Figure 7.7: Example of a digitization tool with reflective markers used for registration.

to the *world* coordinate frame (P_w):

$$\underset{T}{\text{minimize}} \quad \sum_{i=1}^n \|P_w^i - T_0(P_{ct}^i)\| \quad (7.16)$$

where $T_0 \in SE(3)$ is the initial homogeneous transformation guess that maps features described in the CT frame to the *world* coordinate frame and $n = 4$ for the initialization step. Next, as many points as possible are digitized from the surface of the acetabular implant and the surrounding bone. These points are transformed by T_0 and the closest mesh to each of these transformed points are found. A quaternion approach [222] is used to solve (7.16) for the next best transformation (T_1). The process of finding closest point-surface pairs and updating the transformation is repeated iteratively until the algorithm converges (within the order of a few seconds) and the final registration is found (T_{regi}). The stopping criteria is defined as $\epsilon \leq d_{i+1}/d_i \leq 1$, where d_i is the mean surface distance at step i and $\epsilon = 0.999$ is the stopping tolerance.

7.6 Experiment Design and Evaluation Criteria

To evaluate the performance of different components of the developed system in the less-invasive treatment of pelvic osteolysis, several experiments are designed and performed in simulation, phantom, and human cadaver. The simulation environment (Fig. 7.6) serves as an initial test-bed for implementation, debugging, tuning and evaluating the optimization control framework, as well as characterization of the developed system in workspace coverage and dexterity. It incorporates the exact Jacobian derivation and physical properties of the UR positioning robot and the CM as outlined in Section 7.3. One of the main advantages of the simulation framework is that the experiments can be performed safely without any cost or potential damage to the physical system. Moreover, various control strategies could be realized and evaluated quickly.

In addition to simulation, various phantom experiments are carried out to evaluate the performance of different components of the system. To accurately mimic the real surgical scenario of the less invasive treatment of pelvic osteolysis, a phantom model is obtained by performing a segmentation on a human cadaver with an outlined lesion cavity behind the acetabular cup implant created by a clinical collaborator. The phantom model is 3-D-printed (Fig. 7.8) and hard saw-bone phantoms simulating lesions are mounted in difficult-to-reach locations behind the implant. The phantom

CHAPTER 7. SYSTEM INTEGRATION AND EVALUATION

experiment goals are:

1. Testing and further tuning of the controller on the physical system.
2. Exploration of the outlined lesion cavity while maintaining the constraints.
3. Debridement of the simulated saw-bone phantoms.

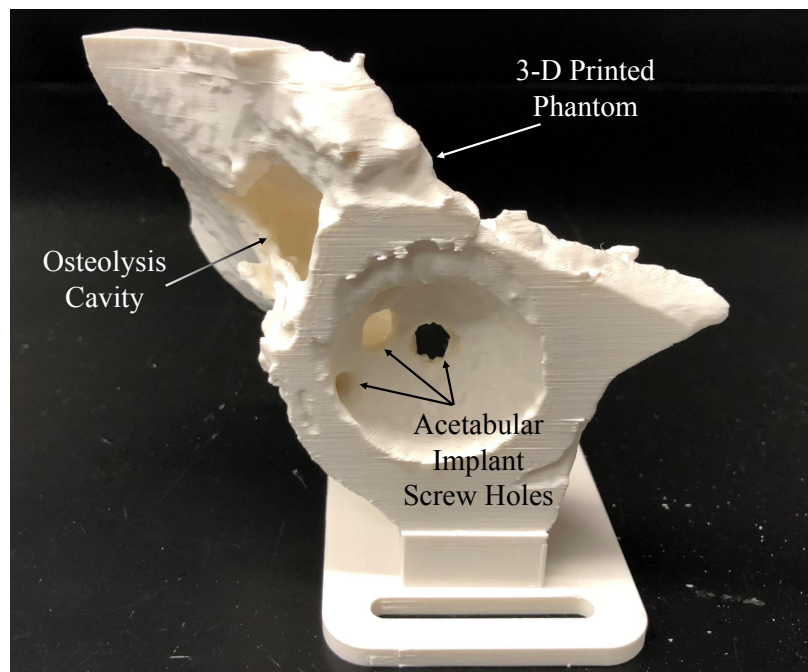


Figure 7.8: Osteolysis phantom 3-D printed from segmented CT.

The final sets of experiments are carried out on a human cadaver with an outlined lesion cavity created by our clinical collaborator who has previously performed conventional treatment of pelvic osteolysis behind the acetabular implant. The goals of the human cadaver experiments are:

CHAPTER 7. SYSTEM INTEGRATION AND EVALUATION

1. Performing and realizing the complete preoperative clinical steps for calibration, registration, and system preparation.
2. Demonstrating the feasibility to reach extremely difficult locations behind the cup by inserting the CM through the implant's screw hole.
3. Full comparison of the reach and workspace behind the implant by conventional rigid tools (e.g. curettes) and our developed system.
4. Drilling/milling of simulated and real bone behind the implant while concurrently controlling the system and maintaining the constraints.

Of note, the UR-5 positioning robot is used for the simulation experiments, while the UR-10 is used for the cadaver experiments. The phantom experiments are performed both with the UR-5 and the UR-10 robots. We evaluate our system's performance from different perspectives, discussed in the following sections:

1. Constrained workspace and reach in confined spaces.
2. Dexterity and manipulability.
3. Constrained controller performance.
4. Sensing accuracy.
5. Planning and debridement performance.

7.6.1 Constrained Workspace

In typical use-case of the system, the motion is subject to constrained such as maintaining the RCM and/or limiting the end-effector's shaft axis range. We refer to the workspace of the system with such constraints as the *constrained workspace* throughout the thesis, which is evaluated both in simulation and human cadaver experiments in various constrained scenarios. In addition, we demonstrate how far behind the acetabular implant can be reached by only bending the CM while fixing the robot's end-effector shaft axis aligned with the screw hole axis (i.e. stationary positioning robot). The system's constrained workspace is compared to a conventional rigid curette passed through the screw hole of the implant.

7.6.2 Dexterity and Manipulability

Conventionally, Yoshikawa's manipulability index [223] has been used as a measure for dexterity of manipulators:

$$\omega(q) = \sqrt{\det(J(q)J^T(q))} \quad (7.17)$$

where $J(q)$ is the unconstrained Jacobian of the manipulator as a function of joints' state q . This measure, however, cannot be directly applied to our system when it is subject to the RCM constraint. Sadeghian et al. [224] previously derived the constrained Jacobian and manipulability index for systems subject to RCM constraint.

CHAPTER 7. SYSTEM INTEGRATION AND EVALUATION

The constrained Jacobian (J_d) is formulated as:

$$J_d = J_s T \begin{bmatrix} I_{n-3} \\ -\underbrace{J_{RCM,II}^{-1} \cdot J_{RCM,I}}_A \end{bmatrix} \quad (7.18)$$

where T is a permutation matrix to rearrange the system's joints order such that $J_{RCM,II} \in \mathbb{R}^{3 \times 3}$ is invertible, I is the identity matrix and J_s is the system Jacobian defined in (7.1). Furthermore, the constrained manipulability ellipsoid and measure could be formulated as [224]:

$$\begin{aligned} \dot{x}_{tip} \underbrace{(J_d J_d^T)^{-1} J_d (I + A^T A) J_d^T (J_d J_d^T)^{-1}}_B \dot{x}_{tip} &= 1 \\ \omega(q) &= \frac{|det(J_d J_d^T)|}{\sqrt{det(J_d (I + A^T A) J_d^T)}} \end{aligned} \quad (7.19)$$

where the eigenvectors of B define the principal axes of the ellipsoid and the eigenvalues of B are the reciprocals of the squares of the ellipsoid's semi-axes, a^{-2} , b^{-2} , and c^{-2} . The manipulability ellipsoid volume is subsequently computed by:

$$v = \frac{4}{3} \pi abc \quad (7.20)$$

7.6.3 Constrained Controller

The concurrent constrained control framework is implemented in simulation (Python) and on physical hardware (C++). Different combinations of objectives and constraints are tested and evaluated. Moreover, the best combination of constraints in a

CHAPTER 7. SYSTEM INTEGRATION AND EVALUATION

practical surgical scenario is studied and strategies for avoiding or recovering from an infeasible optimization problem are provided. The capability of the system in maintaining the constraints is studied and the best parameters for tuning the optimization framework are presented.

7.6.4 Sensing

The system's sensing module is evaluated against ground-truth data in several experiments. This is done in two separate steps: 1) evaluating the performance of the FBG sensor to estimate the tip position of the CM both in free and constrained environments where the CM is interacting with obstacles at various locations along its body, and 2) evaluating the overall system tip position with respect to the base of the UR-10 by combining information from the FBG sensor and the optical tracker reflective jig 2. As outlined in Section 7.3.4, the ground truth data for the tip position is obtained by mounting an optical tracker reflective jig on the CM distal end (jig 1 in Fig. 7.3). It must be noted that the hand-eye calibration (Section 7.5.1) procedure is implicitly assessed in the above-mentioned evaluation process, as it is the bridge between the optical tracker (end-effector shaft pose) and FBG data (CM shape).

7.6.5 Planning and Debridement Performance

As part of the preoperative planning, the registration of the preoperative CT to the phantom and the human cadaver must be performed. To do so, as outlined in Section 7.5.2, the surface of the 3-D printed model in the phantom study and the acetabular implant and the surrounding bone in the human cadaver study are digitized using an optical tracker digitization tool (Fig. 7.7). The registration process is then performed and consequently, any planning on the preoperative CT could be expressed in the robot base coordinate system. With the use of the flexible debridement instruments and the concurrent control of the developed system, we then demonstrate that it is possible to perform drilling and milling tasks both on simulated saw-bone phantom and human cadaver hard bone in confined spaces. This is demonstrated in two locations in the human anatomy, namely pelvic and femur. The former is explored during the less-invasive treatment of pelvic osteolysis behind the acetabular component, whereas the latter is explored in core decompression of the femoral head osteonecrosis while the CM is confined by the surrounding bone.

7.7 Results

7.7.1 Constrained Workspace

The maximum reach behind the acetabular implant using a conventional rigid curette is compared with our developed system in Figs. 7.9(a) and 7.9(b). It should be noted that such dexterity and reach in our system was achieved by only articulating the CM and fixating the UR-10 end-effector's axis stationary and aligned with the screw hole axis, while the curette's handle was unconstrained. Even with such a restricting constraint, points on the back surface of the implant were reachable by our system whereas the curette's range of exploration was quite limited.

The constrained workspace of our system was compared to that of a rigid instrument such as a curette quantitatively in thorough simulation studies. An acetabular cup implant mesh with outside diameter of 50 mm, rim edge thickness of 5 mm, and screw hole diameter of 8 mm was imported in simulation. The desired target area was chosen as a cubic region extended 50 mm deep behind the acetabular implant and covering the entire back surface of the implant (Fig. 7.9(c) and Fig. 7.9(d)). Discretization of this region with 8 mm increments resulted in 264 target points. The RCM constraint was activated and the axis range VF with two different maximum allowable deviation angles ($\phi_a = 30^\circ, 45^\circ$) were applied to the end-effector shaft of the robotic system as well as the handle of the rigid tool. Additionally, five hyperplane VFs were set at the boundary faces of the target region to avoid the CM from protrud-

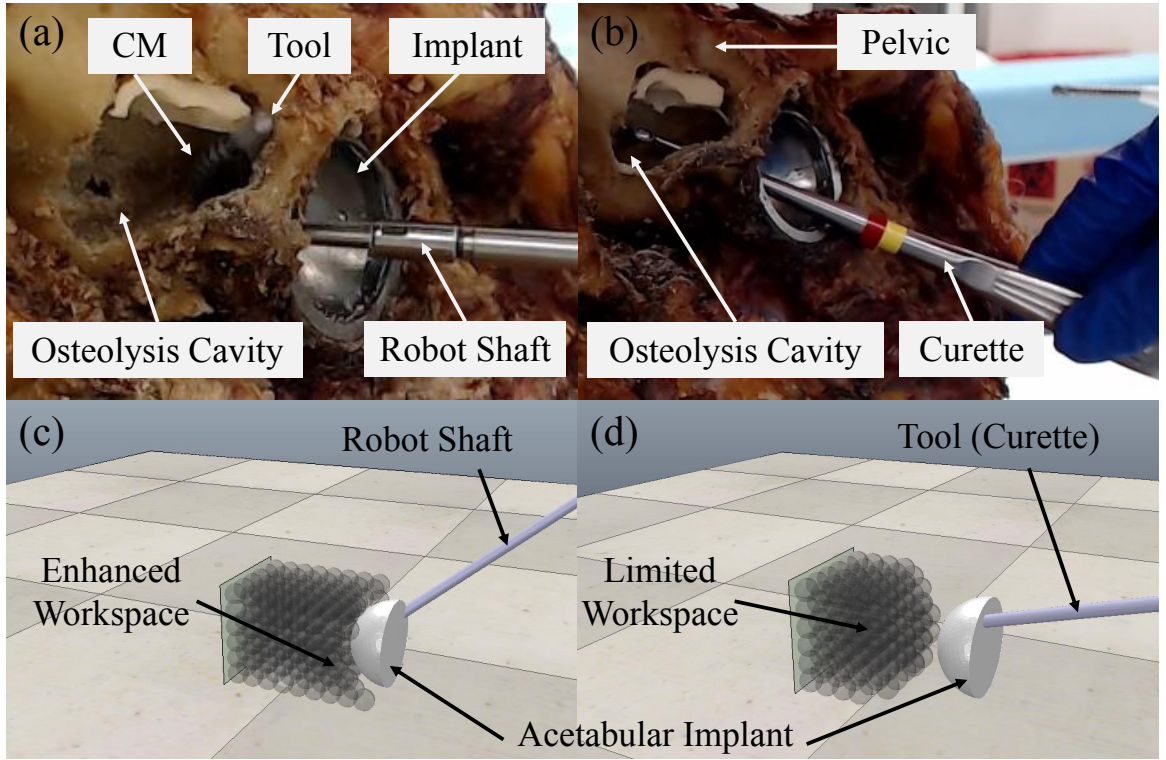


Figure 7.9: Workspace comparison of the developed dexterous robotic system and rigid tools such as a curette in (a) and (b) during cadaver experiments, and in (c) and (d) during simulation experiments.

ing beyond this region. The robotic system and the rigid tool poses were initialized randomly with their axes aligned with the axis of the implant's screw hole. Each target point was flagged as successfully traversed whenever the tip position reached the 2 mm neighborhood of the point, which is a realistic threshold for orthopaedic applications. The ϵ value for the RCM constraint (7.3) was chosen as 1 mm to account for the wiggle room between the CM and the implant's screw hole. If before reaching a target point, the robotic system or rigid tool got to the cone VF boundary (infeasible optimization problem) the controller was switched to the secondary mode to recover from the infeasible situation. For each target point, the controller or rigid

CHAPTER 7. SYSTEM INTEGRATION AND EVALUATION

Table 7.1: Comparison of the workspace coverage behind the implant for robotic system and rigid tool subject to axis range virtual fixture

	Robotic System	Rigid Tool
Axis Range VF (30)	91%	54%
Axis Range VF (45)	98%	71%

tool were allowed to switch to secondary control mode at most three times, otherwise the target point was flagged as unreachable. Table 7.1 summarizes the results for the constrained workspace analysis.

7.7.2 Dexterity and Manipulability

To measure the constrained dexterity and manipulability of our system in confined spaced, we performed experiments in simulation where the system is concurrently controlled behind the acetabular implant while the RCM constraint was active. A set of target goal points were passed to the controller such that the system was enforced to approach the immediate points behind the implant. The goal of this experiment was to demonstrate how the constrained manipulability ellipsoid (7.19) evolves over time as the system's tip approaches the vicinity of the implant. The constrained manipulability measure and the ellipsoid volume were compared for the combined system (UR-5 and CM) and only the UR-5 end-effector shaft without the CM. Fig. 7.10 shows the evolution of the constrained manipulability ellipsoid for the combined system as the system approaches the difficult-to-reach points behind the implant. Figs. 7.10(a) and 7.10(b) indicate the quantitative evolution of the

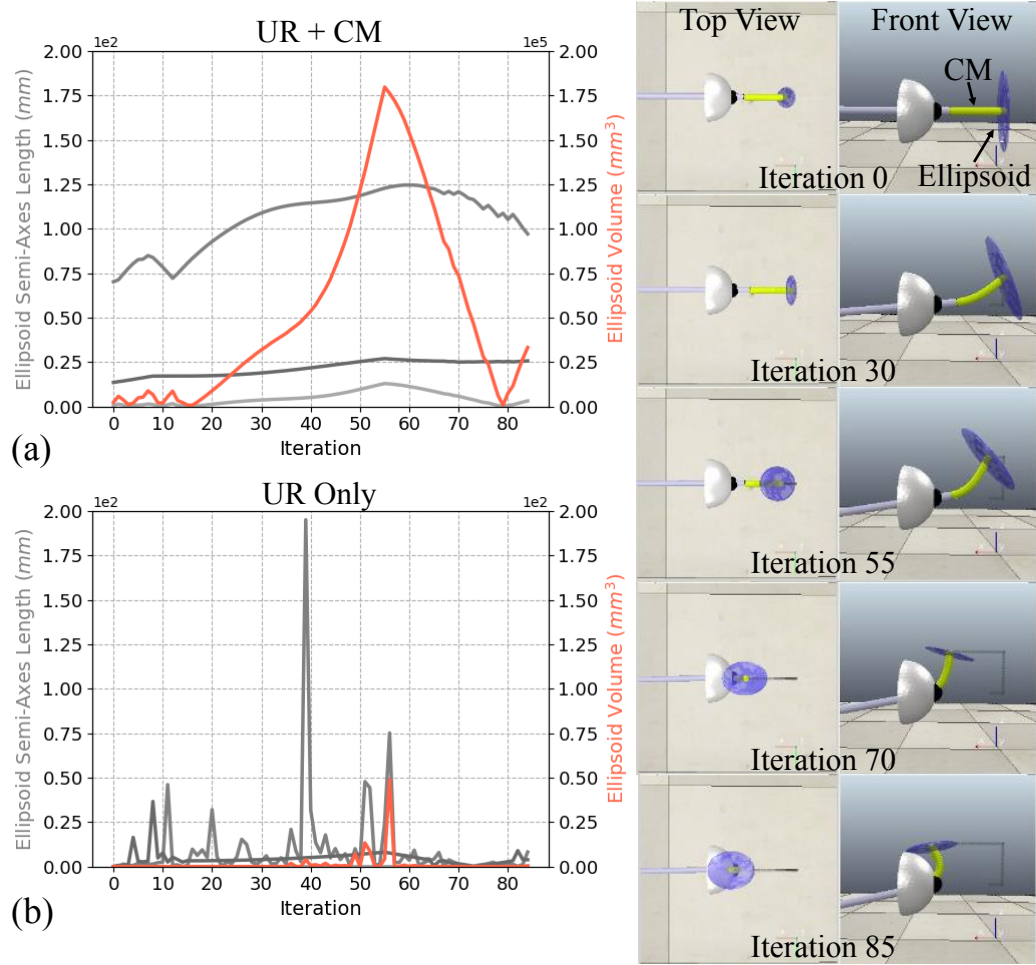


Figure 7.10: The constrained manipulability ellipsoid volume and semi-axes lengths for (a) combination of UR and CM, and (b) UR only. Figures on the right show snapshots of the evolution of the manipulability ellipsoid for the combination of UR and CM.

constrained manipulability volume (red curves) as well as the three principal semi-axes of the ellipsoid (gray curves) for the combined system (UR-5 and CM) and the UR-5 only, respectively. Table 7.2 summarizes the results for the constrained manipulability index (7.19) and constrained manipulability ellipsoid volume (7.20) for the combined system and UR-5 only without the CM.

Table 7.2: Constrained Manipulability Index Comparison

Constrained Manipulability Index				
System	Mean	Std. Dev.	Max	Min
UR Only	8.42 e-17	1.63 e-16	7.53 e-16	1.23 e-50
UR + CM	1.31 e-05	1.28 e-05	4.29 e-05	1.85 e-07

7.7.3 Constrained Controller

The constraints mentioned in Section 7.3 are tested in execution of different surgical plans in reaching desired surgical points behind the acetabular cup implant. Results for maintaining RCM, axis range VF, hyperplane VF, and velocity and joint limit constraints are presented during exploration of the workspace behind the implant. Fig. 7.11(a) shows the distance between the desired programmed RCM point and the closest point to the RCM on the robot's end-effector shaft (7.3). As observed, this distance remains below the specified threshold of 1 mm throughout the execution of the experiment. Fig. 7.11(b) demonstrates the angle between the robot's end-effector shaft and the implant's screw hole axis, which stays below the specified threshold of 45 degrees. Fig. 7.11(c) displays the path traversed by the tip of the CM bounded by the five hyperplane constraints. Table 7.3 summarizes the used joint velocity and position limits. The PD controller parameters were determined experimentally as $k_p = 0.4$ and $k_d = 0.1$ to avoid possible overshoot of the controller.

Sample trajectory tracking scenarios with these control parameters have been demonstrated in Fig. 7.12. In particular, the controller was tested during path fol-

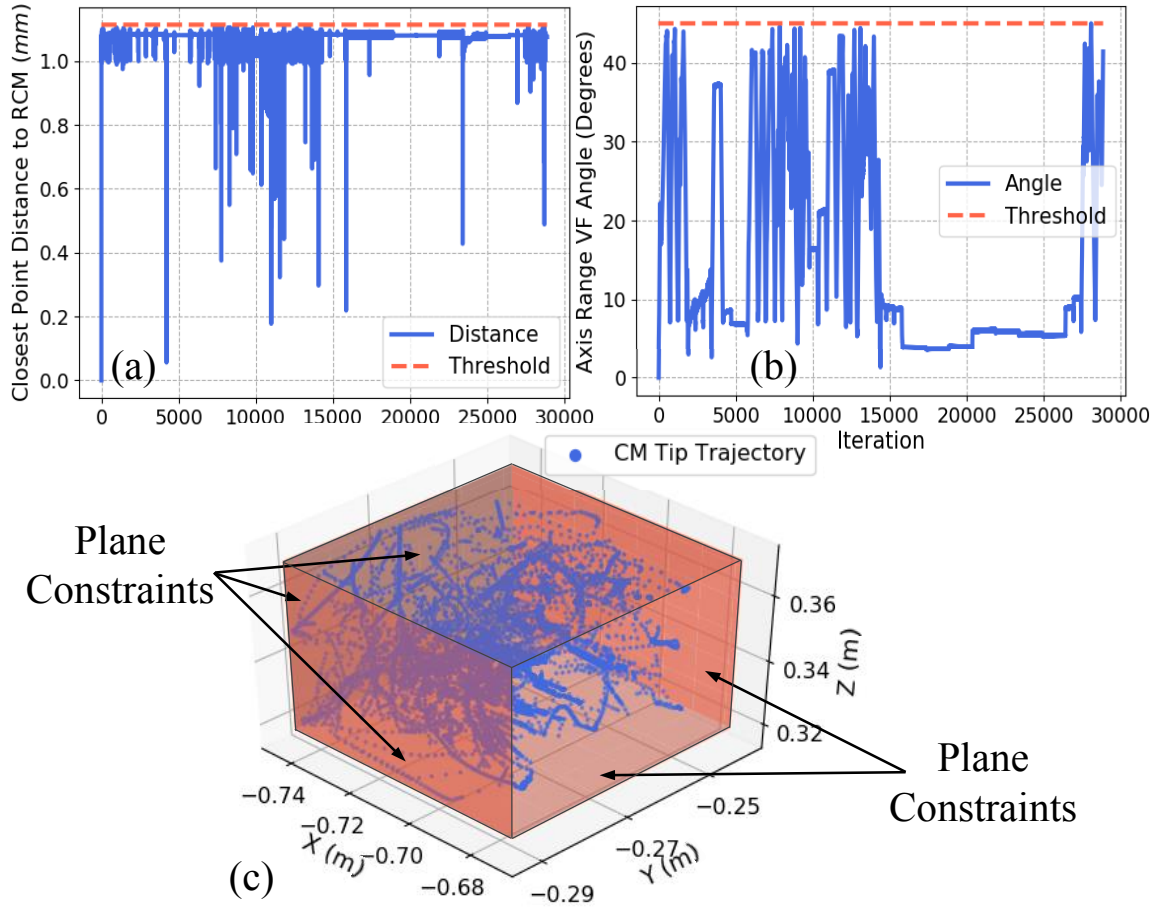


Figure 7.11: Performance of the controller in maintaining the constraints: (a) RCM VF, (b) axis range VF angle, (c) plane constraints bounding the CM's tip position.

lowing of a spiral (Fig. 7.12(a)), a circle (Fig. 7.12(b)), a cube (Fig. 7.12(c)), a surgical plan tracing the entire surface of the osteolysis lesion cavity outlined in the preoperative CT (Fig. 7.12(d)), and a surgical plan for surface debridement of hard sawbone phantom behind the acetabular implant (Fig. 7.12(e)). Using a goal reaching threshold of 1.5 mm, the mean, standard deviation, and maximum error in tracking accuracy for these experiments were 1.47 mm, 0.02 mm, and 1.49 mm, respectively.

Table 7.3: Comparison of Joint Limits in Simulation and Hardware

		UR Joints	Roll	CM
Position Limit	Simulation	$\pm 2\pi$ (rad)	$\pm 2\pi$ (rad)	0-10 (mm)
	Hardware	$\pm 2\pi$ (rad)	$\pm 2\pi$ (rad)	0-7 (mm)
Velocity Limit	Simulation	$\pm 5\text{e-}3$ (rad/s)	$\pm 5\text{e-}2$ (rad/s)	$2\text{e-}1$ (mm/s)
	Hardware	$\pm 3\text{e-}3$ (rad/s)	$\pm 3\text{e-}3$ (rad/s)	$5\text{e-}1$ (mm/s)

7.7.4 Sensing

To evaluate the accuracy of the FBG sensor in estimating the CM tip position, a total of 19 experiments are carried out, 10 of which are in free environment and the other 9 include an obstacle located randomly along the length of the CM's body (Fig. 7.13). A total of 68306 and 61642 samples were collected in the free and obstacle experiments, respectively. The data-driven method outlined in Section 7.3.4 is trained and tested against this data-set with k-fold cross validation. The data-set is split randomly into 80% training and 20% testing data with respect to the number of overall experiment sets and the trained model is tested against the testing data-set ($k = 5$). The tip position estimation error mean and standard deviation of all the 5-fold split combinations are 0.37 mm and 0.12 mm, respectively. In the worst case, the mean, standard deviation, and maximum tip position error is 0.58 mm, 0.27 mm, and 0.88 mm, respectively.

The tip position estimation obtained from the FBG sensor is expressed with respect to the base of the CM. Combining this information with the end-effector shaft

CHAPTER 7. SYSTEM INTEGRATION AND EVALUATION

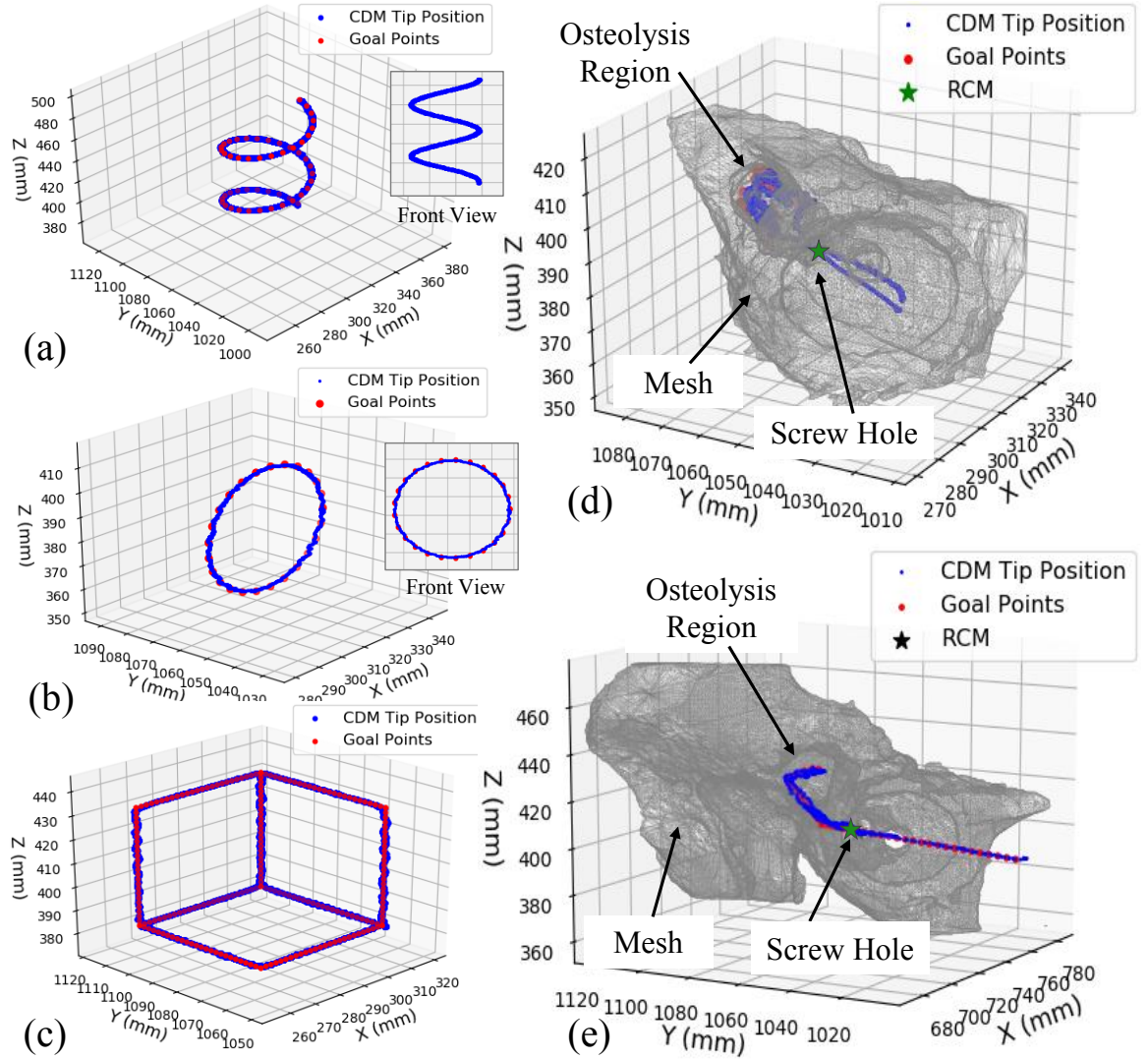


Figure 7.12: Controller performance in executing various motions and surgical plans. (a) a spiral motion, (b) circle, (c) cube, (d) tracing the surface of the outlined osteolysis lesion on the preoperative CT, (e) executing the surgical plan during debridement of hard sawbone phantom

pose obtained from the optical tracker reflective jig 2 (Fig. 7.3) and the transformations obtained from the hand-eye calibration, the CM tip position can be expressed with respect to the base of the entire robotic system and used as feedback in the controller framework (Section 7.3). To evaluate the accuracy of the entire system tip

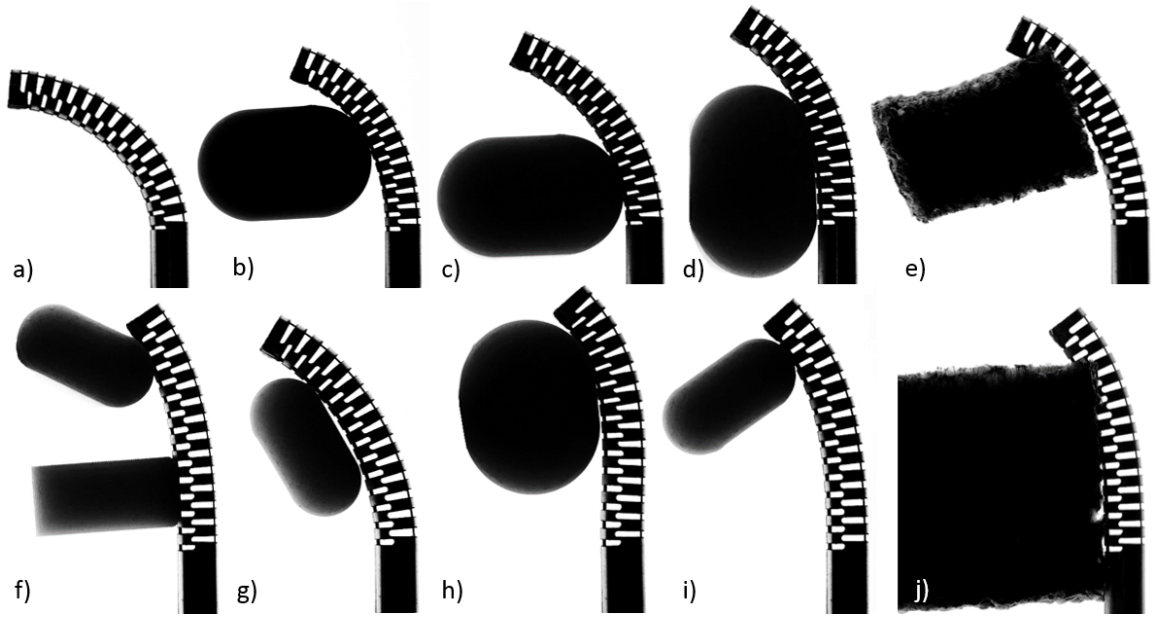


Figure 7.13: Experiments: (a) CM bending in free space, (e) and (j) colliding with soft obstacle, and colliding with hard obstacles (remaining cases).

position estimation, the CM and the positioning robot were moved concurrently in the vicinity of the desired workspace and ground-truth data was obtained by direct sensing of the CM tip position with respect to the base of the robot. The mean and standard deviation of the entire system tip tracking error are 0.50 mm, and 0.18 mm, respectively, with maximum error of 1.46 mm. Such precision in TPE for the entire robotic system provides accurate real-time feedback to the controller when bringing the system tip position to the desired surgical target points.

7.7.5 Planning and Debridement Performance

As outlined in 7.5.2, in the first step of the registration, four points on the screw holes of the implant were chosen as fiducials for finding an initial registration guess

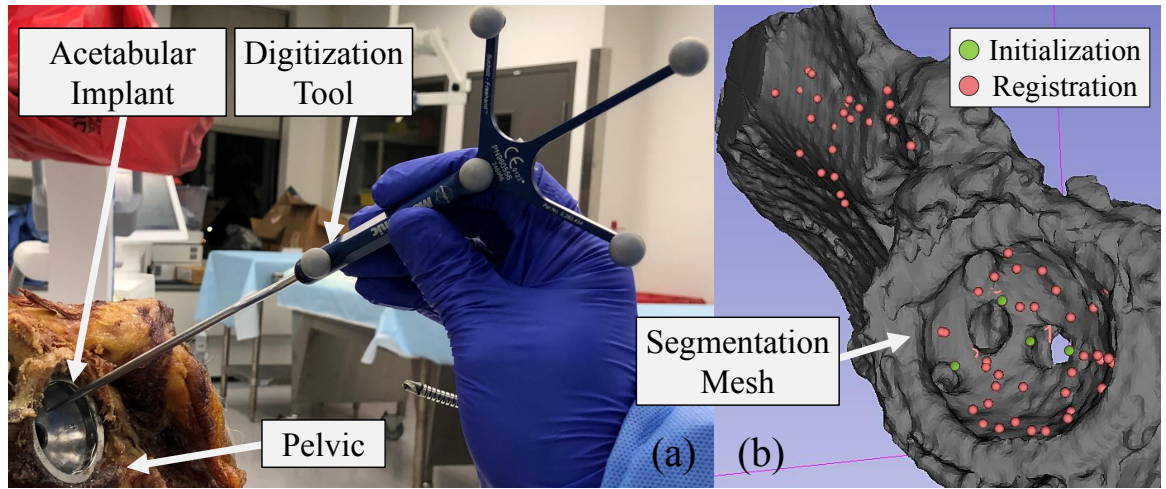


Figure 7.14: The registration procedure. (a) digitization of the acetabular cup implant, (b) the overlayed digitized point cloud on the preoperative CT after registration.

(green points in Fig. 7.14(b)). The root mean square for this step of the registration was 1.80 mm. In the second step, several points were digitized on the surface of the acetabular cup implant and the surrounding exposed bone (overall 76 points). Using this point cloud, the second step of the registration (point cloud to surface registration) was completed and the mean, min, and max residual error for this step were measured as 0.87 mm, 0.02mm, and 3.50 mm, respectively. Fig. 7.14 shows the overlay of the digitized points on the preoperative CT after registration (red points).

Given the registration, any set of desired target points on the patient CT can be transformed to the coordinate system of the robotic system base. To demonstrate the capability of the system in autonomous debridement of simulated phantom and bone lesions, we outlined and executed several surgical paths both in phantom and cadaver studies. Figs. 7.15 and 7.16 show the surface milling capabilities of the system in

CHAPTER 7. SYSTEM INTEGRATION AND EVALUATION

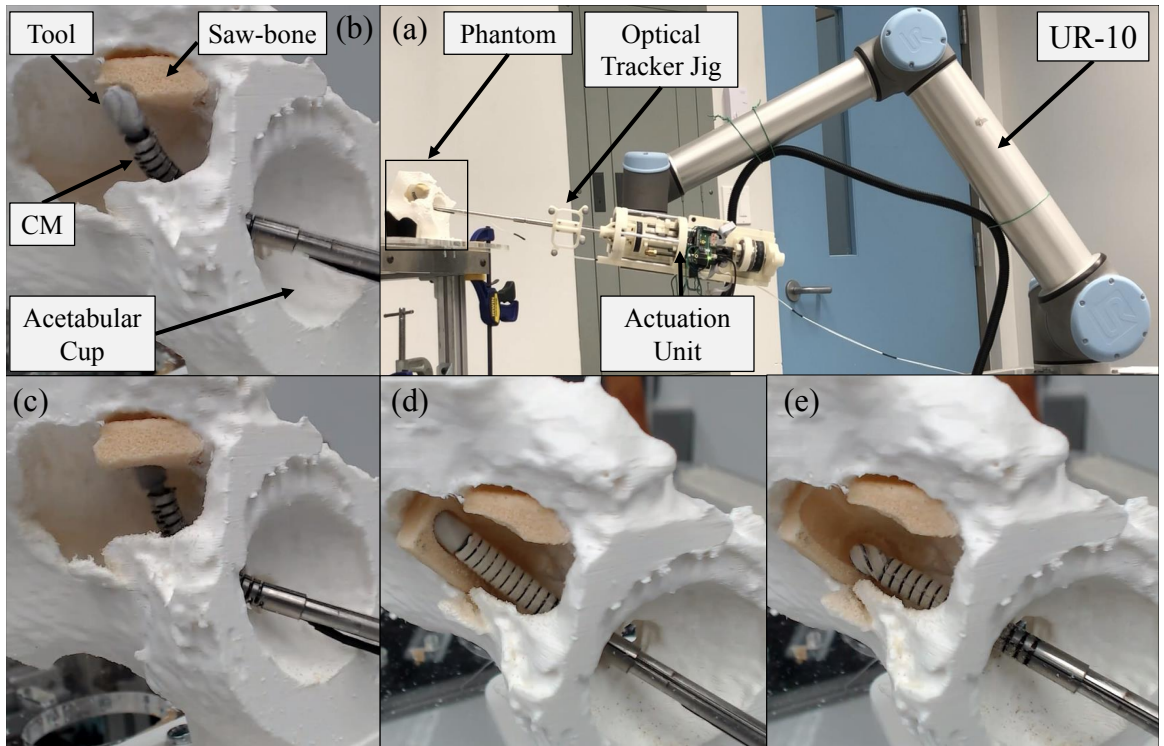


Figure 7.15: Concurrent control of the robotic system during debridement tasks in phantom studies. (a) the experimental setup and the robotic system, (b), (c), (d), and (e) various successful surface debridement tasks on sawbone phantoms mounted on difficult-to-reach locations behind the acetabular cup

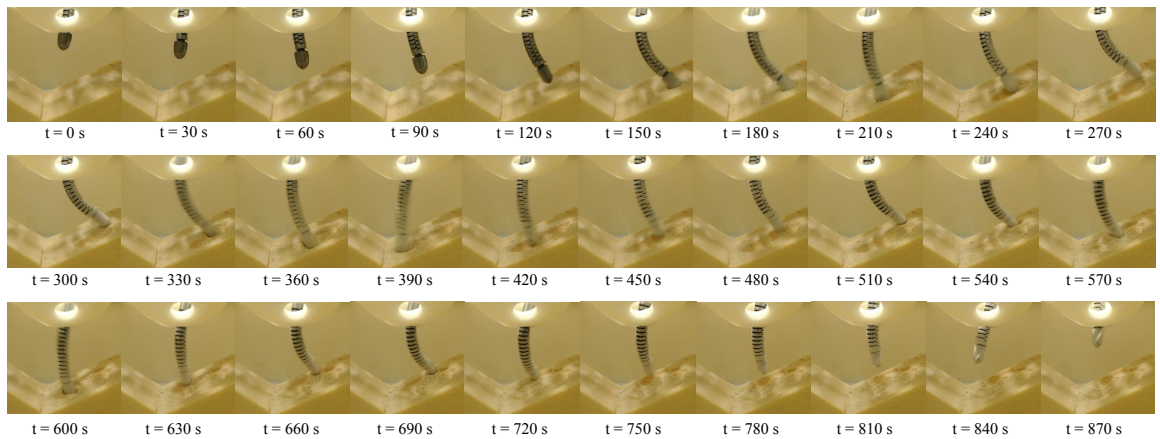


Figure 7.16: Snapshots of the CDM insertion into the acetabular cup component and cutting of the PCF 10 saw-bone phantom based on the planned trajectory.

CHAPTER 7. SYSTEM INTEGRATION AND EVALUATION

various experiments where hard sawbone phantoms with density of 10 and 15 pounds per cubic foot (PCF) are mounted to the back and top of the cavity.

Fig. 7.17 shows the performance of the system in navigating the CM tip position to goal points on desired paths within the workspace of the robotic system, not reachable thoroughly by rigid tools consisting of curvilinear and straight-line segments while the flexible debriding tool is cutting the phantom surfaces with two different densities, (10 and 15 PCF). The desired target trajectories, as well the traversed system tip position during the procedures are shown in Figs. 7.17(a), and 7.17(e). In addition, the preoperative data obtained from the calibration step such as the RCM point, and the acetabular cup rim digitized points, all described with respect to the rigid-link robot's coordinate frame are demonstrated in these figures.

An important aspect of the cutting performance is the velocity with which the flexible tool sweeps the cutting surface (task-space velocity). This velocity is especially important since the system is designed to cut simulated hard bone. To increase the flexibility of the system's user interface, we have incorporated an adjustable velocity percentage parameter, which enables the user to choose what fraction of the generated task-space velocity should be used during cutting. Figs. 7.17(b), and 7.17(f) show the generated task-space velocity for 50% and 80% velocity percentages during cutting, respectively. The mean and standard deviation of the task-space velocity are 2.43 mm/s, and 0.93 mm/s for the 50% ratio, and 3.94 mm/s, and 1.15 mm/s for the 80% ratio. Fig. 7.17(c), and 7.17(g) report the CM tip distance to target goal

CHAPTER 7. SYSTEM INTEGRATION AND EVALUATION

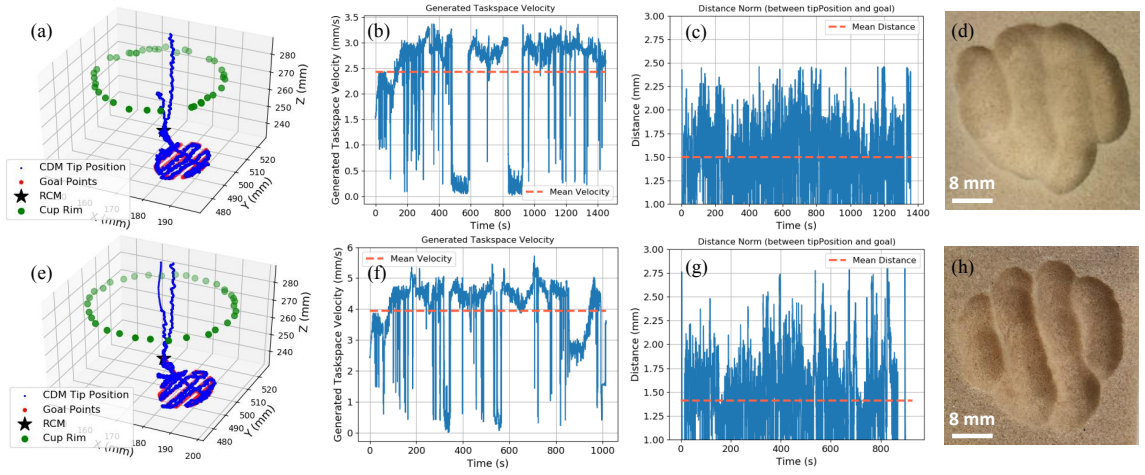


Figure 7.17: The cutting performance for saw-bone phantom PCF 10 (top row) and PCF 15 (bottom row). (a) and (e) the desired cutting trajectory and the tracked CDM tip position; (b) and (f) the generated task-space velocity; (c) and (g) CDM tip distance from the target points during cutting; d and h) the resulting cutting trajectory on the surface for the two phantoms.

points for the entire duration of the cutting experiments. The resulting cut surface for the saw-bone phantoms with PCF 10 and 15 are demonstrated in Fig. 7.17(d), and 7.17(h), respectively. The mean measured cutting volume rate over time for material removal is measured at $0.0083 \text{ mm}^3/\text{s}$.

Similarly, in the cadaver study, drilling and milling of hard bone are demonstrated in Fig. 7.18 while the system of UR-10 and CM are being concurrently controlled to the surgical target points. To make the debridement task further challenging, hard simulated phantom (PCF 15) was mounted at difficult-to-reach locations right behind and above the acetabular cup implant where the lesion area was outlined by our clinical collaborator (Fig. 7.18(d)) and the system successfully reached this area while debriding the hard sawbone. Similar to the controller validation experiments

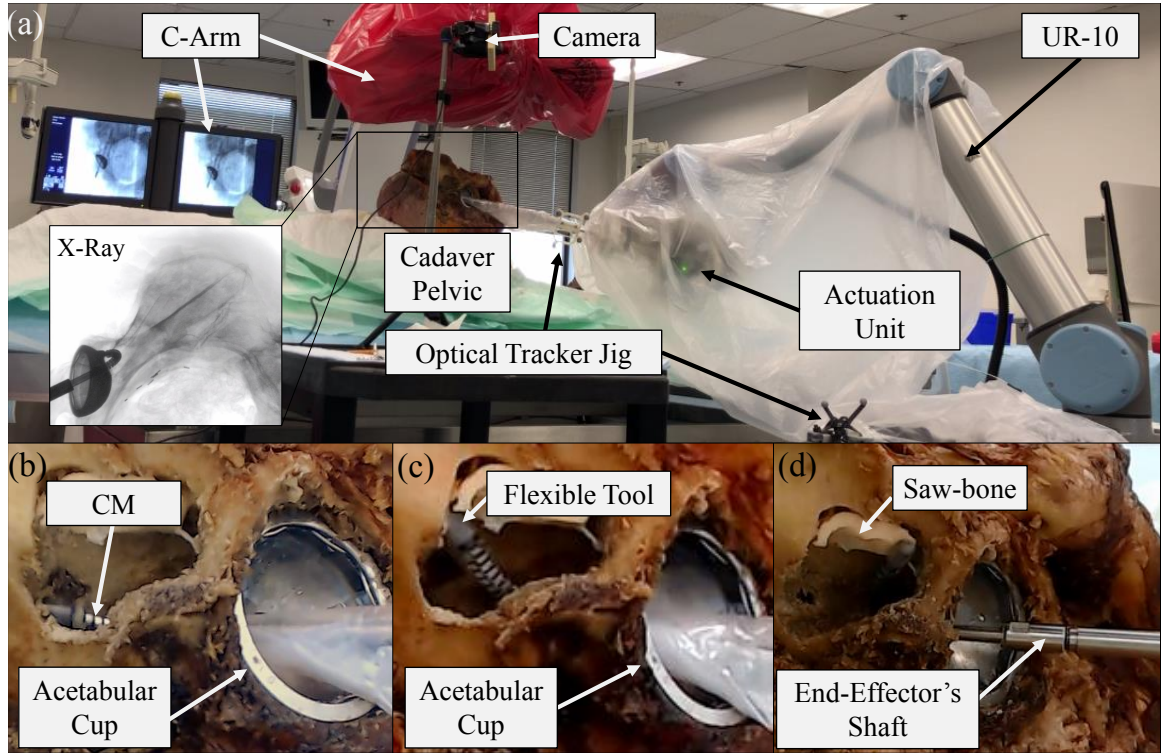


Figure 7.18: Concurrent control of the robotic system during debridement tasks in osteolysis cadaver study. (a) the robotic system deployed in the operating room, (b) drilling task inside hard bone, (c) surface milling task of hard bone, (d) reaching extremely difficult points right behind the implant while milling hard sawbone phantoms.

and using a goal reaching threshold of 1.5 mm, the mean, standard deviation, and maximum error in tracking accuracy for these experiments were 1.47 mm, 0.02 mm, and 1.50 mm, respectively. During the debridement tasks, the flexible instrument's rotation velocity was set to 2250 RPM (see [70] and [69] for further details on the instrument velocity during cutting tasks).

Of note, Fig. 7.19 demonstrates the use of the developed workstation during the curved drilling technique for core decompression of the femoral head. Fig. 7.20 shows X-ray snapshots of both the less-invasive treatment of osteolysis and core decom-

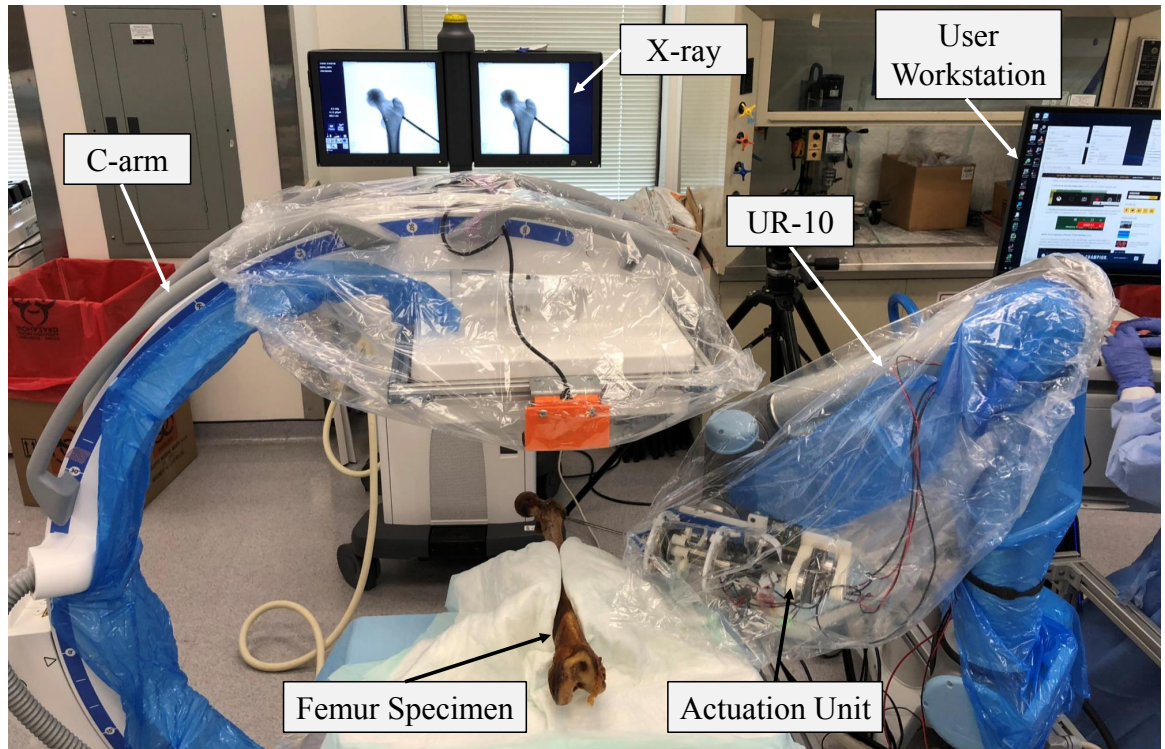


Figure 7.19: Concurrent control of the robotic system during debridement tasks in cadaver study for core decompression of femoral head.

pression of the femoral head using the curved-drilling technique using the developed surgical system. The extreme reach and dexterity of our developed system in confined spaces in human anatomy can be observed in these figures, as the CM tip reaches difficult-to-access sites behind the acetabular implant and the femoral head while milling bone.

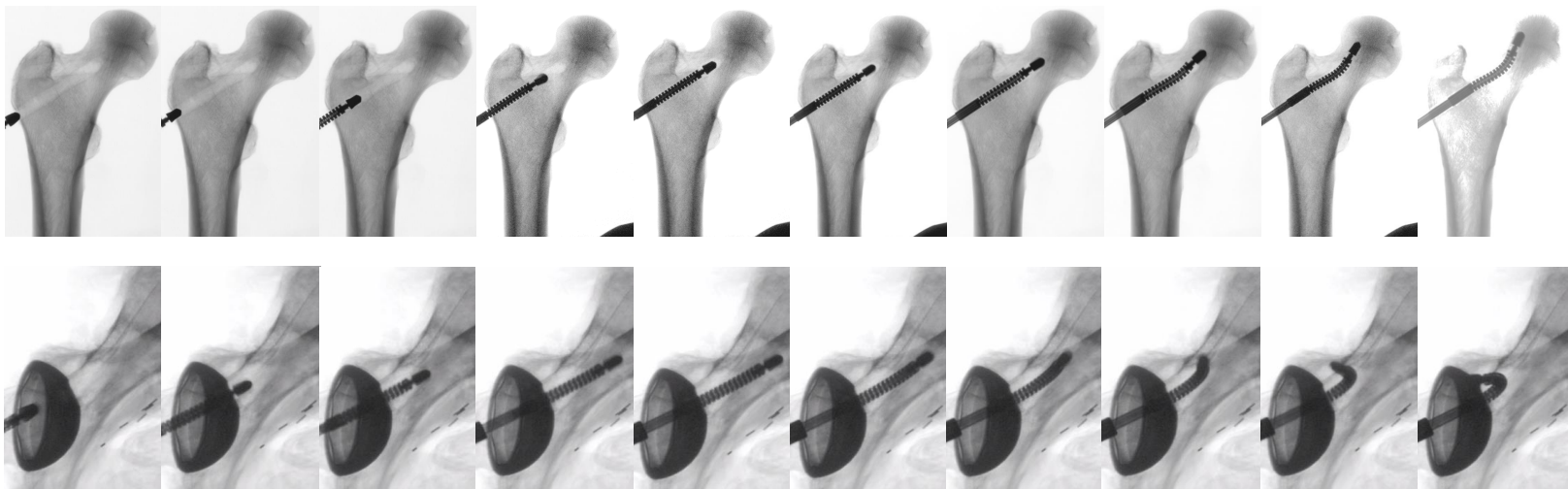


Figure 7.20: X-ray snapshots of two cadaver experiments demonstrating extreme reach and dexterity of the developed system for top row: core decompression of the femoral head osteonecrosis using the curved-drilling technique, and bottom row: less-invasive treatment of pelvic osteolysis behind the acetabular implant.

7.8 Discussion

The constrained workspace analysis results show that our developed system outperforms the conventional rigid tools such as curettes in confined spaces in human anatomies where the rigid tools cannot maneuver as much. This is achieved by the flexibility and extreme bending capabilities of our developed CM. For the case of osteolysis and when restricting the axis range limit to 45° , the combined robotic system can achieve 98% of the lesion area behind the acetabular implant while a rigid tool can at most reach 71% of this area, excluding the most important and problematic locations that are right behind the implant. This limitation worsens if the axis range of motion is restricted further to 30° , where a rigid tool can at most reach 54% of the lesion area while the robotic system can still cover 91% of the area.

The importance of this extended dexterity by the robotic system is realized further in the context of minimally invasive surgery (MIS), where a more restricted axis range limit requires a smaller incision on the patient while most of the lesion area is still reachable. As demonstrated in Fig. 7.9(a), our developed system can reach the surface behind the implant even by only bending the CM while the robot shaft is fixated and aligned with the axis of the implant's screw hole. This can be regarded as a huge advantage of using the robotic system over rigid tools to perform the surgery in a minimally invasive fashion with a small incision point on the patient's skin. In conventional treatment of osteolysis, usually the rigid tool is also inserted from the side of the implant to reach the immediate points behind the implant. The advantage

CHAPTER 7. SYSTEM INTEGRATION AND EVALUATION

of using our robotic system is that the lesion area can be accessed and cleaned out using only the screw hole on the implant without requiring a second incision point on the side.

The evolution of the manipulability ellipsoid in Fig. 7.10 reveals that the addition of the CM to the system enhances the constrained manipulability in two ways. Explicitly, the extreme articulation capabilities of the CM increases the manipulability in its direction of bending. This can be observed in the front view images where the direction of maximum manipulability is in the direction of CM bending. Implicitly, when the CM is bent, additional manipulability is achieved by the actuation unit's roll motor (roll about the end-effector shaft) in the direction perpendicular to the CM's plane of bend. This can be viewed on the top view images where in the earlier iterations (straight CM), the semi-axis of the ellipsoid is relatively small in this direction, while as the CM bends more toward the later iterations, the semi-axis in the direction perpendicular to the CM's plane of bend enlarges.

A comparison of the manipulability ellipsoid semi-axes lengths (gray) and volume (red) in Figs. 7.10(a) and 7.10(b) shows how the manipulability is increased by addition of the CM to the rigid-link robot. Quantitatively, the manipulability ellipsoid's volume is nearly 1000 times more throughout the experiment, where the robotic system without the CM exhibits a very small manipulability in at least one direction resulting in an overall small ellipsoid volume. This difference can be justified by noting firstly that the combined system contains two more degrees of freedom (for roll

CHAPTER 7. SYSTEM INTEGRATION AND EVALUATION

and CM) compared to only the robotic system, and secondly that the degree of freedom achieved by the CM (and roll, when the CM is bent) are completely decoupled from the RCM constraint and only increase the constrained manipulability of the system. The constrained manipulability index is additionally compared in Table 7.2 where the mean manipulability index for the combined system is nearly 10^{12} times larger than that of the robotic system alone when the RCM constraint is active.

The constrained controller results demonstrate that first the optimization framework is successful in maintaining the desired constraints while executing various surgical tasks with great target placement accuracy. It should be noted that the threshold specified for reaching the goal points was set to 1.5 mm during the experiments, which is satisfactory for orthopaedic applications, considering the scales and dimensions of the region of interest. Depending on the application and requirements, this value is adjustable and smaller thresholds could be imposed on the controller in favor of further accuracy at the expense of slightly longer convergence time. For the joint position and velocity constraints, a trade-off between system safety, time and the extent of reach exists. For instance, in the simulation environment we allowed the robotic system to move slightly faster and with greater range compared to the physical system since there is no concern of damage to the system or patient in simulation. From a surgical standpoint, however, to avoid possible bone necrosis caused by the feeding rate of the tool, and considering the safety of the surgical staff, the patient, and the robotic system, extra care must be taken into account.

7.9 Conclusion

This chapter presented the integrated system and preliminary phantom and human cadaver studies demonstrating extreme dexterity, improved patient access and hard bone debridement capabilities using CMs for MIS orthopaedic interventions. While the primary envisioned use-case of the system was MIS orthopaedics, the enhanced dexterity of the system could potentially benefit other surgical applications such as spine and otorhinolaryngology. For potential applications at other scales, the CM dimensions and the choice of the positioning robot can be adjusted accordingly in the next generations of the system. Full surgical autonomy still remains in the realm of science fiction, however, pushing the technological potentials to the boundaries while realizing a meaningful collaboration and team work between the surgeon and robotic systems could greatly benefit healthcare.

The constrained controller framework presented in this chapter involves linear constraints as shown in (7.2). In general, however, nonlinear constraints may be incorporated into the controller. There are computational and accuracy trade-offs between linearly constrained and nonlinearly constrained least squares problems. The algorithms for solving linearly constrained problems (e.g. least squares inequality methods and active set methods) are usually less complex than the algorithms for solving the nonlinearly constrained problems (e.g. reduced-gradient methods and sequential programming methods) [225]. Consequently, solving linearly constrained problems can take less computation time. As a workaround, nonlinear constraints may be linearly

CHAPTER 7. SYSTEM INTEGRATION AND EVALUATION

approximated with a set of hyperplanes (as defined in section 7.3.1.2) to bound a polyhedron that approximates a nonlinear geometric constraint region. An example use-case of such linearization was demonstrated in the formulation of the RCM constraint (section 7.3.1.1). The computational and accuracy trade-offs between the use of a nonlinear constraint and different number of hyperplanes for approximation has been studied in the work of Kapoor [226]. For example, a geometrical spherical constraint can be approximated by 16 hyperplanes with smaller computation time compared to the nonlinear constraint with good accuracy.

7.10 Acknowledgment

I would like to thank all the individuals who, by their contributions, made this work possible. Development of such a system with so many advanced hardware and software components was only achievable by effective team work and close collaboration. Many thanks go to Dr. Mehran Armand, Dr. Russell Taylor, and Dr. Iulian Iordachita for their continuous support and guidance throughout the development of the system. Special thanks to Ms. Rachel Hegeman, without whom, this work would have not been possible. She helped a lot during the development of the system and performing the phantom and cadaver experiments. I would also like to thank my former colleagues Dr. Ryan Murphy, Dr. Farshid Alambeigi, and Mr. Paul Wilkening for their contributions to the development of the system.

Chapter 8

Conclusion

8.1 Summary

In this thesis, we developed a dexterous redundant surgical robotic system for autonomous minimally invasive surgery (MIS) orthopaedic interventions. Even though primary motivation was focused on the less-invasive treatment of osteolysis, the framework and methodologies are applicable to other interventions, orthopaedic related or otherwise. As outlined in previous chapters, other surgeries that could potentially benefit from flexibility and dexterity of the robotic system developed in this work include avascular necrosis of the hip [14, 15] (e.g., core decompression of the femoral head), benign lesion removal [16], treatment of metastatic bone disease [17], shoulder and knee arthroscopic surgeries [18, 19], spine [20], and otorhinolaryngology interventions [21] (e.g. lateral skull base surgery). This list can be extended to any other

CHAPTER 8. CONCLUSION

intervention that requires high dexterity and sufficient rigidity during interactions with hard lesions. The major advantage of the developed system over the state-of-the-art robotic systems for orthopaedic interventions is the autonomous execution of debridement tasks together with enhanced dexterity granted by the continuum manipulator (CM) that enables access to confined and constrained sites in human anatomy. The CM is instrumented with flexible tools and advanced optical fiber sensors that could sense shape and contacts with the surrounding environment.

A variety of autonomous surgical systems have been deployed in the operating rooms for years in orthopaedic applications. The incorporation of rigid-link robots as the core component of these systems does not allow for their adaptation to confined anatomies. The proposed system in this thesis could overcome this limitation by incorporation of a CM that is well suited for orthopaedic applications which enhances dexterity and patient access. Additionally, current paradigm of robot-assisted surgeries depend mostly on an individual surgeon's manual capability. Autonomous robotic surgery, on the other hand, promises enhanced efficacy, safety, and improved surgical outcomes. We demonstrated the feasibility of using a dexterous autonomous system with task autonomy [42] not only to reach difficult-to-access locations in human anatomy, but to successfully mill hard bone as well. It is worthy to mention, however, that in our system, surgeons are still in control of the surgery, i.e. they determine the surgical plan and they monitor and intervene during the surgery, as they see fit. Of note, the control and sensing frameworks described in this thesis are

CHAPTER 8. CONCLUSION

also applicable to semi-autonomous and tele-operated systems.

While in this work, machine learning techniques were incorporated in the sensing components of the system, particularly the fiber Bragg grating (FBG) sensing, other components of the surgical system such as the planning module can potentially benefit from this discipline. An active area of research where learning techniques are being acquired has been the development of robotic surgical assistants that automate portions of a task that are time consuming and tedious by learning from expert demonstration [227]. Another example of such use is the surgical activity recognition using recurrent neural networks [228]. In orthopaedics, researchers have recently incorporated deep learning techniques for automated detection and classification of knee arthroplasty [229]. With recent advancements in machine learning in other fields such as self-driving cars, more rapid adaptation to this domain is expected in autonomous systems developed in the field of medical robotics in the near future, even though safety concerns must be addressed and risks eliminated.

From a surgical workflow stand-point, similar to other medical robotic systems, there is a trade-off between accuracy, surgical outcome, and surgery time. While the calibration steps (hand-eye calibration and FBG sensor preparation) can be performed off-line outside the operating room, deployment and registration of the robotic system in the operating room require inevitable additional time. This additional time can potentially be minimized by familiarizing and training the technical and surgical staff with the robotic system and the robot-assisted surgical workflow.

CHAPTER 8. CONCLUSION

From a design perspective, while there is still room for improvement in future generations of the system, the integration of the flexible debridement tools on the actuation unit was facilitated by incorporation of a central shaft on the actuation unit so that different flexible tools with appropriate tool head sizes could be passed through the shaft and be interchangeably used during the surgery. From the surgical staff and patient safety perspective, the proposed robotic system is optimal since X-ray imaging is an optional component of the system. While and image-based registration procedure could potentially be used, the current proposed surgical workflow relies on high frequency FBG and optical tracker feedback with real-time visualization for intraoperative navigation, leaving intermittent X-ray imaging only as an optional means for confirmation of expected surgical plan execution.

8.2 Limitations and Future Work

The following is a list of the limitations and some relevant directions for future research:

1. The CM used throughout the thesis was designed with requirements associated with less-invasive treatment of osteolysis. While suitable for this application, for other potential applications, CMs with different scales and sizes could be studied and explored.
2. The control frameworks described are independent of the choice of the rigid-

CHAPTER 8. CONCLUSION

link positioning robot. While in this thesis, UR manipulators were incorporated for the system integration and evaluation experiments, these manipulators are primarily designed for industrial applications. As such, other manipulators that are potentially better-suited for medical applications must be studied in the future.

3. Both multi-point (FBG) and distributed (OFDR) fiber optic sensors were fully explored, evaluated, and compared. However, due to interrogation device limitations, only FBG sensors were incorporated for the overall system integration and phantom and cadaver experiments. In the future, distributed sensors must also be incorporated into the system and used in such system evaluations.
4. The control frameworks in this thesis were based on the kinematics of the robotic system. In the future, dynamics may also be explored and strategies based on impedance or hybrid position/force controls may also be incorporated for e.g. controlling the debridement force and CM/bone interaction force for optimal cutting performance.
5. Using a planar CM offers certain advantages for orthopaedic applications where contact forces are relative larger compared to other interventions. However, manipulators capable of 3-D motions may be better suited for applications where extreme manoeuvring capability is required from the CM. Incorporation of such manipulators may potentially eliminate the need for use of bulky positioning

CHAPTER 8. CONCLUSION

robots for additional degrees of freedom. As such, more compact systems could be developed for MIS interventions.

6. This work relied on preoperative patient/CT registration using optical trackers and image-less intraoperative navigation by incorporation of the FBG sensors. Future work could explore the use of image-based approaches where the CM is used as a fiducial and appropriate 2D/3D registration algorithms are applied to register the patient to the robot.
7. Incorporation of endoscopy devices into the CM channels as another means of feedback can potentially improve the navigation tasks.
8. Throughout this dissertation, it was shown that how the data-driven methods could enhance the accuracy of the sensing problems associated with the CMs. A future direction of research may be dedicated to exploration of integrating data- and model-driven methods for these sensing problems to leverage both the underlying physics of the problem as well as the empirical data.
9. The data-driven collision detection algorithm could potentially provide useful information and insight about CM's contacts with the environment. This information could be further augmented with localization of the contacts (region of contact along the body of the manipulator) as well as the contact force values.

Bibliography

- [1] V. Vitiello, S.-L. Lee, T. P. Cundy, and G.-Z. Yang, “Emerging robotic platforms for minimally invasive surgery,” *IEEE reviews in biomedical engineering*, vol. 6, pp. 111–126, 2012.
- [2] R. H. Taylor, A. Menciassi, G. Fichtinger, P. Fiorini, and P. Dario, “Medical robotics and computer-integrated surgery,” in *Springer handbook of robotics*. Springer, 2016, pp. 1657–1684.
- [3] J. Burgner-Kahrs, D. C. Rucker, and H. Choset, “Continuum robots for medical applications: A survey,” *IEEE Transactions on Robotics*, vol. 31, no. 6, pp. 1261–1280, 2015.
- [4] A. H. Gosline, N. V. Vasilyev, E. J. Butler, C. Folk, A. Cohen, R. Chen, N. Lang, P. J. Del Nido, and P. E. Dupont, “Percutaneous intracardiac beating-heart surgery using metal mems tissue approximation tools,” *The International journal of robotics research*, vol. 31, no. 9, pp. 1081–1093, 2012.
- [5] A. Bajo, R. E. Goldman, L. Wang, D. Fowler, and N. Simaan, “Integration

BIBLIOGRAPHY

- and preliminary evaluation of an insertable robotic effectors platform for single port access surgery,” in *2012 IEEE International Conference on Robotics and Automation*. IEEE, 2012, pp. 3381–3387.
- [6] J. S. Schneider, J. Burgner, R. J. Webster III, and P. T. Russell III, “Robotic surgery for the sinuses and skull base: What are the possibilities and what are the obstacles?” *Current opinion in otolaryngology & head and neck surgery*, vol. 21, no. 1, p. 11, 2013.
- [7] J. Burgner, D. C. Rucker, H. B. Gilbert, P. J. Swaney, P. T. Russell, K. D. Weaver, and R. J. Webster, “A telerobotic system for transnasal surgery,” *IEEE/ASME Transactions on Mechatronics*, vol. 19, no. 3, pp. 996–1006, 2013.
- [8] R. A. Beasley, “Medical robots: current systems and research directions,” *Journal of Robotics*, vol. 2012, 2012.
- [9] M. Yip and N. Das, “Robot autonomy for surgery,” *arXiv preprint arXiv:1707.03080*, p. 1, 2017.
- [10] T. L. Ghezzi and O. C. Corleta, “30 years of robotic surgery,” *World journal of surgery*, vol. 40, no. 10, pp. 2550–2557, 2016.
- [11] J. H. Lonner, “Robotics in knee and hip arthroplasty: Current concepts, techniques and emerging uses,” 2019.

BIBLIOGRAPHY

- [12] D. J. Berry, “Periprosthetic fractures associated with osteolysis: a problem on the rise,” *The Journal of arthroplasty*, vol. 18, no. 3, pp. 107–111, 2003.
- [13] C. A. Engh Jr, H. Egawa, S. E. Beykirch, R. H. Hopper Jr, and C. A. Engh, “The quality of osteolysis grafting with cementless acetabular component retention.” *Clinical Orthopaedics and Related Research (1976-2007)*, vol. 465, pp. 150–154, 2007.
- [14] J. H. Herndon and O. E. Aufranc, “Avascular necrosis of the femoral head in the adult: a review of its incidence in a variety of conditions,” *Clinical Orthopaedics and Related Research®*, vol. 86, pp. 43–62, 1972.
- [15] F. Mwale, H. Wang, A. J. Johnson, M. A. Mont, and J. Antoniou, “Abnormal vascular endothelial growth factor expression in mesenchymal stem cells from both osteonecrotic and osteoarthritic hips,” *Bulletin of the NYU hospital for joint diseases*, vol. 69, no. 1, p. S56, 2011.
- [16] A. Toker, K. Ayalp, E. Uyumaz, E. Kaba, Ö. Demirhan, and S. Erus, “Robotic lung segmentectomy for malignant and benign lesions,” *Journal of thoracic disease*, vol. 6, no. 7, p. 937, 2014.
- [17] R. Coleman, “Metastatic bone disease: clinical features, pathophysiology and treatment strategies,” *Cancer treatment reviews*, vol. 27, no. 3, pp. 165–176, 2001.

BIBLIOGRAPHY

- [18] N. C. Small, “Complications in arthroscopic surgery of the knee and shoulder,” *Orthopedics*, vol. 16, no. 9, pp. 985–988, 1993.
- [19] R. Treuting, “Minimally invasive orthopedic surgery: arthroscopy,” *Ochsner Journal*, vol. 2, no. 3, pp. 158–163, 2000.
- [20] N. Lonjon, E. Chan-Seng, V. Costalat, B. Bonnafoux, M. Vassal, and J. Boetto, “Robot-assisted spine surgery: feasibility study through a prospective case-matched analysis,” *European Spine Journal*, vol. 25, no. 3, pp. 947–955, 2016.
- [21] A. Arora, A. Cunningham, G. Chawdhary, C. Vicini, G. S. Weinstein, A. Darzi, and N. Tolley, “Clinical applications of telerobotic ent-head and neck surgery,” *International Journal of Surgery*, vol. 9, no. 4, pp. 277–284, 2011.
- [22] R. J. Murphy, M. D. Kutzer, S. M. Segreti, B. C. Lucas, and M. Armand, “Design and kinematic characterization of a surgical manipulator with a focus on treating osteolysis,” *Robotica*, vol. 32, no. 6, pp. 835–850, 2014.
- [23] M. D. Kutzer, S. M. Segreti, C. Y. Brown, M. Armand, R. H. Taylor, and S. C. Mears, “Design of a new cable-driven manipulator with a large open lumen: Preliminary applications in the minimally-invasive removal of osteolysis,” in *2011 IEEE International Conference on Robotics and Automation*. IEEE, 2011, pp. 2913–2920.

BIBLIOGRAPHY

- [24] M. Armand, M. D. Kutzer, C. Y. Brown, R. H. Taylor, and E. Basafa, “Cable-driven morphable manipulator,” Aug. 22 2017, uS Patent 9,737,687.
- [25] J. A. Singh, “Epidemiology of knee and hip arthroplasty: a systematic review,” *The open orthopaedics journal*, vol. 5, p. 80, 2011.
- [26] S. Kurtz, K. Ong, E. Lau, F. Mowat, and M. Halpern, “Projections of primary and revision hip and knee arthroplasty in the united states from 2005 to 2030,” *JBJS*, vol. 89, no. 4, pp. 780–785, 2007.
- [27] S. M. Kurtz, E. Lau, K. Ong, K. Zhao, M. Kelly, and K. J. Bozic, “Future young patient demand for primary and revision joint replacement: national projections from 2010 to 2030,” *Clinical Orthopaedics and Related Research®*, vol. 467, no. 10, pp. 2606–2612, 2009.
- [28] R. Pivec, A. J. Johnson, S. C. Mears, and M. A. Mont, “Hip arthroplasty,” *The Lancet*, vol. 380, no. 9855, pp. 1768–1777, 2012.
- [29] J. CHARNLEY, “Arthroplasty of the hip: A new operation*.” *Clinical Orthopaedics and Related Research (1976-2007)*, vol. 95, pp. 4–8, 1973.
- [30] R. D. Beckenbaugh and D. M. Ilstrup, “Total hip arthroplasty.” *The Journal of bone and joint surgery. American volume*, vol. 60, no. 3, pp. 306–313, 1978.
- [31] J. S. Siopack and H. E. Jergesen, “Total hip arthroplasty.” *Western journal of medicine*, vol. 162, no. 3, p. 243, 1995.

BIBLIOGRAPHY

- [32] D. J. Hunter and G. H. Lo, “The management of osteoarthritis: an overview and call to appropriate conservative treatment,” *Medical Clinics of North America*, vol. 93, no. 1, pp. 127–143, 2009.
- [33] I. D. Learmonth, C. Young, and C. Rorabeck, “The operation of the century: total hip replacement,” *The Lancet*, vol. 370, no. 9597, pp. 1508–1519, 2007.
- [34] N. P. Hailer, G. Garellick, and J. Kärrholm, “Uncemented and cemented primary total hip arthroplasty in the swedish hip arthroplasty register: evaluation of 170,413 operations,” *Acta orthopaedica*, vol. 81, no. 1, pp. 34–41, 2010.
- [35] K. J. Bozic, S. M. Kurtz, E. Lau, K. Ong, T. P. Vail, and D. J. Berry, “The epidemiology of revision total hip arthroplasty in the united states,” *JBJS*, vol. 91, no. 1, pp. 128–133, 2009.
- [36] J. P. Iannotti, R. A. Balderston, R. E. Booth, R. H. Rothman, J. C. Cohn, and G. Pickens, “Aseptic loosening after total hip arthroplasty: incidence, clinical significance, and etiology,” *The Journal of arthroplasty*, vol. 1, no. 2, pp. 99–107, 1986.
- [37] J. C. Clohisy, G. Calvert, F. Tull, D. McDonald, and W. J. Maloney, “Reasons for revision hip surgery: a retrospective review,” *Clinical Orthopaedics and Related Research®*, vol. 429, pp. 188–192, 2004.
- [38] P. Duffy, J. Sher, and P. Partington, “Premature wear and osteolysis in an

BIBLIOGRAPHY

- ha-coated, uncemented total hip arthroplasty,” *The Journal of bone and joint surgery. British volume*, vol. 86, no. 1, pp. 34–38, 2004.
- [39] T. H. Mallory, A. V. Lombardi Jr, R. A. Fada, J. B. Adams, C. A. Kefauver, and R. W. Eberle, “Noncemented acetabular component removal in the presence of osteolysis: the affirmative,” *Clinical Orthopaedics and Related Research®*, vol. 381, pp. 120–128, 2000.
- [40] P. P. Chiang, D. W. Burke, A. A. Freiberg, and H. E. Rubash, “Osteolysis of the pelvis: evaluation and treatment,” *Clinical Orthopaedics and Related Research®*, vol. 417, pp. 164–174, 2003.
- [41] D. J. Berry, “Management of osteolysis around total hip arthroplasty,” *Orthopedics*, vol. 22, no. 9, pp. 805–808, 1999.
- [42] G.-Z. Yang, J. Cambias, K. Cleary, E. Daimler, J. Drake, P. E. Dupont, N. Hata, P. Kazanzides, S. Martel, R. V. Patel *et al.*, “Medical robotics—regulatory, ethical, and legal considerations for increasing levels of autonomy,” *Sci. Robot*, vol. 2, no. 4, p. 8638, 2017.
- [43] R. H. Taylor, “A perspective on medical robotics,” *Proceedings of the IEEE*, vol. 94, no. 9, pp. 1652–1664, 2006.
- [44] J. H. Lonner and J. F. Fraser, “A brief history of robotics in surgery,” in *Robotics in Knee and Hip Arthroplasty*. Springer, 2019, pp. 3–12.

BIBLIOGRAPHY

- [45] P. Kazanzides, “Robots for orthopaedic joint reconstruction,” *Robotics in surgery: history, current and future applications*, pp. 61–94, 2007.
- [46] N. A. Netravali, M. Börner, and W. L. Bargar, “The use of robodoc in total hip and knee arthroplasty,” in *Computer-Assisted Musculoskeletal Surgery*. Springer, 2016, pp. 219–234.
- [47] T. Siebel and W. Käfer, “Clinical outcome following robotic assisted versus conventional total hip arthroplasty: a controlled and prospective study of seventy-one patients,” *Zeitschrift für Orthopädie und ihre Grenzgebiete*, vol. 143, no. 4, pp. 391–398, 2005.
- [48] M. W. Allen and D. J. Jacofsky, “Evolution of robotics in arthroplasty,” in *Robotics in Knee and Hip Arthroplasty*. Springer, 2019, pp. 13–25.
- [49] J. Rahman, K. Al-Tawil, and W. S. Khan, “Use of robotic-assisted surgery in orthopedics,” in *General Principles of Orthopedics and Trauma*. Springer, 2019, pp. 629–637.
- [50] B. Hagag, R. Abovitz, H. Kang, B. Schmitz, and M. Conditt, “Rio: Robotic-arm interactive orthopedic system makoplasty: user interactive haptic orthopedic robotics,” in *Surgical Robotics*. Springer, 2011, pp. 219–246.
- [51] C. Plaskos, P. Cinquin, S. Lavallée, and A. Hodgson, “Praxiteles: a miniature bone-mounted robot for minimal access total knee arthroplasty,” *The Interna-*

BIBLIOGRAPHY

- tional Journal of Medical Robotics and Computer Assisted Surgery*, vol. 1, no. 4, pp. 67–79, 2005.
- [52] G. R. Klein, D. James, and J. H. Lonner, “Total knee arthroplasty technique: Rosa® knee,” in *Robotics in Knee and Hip Arthroplasty*. Springer, 2019, pp. 185–193.
- [53] L. Vyas, D. Aquino, C.-H. Kuo, J. S. Dai, and P. Dasgupta, “Flexible robotics,” *BJU international*, vol. 107, no. 2, pp. 187–189, 2011.
- [54] T. Baron, “Natural orifice transluminal endoscopic surgery,” *British journal of surgery*, vol. 94, no. 1, pp. 1–2, 2007.
- [55] J. D. Raman, J. A. Cadeddu, P. Rao, and A. Rane, “Single-incision laparoscopic surgery: initial urological experience and comparison with natural-orifice transluminal endoscopic surgery,” *BJU international*, vol. 101, no. 12, pp. 1493–1496, 2008.
- [56] M. F. McGee, M. J. Rosen, J. Marks, R. P. Onders, A. Chak, A. Faulx, V. K. Chen, and J. Ponsky, “A primer on natural orifice transluminal endoscopic surgery: building a new paradigm,” *Surgical innovation*, vol. 13, no. 2, pp. 86–93, 2006.
- [57] S. O’sullivan, N. Nevejans, C. Allen, A. Blyth, S. Leonard, U. Pagallo, K. Holzinger, A. Holzinger, M. I. Sajid, and H. Ashrafian, “Legal, regulatory,

BIBLIOGRAPHY

- and ethical frameworks for development of standards in artificial intelligence (ai) and autonomous robotic surgery,” *The International Journal of Medical Robotics and Computer Assisted Surgery*, vol. 15, no. 1, p. e1968, 2019.
- [58] F. Ficuciello, G. Tamburrini, A. Arezzo, L. Villani, and B. Siciliano, “Autonomy in surgical robots and its meaningful human control,” *Paladyn, Journal of Behavioral Robotics*, vol. 10, no. 1, pp. 30–43, 2019.
- [59] S. O.-R. A. V. S. Committee *et al.*, “Taxonomy and definitions for terms related to on-road motor vehicle automated driving systems,” *SAE Standard J*, vol. 3016, pp. 1–16, 2014.
- [60] A. H. Jinnah, T. D. Luo, J. F. Plate, and R. H. Jinnah, “General concepts in robotics in orthopedics,” in *Robotics in Knee and Hip Arthroplasty*. Springer, 2019, pp. 27–35.
- [61] R. H. Taylor, P. Kazanzides, G. S. Fischer, and N. Simaan, “Medical robotics and computer-integrated interventional medicine,” in *Biomedical Information Technology*. Elsevier, 2020, pp. 617–672.
- [62] T. Haidegger, “Autonomy for surgical robots: Concepts and paradigms,” *IEEE Transactions on Medical Robotics and Bionics*, vol. 1, no. 2, pp. 65–76, 2019.
- [63] S. Sefati, R. Hegeman, F. Alambeigi, I. Iordachita, P. Kazanzides, H. Khanuja, R. Taylor, and M. Armand, “A surgical robotic system for treatment of pelvic

BIBLIOGRAPHY

- osteolysis using an fbg-equipped continuum manipulator and flexible instruments,” *IEEE/ASME Transactions On Mechatronics*, vol. 15, no. 6, pp. 906–915, 2010.
- [64] R. Horaud and F. Dornaika, “Hand-eye calibration,” *The international journal of robotics research*, vol. 14, no. 3, pp. 195–210, 1995.
- [65] Y. Otake, M. Armand, R. S. Armiger, M. D. Kutzer, E. Basafa, P. Kazanzides, and R. H. Taylor, “Intraoperative image-based multiview 2d/3d registration for image-guided orthopaedic surgery: incorporation of fiducial-based c-arm tracking and gpu-acceleration,” *IEEE transactions on medical imaging*, vol. 31, no. 4, pp. 948–962, 2011.
- [66] Y. Otake, R. J. Murphy, M. Kutzer, R. H. Taylor, and M. Armand, “Piecewise-rigid 2d-3d registration for pose estimation of snake-like manipulator using an intraoperative x-ray projection,” in *Medical Imaging 2014: Image-Guided Procedures, Robotic Interventions, and Modeling*, vol. 9036. International Society for Optics and Photonics, 2014, p. 90360Q.
- [67] G. K. Tam, Z.-Q. Cheng, Y.-K. Lai, F. C. Langbein, Y. Liu, D. Marshall, R. R. Martin, X.-F. Sun, and P. L. Rosin, “Registration of 3d point clouds and meshes: A survey from rigid to nonrigid,” *IEEE transactions on visualization and computer graphics*, vol. 19, no. 7, pp. 1199–1217, 2012.
- [68] R. J. Murphy, “Analysis and control of a variable-curvature continuum ma-

BIBLIOGRAPHY

- nipulator for the treatment of osteolysis,” Ph.D. dissertation, Johns Hopkins University, 2015.
- [69] F. Alambeigi, Y. Wang, S. Sefati, C. Gao, R. J. Murphy, I. Iordachita, R. H. Taylor, H. Khanuja, and M. Armand, “A curved-drilling approach in core decompression of the femoral head osteonecrosis using a continuum manipulator,” *IEEE Robotics and Automation Letters*, vol. 2, no. 3, pp. 1480–1487, 2017.
- [70] F. Alambeigi, S. Sefati, R. J. Murphy, I. Iordachita, and M. Armand, “Design and characterization of a debriding tool in robot-assisted treatment of osteolysis,” in *2016 IEEE International Conference on Robotics and Automation (ICRA)*. IEEE, 2016, pp. 5664–5669.
- [71] F. Alambeigi, Y. Wang, R. J. Murphy, I. Iordachita, and M. Armand, “Toward robot-assisted hard osteolytic lesion treatment using a continuum manipulator,” in *2016 38th Annual International Conference of the IEEE Engineering in Medicine and Biology Society (EMBC)*. IEEE, 2016, pp. 5103–5106.
- [72] S. Sefati, F. Alambeigi, I. Iordachita, R. H. Taylor, and M. Armand, “On the effect of vibration on shape sensing of continuum manipulators using fiber bragg gratings,” in *2018 International Symposium on Medical Robotics (ISMR)*. IEEE, 2018, pp. 1–6.
- [73] S. Sefati, R. Hegeman, I. Iordachita, H. Khanuja, R. Taylor, and M. Armand, “A dexterous robotic system for autonomous debridement of osteolytic bone

BIBLIOGRAPHY

- lesions in confined spaces: First human cadaver study,” *IEEE Transactions on Robotics*, pp. 1–17, 2020.
- [74] K. Xu and N. Simaan, “Analytic formulation for kinematics, statics, and shape restoration of multibackbone continuum robots via elliptic integrals,” *Journal of Mechanisms and Robotics*, vol. 2, no. 1, 2010.
- [75] W. S. Rone and P. Ben-Tzvi, “Multi-segment continuum robot shape estimation using passive cable displacement,” in *2013 IEEE International Symposium on Robotic and Sensors Environments (ROSE)*. IEEE, 2013, pp. 37–42.
- [76] D. Trivedi and C. D. Rahn, “Model-based shape estimation for soft robotic manipulators: The planar case,” *Journal of Mechanisms and Robotics*, vol. 6, no. 2, 2014.
- [77] A. Gao, R. J. Murphy, H. Liu, I. I. Iordachita, and M. Armand, “Mechanical model of dexterous continuum manipulators with compliant joints and tendon/external force interactions,” *IEEE/ASME Transactions on Mechatronics*, vol. 22, no. 1, pp. 465–475, 2016.
- [78] R. Roy, L. Wang, and N. Simaan, “Modeling and estimation of friction, extension, and coupling effects in multisegment continuum robots,” *IEEE/ASME Transactions on Mechatronics*, vol. 22, no. 2, pp. 909–920, 2016.
- [79] J. Jung, R. S. Penning, and M. R. Zinn, “A modeling approach for robotic

BIBLIOGRAPHY

- catheters: effects of nonlinear internal device friction,” *Advanced Robotics*, vol. 28, no. 8, pp. 557–572, 2014.
- [80] J. Ha, G. Fagogenis, and P. E. Dupont, “Modeling tube clearance and bounding the effect of friction in concentric tube robot kinematics,” *IEEE Transactions on Robotics*, vol. 35, no. 2, pp. 353–370, 2018.
- [81] H. Yuan, L. Zhou, and W. Xu, “A comprehensive static model of cable-driven multi-section continuum robots considering friction effect,” *Mechanism and Machine Theory*, vol. 135, pp. 130–149, 2019.
- [82] M. S. Moses, R. J. Murphy, M. D. Kutzer, and M. Armand, “Modeling cable and guide channel interaction in a high-strength cable-driven continuum manipulator,” *IEEE/ASME Transactions on Mechatronics*, vol. 20, no. 6, pp. 2876–2889, 2015.
- [83] A. M. Franz, T. Haidegger, W. Birkfellner, K. Cleary, T. M. Peters, and L. Maier-Hein, “Electromagnetic tracking in medicine—a review of technology, validation, and applications,” *IEEE transactions on medical imaging*, vol. 33, no. 8, pp. 1702–1725, 2014.
- [84] C. Shi, X. Luo, P. Qi, T. Li, S. Song, Z. Najdovski, T. Fukuda, and H. Ren, “Shape sensing techniques for continuum robots in minimally invasive surgery: A survey,” *IEEE Transactions on Biomedical Engineering*, vol. 64, no. 8, pp. 1665–1678, 2016.

BIBLIOGRAPHY

- [85] S. Song, Z. Li, H. Yu, and H. Ren, “Electromagnetic positioning for tip tracking and shape sensing of flexible robots,” *IEEE Sensors Journal*, vol. 15, no. 8, pp. 4565–4575, 2015.
- [86] H. Thien, M. Stommel, F. Le Daheron, A. Le Page, Z. Deng, and W. Xu, “Embedded infrared imaging to measure the deformation of a soft robotic actuator,” in *2016 International Conference on Image and Vision Computing New Zealand (IVCNZ)*. IEEE, 2016, pp. 1–6.
- [87] J. M. Croom, D. C. Rucker, J. M. Romano, and R. J. Webster, “Visual sensing of continuum robot shape using self-organizing maps,” in *2010 IEEE International Conference on Robotics and Automation*. IEEE, 2010, pp. 4591–4596.
- [88] D. B. Camarillo, K. E. Loewke, C. R. Carlson, and J. K. Salisbury, “Vision based 3-d shape sensing of flexible manipulators,” in *2008 IEEE International Conference on Robotics and Automation*. IEEE, 2008, pp. 2940–2947.
- [89] M. M. Dalvand, S. Nahavandi, and R. D. Howe, “High speed vision-based 3d reconstruction of continuum robots,” in *2016 IEEE International Conference on Systems, Man, and Cybernetics (SMC)*. IEEE, 2016, pp. 000 618–000 623.
- [90] W. Xu, R. P. L. Foong, and H. Ren, “Maker based shape tracking of a flexible serpentine manipulator,” in *2015 IEEE International Conference on Information and Automation*. IEEE, 2015, pp. 637–642.

BIBLIOGRAPHY

- [91] J. Burgner, S. D. Herrell, and R. J. Webster, “Toward fluoroscopic shape reconstruction for control of steerable medical devices,” in *ASME 2011 Dynamic Systems and Control Conference and Bath/ASME Symposium on Fluid Power and Motion Control*. American Society of Mechanical Engineers Digital Collection, 2011, pp. 791–794.
- [92] E. J. Lobaton, J. Fu, L. G. Torres, and R. Alterovitz, “Continuous shape estimation of continuum robots using x-ray images,” in *2013 IEEE International Conference on Robotics and Automation*. IEEE, 2013, pp. 725–732.
- [93] H. Ren, N. V. Vasilyev, and P. E. Dupont, “Detection of curved robots using 3d ultrasound,” in *2011 IEEE/RSJ International Conference on Intelligent Robots and Systems*. IEEE, 2011, pp. 2083–2089.
- [94] H. Ren and P. E. Dupont, “Tubular enhanced geodesic active contours for continuum robot detection using 3d ultrasound,” in *2012 IEEE International Conference on Robotics and Automation*. IEEE, 2012, pp. 2907–2912.
- [95] R. G. Younge, B. S. Ramamurthy, N. Tanner, R. L. Schlesinger, and E. Udd, “Optical fiber shape sensing systems,” Nov. 1 2011, uS Patent 8,050,523.
- [96] R. Kashyap, *Fiber bragg gratings*. Academic press, 2009.
- [97] R. Xu, A. Yurkewich, and R. V. Patel, “Curvature, torsion, and force sensing

BIBLIOGRAPHY

- in continuum robots using helically wrapped fbg sensors,” *IEEE Robotics and Automation Letters*, vol. 1, no. 2, pp. 1052–1059, 2016.
- [98] H. Liu, A. Farvardin, S. A. Pedram, I. Iordachita, R. H. Taylor, and M. Armand, “Large deflection shape sensing of a continuum manipulator for minimally-invasive surgery,” in *2015 IEEE International Conference on Robotics and Automation (ICRA)*. IEEE, 2015, pp. 201–206.
- [99] M. Froggatt and J. Moore, “High-spatial-resolution distributed strain measurement in optical fiber with rayleigh scatter,” *Applied Optics*, vol. 37, no. 10, pp. 1735–1740, 1998.
- [100] S. Sefati, F. Alambeigi, I. Iordachita, M. Armand, and R. J. Murphy, “Fbg-based large deflection shape sensing of a continuum manipulator: Manufacturing optimization,” in *2016 IEEE SENSORS*. IEEE, 2016, pp. 1–3.
- [101] S. Sefati, M. Pozin, F. Alambeigi, I. Iordachita, R. H. Taylor, and M. Armand, “A highly sensitive fiber bragg grating shape sensor for continuum manipulators with large deflections,” in *2017 IEEE SENSORS*. IEEE, 2017, pp. 1–3.
- [102] D. A. Krohn, T. MacDougall, and A. Mendez, *Fiber optic sensors: fundamentals and applications*. Spie Press Bellingham, Washington, USA, 2014.
- [103] S. Yin and P. Ruffin, “Fiber optic sensors,” *Wiley Encyclopedia of Biomedical Engineering*, 2006.

BIBLIOGRAPHY

- [104] Y.-L. Park, S. Elayaperumal, B. Daniel, S. C. Ryu, M. Shin, J. Savall, R. J. Black, B. Moslehi, and M. R. Cutkosky, “Real-time estimation of 3-d needle shape and deflection for mri-guided interventions,” *IEEE/ASME Transactions On Mechatronics*, vol. 15, no. 6, pp. 906–915, 2010.
- [105] K. R. Henken, J. Dankelman, J. J. van den Dobbelsteen, L. K. Cheng, and M. S. van der Heiden, “Error analysis of fbg-based shape sensors for medical needle tracking,” *IEEE/ASME Transactions on mechatronics*, vol. 19, no. 5, pp. 1523–1531, 2013.
- [106] R. J. Roesthuis, M. Kemp, J. J. van den Dobbelsteen, and S. Misra, “Three-dimensional needle shape reconstruction using an array of fiber bragg grating sensors,” *IEEE/ASME transactions on mechatronics*, vol. 19, no. 4, pp. 1115–1126, 2013.
- [107] M. Abayazid, M. Kemp, and S. Misra, “3d flexible needle steering in soft-tissue phantoms using fiber bragg grating sensors,” in *2013 IEEE International Conference on Robotics and Automation*. IEEE, 2013, pp. 5843–5849.
- [108] N. J. van de Berg, J. Dankelman, and J. J. van den Dobbelsteen, “Design of an actively controlled steerable needle with tendon actuation and fbg-based shape sensing,” *Medical engineering & physics*, vol. 37, no. 6, pp. 617–622, 2015.
- [109] N. Shahriari, R. J. Roesthuis, N. J. van de Berg, J. J. van den Dobbelsteen, and S. Misra, “Steering an actuated-tip needle in biological tissue: Fusing fbg-

BIBLIOGRAPHY

- sensor data and ultrasound images,” in *2016 IEEE International Conference on Robotics and Automation (ICRA)*. IEEE, 2016, pp. 4443–4449.
- [110] J. Arkwright, S. Doe, M. Smith, N. Blenman, I. Underhill, S. Maunder, J. Glasscock, B. Lim, M. Szczesniak, P. Dinning *et al.*, “A fibre bragg grating manometry catheter for in-vivo diagnostics of swallowing disorders,” in *OECC/ACOPT 2008-Joint Conference of the Opto-Electronics and Communications Conference and the Australian Conference on Optical Fibre Technology*. IEEE, 2008, pp. 1–2.
- [111] J. W. Arkwright, I. D. Underhill, S. A. Maunder, N. Blenman, M. M. Szczesniak, L. Wiklendt, I. J. Cook, D. Z. Lubowski, and P. G. Dinning, “Design of a high-sensor count fibre optic manometry catheter for in-vivo colonic diagnostics,” *Optics express*, vol. 17, no. 25, pp. 22 423–22 431, 2009.
- [112] S. Voigt, M. Rothhardt, M. Becker, T. Lüpke, C. Thieroff, A. Teubner, and J. Mehner, “Homogeneous catheter for esophagus high-resolution manometry using fiber bragg gratings,” in *Optical Fibers and Sensors for Medical Diagnostics and Treatment Applications X*, vol. 7559. International Society for Optics and Photonics, 2010, p. 75590B.
- [113] P. Polygerinos, D. Zbyszewski, T. Schaeffter, R. Razavi, L. D. Seneviratne, and K. Althoefer, “Mri-compatible fiber-optic force sensors for catheterization procedures,” *IEEE Sensors Journal*, vol. 10, no. 10, pp. 1598–1608, 2010.

BIBLIOGRAPHY

- [114] C. Shi, S. Giannarou, S.-L. Lee, and G.-Z. Yang, “Simultaneous catheter and environment modeling for trans-catheter aortic valve implantation,” in *2014 IEEE/RSJ International Conference on Intelligent Robots and Systems*. IEEE, 2014, pp. 2024–2029.
- [115] A. Othonos, K. Kalli, D. Pureur, and A. Mugnier, “Fibre bragg gratings,” in *Wavelength Filters in Fibre Optics*. Springer, 2006, pp. 189–269.
- [116] R. J. Roesthuis, S. Janssen, and S. Misra, “On using an array of fiber bragg grating sensors for closed-loop control of flexible minimally invasive surgical instruments,” in *2013 IEEE/RSJ International Conference on Intelligent Robots and Systems*. IEEE, 2013, pp. 2545–2551.
- [117] F. Khan, A. Denasi, D. Barrera, J. Madrigal, S. Sales, and S. Misra, “Multi-core optical fibers with bragg gratings as shape sensor for flexible medical instruments,” *IEEE sensors journal*, 2019.
- [118] H. Liu, A. Farvardin, R. Grupp, R. J. Murphy, R. H. Taylor, I. Iordachita, and M. Armand, “Shape tracking of a dexterous continuum manipulator utilizing two large deflection shape sensors,” *IEEE sensors journal*, vol. 15, no. 10, pp. 5494–5503, 2015.
- [119] X. Wang, G. Fang, K. Wang, X. Xie, K.-H. Lee, J. D. Ho, W. L. Tang, J. Lam, and K.-W. Kwok, “Eye-in-hand visual servoing enhanced with sparse strain

BIBLIOGRAPHY

- measurement for soft continuum robots,” *IEEE Robotics and Automation Letters*, vol. 5, no. 2, pp. 2161–2168, 2020.
- [120] S. C. Ryu and P. E. Dupont, “Fbg-based shape sensing tubes for continuum robots,” in *Robotics and Automation (ICRA), 2014 IEEE International Conference on*. IEEE, 2014, pp. 3531–3537.
- [121] J. Wei, S. Wang, J. Li, and S. Zuo, “Novel integrated helical design of single optic fiber for shape sensing of flexible robot,” *IEEE Sensors Journal*, vol. 17, no. 20, pp. 6627–6636, 2017.
- [122] A. Farvardin, R. J. Murphy, R. B. Grupp, I. Iordachita, and M. Armand, “Towards real-time shape sensing of continuum manipulators utilizing fiber bragg grating sensors,” in *2016 6th IEEE International Conference on Biomedical Robotics and Biomechatronics (BioRob)*. IEEE, 2016, pp. 1180–1185.
- [123] K. O. Hill and G. Meltz, “Fiber bragg grating technology fundamentals and overview,” *Journal of lightwave technology*, vol. 15, no. 8, pp. 1263–1276, 1997.
- [124] D. B. Judd, “Fresnel reflection of diffusely incident light,” *J. Res. Natl. Bur. Stand*, vol. 29, no. 5, p. 329, 1942.
- [125] S. Timoshenko and D. H. Young, *Elements of strength of materials*. Van Nostrand New York, 1968.

BIBLIOGRAPHY

- [126] F. P. Beer, R. Johnston, J. Dewolf, and D. Mazurek, “Mechanics of materials, mcgraw-hill,” *New York*, pp. 150–233, 1981.
- [127] D. K. Gifford, M. E. Froggatt, and S. T. Kreger, “High precision, high sensitivity distributed displacement and temperature measurements using ofdr-based phase tracking,” in *21st International Conference on Optical Fiber Sensors*, vol. 7753. International Society for Optics and Photonics, 2011, p. 77533I.
- [128] P. S. Westbrook, T. Kremp, K. S. Feder, W. Ko, E. M. Monberg, H. Wu, D. A. Simoff, T. F. Taunay, and R. M. Ortiz, “Continuous multicore optical fiber grating arrays for distributed sensing applications,” *Journal of Lightwave Technology*, vol. 35, no. 6, pp. 1248–1252, 2017.
- [129] F. Parent, S. Loranger, K. K. Mandal, V. L. Iezzi, J. Lapointe, J.-S. Boisvert, M. D. Baiad, S. Kadoury, and R. Kashyap, “Enhancement of accuracy in shape sensing of surgical needles using optical frequency domain reflectometry in optical fibers,” *Biomedical optics express*, vol. 8, no. 4, pp. 2210–2221, 2017.
- [130] F. Parent, M. Gérard, F. Monet, S. Loranger, G. Soulez, R. Kashyap, and S. Kadoury, “Intra-arterial image guidance with optical frequency domain reflectometry shape sensing,” *IEEE transactions on medical imaging*, vol. 38, no. 2, pp. 482–492, 2018.
- [131] F. Monet, S. Sefati, P. Lorre, A. Poiffaut, S. Kadoury, M. Armand, I. Iordachita, and R. Kashyap, “High-resolution optical fiber shape sensing of con-

BIBLIOGRAPHY

- tinuum robots: A comparative study,” in *2020 International Conference on Robotics and Automation*. IEEE, 2020, pp. 1–7.
- [132] F. Monet, S. Loranger, V. Lambin-Iezzi, A. Drouin, S. Kadoury, and R. Kashyap, “The rogue: a novel, noise-generated random grating,” *Optics express*, vol. 27, no. 10, pp. 13 895–13 909, 2019.
- [133] P. Lorre, F. Monet, M. Gauthier, A. Poiffaut, A. Roberge, S. Kadoury, and R. Kashyap, “Extruded optical fiber triplets for 3d shape sensing for minimally invasive surgery,” in *Seventh European Workshop on Optical Fibre Sensors*, vol. 11199. International Society for Optics and Photonics, 2019, p. 111991L.
- [134] A. Cormack, “Reconstruction of densities from their projections, with applications in radiological physics,” *Physics in Medicine & Biology*, vol. 18, no. 2, p. 195, 1973.
- [135] C. Q. Donhowe, S. J. Blumenkranz, and V. Duindam, “Systems and methods for reducing measurement error in optical fiber shape sensors,” Aug. 30 2016, uS Patent 9,429,696.
- [136] V. Duindam, G. M. Prisco, D. Q. Larkin, S. P. DiMaio, and D. Panescu, “Steerable flexible needle with embedded shape sensing,” May 2 2017, uS Patent 9,636,040.
- [137] P. Chopra, V. Duindam, T. Zhao, and J. A. Cole, “Shape sensor systems

BIBLIOGRAPHY

- for tracking interventional instruments and methods of use,” Mar. 20 2018, uS Patent 9,918,659.
- [138] B. S. Ramamurthy, N. A. Tanner, R. G. Younge, and R. L. Schlesinger, “Robotic instrument systems and methods utilizing optical fiber sensor,” Nov. 17 2015, uS Patent 9,186,046.
- [139] M. L. Flexman and D. P. Noonan, “Fiber-optical realshape sensing for fluoroscopic surgical navigation,” Jun. 7 2018, uS Patent App. 15/736,124.
- [140] M. L. Flexman, N. N. Kahya, and M. B. Van Der Mark, “Fiber-optic realshape sensing feeding tube,” Feb. 14 2019, uS Patent App. 16/078,047.
- [141] D. P. Noonan, M. L. Flexman, and D. Dijkkamp, “Universal fiber-optical realshape insert,” Jun. 7 2018, uS Patent App. 15/578,860.
- [142] C. Chen and L. Shieh, “A novel approach to linear model simplification,” *International Journal of Control*, vol. 8, no. 6, pp. 561–570, 1968.
- [143] Y. LeCun, Y. Bengio, and G. Hinton, “Deep learning,” *nature*, vol. 521, no. 7553, pp. 436–444, 2015.
- [144] G.-Z. Yang, J. Bellingham, P. E. Dupont, P. Fischer, L. Floridi, R. Full, N. Jacobstein, V. Kumar, M. McNutt, R. Merrifield *et al.*, “The grand challenges of science robotics,” *Science robotics*, vol. 3, no. 14, p. eaar7650, 2018.

BIBLIOGRAPHY

- [145] S. Sefati, S. Sefati, I. Iordachita, R. H. Taylor, and M. Armand, “Learning to detect collisions for continuum manipulators without a prior model,” in *International Conference on Medical Image Computing and Computer-Assisted Intervention*. Springer, 2019, pp. 182–190.
- [146] S. Sefati, R. Hegeman, F. Alambeigi, I. Iordachita, and M. Armand, “Fbg-based position estimation of highly deformable continuum manipulators: Model-dependent vs. data-driven approaches,” in *2019 International Symposium on Medical Robotics (ISMR)*. IEEE, 2019, pp. 1–6.
- [147] S. Sefati, C. Gao, I. Iordachita, R. Taylor, and M. Armand, “Data-driven shape sensing of continuum manipulators in constrained spaces via deep neural networks using fiber bragg grating,” *IEEE Sensors Journal*, pp. 1–10, 2020.
- [148] R. Hartley and A. Zisserman, *Multiple view geometry in computer vision*. Cambridge university press, 2003.
- [149] A. Deguet, R. Kumar, R. Taylor, and P. Kazanzides, “The cisst libraries for computer assisted intervention systems,” in *MICCAI Workshop on Systems and Arch. for Computer Assisted Interventions, Midas Journal*, vol. 71, 2008.
- [150] B. Vagvolgyi, S. DiMaio, A. Deguet, P. Kazanzides, R. Kumar, C. Hasser, and R. Taylor, “The surgical assistant workstation,” in *Proc MICCAI Workshop: Systems and Architectures for Computer Assisted Interventions*, 2008, pp. 1–8.

BIBLIOGRAPHY

- [151] C. Shang, F. Yang, D. Huang, and W. Lyu, “Data-driven soft sensor development based on deep learning technique,” *Journal of Process Control*, vol. 24, no. 3, pp. 223–233, 2014.
- [152] X. Yuan, Y. Gu, Y. Wang, C. Yang, and W. Gui, “A deep supervised learning framework for data-driven soft sensor modeling of industrial processes,” *IEEE Transactions on Neural Networks and Learning Systems*, 2019.
- [153] A. Bajo and N. Simaan, “Finding lost wrenches: Using continuum robots for contact detection and estimation of contact location,” in *2010 IEEE international conference on robotics and automation*. IEEE, 2010, pp. 3666–3673.
- [154] D. C. Rucker and R. J. Webster, “Deflection-based force sensing for continuum robots: A probabilistic approach,” in *2011 IEEE/RSJ International Conference on Intelligent Robots and Systems*. IEEE, 2011, pp. 3764–3769.
- [155] A. Bajo and N. Simaan, “Kinematics-based detection and localization of contacts along multisegment continuum robots,” *IEEE Transactions on Robotics*, vol. 28, no. 2, pp. 291–302, 2011.
- [156] S. Tully, A. Bajo, G. Kantor, H. Choset, and N. Simaan, “Constrained filtering with contact detection data for the localization and registration of continuum robots in flexible environments,” in *2012 IEEE International Conference on Robotics and Automation*. IEEE, 2012, pp. 3388–3394.

BIBLIOGRAPHY

- [157] M. Khoshnam and R. V. Patel, “Estimating contact force for steerable ablation catheters based on shape analysis,” in *2014 IEEE/RSJ International Conference on Intelligent Robots and Systems*. IEEE, 2014, pp. 3509–3514.
- [158] Y. Chen, L. Wang, K. Galloway, I. Godage, N. Simaan, and E. Barth, “Modal-based kinematics and contact detection of soft robots,” *arXiv preprint arXiv:1906.11654*, 2019.
- [159] H. Yuan, P. W. Y. Chiu, and Z. Li, “Shape-reconstruction-based force sensing method for continuum surgical robots with large deformation,” *IEEE Robotics and Automation Letters*, vol. 2, no. 4, pp. 1972–1979, 2017.
- [160] B. Gonenc, A. Chamani, J. Handa, P. Gehlbach, R. H. Taylor, and I. Iordachita, “3-dof force-sensing motorized micro-forceps for robot-assisted vitreoretinal surgery,” *IEEE sensors journal*, vol. 17, no. 11, pp. 3526–3541, 2017.
- [161] I. Iordachita, Z. Sun, M. Balicki, J. U. Kang, S. J. Phee, J. Handa, P. Gehlbach, and R. Taylor, “A sub-millimetric, 0.25 mm resolution fully integrated fiber-optic force-sensing tool for retinal microsurgery,” *International journal of computer assisted radiology and surgery*, vol. 4, no. 4, pp. 383–390, 2009.
- [162] C. Lea, R. Vidal, A. Reiter, and G. D. Hager, “Temporal convolutional networks: A unified approach to action segmentation,” in *European Conference on Computer Vision*. Springer, 2016, pp. 47–54.

BIBLIOGRAPHY

- [163] C. Gao, X. Liu, M. Peven, M. Unberath, and A. Reiter, “Learning to see forces: Surgical force prediction with rgb-point cloud temporal convolutional networks,” in *OR 2.0 Context-Aware Operating Theaters, Computer Assisted Robotic Endoscopy, Clinical Image-Based Procedures, and Skin Image Analysis*. Springer, 2018, pp. 118–127.
- [164] M. Khoshnam and R. V. Patel, “A pseudo-rigid-body 3r model for a steerable ablation catheter,” in *2013 IEEE International Conference on Robotics and Automation*. IEEE, 2013, pp. 4427–4432.
- [165] T. Greigarn and M. C. Çavuşoğlu, “Pseudo-rigid-body model and kinematic analysis of mri-actuated catheters,” in *2015 IEEE International Conference on Robotics and Automation (ICRA)*. IEEE, 2015, pp. 2236–2243.
- [166] T. Greigarn, R. Jackson, T. Liu, and M. C. Çavuşoğlu, “Experimental validation of the pseudo-rigid-body model of the mri-actuated catheter,” in *2017 IEEE International Conference on Robotics and Automation (ICRA)*. IEEE, 2017, pp. 3600–3605.
- [167] D. P. Kingma and J. Ba, “Adam: A method for stochastic optimization,” *arXiv preprint arXiv:1412.6980*, 2014.
- [168] O. González, H. Shrikumar, J. A. Stankovic, and K. Ramamritham, “Adaptive fault tolerance and graceful degradation under dynamic hard real-time scheduling,” in *Proceedings Real-Time Systems Symposium*. IEEE, 1997, pp. 79–89.

BIBLIOGRAPHY

- [169] B. Johnson, “Fault-tolerant microprocessor-based systems,” *IEEE Micro*, no. 6, pp. 6–21, 1984.
- [170] T. A. Mattei, A. H. Rodriguez, D. Sambhara, and E. Mendel, “Current state-of-the-art and future perspectives of robotic technology in neurosurgery,” *Neurosurgical review*, vol. 37, no. 3, pp. 357–366, 2014.
- [171] R. J. Hendrick, S. D. Herrell, and R. J. Webster, “A multi-arm hand-held robotic system for transurethral laser prostate surgery,” in *2014 IEEE international conference on robotics and automation (ICRA)*. IEEE, 2014, pp. 2850–2855.
- [172] J. Li and J. Xiao, “Exact and efficient collision detection for a multi-section continuum manipulator,” in *2012 IEEE International Conference on Robotics and Automation*. IEEE, 2012, pp. 4340–4346.
- [173] L. He, Y. Chao, K. Suzuki, and K. Wu, “Fast connected-component labeling,” *Pattern recognition*, vol. 42, no. 9, pp. 1977–1987, 2009.
- [174] M. L. Comer and E. J. Delp, “Morphological operations for color image processing,” *J. Electronic Imaging*, vol. 8, no. 3, pp. 279–289, 1999.
- [175] J. H. Friedman, “Greedy function approximation: a gradient boosting machine,” *Annals of statistics*, pp. 1189–1232, 2001.
- [176] S. Matinfar, M. A. Nasser, U. Eck, M. Kowalsky, H. Roodaki, N. Navab, C. P.

BIBLIOGRAPHY

- Lohmann, M. Maier, and N. Navab, “Surgical soundtracks: automatic acoustic augmentation of surgical procedures,” *International journal of computer assisted radiology and surgery*, vol. 13, no. 9, pp. 1345–1355, 2018.
- [177] F. Pedregosa, G. Varoquaux, A. Gramfort, V. Michel, B. Thirion, O. Grisel, M. Blondel, P. Prettenhofer, R. Weiss, V. Dubourg *et al.*, “Scikit-learn: Machine learning in python,” *Journal of machine learning research*, vol. 12, no. Oct, pp. 2825–2830, 2011.
- [178] V. J. Manzo, *Max/MSP/Jitter for music: A practical guide to developing interactive music systems for education and more*. Oxford University Press, 2016.
- [179] M. Alber, A. B. Tepole, W. R. Cannon, S. De, S. Dura-Bernal, K. Garikipati, G. Karniadakis, W. W. Lytton, P. Perdikaris, L. Petzold *et al.*, “Integrating machine learning and multiscale modeling—perspectives, challenges, and opportunities in the biological, biomedical, and behavioral sciences,” *npj Digital Medicine*, vol. 2, no. 1, pp. 1–11, 2019.
- [180] R. E. Kalman, “A new approach to linear filtering and prediction problems,” *Transactions of the ASME—Journal of Basic Engineering*, vol. 82, no. Series D, pp. 35–45, 1960.
- [181] E. A. Wan and R. Van Der Merwe, “The unscented kalman filter for nonlinear estimation,” in *Proceedings of the IEEE 2000 Adaptive Systems for Signal Pro-*

BIBLIOGRAPHY

- cessing, Communications, and Control Symposium (Cat. No. 00EX373)*. Ieee, 2000, pp. 153–158.
- [182] E. de Bezenac, A. Pajot, and P. Gallinari, “Deep learning for physical processes: Incorporating prior scientific knowledge,” *Journal of Statistical Mechanics: Theory and Experiment*, vol. 2019, no. 12, p. 124009, 2019.
- [183] Y. Long, X. She, and S. Mukhopadhyay, “Hybridnet: integrating model-based and data-driven learning to predict evolution of dynamical systems,” *arXiv preprint arXiv:1806.07439*, 2018.
- [184] M. Omran, C. Lassner, G. Pons-Moll, P. Gehler, and B. Schiele, “Neural body fitting: Unifying deep learning and model based human pose and shape estimation,” in *2018 international conference on 3D vision (3DV)*. IEEE, 2018, pp. 484–494.
- [185] L. Xiong, G. Jiang, Y. Guo, and H. Liu, “A three-dimensional fiber bragg grating force sensor for robot,” *IEEE Sensors Journal*, vol. 18, no. 9, pp. 3632–3639, 2018.
- [186] Y. Guo, J. Kong, H. Liu, H. Xiong, G. Li, and L. Qin, “A three-axis force fingertip sensor based on fiber bragg grating,” *Sensors and Actuators A: Physical*, vol. 249, pp. 141–148, 2016.
- [187] B. Gonenc and I. Iordachita, “Fbg-based transverse and axial force-sensing

BIBLIOGRAPHY

- micro-forceps for retinal microsurgery,” in *2016 IEEE SENSORS*. IEEE, 2016, pp. 1–3.
- [188] G. Robinson and J. B. C. Davies, “Continuum robots-a state of the art,” in *Proceedings 1999 IEEE international conference on robotics and automation (Cat. No. 99CH36288C)*, vol. 4. IEEE, 1999, pp. 2849–2854.
- [189] I. D. Walker, H. Choset, and G. S. Chirikjian, “Snake-like and continuum robots,” in *Springer Handbook of Robotics*. Springer, 2016, pp. 481–498.
- [190] N. Simaan, K. Xu, W. Wei, A. Kapoor, P. Kazanzides, R. Taylor, and P. Flint, “Design and integration of a telerobotic system for minimally invasive surgery of the throat,” *The International journal of robotics research*, vol. 28, no. 9, pp. 1134–1153, 2009.
- [191] M. Mahvash and P. E. Dupont, “Stiffness control of surgical continuum manipulators,” *IEEE Transactions on Robotics*, vol. 27, no. 2, pp. 334–345, 2011.
- [192] R. S. Penning and M. R. Zinn, “A combined modal-joint space control approach for continuum manipulators,” *Advanced Robotics*, vol. 28, no. 16, pp. 1091–1108, 2014.
- [193] T. Mahl, A. E. Mayer, A. Hildebrandt, and O. Sawodny, “A variable curvature modeling approach for kinematic control of continuum manipulators,” in *2013 American Control Conference*. IEEE, 2013, pp. 4945–4950.

BIBLIOGRAPHY

- [194] T. Mahl, A. Hildebrandt, and O. Sawodny, “A variable curvature continuum kinematics for kinematic control of the bionic handling assistant,” *IEEE transactions on robotics*, vol. 30, no. 4, pp. 935–949, 2014.
- [195] M. K. Sutar, P. Pathak, N. Mehta, A. Sharma, and V. K. Gupta, “Inverse kinematics and control of 4-degree-of-freedom wire-actuated in vivo robot,” *Proceedings of the Institution of Mechanical Engineers, Part I: Journal of Systems and Control Engineering*, vol. 229, no. 2, pp. 77–91, 2015.
- [196] A. Bajo, R. B. Pickens, S. D. Herrell, and N. Simaan, “Constrained motion control of multisegment continuum robots for transurethral bladder resection and surveillance,” in *2013 IEEE International Conference on Robotics and Automation*. IEEE, 2013, pp. 5837–5842.
- [197] P. E. Dupont, J. Lock, B. Itkowitz, and E. Butler, “Design and control of concentric-tube robots,” *IEEE Transactions on Robotics*, vol. 26, no. 2, pp. 209–225, 2009.
- [198] D. C. Rucker, B. A. Jones, and R. J. Webster III, “A geometrically exact model for externally loaded concentric-tube continuum robots,” *IEEE Transactions on Robotics*, vol. 26, no. 5, pp. 769–780, 2010.
- [199] D. C. Rucker and R. J. Webster III, “Statics and dynamics of continuum robots with general tendon routing and external loading,” *IEEE Transactions on Robotics*, vol. 27, no. 6, pp. 1033–1044, 2011.

BIBLIOGRAPHY

- [200] R. Xu, A. Asadian, A. S. Naidu, and R. V. Patel, “Position control of concentric-tube continuum robots using a modified jacobian-based approach,” in *2013 IEEE International Conference on Robotics and Automation*. IEEE, 2013, pp. 5813–5818.
- [201] H. B. Gilbert, D. C. Rucker, and R. J. Webster III, “Concentric tube robots: The state of the art and future directions,” in *Robotics Research*. Springer, 2016, pp. 253–269.
- [202] W. Wei and N. Simaan, “Modeling, force sensing, and control of flexible canulas for microstent delivery,” *Journal of Dynamic Systems, Measurement, and Control*, vol. 134, no. 4, 2012.
- [203] J. Li and J. Xiao, “Task-constrained continuum manipulation in cluttered space,” in *2014 IEEE International Conference on Robotics and Automation (ICRA)*. IEEE, 2014, pp. 2183–2188.
- [204] M. C. Yip and D. B. Camarillo, “Model-less feedback control of continuum manipulators in constrained environments,” *IEEE Transactions on Robotics*, vol. 30, no. 4, pp. 880–889, 2014.
- [205] ———, “Model-less hybrid position/force control: a minimalist approach for continuum manipulators in unknown, constrained environments,” *IEEE Robotics and Automation Letters*, vol. 1, no. 2, pp. 844–851, 2016.

BIBLIOGRAPHY

- [206] S. Sefati, R. J. Murphy, F. Alambeigi, M. Pozin, I. Iordachita, R. H. Taylor, and M. Armand, “Fbg-based control of a continuum manipulator interacting with obstacles,” in *2018 IEEE/RSJ International Conference on Intelligent Robots and Systems (IROS)*. IEEE, 2018, pp. 6477–6483.
- [207] J. Funda, R. H. Taylor, B. Eldridge, S. Gomory, and K. G. Gruben, “Constrained cartesian motion control for teleoperated surgical robots,” *IEEE Transactions on Robotics and Automation*, vol. 12, no. 3, pp. 453–465, 1996.
- [208] A. Kapoor, N. Simaan, and R. H. Taylor, “Suturing in confined spaces: constrained motion control of a hybrid 8-dof robot,” in *ICAR’05. Proceedings., 12th International Conference on Advanced Robotics, 2005*. IEEE, 2005, pp. 452–459.
- [209] A. Kapoor, M. Li, and R. H. Taylor, “Constrained control for surgical assistant robots.” in *ICRA*, 2006, pp. 231–236.
- [210] M. Li, A. Kapoor, and R. H. Taylor, “A constrained optimization approach to virtual fixtures,” in *2005 IEEE/RSJ International Conference on Intelligent Robots and Systems*. IEEE, 2005, pp. 1408–1413.
- [211] R. J. Murphy, Y. Otake, R. H. Taylor, and M. Armand, “Predicting kinematic configuration from string length for a snake-like manipulator not exhibiting constant curvature bending,” in *2014 IEEE/RSJ International Conference on Intelligent Robots and Systems*. IEEE, 2014, pp. 3515–3521.

BIBLIOGRAPHY

- [212] R. T. Farouki and V. Rajan, “On the numerical condition of polynomials in bernstein form,” *Computer Aided Geometric Design*, vol. 4, no. 3, pp. 191–216, 1987.
- [213] P. Wilkening, F. Alambeigi, R. J. Murphy, R. H. Taylor, and M. Armand, “Development and experimental evaluation of concurrent control of a robotic arm and continuum manipulator for osteolytic lesion treatment,” *IEEE robotics and automation letters*, vol. 2, no. 3, pp. 1625–1631, 2017.
- [214] F. Alambeigi, R. J. Murphy, E. Basafa, R. H. Taylor, and M. Armand, “Control of the coupled motion of a 6 dof robotic arm and a continuum manipulator for the treatment of pelvis osteolysis,” in *2014 36th annual international conference of the IEEE engineering in medicine and biology society*. IEEE, 2014, pp. 6521–6525.
- [215] F. Alambeigi, S. Sefati, and M. Armand, “A convex optimization framework for constrained concurrent motion control of a hybrid redundant surgical system,” in *2018 Annual American Control Conference (ACC)*. IEEE, 2018, pp. 1158–1165.
- [216] M. W. Spong and M. Vidyasagar, *Robot dynamics and control*. John Wiley & Sons, 2008.
- [217] W. J. Schroeder, B. Lorensen, and K. Martin, *The visualization toolkit: an object-oriented approach to 3D graphics*. Kitware, 2004.

BIBLIOGRAPHY

- [218] E. Rohmer, S. P. Singh, and M. Freese, “Coppeliasim (formerly v-rep): a versatile and scalable robot simulation framework.”
- [219] K. P. Hawkins, “Analytic inverse kinematics for the universal robots ur-5/ur-10 arms,” Georgia Institute of Technology, Tech. Rep., 2013.
- [220] J. C. Chou and M. Kamel, “Quaternions approach to solve the kinematic equation of rotation, $a/a/x = a/x/a/b$, of a sensor-mounted robotic manipulator,” in *Proceedings. 1988 IEEE International Conference on Robotics and Automation*. IEEE, 1988, pp. 656–662.
- [221] F. C. Park and B. J. Martin, “Robot sensor calibration: solving $ax = xb$ on the euclidean group,” *IEEE Transactions on Robotics and Automation*, vol. 10, no. 5, pp. 717–721, 1994.
- [222] P. J. Besl and N. D. McKay, “Method for registration of 3-d shapes,” in *Sensor fusion IV: control paradigms and data structures*, vol. 1611. International Society for Optics and Photonics, 1992, pp. 586–606.
- [223] T. Yoshikawa, “Manipulability of robotic mechanisms,” *The international journal of Robotics Research*, vol. 4, no. 2, pp. 3–9, 1985.
- [224] H. Sadeghian, F. Zokaei, and S. H. Jazi, “Constrained kinematic control in minimally invasive robotic surgery subject to remote center of motion constraint,” *Journal of Intelligent & Robotic Systems*, vol. 95, no. 3-4, pp. 901–913, 2019.

BIBLIOGRAPHY

- [225] I. Griva, S. G. Nash, and A. Sofer, *Linear and nonlinear optimization*. Siam, 2009, vol. 108.
- [226] A. Kapoor, *Motion constrained control of robots for dexterous surgical tasks*. The Johns Hopkins University, 2008.
- [227] C. E. Reiley, E. Plaku, and G. D. Hager, “Motion generation of robotic surgical tasks: Learning from expert demonstrations,” in *2010 Annual International Conference of the IEEE Engineering in Medicine and Biology*. IEEE, 2010, pp. 967–970.
- [228] R. DiPietro, C. Lea, A. Malpani, N. Ahmidi, S. S. Vedula, G. I. Lee, M. R. Lee, and G. D. Hager, “Recognizing surgical activities with recurrent neural networks,” in *International conference on medical image computing and computer-assisted intervention*. Springer, 2016, pp. 551–558.
- [229] H. Y. Paul, J. Wei, T. K. Kim, H. I. Sair, F. K. Hui, G. D. Hager, J. Fritz, and J. K. Oni, “Automated detection & classification of knee arthroplasty using deep learning,” *The Knee*, 2019.

Vita

Shahriar Sefati received his M.S.E. in Computer Science from the Johns Hopkins University (JHU) in 2017, where he is currently a Ph.D. candidate in the Department of Mechanical Engineering and a member of the Biomechanical- and Image-Guided Surgical Systems (BIGSS) Laboratory, as part of the Laboratory for Computational Sensing and Robotics (LCSR). Prior to joining JHU, he received his B.Sc. in Mechanical Engineering from Sharif University of Technology, Tehran, Iran, in 2014. His research interests are robotics, machine learning, and autonomous systems.